DIFFERING ROLES OF DISORDER: NON-FERMI-LIQUID BEHAVIOR IN $UCu_{5-x}Ni_x$ AND CURIE TEMPERATURE ENHANCEMENT IN $UCu_2Si_{2-x}Ge_x$

By

DANIEL J. MIXSON II

A DISSERTATION PRESENTED TO THE GRADUATE SCHOOL
OF THE UNIVERSITY OF FLORIDA IN PARTIAL FULFILLMENT
OF THE REQUIREMENTS FOR THE DEGREE OF
DOCTOR OF PHILOSOPHY

UNIVERSITY OF FLORIDA

2005

This work is dedicated to my Lord and Savior Jesus Christ. *I can do all things through Christ which strengthens me.-Philippians 4:13*

ACKNOWLEDGMENTS

The Lord has placed a lot of special people in my life. Thus, the thoroughness of the acknowledgments may exceed that of the actual dissertation. I will attempt to thank everyone in the order in which they were introduced into my life.

My first thank you goes to my parents, Dan and Judy Mixson, for their love which includes discipline and support. My sister, Venessa, has been very supportive of all my undertakings. I also want to thank all four of my grandparents who played and are continuing to play a major role in my life: Jim and Sue Mixson; Marion and Winonah Pettit.

I need to recognize my high school physics teacher, Mr. Dan Pate, who served as a mentor to me during my last two years of high school. His inspiration and encouragement were indispensable.

A broad thank you goes to my undergraduate institution, Mississippi State University. The academics were good, but the life lessons I learned hopefully will never be forgotten.

The majority of these acknowledgments are directed to people affiliated with the Department of Physics at the University of Florida (UF). First, I want to thank the two graduate coordinators in the Department of Physics during my time at Florida: Dr. John Yelton and Dr. Mark Meisel. Also, special thanks go to the Department of Physics Student Services personnel who were affiliated with graduate student affairs: Mrs. Susan Rizzo and Mrs. Darlene Latimer. I also want to thank all the faculty who were instructors in the graduate classes I took: Dr. Pierre Sikivie, Dr. Richard Woodard, Dr. Charles Thorn, Dr. James Fry, Dr.

Charles Hopper, Dr. Fred Sharifi, Dr. James Dufty, Dr. Alan Dorsey, Dr. David Tanner, Dr. Robert Coldwell, Dr. Andrey Korytov, and Dr. F. Eugene Dunnam.

I also want to acknowledge the personnel/professors I served under during my "instructor" years: Mr. Greg Martin, Mr. Ray Thomas, Dr. Robert DeSerio, Dr. Dmitrii Maslov, Dr. John Klauder, Dr. Gary Ihas, and Dr. Andrew Rinzler.

The most influential professor upon my physics career at UF has to be Dr. Greg Stewart. I want to thank him for allowing me to work in his lab these past four years. I especially want to thank him for funding me these past two years [with money from a Department of Energy (DOE) grant] and for allowing me to go to Los Alamos National Laboratory (LANL) during the Summer of 2004.

There are many people affiliated with Dr. Stewart's lab that have influenced my research career. First, special thanks go to Dr. Jungsoo Kim for showing me the "ins and outs" of the lab. I am indebted to the following people who were/are affiliated with Dr. Stewart's lab: Mr. Josh Alwood, Mr. Patrick Watts, Mr. Adam Bograd, Mr. Michael Swick, Mr. Tim Jones, and Mr. Don Burnette. I would also like to acknowledge Dr. Bohdan Andraka and members of his group I have interacted with in some form: Dr. Richard Pietri and Mr. Costel Rotundu.

I would also like to recognize Mr. Ju-Hyun Park of Dr. Meisel's lab. His extensive knowledge was very useful for magnetization measurements I took.

I want to thank the following personnel who help make up part of the infrastructure in the Department of Physics at UF and who have been more than willing to assist me: Mrs. Janet Germay, Mr. Pete Axson, Mr. Marc Link, Mr. Edward Storch, Mr. Bill Malphurs, Mr. John Mocko, Mr. Greg Bennett, Mr. Jay Horton, Mr. John Graham, Mr. Greg Labbe, Mr. Bryan Allen, and Mr. Brent Nelson.

I am very grateful to the following five members of my dissertation committee who have taken time out of their busy schedules to serve: Dr. Greg Stewart (chair), Dr. Bohdan Andraka, Dr. Pradeep Kumar, Dr. Dinesh Shah, and Dr. David Tanner.

The following people helped me broaden my knowledge of condensed matter physics at LANL in the Summer of 2004: Dr. John Sarrao, Dr. Eric Bauer, Dr. Veronika Fritzsch, Mr. Jason Leonard, Dr. Mike Hundley, and Dr. Joe Thompson.

Finally, I would like to recognize people around the world I have had the chance to collaborate with on the $UCu_{5-x}Ni_x$ and $UCu_2Si_{2-x}Ge_x$ systems. Special thanks go to Dr. E.-W. Scheidt and Prof. W. Scherer at the University of Augsburg for their low temperature measurements on the specific heat of the $UCu_{5-x}Ni_x$ system with a dilution refrigerator. Also, I would like to thank Drs. T. Murphy and E. Palm at the National High Magnetic Field Laboratory (NHMFL) in Tallahassee, FL, for their low temperature resistivity measurements on the $UCu_{5-x}Ni_x$ system. Also, I would like to thank Prof. A.H. Castro Neto (Boston University) for his communication on the Griffiths phase disorder model and in trying to help me understand how the model applies to the $UCu_{5-x}Ni_x$ system. Lastly, I am very grateful to Dr. M.B. Silva Neto and Prof. A.H. Castro Neto for their theoretical efforts on the $UCu_2Si_{2-x}Ge_x$ system.

TABLE OF CONTENTS

page

ACKNOWLEDGMENTS iii
LIST OF TABLES viii
LIST OF FIGURES ix
ABSTRACT xi

CHAPTER

1 INTRODUCTION 1

- 1.1 NFL Behavior in $UCu_{5-x}Ni_x$ 2
  - 1.1.1 $UCu_{5-x}Pd_x$ 2
  - 1.1.2 $UCu_{5-x}Ni_x$ 10
- 1.2 Curie Temperature Enhancement in $UCu_2Si_{2-x}Ge_x$ 16

2 THEORY 23

- 2.1 Non-Fermi-Liquid Theory 23
  - 2.1.1 Introduction 23
  - 2.1.2 Fermi-Liquids 24
  - 2.1.3 Non-Fermi-liquids 25
- 2.2 Curie Temperature Enhancement Theory 40

3 EXPERIMENTAL TECHNIQUES 46

- 3.1 Arc-Melting 46
- 3.2 X-Ray Diffraction/Lattice Parameter Determination from X-Ray Diffraction 49
- 3.3 Magnetic Susceptibility 53
  - 3.3.1 DC Magnetic Susceptibility 53
  - 3.3.2 AC Magnetic Susceptibility 54
- 3.4 Cryogenics 55
- 3.5 Probes 56
- 3.6 DC Resistivity 60
- 3.7 Specific Heat 62

CHAPTER

4 $UCu_{5-x}Ni_x$ RESULTS AND DISCUSSION 74

- 4.1 Lattice Parameter Values for $UCu_{5-x}Ni_x$ 74
- 4.2 DC Electrical Resistivity Results for $UCu_{5-x}Ni_x$ 79
  - 4.2.1 DC Electrical Resistivity Discussion for $UCu_{5-x}Ni_x$ 79
- 4.3 Magnetization Results for $UCu_{5-x}Ni_x$ 85
  - 4.3.1 Magnetization Discussion for $UCu_{5-x}Ni_x$ 86
- 4.4 AC Magnetic Susceptibility Results for $UCu_{5-x}Ni_x$ 89
  - 4.4.1 AC Magnetic Susceptibility Discussion for $UCu_{5-x}Ni_x$ . . . 89
- 4.5 DC Magnetic Susceptibility Results for $UCu_{5-x}Ni_x$ 92
  - 4.5.1 DC Magnetic Susceptibility Discussion for $UCu_{5-x}Ni_x$ . . . 95
- 4.6 $UCu_{5-x}Ni_x$ Specific Heat Results 102
  - 4.6.1 $UCu_{5-x}Ni_x$ Specific Heat Discussion 114

5 $UCu_2Si_{2-x}Ge_x$ RESULTS AND DISCUSSION 136

- 5.1 $UCu_2Si_{2-x}Ge_x$ Results 139
- 5.2 $UCu_2Si_{2-x}Ge_x$ Discussion 142
  - 5.2.1 T_C Enhancement 142
  - 5.2.2 Resistivity displaying electrons in the ballistic or diffusive regime 143

6 CONCLUSIONS AND FUTURE WORK 157

- 6.1 $UCu_{5-x}Ni_x$ Conclusions 157
- 6.2 Future Work Derived from $UCu_{5-x}Ni_x$ Results 159
- 6.3 $UCu_2Si_{2-x}Ge_x$ Conclusions 163
- 6.4 $UCu_2Si_{2-x}Ge_x$ Future Work 164

APPENDIX 166

A LATTICE PARAMETER GRAPHS 166

B MAGNETORESISTANCE GRAPHS 169

C $UCu_{5-x}Ni_x$ MAGNETIC SUSCEPTIBILITY GRAPHS 172

D $UCu_{5-x}Ni_x$ SPECIFIC HEAT GRAPHS 177

REFERENCES 185

BIOGRAPHICAL SKETCH 195

LIST OF TABLES

Table page

4–1 Lattice parameter values for the nine $UCu_{5-x}Ni_x$ compounds. 126

4–2 The low temperature resistivity results for $UCu_{5-x}Ni_x$ samples. 127

4–3 The low temperature resistivity results for $UCu_{5-x}Ni_x$ samples. 128

4–4 Magnetization data for $UCu_{5-x}Ni_x$ annealed 14 days at 750°C. 129

4–5 AC susceptibility results for select $UCu_{5-x}Ni_x$ samples. 130

4–6 DC magnetic susceptibility results for annealed $UCu_{5-x}Ni_x$. 131

4–7 Fit results for $UCu_{5-x}Ni_x$ dc susceptibility data at 1 kG and 1 T. . . . 132

4–8 Fit results for $UCu_{5-x}Ni_x$ dc susceptibility data at 2 T and 3 T. . . . 133

4–9 Fit results for $UCu_{5-x}Ni_x$ dc susceptibility data at 4 T. 134

4–10 Specific heat results for annealed $UCu_{5-x}Ni_x$ samples. 135

5–1 Magnetic susceptibility and resistivity results for unannealed $UCu_2Si_{2-x}Ge_x$ samples (I). 153

5–2 Magnetic susceptibility and resistivity results for unannealed $UCu_2Si_{2-x}Ge_x$ samples (II). 154

5–3 Magnetic susceptibility and resistivity results for annealed $UCu_2Si_{2-x}Ge_x$ samples (I). 155

5–4 Magnetic susceptibility and resistivity results for annealed $UCu_2Si_{2-x}Ge_x$ samples (II). 156

LIST OF FIGURES

Figure page

1–1 The conventional unit cell for the $AuBe_5$ crystal structure. 3

1–2 The unit cell for the tetragonal $ThCr_2Si_2$ crystal structure. 18

2–1 The Doniach phase diagram taken from Ref. [21]. 35

2–2 The Griffiths phase diagram taken from Ref. [21]. 41

2–3 Curie temperature predictions by Silva Neto and Castro Neto. 45

3–1 Cross-section of a helium 3 probe. 58

3–2 Schematic diagram outlining the thermal relaxation method. 64

3–3 An overhead and bottom view of the mounted sample platform. . . . 65

4–1 Lattice parameter values for unannealed $UCu_{5-x}Ni_x$ compounds. . . . 75

4–2 Lattice parameter values for annealed $UCu_{5-x}Ni_x$ compounds. 76

4–3 Low temperature normalized resistivity for $UCu_{5-x}Ni_x$ samples. . . . 80

4–4 Magnetization for $UCu_{5-x}Ni_x$ samples annealed 14 days at 750°C. . . 87

4–5 AC susceptibility data for annealed $UCu_{4.5}Ni_{0.5}$. 90

4–6 DC susceptibility for annealed UCu_4Ni in different magnetic fields. . . 93

4–7 Low temperature dc susceptibility for annealed $UCu_{5-x}Ni_x$ samples. . 94

4–8 Semilog plot of dc magnetic susceptibility for UCu_4Ni. 99

4–9 Log-log plot of dc magnetic susceptibility for UCu_4Ni. 100

4–10 Specific heat for eight annealed $UCu_{5-x}Ni_x$ samples. 103

4–11 $UCu_{5-x}Ni_x$ specific heat results on a semilog plot. 105

4–12 $UCu_{5-x}Ni_x$ specific heat results on a log-log plot. 106

4–13 Specific heat of $UCu_{4.1}Ni_{0.9}$ in 0, 3, and 6 T. 108

4–14 Specific heat of $UCu_{3.9}Ni_{1.1}$ in 0, 3, and 6 T. 109

4–15 Specific heat of $UCu_{3.8}Ni_{1.2}$ in 0, 3, and 6 T. 110

4–16 Specific heat of UCu_4Ni in 0, 2, 3, and 6 T. 111

4–17 Specific heat of $UCu_{3.95}Ni_{1.05}$ in 0, 2, 3, and 6 T. 112

4–18 Phase diagram for $UCu_{5-x}Ni_x$ and $UCu_{5-x}Pd_x$. 115

4–19 Specific heat data at 6 T for $UCu_{5-x}Ni_x$ samples. 124

5–1 T_C determination for annealed UCu_2Ge_2. 138

5–2 Resistivity versus temperature for UCu_2SiGe. 140

5–3 T_C phase diagram for $UCu_2Si_{2-x}Ge_x$. 144

5–4 The reciprocal RRR values for annealed $UCu_2Si_{2-x}Ge_x$. 146

5–5 Phase diagram for unannealed $UIr_{1-x}Pt_xAl$ system. 152

6–1 DC magnetic susceptibility results for $UCu_{5-x}Co_x$. 162

A–1 Theoretical and experimental x-ray diffraction patterns for annealed UCu_4Ni. 167

A–2 Lattice parameter values versus corresponding error function values for annealed UCu_4Ni. 168

B–1 Low temperature magnetoresistance measurements of annealed UCu_4Ni. 170

B–2 Low temperature magnetoresistance measurements of annealed $UCu_{3.95}Ni_{1.05}$. 171

C–1 Semilog and log-log plots of $UCu_{4.1}Ni_{0.9}$ dc susceptibility. 173

C–2 Semilog and log-log plots of $UCu_{3.95}Ni_{1.05}$ dc susceptibility. 174

C–3 Semilog and log-log plots of $UCu_{3.9}Ni_{1.1}$ dc susceptibility. 175

C–4 Semilog and log-log plots of $UCu_{3.8}Ni_{1.2}$ dc susceptibility. 176

D–1 The determination of $T_{Néel}$ for annealed $UCu_{4.4}Ni_{0.6}$. 178

D–2 Specific heat of annealed UCu_4Ni in 6 and 13 T. 179

D–3 Specific heat of UCu_4Ni in 13 T with Castro Neto-Jones fit. 180

D–4 $UCu_{4.1}Ni_{0.9}$ specific heat data in 3 T and 6 T on a log-log plot. 181

D–5 UCu_4Ni specific heat data in 2 T and 3 T on a log-log plot. 182

D–6 $UCu_{3.95}Ni_{1.05}$ specific heat data in 2 T on a log-log plot. 183

D–7 $UCu_{3.8}Ni_{1.2}$ specific heat data in 3 T on a log-log plot. 184

Abstract of Dissertation Presented to the Graduate School
of the University of Florida in Partial Fulfillment of the
Requirements for the Degree of Doctor of Philosophy

DIFFERING ROLES OF DISORDER: NON-FERMI-LIQUID BEHAVIOR IN $UCu_{5-x}Ni_x$ AND CURIE TEMPERATURE ENHANCEMENT IN $UCu_2Si_{2-x}Ge_x$

By

Daniel J. Mixson II

May 2005

Chair: Gregory R. Stewart
Major Department: Physics

Disorder may be created by the substitution of one element for another where the elements are found on the periodic chart of elements. One compound that has structural disorder is $UCu_{5-x}Ni_x$ where the transition element, copper, is replaced with another transition element, nickel. Another compound that has disorder is $UCu_2Si_{2-x}Ge_x$ where silicon atoms are substituted with isovalent germanium elements. The disorder in these two compounds leads to interesting physics at low temperatures.

UCu_5 is antiferromagnetic at around 16 K; however, the antiferromagnetism may be suppressed by doping nickel atoms onto the copper sites in the unit cell. The antiferromagnetic transition is suppressed to zero for the UCu_4Ni compound, leading to non-Fermi-liquid (NFL) behavior due to a quantum critical point. Multiple $UCu_{5-x}Ni_x$ compounds with small changes in the stoichiometry are synthesized around UCu_4Ni in order to investigate if the cause of NFL behavior crosses over from a quantum critical point to rare strongly coupled magnetic clusters in a Griffiths phase scenario. The investigation is carried out by performing

the following measurements on $UCu_{5-x}Ni_x$ compounds: 1) x-ray diffraction; 2) direct current (dc) magnetic susceptibility as a function of temperature in various magnetic fields; 3) alternating current (ac) susceptibility; 4) magnetization measurements as a function of magnetic fields; 5) low temperature dc resistivity; and 6) low temperature specific heat in zero and applied magnetic fields (up to 13 T).

UCu_2Ge_2 and UCu_2Si_2 are ferromagnets with ferromagnetic ordering temperatures, T_{Curie}, occurring at around 108.5 K and 102.5 K respectively. Various compounds lying between the two aforementioned ferromagnets on the $UCu_2Si_{2-x}Ge_x$ phase diagram were synthesized in order to test theoretical predictions made concerning the nonmonotonic behavior of T_{Curie} as a function of the amount of structural disorder. The nonmonotonic behavior was confirmed by measuring the dc magnetic susceptibility. As the amount of disorder is varied, the electron scattering crosses over from a ballistic regime for no structural disorder to a diffusive regime when disorder is present. This crossover is proven by dc resistivity measurements.

CHAPTER 1
INTRODUCTION

The chemical substitution of one element for another element has been a longstanding practice in the condensed matter physics community. In fact, the first system published that claimed non-Fermi-liquid (NFL) behavior [i.e., deviations occurred from Fermi liquid behavior: at low temperatures, ρ (the resistivity) = ρ_0 + AT^2, χ (magnetic susceptibility) and C/T (specific heat divided by temperature) approach a constant value as T → 0 K] was $Y_{1-x}U_xPd_3$ by Seaman *et al.* [136]. This NFL behavior in $Y_{1-x}U_xPd_3$ was attributed to disorder created by the chemical substitution of yttrium atoms for uranium atoms [93]. Another such alloy that displays NFL behavior at low temperatures due to disorder is $UCu_{5-x}Pd_x$. The characteristics of the $UCu_{5-x}Pd_x$ system will be discussed and the motivation behind the study of the isostructural $UCu_{5-x}Ni_x$ system will be clarified.

A second part of this dissertation concerns the ferromagnetic behavior of the ternary $UCu_2Si_{2-x}Ge_x$ compounds. The driving force behind these compounds is disorder, specifically the silicon/germanium sublattice disorder introduced by substituting (or doping) germanium atoms onto silicon atom sites in the unit cell (the fundamental "building block" of any crystal structure). Silva Neto and Castro Neto have made theoretical predictions that this sublattice disorder combined with thermal and quantum fluctuations will enhance Curie temperature values in quantum ferromagnets [137]. A discussion of why the $UCu_2Si_{2-x}Ge_x$ system was chosen to test the theory will be carried out.

1.1 NFL Behavior in $UCu_{5-x}Ni_x$

1.1.1 $UCu_{5-x}Pd_x$

$UCu_{5-x}Pd_x$ was the first system to display NFL behavior with no dilution of the *f*-atom (i.e., the uranium atom) site [143]. UCu_5 is an antiferromagnet with a Néel temperature, T_N, around 15 K [104]. The palladium (Pd) atoms are doped onto the copper (Cu) atom sites and this suppresses the antiferromagnetic ordering temperature. Andraka and Stewart reported that doping the Cu sites with Pd suppressed the antiferromagnetism at $x \approx 0.75$ and that UCu_4Pd displayed NFL behavior with a power law divergence in the specific heat ($C/T \sim T^{-0.32}$ for 1-10 K) and a linear dependence in the resistivity ($\rho = \rho_0$ - a T for 0.3 to 10 K, with $\rho_0 = 375\ \mu\Omega$ cm and a = 6.3 $\mu\Omega$ cm K^{-1}) [4]. More recent measurements down to lower temperatures have shown that UCu_4Pd orders antiferromagnetically below $T_N = 190$ milliKelvin (mK) while $UCu_{3.9}Pd_{1.1}$ shows no ordering temperature down to the lowest measurable temperature [77].

UCu_5 crystallizes in the $AuBe_5$ structure with the beryllium sublattice possessing two inequivalent beryllium sites. A schematic drawing of the $AuBe_5$ crystal structure is shown in Fig. 1–1 on page 3 [27]. The $AuBe_5$ structure is cubic with twenty-four atoms occupying a unit cell. So, for UCu_5, there are four uranium (U) atoms and twenty Cu atoms. The U atoms occupy the face-centered cubic (fcc) sites (denoted 4a). The Cu atoms are divided up among sixteen smaller sites (called 16e sites) and four larger sites (called 4c sites). When the Cu atoms are replaced by Pd atoms in $UCu_{5-x}Pd_x$ compounds and since Pd atoms are larger than Cu atoms, one might expect an ordered model for the UCu_4Pd sample: the U atoms would occupy the 4a sites, the Pd atoms would occupy the 4c sites, and the Cu atoms would occupy the 16e sites. Some compounds do exhibit this ordered arrangement in the $AuBe_5$ structure: $AgErCu_4$ [145] and $ErMnNi_4$ [43]. Despite claims by Chau *et al.* using a high-intensity powder diffractometer that UCu_4Pd

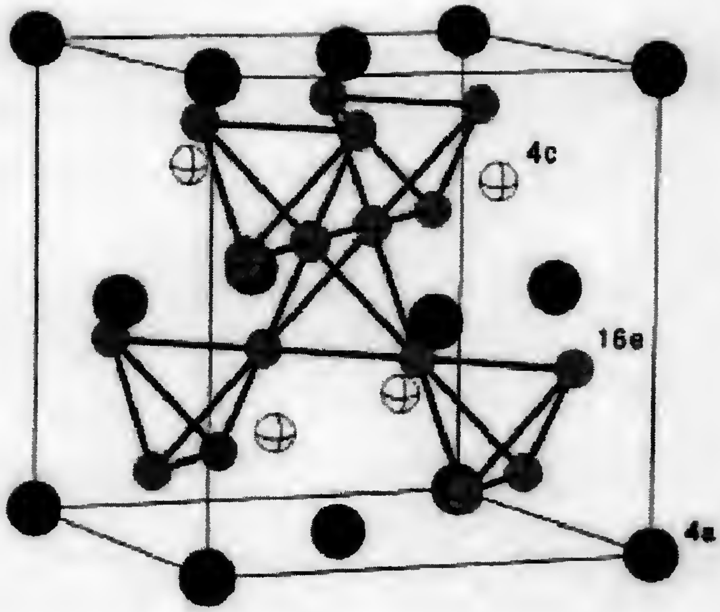

Figure 1–1: The conventional unit cell for the cubic $AuBe_5$ crystal structure. The 4a sites are located on the edges of the cube and in the center of each square face. The 4c and 16e sites are crystallographically inequivalent sites with the 4c site larger than the 16e site. The drawing is taken from the paper by Chau *et al.* [27].

is chemically ordered [27], Pd/Cu disorder does exist on the 4c and 16e sites with experimental evidence coming from MacLaughlin *et al.* using magnetic resonance measurements [93], Booth *et al.* using extended x-ray-absorption fine-structure (EXAFS) [15], and Weber *et al.* using unannealed and annealed $UCu_{5-x}Pd_x$ lattice parameter values [160]. MacLaughlin *et al.* found that muons are relaxed rapidly in UCu_4Pd and this rapid relaxation comes from a large disorder effect. Booth *et al.* revealed that for the unannealed UCu_4Pd, 24 ± 3% of the Pd occupies the majority sites (the 16e sites) instead of all the Pd occupying the minority 4c sites. Then, Weber *et al.* found that annealing UCu_4Pd decreased the lattice parameters compared to unannealed UCu_4Pd. These results from the lattice parameters indicate that Pd atoms are rearranged from the 16e to the 4c sites. However, Booth *et al.* performed EXAFS measurements on annealed UCu_4Pd samples made by Weber *et al.* and still found that 19% of the Pd is located on the 16e sites [16]. Clearly, UCu_4Pd shows Cu/Pd disorder on the Cu sublattices.

The disorder in $UCu_{5-x}Pd_x$ leads to unique low temperature properties in the specific heat, especially for the UCu_4Pd compound. Andraka and Stewart proposed, based upon their results, that UCu_4Pd lies near the suppression of a second order phase transition, $T_N = 0$ [4]. This quantum critical point (QCP) (i.e., $T_N = 0$) was thought to be the source of NFL behavior for the thermodynamic properties at finite temperatures. As mentioned earlier, power law behavior was found between 1 and 10 K while the lowest temperature C/T data fell under the power law curve by as much as 16% at 0.34 K [4]. Then Scheidt *et al.* extended the specific heat measurements down to lower temperatures and found that for unannealed UCu_4Pd, the specific heat data leveled off at around 0.2 K [130]. The specific heat of unannealed UCu_4Pd showed logarithmic temperature dependence over a decade of temperature (0.2 K to 2 K) in agreement with the work of Vollmer *et al.* [156]. However, there is disagreement concerning the behavior below 200 mK. Scheidt *et al.* measured ac susceptibility as a function of frequency and found a peak at $\sim$ 0.24 K at 95.5 Hz that shifted to 0.27 K at 995 Hz. This large shift in the ac susceptibility peak with frequency was strong evidence for superparamagnetism associated with spin clusters [105]. This magnetism at lowest temperatures was consistent with the theoretical efforts of Castro Neto *et al.* [20] in which the formation of magnetic clusters (i.e., Griffiths phase behavior [57]) in highly correlated systems is caused by disorder that leads to competition between the Kondo and Ruderman-Kittel-Kasuya-Yosida (RKKY) interaction. In addition, unpublished results by Dr. Jungsoo Kim that measured the specific heat of UCu_4Pd in various magnetic fields showed a magnetic field induced peak, a feature that is indicative of a possible Griffiths phase disorder description. On the other hand, Vollmer *et al.* concluded that below 0.2 K, there is spin-glass freezing of the U magnetic moments in UCu_4Pd. Different interpretations have continued to carry on. Körner *et al.* then stated that UCu_4Pd is antiferromagnetic with $T_N = 190$ mK and simultaneously shows evidence of spin glass behavior below T_N from specific heat and ac susceptibility measurements [77]. Then Weber *et al.* performed experiments on annealed samples of UCu_4Pd [160]. Not only did they perform lattice parameter measurements as stated earlier, but also specific heat data at low temperatures were taken. Annealing the UCu_4Pd sample for 14 days at 750 °C suppressed the antiferromagnetic transition with no hint of the transition down to the lowest measured temperature of 80 mK. Also, the logarithmic temperature dependence of the specific heat now covered more than two decades of temperature starting from 80 mK. This expansion of the logarithmic temperature dependence suggested that crystallographic order could be an alternative tuning parameter for NFL behavior besides pressure [14], doping [5], or magnetic field [61]. This logarithmic temperature dependence also suggests that the Kondo disorder model (consisting of a broad distribution $P(T_K)$

of Kondo temperatures, T_K, which extends down to very low temperatures [11, 99]) could be a plausible explanation for the NFL behavior in UCu_4Pd [11]. Another interpretation based upon $C/T \approx \log T$ concerns ordered systems near a QCP [143]. Unfortunately, these major theories (Griffiths phase, ordered systems, Kondo disorder model are discussed in greater detail in the "Theory" chapter) based upon the specific heat data have gaps in their interpretation. For example, the specific heat data in annealed UCu_4Pd are not consistent with the theoretically predicted power-law behavior, $C/T \propto T^{-1+\lambda}$, for the Griffiths phase model [160] while ordered systems (e.g., UBe_{13}) near a QCP do not show a magnetic field induced peak in C/T [143]. The Kondo disorder model is not a valid interpretation based upon resistivity data discussed below.

The dc electrical resistivity for $UCu_{5-x}Pd_x$ has been measured by several groups. The first electrical resistivity measurements for UCu_4Pd were reported by Andraka and Stewart [4]. For temperatures lower than 10 K, the UCu_4Pd resistivity was approximately linear in T: $\rho \approx \rho_0$ (1 - T/T_0) where $\rho_0 \approx 375$ $\mu\Omega$ cm and $T_0 = 60$ K. This linear temperature dependence of ρ gave experimental evidence for a non-Fermi-liquid ground state. Chau and Maple then measured the electrical resistivity for unannealed $UCu_{5-x}Pd_x$ with concentrations ranging from x = 0 to x = 1.5 [26]. They found that $\rho(T)$ increases monotonically with decreasing T and does not display a peak or downturn at low temperatures. Experimental evidence also proved that the resistivity of the Pd-substituted samples increases with increasing Pd concentration. Specifically, Chau and Maple fit the electrical resistivity data for UCu_4Pd to $\rho \approx \rho_0$ (1 - T/T_0) below 10 K and found $\rho_0 = 258$ $\mu\Omega$ cm and $T_0 = 63$ K, numbers that are comparable to Andraka and Stewart's results. This linear dependence in the resistivity suggested that the NFL behavior in UCu_4Pd may be explained by a Kondo disorder model. The results of Weber *et al.* seem to suggest otherwise [160]. First, annealing UCu_4Pd

samples drops the residual resistivity, ρ_0, by a factor of about 2.5. Then, the linear temperature dependence that was reported previously for the unannealed samples disappears with annealing. The resistivity of the annealed samples has a Kondo-like minimum around 35 K. However, the resistivity of the 14-day UCu_4Pd annealed sample for 2 K $\leq$ T $\leq$ 8 K may be described by a Fermi-liquid expansion $\rho - \rho_r = AT^2 + BT^4$ where $\rho_r = 141.5\ \mu\Omega$ cm, A = -0.024 $\mu\Omega$ cm K^{-2}, and B = -0.00013 $\mu\Omega$ cm K^{-4} [160]. Weber *et al.* note that the sign of A in the expansion above is unusual for *f* moments forming a Kondo lattice. Thus, Weber *et al.* conclude that the Kondo disorder model is not applicable for annealed UCu_4Pd and suggest it is not the origin for NFL behavior in unannealed UCu_4Pd either.

The third major measurement performed on $UCu_{5-x}Pd_x$ samples concerns dc magnetic susceptibility measurements. Andraka and Stewart reported that dc magnetic susceptibility of UCu_4Pd could be approximated by $T^{-\delta}$ at low fields (100 G) from 10 K down to 1.8 K [4]. This χ temperature dependence is consistent, although coincidental with an overcompensated four-channel magnetic Kondo model [129]. It will be noted here (although not important to one of the two subjects of this dissertation) that a spin glass freezing temperature of 2 K was measured for the UCu_3Pd_2 composition [4]. Chau and Maple then measured the dc magnetic susceptibility for $UCu_{5-x}Pd_x$ and were able to fit the low temperature χ data for UCu_4Pd to $\chi(T) = \chi_0 \ln(T/T_0)$ for 2 K < T < 10 K [26]. Plus, Chau and Maple state that above x = 1.5, the $UCu_{5-x}Pd_x$ system exhibits spin-glass freezing. They also mention that for the low temperature χ data, it is difficult to distinguish between a logarithmic and a weak-power-law temperature dependence [26]. Vollmer *et al.* then measured the magnetic susceptibility down to 0.08 K for UCu_4Pd [156]. The low temperature χ data according to Vollmer *et al.* suggest a spin-glass transition around 0.2 K due to the splitting between zero-field cooled magnetization and field-cooled magnetization. Körner *et al.* confirmed the evidence of spin glass behavior below the antiferromagnetic transition temperature for unannealed UCu_4Pd by dc-susceptibility measurements [77].

All of these interesting results from the specific heat, resistivity, ac susceptibility, and dc susceptibility prove no current theoretical model is able to explain all the current elements of the experimental data [16]. New theories are being developed to try to explain all the different data such as a Kondo/quantum spin-glass critical point [56]. These results have also led researchers to further explore the role of disorder in the $UCu_{5-x}Pd_x$ system, especially for UCu_4Pd.

Expanding upon their research on unannealed UCu_4Pd [15], Booth *et al.* made EXAFS measurements on UCu_4Pd as a function of annealing time [16]. Their results show that the main effect of annealing is to decrease the fraction of Pd atoms on the nominally Cu 16e sites, confirming the conclusions reached by Weber *et al.* concerning annealing upon UCu_4Pd [160]. Booth *et al.* also conclude that disorder must be included in any complete microscopic theory of NFL properties in the $UCu_{5-x}Pd_x$ system.

MacLaughlin *et al.* performed magnetic resonance measurements upon the $UCu_{5-x}Pd_x$ system and also concluded that structural disorder is a major factor in NFL behavior. The longitudinal-field muon spin rotation (μSR) relaxation measurements on $UCu_{5-x}Pd_x$ at low fields reveal a wide distribution of muon relaxation rates and divergences in the frequency dependence of spin correlation functions [93]. Interestingly, the divergences seem to be due to slow dynamics associated with quantum spin-glass behavior, rather than quantum criticality as in a uniform system (such as $CeNi_2Ge_2$ [68, 140], $YbRh_2Si_2$ [151], and doped alloys that include $CeCu_{5.9}Au_{0.1}$ [158, 157, 3] and $Ce(Ru_{1-x}Rh_x)_2Si_2$ where $x \approx 0.5$ [164, 165]) because of the observed strong inhomogeneity in the muon relaxation rate, and the strong and frequency-dependent low-frequency fluctuation. In conclusion, the disorder in the $UCu_{5-x}Pd_x$ system, especially in UCu_4Pd, has led to considerable interest from researchers and a search to look for compounds in the $AuBe_5$ cubic structure that possesses sublattice disorder.

When searching for compounds that crystallize in the $AuBe_5$ structure and that display possibly the same behavior as $UCu_{5-x}Pd_x$, two factors should be taken into consideration. The first factor concerns the substitution of transition metals for Cu using UCu_5 as the starting point. For example, the substitution of Au for Cu (i.e., $UCu_{5-x}Au_x$) leads to an initial increase in T_N up to x = 2, but T_N decreases above x = 2 [150] while the substitution of Ag for Cu does not show the same rapid suppression of magnetic ordering as $UCu_{5-x}Pd_x$ does [117]. Also, the substitution of Ag or Au for Cu did not result in any NFL behavior. Chau and Maple point out that the Au and Ag atoms have a completely filled *d*-electron shell and the same valence as Cu [26]. There could be a correlation between substituting atoms with the same valence and lack of NFL behavior since Pd atoms have a partially filled *d* shell and a different valence. Since the complete subshell configuration atoms with d^{10} show no NFL behavior, this might possibly extend to the half filled subshell configuration atoms with d^5 due to their stability (or lower total energy). The second factor concerns how much of a dopant atom may be substituted in the UCu_5 cubic cell. For example, when x approaches 2.4 for the $UCu_{5-x}Pd_x$ system, a mixture of cubic and hexagonal phases appears and may run until x = 5 [26]. The supposition concerning the secondary hexagonal phase may be related to studies that showed the hexagonal $CaCu_5$ type structure may exist with atomic radii ratios (Ca site/Cu site) ranging from 1.29 to 1.61 and that below this range, cubic $AuBe_5$-type compounds are formed [42, 19]. A possibility is that the hybridization between the Pd and Cu atoms reduces the apparent radii of those atoms and thus the atomic radii ratio of some U/Cu-Pd atoms (maybe the ratio between nearest atoms) now lies above 1.29 while other ratios are below 1.29. Thus, the mixture of cubic and hexagonal crystal phases.

It has been known that uranium forms the cubic $AuBe_5$ structure only with Ni, Cu, and Pt atoms [150]. The UCu_5 has been well chronicled with its antiferromagnetic ordering around 15 K [101, 104]. In addition, UCu_5 undergoes another phase transition around 1 K (in the electrical resistivity and magnetic measurements) and this was the first example of such a distinct enhancement effect that occurs in a magnetically ordered material [117, 115]. Then, Chau and Maple doped UCu_5 with Pt and found a region in the phase diagram where the low temperature physical properties exhibit NFL behavior [26]. This then leaves UCu_5 to be doped with Ni since Ni has the same valence as Pd and Pt and the d-electron shell is not full or half-full. The main difference between the dopant atoms nickel and palladium is that the replacement Ni atoms are smaller than the Cu atoms as opposed to the larger Pd atoms replacing Cu atoms. Sublattice order for $x \sim 1$ should not occur in $UCu_{5-x}Ni_x$ as happened in $UCu_{5-x}Pd_x$. Thus, the answer to the question of any NFL behavior in $UCu_{5-x}Ni_x$ as $T_N \to 0$ being due to disorder or quantum critical behavior should be better differentiable.

1.1.2 $UCu_{5-x}Ni_x$

The first part of this section will review in chronological order previous works performed on the $UCu_{5-x}Ni_x$ system. The surname of the first author and the publication year will serve as the title for each work's review. One will see that the majority of the literature has mainly centered around UCu_4Ni, possibly in hopes of searching for interesting behavior as found in UCu_4Pd.

1.1.2.1 van Daal 1975

The first work performed on the $UCu_{5-x}Ni_x$ system was done by van Daal *et al.* who measured lattice constants for $0 \leq x \leq 5$ along with the susceptibility, specific heat, electrical resistivity, and absolute Seebeck coefficients as a function of temperature [153]. The susceptibility reveals that UNi_5 has a U^{4+} (tetravalent) state while on the Cu-rich end of the system (especially for $0 \leq x \leq 1$), the uranium ions are mixed tetravalent and trivalent (U^{3+}). van Daal *et al.* suggest that this mixed valency is possibly the source of the anomalies observed in the Cu-rich compounds ($0 < x < 1$): an extra increase of the lattice constants, an extremely high electronic specific heat, a resistivity varying in the paramagnetic range in proportion to $\log_{10} T$ at high temperatures and to $1 - (T/T^*)^2$ at low temperatures and being extremely sensitive to deviations from stoichiometry, and a Seebeck coefficient showing large negative peaks at low temperature [153].

1.1.2.2 Chakravarthy 1991

Chakravarthy *et al.* performed neutron diffraction measurements on Cu-rich compounds, in particular, x = 0.0, 0.2, and 0.5 [22]. The conclusions made are that UCu_5 is an itinerant magnet involving a strong hybridization of 5f electrons with the conduction electrons. For $UCu_{4.8}Ni_{0.2}$, the suppression of long-range magnetic order (LRO) by small substitution of Cu by Ni indicates the enhancement of the interaction of 5f electrons with the conduction electrons [22]. However, T_N is not significantly affected (12 K for x = 0.2). Thus, the band structure may be responsible for the LRO [159]. The third composition, $UCu_{4.5}Ni_{0.5}$, did not show LRO down to 1.5 K and the authors suggested that the suppression of the ordered magnetic moment of the U ion causes the LRO to disappear in the x = 0.5 system [22].

1.1.2.3 López de la Torre 1998

López de la Torre *et al.* made electrical resistivity and magnetic susceptibility measurements down to 0.4 K for $UCu_{4.5}Ni_{0.5}$ and UCu_4Ni samples [89]. For $UCu_{4.5}Ni_{0.5}$, the magnetic susceptibility displays an irreversibility below a broad maximum for a zero-field cooled (ZFC) and field-cooled (FC) regime and the maximum is the “freezing temperature” for a spin glass at about 6 K. For UCu_4Ni, the magnetic susceptibility shows no spin glass or magnetic order feature down to 0.4 K. No saturation in the magnetic susceptibility is apparent at low temperatures and an asymptotic $T^{1/2}$ dependence describes quite accurately the magnetic susceptibility from 0.4 K to 2.5 K [89]. The electrical resistivity measurements for UCu_4Ni showed that all samples had linear temperature dependence from 0.4 K to ~ 30-40 K. Also, annealing did not change the low temperature electrical resistivity properties significantly; however, the electrical resistivity values did show a large sample dependence. The authors raise the question of whether or not this NFL behavior is attributable to a two-channel Kondo effect [136], a quantum phase transition at $T = 0$ [5, 158], or disorder (specifically Kondo disorder) [39].

1.1.2.4 López de la Torre 2000

López de la Torre *et al.* try to address the previous question by applying the Kondo disorder model to the magnetic, electrical, and thermal properties of UCu_4Ni [90]. The claim is that the existence of two nonequivalent copper sites in the $AuBe_5$ cubic structure is the origin of the crystallographic disorder resulting in a distribution of Kondo temperatures [11, 15]. The phenomenological Kondo disorder model given by Bernal *et al.* [11] was used to describe the magnetic susceptibility data in a 1 T field and the fit described the data over two decades of temperature. López de la Torre *et al.* and van Daal *et al.* both agree that UCu_4Ni is in a mixed valence state between U^{3+} ($J = 3/2$ where J is the effective angular momentum) and U^{4+} ($J = 1$). The electronic specific heat measurements for the UCu_4Ni sample show typical NFL - $\log_{10}$ T dependence from 0.9 K to 9 K [90]. A comparison between the experimental specific heat results and a calculation made using a distribution of Kondo temperatures (similar to Graf *et al.* [55]) and applying the resonant-level model for the specific heat of a single Kondo impurity [135] show pretty good agreement from about 1 K to 10 K [90]. López de la Torre *et al.* observed an upturn in the specific heat around 0.9 K and they think the origin may be some form of spin-glass-like freezing at temperatures below their experimental limit (0.4 K). The upturn in the specific heat may also be related to the inflection in the magnetic susceptibility around 1 K [90]. The conclusion by López de la Torre *et al.* is that the Kondo disorder model could play a significant role in the NFL behavior reported in UCu_4Ni.

1.1.2.5 López de la Torre 2003

López de la Torre *et al.* made electrical resistivity measurements of $UCu_{4.75}Ni_{0.25}$ and UCu_4Ni over a wide temperature range (0.4 - 800 K) [88]. In summary, the high-temperature electrical properties of UCu_4Ni and $UCu_{4.75}Ni_{0.25}$ were explained in terms of single-impurity Kondo behavior. The interesting part of this paper concerns the high values of the electrical resistivities ($\rho(0) \sim 440\ \mu\Omega$ cm and ρ is usually well above 100 $\mu\Omega$ cm over the entire experimental temperature range). The rather poor electrical conductivity would indicate that the electronic mean free path is close to the interatomic distance and $k_F\, \ell$ is of the order unity where ℓ is the mean free path. This class of strongly correlated electron systems that approaches the Ioffe-Regel limit for the metallic state includes high-T_C superconductors, fullerenes, and ferromagnetic perovskites (e.g., $SrRuO_3$), which all have properties suggesting some sort of NFL behavior [154]. In the results part of this dissertation, these reported high electrical resistivity values will be revisited.

1.1.2.6 Present Work

One reason for studying the $UCu_{5-x}Ni_x$ system concerns the fact that the Kondo disorder model may not be the best explanation for the NFL behavior present in the experimental data. For example, a quantum critical point (QCP) may also be a possibility since the antiferromagnetic temperature (a second order phase transition) is suppressed to zero and the QCP has a large influence on the measured properties at finite temperatures [143]. However, some recent research on the isostructural $UCu_{5-x}Pd_x$ system has suggested that theories that limit the cause of NFL behavior to just one phenomena such as disorder or a quantum critical point may not be the best explanation. In fact, theories that combine quantum critical points with disorder may explain all the different data of systems such as $UCu_{5-x}Pd_x$ and $UCu_{5-x}Ni_x$ [16]. One such model in which the magnetic ordering temperature, T_{order}, has been suppressed via doping based on the effects of the accompanying disorder is the Griffiths phase disorder model. In the Griffiths phase model, disorder leads to tunneling between closely spaced energy levels in rare strongly coupled magnetic clusters [21]. The Griffiths phase model depends on the strong magnetic fluctuations produced "near" a QCP. The Griffiths phase model predicts that χ and C/T follow a power law temperature dependence, $T^{-1+\lambda}$ [20]. One of the unique features of the Griffiths phase model is that once a crossover magnetic field is determined (from magnetization versus field measurements), a magnetic field around the crossover field induces a peak in C/T at low temperatures ($C/T \approx (H^{2+\lambda/2}/T^{3-\lambda/2})\exp(-\mu_{eff.}H/k_BT)$) and the induced peak broadens and moves to higher temperatures for higher fields. Two systems in which the NFL behavior may be explained by the Griffiths phase model and that demonstrate field induced peaks are $Ce_{1-x}Th_xRhSb$ [74] and $Ce_{1-x}La_xRhIn_5$ [73].

The field induced peak is unique to the Griffiths phase model. This should not be confused with the peaks in magnetic fields for the multichannel Kondo problem [132]. There are distinct differences. First, the Griffiths phase model predicts that for zero magnetic field, the specific heat (C) follows T^{λ} behavior as mentioned earlier. In contrast, the specific heat for a Kondo system like CrCu [149] shows a peak in zero magnetic field. The peak in the specific heat for a Kondo system shifts towards higher temperatures and the height of the peak also grows as the magnetic field is increased. The Griffiths phase explanation differs since, although the field induced peak moves up in temperature, it broadens and decreases in size with increasing field.

For the present work, eight different $UCu_{5-x}Ni_x$ compounds were produced with x ranging from 0.6 to 1.2. The reason for such a large variation in the concentrations is to explore whether or not clear distinctions may be made concerning the cause of NFL behavior at different concentrations. In fact, small variant concentrations (i.e., x = 1.05, 1.1, and 1.2) have been made near UCu_4Ni, the concentration where T_N is approximately zero. A possible crossover concentration level might be found where one concentration's NFL behavior may be explained by a QCP while increasing the Ni concentration by 5% could cause the NFL behavior to be due to another model, like a disorder model. Also, the Griffiths phase model is predicated upon strong magnetic fluctuations "near" a QCP; it would be interesting to see if "near" could be quantified in terms of the Ni concentrations. The only system investigated by small variations of doping around the QCP was $UCu_{5-x}Pd_x$, where the quantum critical concentration was $x \approx 1$ as discussed earlier. The problem with $UCu_{5-x}Pd_x$ was the preferential sublattice ordering of the larger Pd atoms on the minority 4c site (in the $AuBe_5$ structure) occurring in UCu_4Pd as discussed previously [16]. In fact, MacLaughlin *et al.* concluded that there were still signs of disorder on annealed UCu_4Pd [93]. The $UCu_{5-x}Ni_x$ system should not have to contend with a preferential sublattice ordering since the Ni atoms are smaller than the Cu atoms. Thus, the smaller Ni atoms will be distributed at slightly less than the 25% level on the majority 16e sites (i.e., the physically smaller Be site in the $AuBe_5$ structure) for UCu_4Ni, with some small fraction in the energetically more unfavorable larger 4c sites. This conclusion will be discussed when the lattice parameter values are presented in the "$UCu_{5-x}Ni_x$ Results and Discussion" chapter. Thus, all concentrations around UCu_4Ni should have a significant amount of disorder present.

In addition to the lattice parameters for all eight concentrations being reported, direct current (dc) resistivity, magnetization as a function of field, alternating current (ac) susceptibility down to 2 K, direct current (dc) magnetic susceptibility down to 2 K, and heat capacity in zero field along with heat capacity in magnetic fields for concentrations around the QCP composition will be reported in the "$UCu_{5-x}Ni_x$ Results and Discussion" chapter. To date, a complete and thorough characterization of the $UCu_{5-x}Ni_x$ system around the QCP has not been reported in the literature. The measurements reported here will try to answer if clear distinctions can be made about the sources of NFL behavior (i.e., quantum criticality and disorder) at various Ni concentrations around the QCP (i.e., UCu_4Ni). Also, the measurements will try to clarify the role of Griffiths phase model for NFL behavior in the $UCu_{5-x}Ni_x$ system. An attempt to determine the concentration range for which the Griffiths phase model applies will be made.

1.2 Curie Temperature Enhancement in $UCu_2Si_{2-x}Ge_x$

A Curie temperature, T_C, enhancement as a function of disorder was predicted by Silva Neto and Castro Neto [137]. The fundamental idea behind this enhancement effect concerns electrons scattering from the localized moments and acting as a heat bath for the spin dynamics. Then, the dissipation that arises from the electronic diffusion in the case of structurally disordered ferromagnets is what affects the Curie temperature.

The study of ferromagnetism in disordered alloys has received renewed interest in recent years due to the development of $Ga_{1-x}Mn_xAs$ [114, 110, 112] and $In_{1-x}Mn_xAs$ [113] as ferromagnetic semiconductors (with $x \approx$ 1-10%). In fact, there are now reports of ferromagnetism (some at room temperatures and above) in several magnetically doped semiconductors [36], e.g., GaMnP [146], GaMnN [125], GeMn [118], GaMnSb [29]. However, the observed ferromagnetism in dilute magnetic semiconductor (DMS) systems like GaMnAs is not just associated with disorder created by the random positions of the magnetic dopants, but also the thermal fluctuations of magnetic moments along with impurity band and discrete lattice effects playing an integral part if the magnetic coupling can be assumed to be a simple local exchange coupling between local impurity moments and carrier spins [36]. Thus, trying to isolate the effects of disorder on the ferromagnetism in a DMS to test the proposed theory by Silva Neto and Castro Neto is impossible due to the aforementioned complexities in a DMS.

The choice of a ferromagnetic material to test the theory of Silva Neto and Castro Neto depends upon being able to test the effect of structural disorder on the ferromagnetic properties without introducing sundry complications [138]. De Long *et al.* investigated over 100 metallic Ce and U compounds to look for trends in the occurrence of ferromagnetism and to consider parameters such as the closest f-atom separation (notated by d) [37]. For example, Hill observed that f-state magnetic order did not occur for $d < d_H$, where $d_H \equiv 3.4$ or 3.5 Å, the respective "Hill limits" for f-state localization in Ce- and U-based materials [65]. Thus, when trying to induce structural disorder upon the selected compound, it is important not to inadvertently change the f-atom separation because it would be very difficult then to distinguish the change in T_C between structural disorder and f atom separation. De Long *et al.* also mention that hybridization of f-levels with non-f conduction states has an effect upon the ferromagnetism [37]. This pretty much rules out any binary ferromagnetic compounds since doping on one of the two atoms not only would create structural disorder, but also the doping would affect the hybridization.

The two ferromagnets, UCu_2Si_2 and UCu_2Ge_2, meet the conditions outlined above. UCu_2Si_2 is a ferromagnet at 103 K (with an antiferromagnetic transition right above at 107 K) [37] while UCu_2Ge_2 is a ferromagnet at 107 K (with a controversial antiferromagnetic transition at around 43 K [78, 47]) [37]. UCu_2Ge_2 and UCu_2Si_2 are isostructural, crystallizing in the $ThCr_2Si_2$ structure [28]. The

$ThCr_2Si_2$ structure is shown in Fig. 1–2 on page 18. In Fig. 1–2, one can see

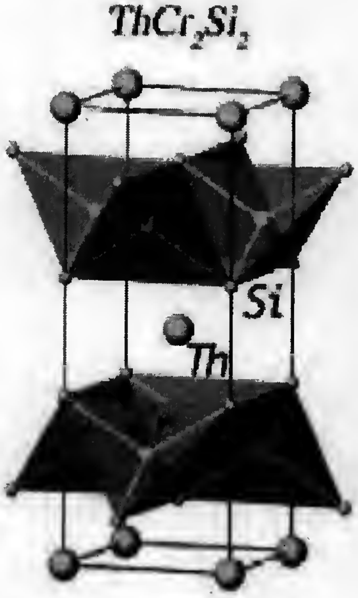

Figure 1–2: The unit cell for the tetragonal $ThCr_2Si_2$ crystal structure. The c-axis is up in this diagram, running parallel to the longest dimension of the unit cell. The $ThCr_2Si_2$ is layered with Th-Si-Cr_2-Si-Th planes stacked along the c axis. This diagram was taken from the paper by Welter *et al.* [161].

that for the $UCu_2(Si, Ge)_2$ compounds, the U atoms replace the Th atoms, the Cu atoms (the transition metal, T) replace the Cr atoms, and the Ge atoms replace the Si atoms for UCu_2Ge_2. The shading in Fig. 1–2 also highlights the tetraderal coordination of the Si (or Ge) around the T ion with small T-Si (Ge) distances: 2.40 Å for UCu_2Si_2 and 2.42 Å for UCu_2Ge_2 [28]. The smallest distance between two neighboring U atoms is well above the Hill limit for a U-compound (3.5 Å): 3.98 Å for UCu_2Si_2 and 4.05 Å for UCu_2Ge_2 [37]. It was decided that the structural disorder could be intentionally created by doping Ge onto the Si site in UCu_2Si_2 and that 9 compounds with differing Ge concentration levels (x = 0, 0.2, 0.4, 0.6, 1, 1.4, 1.6, 1.8, and 2) would be arc-melted to investigate whether or not nonmonotonic behavior exists for T_C as predicted by Silva Neto and Castro Neto.

The replacement of Si atoms with Ge atoms should not affect the magnetic sublattice in the $UCu_2Si_{2-x}Ge_x$ compounds. The structural disorder will occur on the p orbitals deep within the isovalent Si and Ge atoms. The structural disorder will affect the conduction band due to the complex p-d hybridization between the T ion and Si/Ge as seen in Fig. 1–2. Thus, the strong hybridization between the T ions and the U ions should not be directly affected by this intentional structural disorder. This is in agreement with the neutron diffraction and magnetization measurements of Chełmicki *et al.* that gave no magnetic moment on a copper ion [28]. In fact, the explanation by Chełmicki *et al.* for why the T ion does not carry a magnetic moment originates from the coordination of a T ion by silicon/germanium atoms. Four silicon atoms are located at the corners of a flattened tetrahedron around each T ion as shown in the shaded part of Fig. 1–2 on page 18. The short T-Si/Ge distances amount to less than the sum of atomic radii of T and Si/Ge [28]. Thus, the overlap (or hybridization) of electronic shells and electron density transfer from the 3p shell of the silicon/germanium to the 3d shell of the Cu ion in $UCu_2Si_{2-x}Ge_x$ compounds is what probably vanquishes the magnetic moment on the Cu ion. Mössbauer studies on isostructural $NpFe_2Si_2$ [109] and $REFe_2Si_2$ (where RE is a rare earth element) intermetallics [51, 108] show that the T ion does not carry a magnetic moment. The information by Chełmicki *et al.* justifies that the Si/Ge exchange creating sublattice disorder will not affect the long-range magnetic ordering of uranium moments in $UCu_2Si_{2-x}Ge_x$.

The effective magnetic moments and the isotropic RKKY mechanism determined by Chełmicki *et al.* were used by Dr.s Silva Neto and Castro Neto to calculate the nonmonotonic dependence of T_C [137]. The effective magnetic moment, $\mu_{eff.}$, for UCu_2Si_2 was determined to be 3.58 Bohr magnetons (μ_B) from the inverse susceptibility versus temperature curve using the Curie-Weiss law [28]. The

$3.58\mu_B$ value is the exact value calculated for a free ion configuration of U^{4+} assuming $^3H_4$ as a ground state. The $\mu_{eff.}$ value for the U ion in UCu_2Ge_2 is $2.40\mu_B$. Possible reasons for why the effective moment is lower in UCu_2Ge_2 are crystal field effects or magnetic moment compensation [138]. The magnetic interactions of the U ions may be explained by an isotropic RKKY model, in agreement with neutron diffraction and magnetization data [28]. This model was also successful in explaining the magnetic interactions in isostructural UPd_2Si_2, URh_2Si_2, and UPd_2Ge_2 [122]. The details of using this isotropic RKKY mechanism will be discussed in the "Theory" chapter of this dissertation.

One important point that cannot be emphasized enough concerns the Si/Ge sublattice disorder that is intentionally created and differs from other alloying experiments on the UCu_2Si_2 and UCu_2Ge_2 compounds. Since Si and Ge are isovalent, the carrier density is not changed. In contrast, the carrier density changes in the $UNi_{2-x}Cu_xGe_2$ system along with the magnetic sublattice since the hybridization between the U and Cu ions is altered by the substitution of the Ni atoms. Also studies done on the $UNi_{2-x}Cu_xGe_2$ system [82, 79] show that the ferromagnetic phase only exists for $1.20 \leq x \leq 2$ in the $UNi_{2-x}Cu_xGe_2$ magnetic phase diagram. In fact, for $x \geq 0.75$ (i.e., the samples closest to pure UCu_2Ge_2), there is a ferromagnetic-to-commensurate crossover. For example, for $x = 0.95$, a T_C value of 110 K was observed in ac-susceptibility measurements while at 94 K, the sample underwent another transition to an antiferromagnetic phase [79]. Kuznietz *et al.* even state that the transition metal sublattices determine the type of ordering on the uranium sublattice in the UM_2X_2 (where M = Co, Ni, Cu and X = Si, Ge) systems [79]. For the UCu_2Si_2 side of the phase diagram, neutron-diffraction results by Kuznietz *et al.* upon $UNi_{0.30}Cu_{1.70}Si_2$ show that $\approx 93\%$ of the sample volume orders antiferromagnetically while the other 7% orders ferromagnetically [81]. It should be clear from the examples above that it would be very difficult to individually distinguish the effects on T_C between the disorder acting on the transition metal's conduction electrons and disorder altering the magnetic sublattice. Thus, familiarity and acknowledgment concerning the tremendous amount of work on the magnetism of UCu_2Si_2 [63, 128, 96] and UCu_2Ge_2 [23, 102, 45, 148] is revealed, e.g., $UCo_{2-x}Cu_xGe_2$ [80, 41] and $U_{1-x}Y_xCu_2Si_2$ [64, 62]. However, despite all this research, this $UCu_2Si_{2-x}Ge_x$ is unique because it is the first project to try and isolate the effects of disorder upon T_C by creating structural disorder at the Si/Ge site (i.e., the 4*e* site of the $ThCr_2Si_2$ crystal structure).

A final factor in determining the T_C enhancement for $UCu_2Si_{2-x}Ge_x$ concerns minor changes in the stoichiometry of the $UCu_2Si_{2-x}Ge_x$ system. Particular attention to the stoichiometry in the $UCu_2Si_{2-x}Ge_x$ compounds is paid in the "Experimental Techniques" chapter and the "$UCu_2Si_{2-x}Ge_x$ Results and Discussion" chapter. Kuznietz *et al.* point out that small deviations from stoichiometry on the copper sublattice alters the number of conduction electrons [79]. The effect of small stoichiometry changes upon the magnetic properties is closely monitored since predictions by Silva Neto and Castro Neto originate from conduction electrons on the Cu sublattice scattering from the localized U spins [137] as discussed earlier. In fact, multiple samples with the same Si/Ge concentration are synthesized in order to compare the stoichiometry differences to the experimentally determined T_C values.

The low temperature resistivity on the $UCu_2Si_{2-x}Ge_x$ compounds is also measured. Low temperature resistivity predictions for the scattering of conduction electrons from localized spin fluctuations have the resistivity varying as T^2 as observed in dilute Pd-Ni alloys [131] and dilute Ir-Fe alloys [70]. This Fermi-liquid like resistivity behavior is expected for the $UCu_2Si_{2-x}Ge_x$ compounds. Also, the resistivity measurements are expected to provide insight into the type of dissipation occurring from the scatter of the conduction electrons. The two main sources of dissipation are Landau damping for clean magnets and electronic diffusion for structurally disordered magnets [137]. The electrons in the Landau damping case have a longer mean free path than the electrons in the diffusive case. Thus, the resistivity for the Landau damping electrons (i.e., the ballistic electrons) is expected to be smaller than the diffusive electrons.

CHAPTER 2
THEORY

2.1 Non-Fermi-Liquid Theory

2.1.1 Introduction

The discovery of the electron in 1897 by J.J. Thomson has led to many theories concerning the behavior of electrons in metals. In 1900, P. Drude formulated his theory of metallic conduction by using a slightly modified method of the kinetic theory of a neutral dilute gas. Unfortunately, the Drude model was not accurate in predicting many physical properties, such as the specific heat of a metal. A quarter of a century passed until Sommerfeld's model solved the problem by using the Pauli exclusion principle's requirement that the electronic velocity distribution is the quantum Fermi-Dirac distribution instead of the classical Maxwell-Boltzmann distribution. After the passing of another quarter century or so, L.D. Landau introduced his Fermi-liquid theory that was able to explain many physical properties in metals such as Cu and Al. All of the previous models made use of an independent electron approximation or free electron model.

As one comes to present day, complex metals have been discovered where at low temperatures, the electron-electron interactions cannot be simply ignored or slightly modified with respect to the free electron case. The strong electronic correlations lead to non-Fermi-liquid behavior. In fact, non-Fermi-liquid behavior has been observed in metals with disorder, such as $UCu_{5-x}Pd_x$ [4]. The theory will begin with some of Landau's arguments for Fermi-liquid theory and then explore some of the theories characterizing non-Fermi-liquid behavior.

2.1.2 Fermi-Liquids

In 1957, L.D. Landau proposed his Fermi-liquid theory. The original intent of the theory was to explain the liquid state of the isotope of helium of mass number 3 [7]. However, Fermi-liquid theory is now being applied to the theory of electron-electron interactions in metals.

Landau's Fermi-liquid theory has two main points. First, the electrons that are within k_BT of the Fermi energy and that do have interactions with each other do not ruin the success of the independent electron picture in explaining low-energy metallic properties. Secondly, single electrons are not just being considered anymore, but rather quasiparticles (or quasielectrons). These quasiparticles share many of the properties of non-interacting electrons, but quasiparticles are like electrons that have been perturbed from their non-interacting state by means of interaction [134].

Instead of going through a quantitative analysis as Landau did to obtain respective thermodynamic and transport properties [83, 84, 85] of a Fermi liquid, a qualitative analysis is more appropriate for this dissertation. The quasiparticles that are of most importance are those that are within k_BT of the Fermi surface as stated above. Most quasiparticles in metals are so far buried down below the Fermi surface that they are unable to obtain the required energy needed to reach an unoccupied quantum state. Thus, only quasiparticles within k_BT of the Fermi surface can contribute k_B to the specific heat and the specific heat grows linearly with temperature. Likewise, only quasiparticles within μ_BB (where B is an external magnetic field) of the Fermi surface can magnetize with a magnetic moment proportional to μ_B leading to a temperature independent magnetic susceptibility [134]. If the temperature is above absolute zero, then some energy levels above the Fermi energy will be occupied within a range of k_BT of the Fermi surface. Therefore, the scattering rate for the quasiparticles near the Fermi surface is proportional to T^2. Since the resistivity is proportional to the scattering rate, the low temperature resistivity goes like T^2.

2.1.3 Non-Fermi-liquids

In 1991, Seaman *et al.* discovered low-temperature measurements of specific heat, magnetic susceptibility, and electrical resistivity on the $Y_{1-x}U_xPd_3$ system that were contradictory to Landau's Fermi-liquid theory [136]. Specifically, the compound $Y_{0.8}U_{0.2}Pd_3$ displayed a linear low temperature behavior in its resistivity and a logarithmic relationship in its low temperature heat capacity for over a decade of temperature in both. To date, over fifty systems have been discovered that do not obey Landau's Fermi liquid theory [143].

Since the discovery of $Y_{0.8}U_{0.2}Pd_3$ displaying this non-Fermi-liquid (NFL) behavior, there has been considerable interest in explaining this NFL behavior by condensed matter theoreticians. The various theories are segregated into three general categories: 1) multichannel Kondo models; 2) models where the magnetic phase boundary lies near 0 K (i.e., the quantum critical point); and 3) models based on disorder. A synopsis of the various theories will be given while particular attention will be paid to models that are applicable to $UCu_{5-x}Ni_x$.

2.1.3.1 Multichannel Kondo Model

The multichannel Kondo effect is based upon single-impurity physics. The multichannel Kondo effect is described by a quantum impurity spin **S** that is coupled antiferromagnetically to n degenerate channels of spin-$\frac{1}{2}$ conduction electrons [1]. The so-called Kondo lattice Hamiltonian is derived from the Anderson Hamiltonian to describe the single-impurity multichannel Kondo model [143]:

$$H_K = \sum_{k,m,\sigma} \epsilon_k a^\dagger_{km\sigma} a_{km\sigma} + J \sum_{k,k',m,\sigma,\sigma'} \mathbf{S} \cdot a^\dagger_{km\sigma} \sigma_{\sigma\sigma'} a_{k'm\sigma'} \qquad (2.1)$$

where ϵ_k is the conduction-electron dispersion relation, $a^\dagger_{km\sigma}$ and $a_{km\sigma}$ are creation and annihilation operators on electrons with momentum **k** and spin projection

m, J is the antiferromagnetic coupling constant between the localized impurity spins and the conduction electrons, **S** is the localized spin impurity, and $\sigma_{\sigma\sigma'}$ are the Pauli spin matrices. Three distinct cases arrive from the above Hamiltonian between the n channels (or flavors) of the conduction electrons and the impurity spin S [143]:

1. If n = 2S, the conduction-electron channels fully screen the impurity spin channels and a singlet ground state arises. This leads to Fermi-liquid behavior as described above.
2. If n < 2S, the conduction-electron channels only partially screen the impurity spin channels and no singlet ground state exists. The result is a new effective Kondo effect with a net spin S' = S - n/2 [25]. The ground state is Fermi-liquid-like and mirrors the model of Coqblin and Schrieffer [30] (n = 1, S ≥ 1/2).
3. If n > 2S, the local spin is "overcompensated" yielding a critical ground state with a non-Fermi-liquid excitation spectrum [75]. The result of this overcompensation is power-law or logarithmic behavior in measured physical quantities like magnetization, resistivity, and specific heat as the temperature and external field approach zero.

The third case is particularly interesting since the low temperature dependence of the magnetic susceptibility, specific heat, and resistivity depend upon the number of channels of conduction electrons, n, and the impurity spin S. For example, if n = 2 ("two-channel") and S = 1/2, then the low temperature, zero-field magnetic susceptibility and specific heat divided by temperature, C/T, go approximately like $\log(T/T_K)$ [132]. Such logarithmic temperature dependence has been observed in systems such as $Y_{1-x}U_xPd_3$ [136] and $Th_{1-x}U_xPd_2Al_3$ [34, 38]. Also, the low temperature resistivity at zero-field behaves like $\rho_o - A\sqrt{T}$ [91]. Unfortunately, this low-temperature resistivity has not been observed in many NFL systems. The reason may be that the low-temperature resistivity predictions were made in the dilute impurity limit while the NFL behavior in systems crops up more in the concentrated limit.

Cox and Zawadowski [32] have addressed this concentrated limit. It is a special case of the multichannel Kondo effect that has a quadrupolar origin. The NFL behavior in this model results from an effective exchange interaction between pseudospins and the electric quadrupole moment of the groundstate [25]. However, no system has met the strict requirements required by this quadrupolar Kondo effect.

The multichannel Kondo model portrays NFL behavior as single-ion in nature [21]. This means that each impurity moment is treated independently and concentrated systems might not be of single-ion character since no interaction between the impurities is taken into effect.

2.1.3.2 Quantum Critical Point

The second general theoretical category describing non-Fermi-liquid behavior is quantum critical point models. The quantum critical point theories arise from the critical phenomena that occur at or near a zero temperature phase transition. Classically, a phase transition would occur at a nonzero temperature and temperature would be the control parameter. The temperature parameter would control the thermal fluctuations and if the thermal fluctuations have characteristic energies ($h\omega^*$, where ω^* is the frequency associated with the fluctuations) much less than $k_B T_C$ (where T_C is the critical temperature of a phase transition), then the fluctuations may be described by classical statistics [25]. However, in 1976, Hertz [60] considered the case when the critical temperature is at $T = 0$. The fluctuations would have zero thermal energies. Thus, quantum mechanical fluctuations would arise that could not be controlled by temperature. These fluctuations may be controlled by chemical substitution, external pressure, or magnetic field. An example of pressure control is $CePd_2Si_2$ where a pressure of $\sim$ 28 kbar suppresses antiferromagnetism, induces superconductivity at 0.43 K, and shows NFL behavior in the electrical resistivity ($\rho(T) \propto T^{1.2}$) [58]. The idea is that one of the aforementioned control parameters "tune" a system from an ordered ground state to a non-ordered state crossing a quantum critical point [143]. The assumption is that at low enough temperatures, the system's behavior will be dictated by quantum effects despite not being able to measure thermodynamic properties at T = 0 [139]. At these low temperatures, non-Fermi-liquid behavior appears at or near a quantum critical point since usually a magnetic phase transition is suppressed. The quantum critical point theory is relevant to the $UCu_{5-x}Ni_x$ system because doping UCu_5 with Ni suppresses the long range antiferromagnetic order and $T_{Néel}$ approaches zero.

As mentioned above, measurements at T = 0 cannot be performed. Thus, in order to confirm whether or not the NFL behavior is due to a quantum critical point, one must analyze scaling behavior [152] (either for temperature or frequency) on finite-temperature properties and compare to predictions made by several different models. A synopsis of each model with key points is provided below.

The first theoretical model was developed by Tsvelik and Reizer [152]. This theory matched the low-temperature thermodynamics measured in $U_{0.2}Y_{0.8}Pd_3$ and $UCu_{3.5}Pd_{1.5}$ [136, 5, 4]. The theoretical model states that the two previous systems are on the verge of a phase transition that occurs at zero temperature and results in a domination by collective bosonic modes. The model also matched the correct scaling analysis of the low-temperature properties [4]:

$$\text{magnetization}: \quad M = \frac{H}{T^{\gamma}} f\left(\frac{H}{T^{\beta+\gamma}}\right)$$

$$\text{specific heat}: \quad \frac{c_v(H,T)}{T} - \frac{c_v(0,T)}{T} = g\left(\frac{H}{T^{\beta+\gamma}}\right)$$

where $\gamma = 0.25 - 0.3$; $\beta + \gamma = 1.2 - 1.3$; (the model predicted a scaling dimension of 4/3) and f and g are nonsingular scaling functions. Along with the above scaling analysis, the specific heat has a logarithmic divergence and the dc magnetic susceptibility has a divergent form ($T^{-\gamma}$) at low temperatures.

A second theoretical model investigating quantum critical phenomena was developed by Hertz [60] and Millis [97]. A major assumption is made to integrate out the fermions (i.e., the conduction electrons) and thus the problem is reduced to the study of an effective bosonic theory describing fluctuations of the ordering field [97]. Results depend crucially upon the value of d + z, where d is the spatial dimension and z the dynamic exponent (z=2 for the antiferromagnet and z=3 for the ferromagnet) of the T = 0 transition [60]. All of the cases considered except for the two-dimensional antiferromagnet have an effective dimension, (d+z), greater than their upper critical dimension [60]. Hyperscaling (which is used to derive the scaling analysis mentioned in the previous paragraph) has been shown not to apply to systems above their upper critical dimension [17, 121]. Phase diagrams with crossover temperature relationships between various regions have been obtained for different cases (e.g., two spatial dimensions and dimensions larger than two [97]). None of the derived relationships for measured properties in this model are applicable to the $UCu_{5-x}Ni_x$ system.

A third theoretical model investigating quantum critical phenomena was developed by Moriya and Takimoto [103] and it involves spin fluctuations in heavy electron systems around their antiferromagnetic instability. This idea is particularly applicable to the $UCu_{5-x}Ni_x$ system since the heavy electron system UCu_5 has its Néel temperature suppressed by Ni doping. This theory is based on exchange-enhanced spin fluctuations playing a major role in displaying various anomalous properties around the magnetic phase boundary. Moriya and Takimoto addressed the problem of coupling among the different modes of spin fluctuations in heavy electron systems [103]. Their answer was to take a phenomenological point of view by using a sum rule for the local spin fluctuations valid in the strong correlation limit:

$$S_{L0}^{2} + S_{LT}^{2} = S_{L}^{2}$$

where S_{L0} is the mean square local amplitude of the zero point, S_{LT} is the mean square local amplitude of the thermal spin fluctuations, and S_L is the amplitude of the local spin density that takes a constant value. The sum rule is then used to calculate the reduced inverse staggered susceptibility in the low temperature limit, y_o, for a nearly antiferromagnetic metal:

$$\mathrm{y}_o = \frac{1}{2\mathrm{T_A}\chi_\mathrm{Q}(0)}$$

where T_A is a characteristic energy parameter and $\chi_\mathrm{Q}(0)$ is the local dynamical susceptibility for the antiferromagnetic wave vector Q. This expression has the same form as in the self-consistent renormalization (SCR) theory for weak itinerant antiferromagnetism [103]. The parameter y_o goes to zero as the magnetic instability is approached; in fact, at the critical boundary, y_o equals zero [103]. Thus, the value of y_o gives a prediction for the proximity to the magnetic instability [143]. The value of y_o is obtained by fitting the specific heat and electrical resistivity data.

Moriya and Takimoto made predictions for the specific heat and electrical resistivity due to the spin fluctuations. When $\mathrm{y}_o = 0$, the specific heat takes a finite value, γ_o, and starts to decrease with increasing temperature proportionally to $\mathrm{T}^{1/2}$. Immediately after the square root behavior, the specific heat shows a negative logarithmic behavior in a certain range of temperature (over about 60% of a decade in temperature above the $\gamma_o - \mathrm{AT}^{0.5}$ behavior [143]). Interestingly, as one gets further from the phase boundary (i.e., $\mathrm{y}_o \neq 0$), Fermi-liquid behavior arises and the range of linear specific heat increases with increasing y_o. The electrical resistivity at the critical boundary is proportional to $T^{3/2}$ at low temperatures and as the temperature increases, there is a certain range where the resistivity is almost linear in T. The electrical resistivity is similar to the specific heat in that as one moves further away from the antiferromagnetic critical boundary, there exists a normal Fermi-liquid behavior at low temperatures. Physically, the interpretation of the departure from the $T^{1/2}$ behavior to the logarithmic dependence in the specific heat and crossover from the $T^{3/2}$ behavior to the linear dependence in the electrical resistivity is that at the lowest temperatures, the coupling among the different modes of the spin fluctuations is small in magnitude; however, as the temperature increases, the coupling also increases [143]. Application of Moriya and Takimoto's theory will be discussed later on.

Several other theoretical models exist describing quantum critical phenomena. However, in the interest of relevance to this dissertation, one should be directed to Dr. Stewart's review article [143] for a complete summary of all theoretical models pertaining to the quantum critical point.

2.1.3.3 Disorder

The third theoretical category describing non-Fermi-liquid behavior concerns models based on a disorder. These models originate from the multichannel Kondo model. It was previously discussed that when the conduction-electron channels are sufficient to compensate the impurity spin, then Fermi-liquid behavior occurs. T_K is the Kondo temperature below which the conduction electrons fully screen the local impurity spin for $S = 1/2$ and $n = 1$ (the number of conduction-electron bands). The disorder model has been proposed to reduce T_K to lower temperatures for some of the magnetic impurities and thus, some of the long-range magnetic order survives leading to non-Fermi-liquid behavior. The Kondo temperature, T_K, is given as follows [76]:

$$k_B T_K \approx \epsilon_F \exp^{-1/N(0)J}$$

where ϵ_F is the Fermi energy, N(0) is the density of states at the Fermi energy, and J is the exchange constant between the local moment and conduction-electron. Mathematically, if disorder could increase N(0), J, or both, then the Kondo temperature could be lowered below the average T_K. Thus, if the temperature were at average T_K, then not all magnetic impurity spins would be compensated for and the uncompensated spins would lead to NFL behavior.

The first disorder driven model was constructed from the work of Dobrosavljević *et al.* [39] and Bhatt and Fisher [12]. Then, Bernal *et al.* [11] used this "Kondo disorder" model to explain the large inhomogeneous nuclear magnetic resonance (NMR) linewidths they observed in $UCu_{5-x}Pd_x$. The large linewidths reflected a broad distribution of local uranium spin static susceptibilities that were considered to be due to a probability distribution, $P(T_K)$, of Kondo temperatures. The distribution of Kondo temperatures was assumed to be due to disorder. The uniform magnetic susceptibility, $\chi(H,T) \equiv M(H,T)/H$, was thought of as the average of $\chi(H, T;T_K)$ over $P(T_K)$ and fits on $\chi(H,T)$ were used to obtain parameters characterizing $P(T_K)$. The NMR linewidths, which come from the distribution of Knight shifts and measure directly the width of the distribution $P(\chi)$ of χ, were found to agree well with the Kondo disorder model and no further fitting of $P(T_K)$ was required. The temperature and field dependence of the specific heat agreed well with the Kondo disorder model.

The Kondo disorder model was extended further by Miranda *et al.* [98, 100, 99], who focused on non-Fermi-liquid behavior due to the interaction between disorder and strong electron-electron correlations. Their theory sums up as a small amount of disorder playing a major role in the low-temperature logarithmic divergence in magnetic susceptibility and specific heat along with the linear behavior in the low temperature resistivity [25].

Not only was the multichannel Kondo model mixed with disorder, but also spin fluctuations near a quantum critical point were mixed with disorder. Rosch [126] explained that the reason why the resistivity varies as T^{α} where α is between 1 and 1.5 for various systems [68, 95, 53] is due to the interplay between quantum-critical antiferromagnetic spin fluctuations and impurity scattering in a conventional Fermi-liquid. In other words, the dependence of the exponent depended on sample quality. The disorder in a sample was quantified by taking the inverse of the residual resistivity ratio: $R(T\rightarrow 0)/R(T\rightarrow 300\ K)$.

The most relevant disorder model to $UCu_{5-x}Ni_x$ involves a model proposed by Castro Neto *et al.* [21, 20]. The model by Castro Neto *et al.* takes place in a disordered environment and features the competition between the Kondo effect and Ruderman-Kittel-Kasuya-Yosida (RKKY) interaction (i.e., magnetic ordering) as represented by the Hamiltonian in Eq. 2.1. The problem with studying this competition is the fact that both the RKKY interaction and the Kondo effect have origins on the same magnetic coupling between spins and electrons [21]. However, perturbation theory may be used to treat the RKKY interaction since the RKKY interaction depends on electronic states on the Fermi-surface and states embedded inside the Fermi-surface while the Kondo effect just affects the Fermi surface. The RKKY interaction leads to an order of the magnetic moments while the Kondo coupling leads to the destruction of long-range order in a magnetically ordered system.

In the model by Castro Neto *et al.*, disorder also affects the magnetic order in these systems. For a ligand system (e.g., $UCu_{5-x}Ni_x$, the metallic Cu atoms are replaced by Ni atoms), if the metallic atoms are replaced with smaller metallic atoms (as is the case for $UCu_{5-x}Ni_x$), then the difference in size between the metallic atoms leads to a local lattice contraction which modifies the local hybridization matrix elements [21]. Large local effects in the system can occur because the local hybridization matrix elements are exponentially sensitive to the overlap between different angular momentum orbitals. Also, the local value of the exchange constant between the conduction electrons and the localized moments, J in Eq. 2.1, changes due to the change in the local hybridization matrix elements.

Castro Neto *et al.* disagree with the interpretations of the Doniach argument [40] which are based on homogeneous changes in the exchange constants between conduction electrons and magnetic moments. It is true that when the local exchange constant, $J(i)$, is below a critical value J_C, the RKKY energy scale is larger than the Kondo temperature as shown in Fig. 2–1 on page 35. However, Castro Neto and Jones argue that since disorder is present in the system, the moment can *locally* order with its environment as the system is cooled down [21]. The Doniach argument differs because it is based on a global change in the exchange constant, J, instead of just a local change. Doniach's picture predicts a change in the exchange constant over the entire lattice and the ordering temperature in Fig. 2–1 vanishes at a quantum critical point where the system goes from ordered state to fully Kondo compensated state [21]. The picture by Castro Neto and Jones represents a quantum percolation problem where moments are compensated due to local effects and that a local change in a coupling constant does not immediately imply a change of the "average coupling" constant. Thus, even if chemical substitution occurs on a non-magnetic site, individual moments will be compensated for magnetically due to the distribution of exchange constants in the presence of disorder [21]. At some critical doping concentration, long-range magnetic order will be suppressed and the system will enter a paramagnetic phase. However, since Castro Neto and Jones argue that the situation is a percolation problem, the paramagnetic phase can still contain clusters of atoms in a relatively ordered state.

The alloying of a metallic atom with a different metallic atom is what leads to this percolation problem. In this percolation problem, the interest lies in the

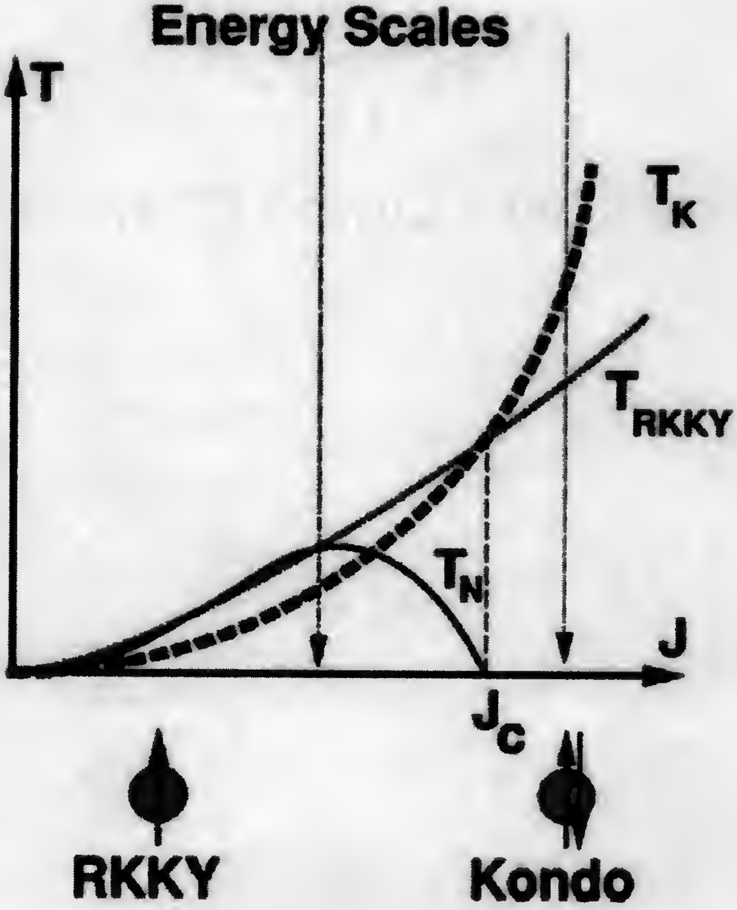

Figure 2–1: The Doniach phase diagram taken from Ref. [21]. The thick dashed line is the Kondo temperature, $T_K \approx E_F e^{-1/N(0)J}$. The thin dashed line is the RKKY temperature, $T_{RKKY} \propto [N(0)J]^2$. The continuous line that equals zero at J_C is the ordering temperature, T_N.

paramagnetic phase or when p > p_C, where p is a percolation parameter (related to the density of quenched moments) and p_C is the percolation threshold of the lattice. When p > p_C, then there are only finite clusters of magnetic moments (i.e., magnetic atoms) which are more coupled than the average [21]. Castro Neto and Jones assumed that these clusters do not have strong interactions amongst themselves and that to a first approximation, they can be thought of as isolated and permeated by a paramagnetic matrix. Castro Neto and Jones termed the behavior of a cluster of N atoms in the presence of a paramagnetic environment as the N-impurity-cluster Kondo effect.

The N-impurity-cluster Kondo effect involves a cluster of N magnetic moments close to a quantum critical point (due to the presence of disorder). If N is large, then the magnetic cluster may be considered as a large magnetic grain. The ground state is either a full ferromagnet or antiferromagnet. The ground state of the cluster has to be at least doubly degenerate due to time-reversal symmetry and the cluster can fluctuate quantum mechanically (i.e., tunnel) between the two degenerate states in the absence of an applied magnetic field [21]. Since the magnetic clusters can tunnel in the presence of a metallic environment, this produces dissipation (due to particle-hole excitations in the conduction band [21]).

Castro Neto and Jones show that the sources for tunneling depend upon the symmetry of the system. To summarize, if the magnetic cluster has XYZ symmetry or very low spin isotropy and N_C is the threshold limit of spins in a given cluster above which the Kondo effect ceases to occur, then N_C is the maximum number of magnetic moments that can still tunnel due to the anisotropy in the RKKY interaction. If N > N_C, then there is no Kondo effect and the tunneling ceases along with cluster motion due to freezing. The other case involves XXZ or Heisenberg symmetry. For this case, the only source of tunneling is the Kondo effect. This Kondo effect is due to the dissipative dynamics of states [21].

Dissipation is vital in this case because it allows tunneling to vanish for a finite number of spins given by N_C.

As mentioned above, tunneling and dissipation are created when a set of magnetic impurities interacts through a conduction band. Castro Neto and Jones also show that three different energy scales are created in the mean-field-like picture: the ordering temperature, the tunneling energy, and the damping energy [21]. Castro Neto and Jones explored how these different energy scales would affect the Kondo lattice. If the previous example of a ligand system having its metallic atom replaced by a smaller atom is used again, then the lattice locally contracts resulting in local matrix elements that have exponentially large values and the local exchange parameter may be much larger than the average exchange in the lattice [21]. The calculations by Castro Neto and Jones reveal that this problem is equivalent to an anisotropic d+1 classical Ising model with long-range interactions in the imaginary-time direction, and short-range interactions in the space direction. The solution to this problem involves extending the quantum droplet model of Thill and Huse [147] in the context of insulating magnets. In the paramagnetic phase, the quantum droplets are the magnetic clusters. A distribution of the energy scales (or cluster Kondo temperatures) is fixed by the percolation theory mentioned above and this distribution arises from a distribution of cluster sizes. The behavior of this statistical problem reveals that as the critical number of spins, N_C, is finite, the distribution for the energy levels diverges logarithmically; however, as $N_C \rightarrow \infty$, there is a crossover in the problem to a power-law distribution for the energy levels. Now that the distribution of the energy scales has been obtained, the actual physical properties of these magnetic clusters were calculated by Castro Neto and Jones.

Castro Neto and Jones considered two distinct domains of temperature for the physical properties: $T < T^*$ and $T > T^*$ where T^* is a crossover temperature. The crossover temperature values depend upon the source of tunneling. For example, if the source is RKKY interaction, then the critical number of magnetic clusters for which tunneling ceases is very large and the crossover temperature is effectively zero [21]. For the case where the Kondo effect is the source of tunneling, then the crossover temperature is on the order of magnitude of about 0.5 K for a ligand system [21].

The asymptotic behavior of the magnetic susceptibility and specific heat is considered for temperatures less than the crossover temperature. Interestingly, there are no analytic expressions for the magnetic susceptibility and specific heat of a Kondo system [31]. For $\mathrm{T} \ll \mathrm{T}^*$, tunneling ceases and the tunnel splitting is zero. The spin cluster motion is frozen and dissipation dominates the spin dynamics. This leads to a divergent behavior in the susceptibility at low temperatures [21]:

$$\overline{\chi}(\mathrm{T}) \propto \frac{1}{\mathrm{T}\ln(\mathrm{W}/\mathrm{T})} \tag{2.2}$$

where $\mathrm{W} \approx \mathrm{E_F}$, the Fermi energy. Similarly, the specific heat diverges for extremely low temperatures [21]:

$$\overline{\gamma}(\mathrm{T}) \propto \frac{1}{\mathrm{T}\ln^2(\mathrm{W}/\mathrm{T})} \tag{2.3}$$

Unfortunately, the measurement of temperatures below the crossover temperature is physically impossible except for a few rare earth cases [21].

The temperature range above the crossover temperature and below the average RKKY interaction energy gives rise to physical properties that are indicative of quantum Griffiths-McCoy singularities in a paramagnetic phase [57]. For temperatures above the crossover temperature, a power-law behavior is present for the magnetic susceptibility [21]: $\chi(\mathrm{T}) \propto \mathrm{T}^{-1+\lambda}$, where $\lambda < 1$. In the high temperature limit, the susceptibility goes like normal Curie behavior: $\chi(\mathrm{T}) \propto 1/T$. Likewise, power-law behavior is present in the specific heat: $\mathrm{C_V}(\mathrm{T}) \propto \mathrm{T}^{-1+\lambda}$, with $\lambda < 1$. The lambda values above do not have to be the same, contrary to an earlier work [20]. Castro Neto and Jones caution that the temperature above the crossover temperature should not exceed the order of the ordering temperature of the pure system because the magnetic clusters will decompose.

Castro Neto and Jones also consider physical quantities with the application of an external magnetic field, H, and in the temperature regime above the crossover temperature. The response functions are calculated by knowledge of the dynamical exponent in the Griffiths-McCoy phase. The first physical quantity to be considered is the magnetization and Castro-Neto and Jones observed that the magnetization has a scaling form

$$\overline{M}(\mathrm{H},\mathrm{T}) = \frac{H}{\mathrm{T}^{1-\lambda}} f_\lambda\left(\frac{\mathrm{H}}{\mathrm{T}}, \frac{\mathrm{T}}{\omega_\mathrm{o}}\right) \tag{2.4}$$

where f_λ(x,y) is a simple scaling function and ω_o is the attempt frequency of the cluster. The focus will be on the case of $\omega_\mathrm{o} \gg \mathrm{T}, \mathrm{E_H}$ (where $\mathrm{E_H}$ is the magnetic energy of the cluster that is proportional to H); thus, the scaling function above will just be dependent on H/T. If $\mathrm{T} \gg \mathrm{E_H}$ (i.e., the low-field limit), then Castro Neto and Jones calculated the scaling function to be $f_\lambda(\mathrm{x},0) \approx 1$ when $\mathrm{x} \rightarrow 0$. The magnetization has a linear dependence with the magnetic field at constant temperature or the magnetization diverges at low temperatures like $\mathrm{T}^{\lambda-1}$ for $\lambda < 1$ at constant magnetic field. If $\mathrm{E_H} \gg \mathrm{T}$, then the high-field limit has the magnetization scaling like H^λ and the susceptibility $\left(\chi = \mathrm{d}\overline{\mathrm{M}}/\mathrm{dH}\right)$ goes like $\mathrm{H}^{\lambda-1}$ [21]. The following conclusion may be drawn about the scaling function: $f_\lambda(\mathrm{x}, 0) \approx \mathrm{x}^{\lambda-1}\,\mathrm{as}\,\mathrm{x} \rightarrow \infty$. One important note that will be further explored in the "$\mathrm{UCu}_{5-x}\mathrm{Ni}_x$ Results and Discussion" chapter is that the lambda in the high-field magnetization should equal the lambda determined from the low-field, low-temperature magnetic susceptibility.

Castro Neto and Jones also calculate low-temperature limits in the context of specific heat. Their calculations yield a scaling form

$$\overline{C_V}(H,T) = T^{\lambda} g_{\lambda}\left(\frac{H}{T}, \frac{T}{\omega_o}\right) \tag{2.5}$$

where $g_{\lambda}(x,y)$ is a scaling function. Just like the magnetization case, the scaling function will only be dependent upon one variable, $g_{\lambda}(x,0)$, since it is assumed $\omega_o \gg E_H, T$. For low fields, the specific-heat coefficient, $\overline{C_V}(H,T)/T$, diverges at low temperatures like $T^{\lambda-1}$. The scaling function behavior is then $g_{\lambda}(x,0) \rightarrow 1$ for $x \rightarrow 0$. In the case of high fields, the dominant behavior is a little more complicated:

$$\overline{C_V}(H,T) \propto \frac{H^{2+\lambda/2}}{T^{2-\lambda/2}} \exp\left\{\frac{-H}{T}\right\} \tag{2.6}$$

The scaling behavior is $g_{\lambda}(x,0) \rightarrow e^{-x} x^{2+\lambda/2}$ as $x \rightarrow \infty$. The more complicated scaling behavior is from a Schottky anomaly due to the high magnetic field [21]. The scaling behavior for the magnetization and specific heat is summarized in Fig. 2–2 on page 41 (taken from Ref. [21]).

In concluding this theory of Griffiths-McCoy singularities in the paramagnetic region close to the quantum critical point for magnetic orders of U and Ce intermetallics, Castro Neto and Jones have made predictions for the behavior of the imaginary part of the average frequency dependent susceptibility, the nonlinear magnetic susceptibility, the Knight shift measurement in NMR, and neutron scattering [21]. All the behaviors at low temperatures are based upon the quantum-mechanical response of magnetic clusters. Experiment has shown that these magnetic clusters may be the source of NFL behavior in $Ce_{1-x}La_xRhIn_5$ [73] and $Ce_{1-x}Th_xRhSb$ [74].

2.2 Curie Temperature Enhancement Theory

The enhancement (i.e., the unexpected nonmonotonicity) of the Curie temperature, T_C, was predicted by Silva Neto and Castro Neto [137]. Silva Neto and

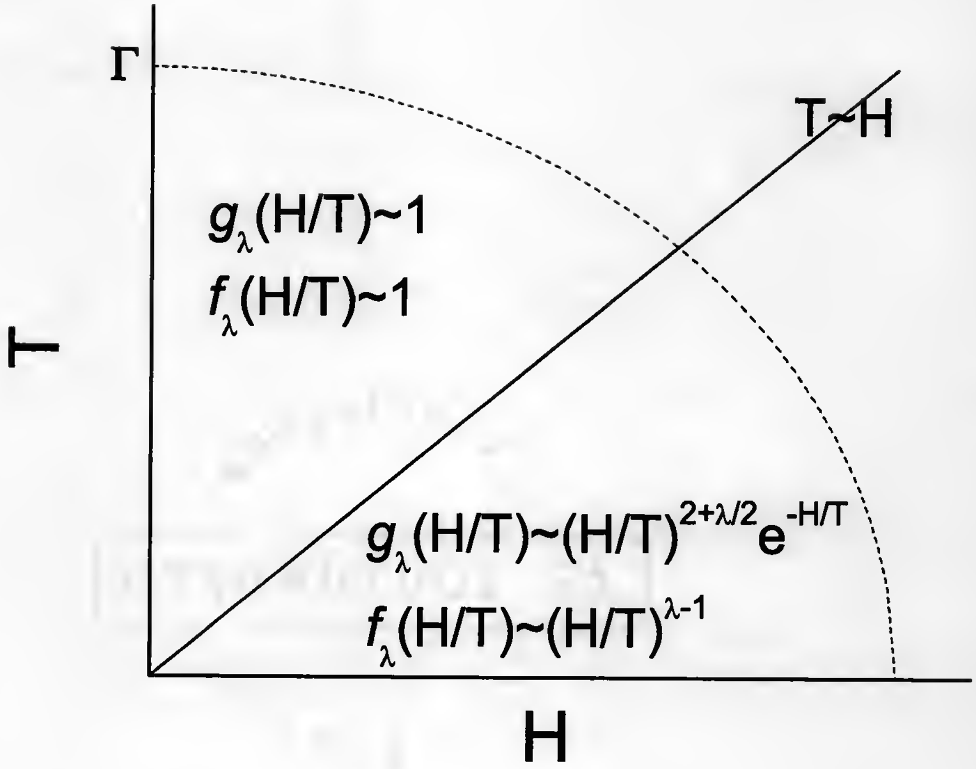
Γ
T~H
g_λ(H/T)~1
f_λ(H/T)~1
T
g_λ(H/T)~(H/T)$^{2+\lambda/2}$e$^{-H/T}$
f_λ(H/T)~(H/T)$^{\lambda-1}$
H

Figure 2–2: The Griffiths phase diagram taken from Ref. [21]. T-H phase diagram showing the behavior of the scaling functions for magnetization, f_λ(H/T), and specific heat, g_λ(H/T). The T $\sim$ H line is the crossover behavior between the high and low field limits. Γ is the average RKKY interaction in the system and above Γ, the magnetic cluster does not exist.

Castro Neto believe that their study in the realm of quantum ferromagnets is applicable to a wide class of systems:

1. heavy-fermion compounds such as $URu_{2-x}Re_xSi_2$ [35] and $Th_{1-x}U_xCu_2Si_2$ [87];
2. dilute magnetic semiconductors such as $Ga_{1-x}Mn_xAs$ [111];
3. ferromagnetic dichalcogenides such as $CeTe_2$ [69];
4. manganites such as $La_{1-x}Sr_xMnO_3$ [67]; and
5. two-dimensional electron systems in the quantum Hall regime [10].

The Curie temperature enhancement theory starts from the premise that local moments couple directly to an itinerant electron liquid and this premise can be expressed mathematically by the Hamiltonian [137]

$$\mathrm{H} = -\mathrm{J}\sum_{(\mathrm{i,j})} \mathbf{S}_\mathrm{i} \cdot \mathbf{S}_\mathrm{j} + \mathrm{J_K} \sum_{\mathrm{i},\sigma,\sigma'} \mathbf{S}_\mathrm{i} \cdot \mathrm{c}^\dagger_{\mathrm{i},\sigma}\, \overrightarrow{\sigma}_{\sigma,\sigma'}\, \mathrm{c}_{\mathrm{i},\sigma'} + \mathrm{H_e} \tag{2.7}$$

where J is a Heisenberg exchange between localized spins $\mathbf{S}_\mathrm{i}$ (total spin S), $\mathrm{J_K}$ is an exchange coupling between localized spins and conduction electrons, $\mathrm{c}^\dagger_{\mathrm{i},\sigma}$ $(\mathrm{c}_{\mathrm{i},\sigma})$ is the creation (annihilation) electron operator, $\overrightarrow{\sigma}$ are the Pauli matrices, and $\mathrm{H_e}$ describes the conduction electrons. Silva Neto and Castro Neto find for the case of a metallic system described by the Hamiltonian in Eq. 2.7 that dissipation (due to disorder) results from electrons scattering off localized moments and acting as a heat bath for the spin dynamics. The two main sources of dissipation are Landau damping in the case of clean magnets and electronic diffusion in the case of structurally disordered magnets [49, 44]. The effects of dissipation upon T_C will be discussed.

To begin their study of the dissipative problem, Silva Neto and Castro Neto considered an action of the form [124]

$$\mathrm{S_o}(\mathbf{n}) = \int_0^\beta \mathrm{d}\tau \int \mathrm{d^d}\mathbf{x} \left\{ \mathrm{M_o}\mathbf{A}(\mathbf{n}) \cdot \partial_\mathrm{T}\mathbf{n} + \frac{\rho_\mathrm{s}^0}{2} (\nabla\mathbf{n})^2 \right\} \tag{2.8}$$

where $\beta = 1/\mathrm{T}$, $\mathbf{n}$ is a N-component vector that represents the local magnetization, ρ_s^0 is the spin-stiffness, and $\mathrm{M_o}$ is the magnetization density in the ground state. The reason for showing this action is that the first term of the expansion inside the integral is a topological term (the kinematical Berry phase [123, 59]) described by the vector potential $\mathbf{A}$ of a Dirac monopole at the origin of spin space. This term signals the presence of localized moments [137]. This term is the main difference between the action of Silva Neto and Castro Neto and the action used by Hertz in his famous study of itinerant quantum critical phenomena [60]. Hertz did not include such a topological term. The topological term, along with dissipation, plays a vital role in the behavior of the Curie temperature [137].

Silva Neto and Castro Neto determined the effects of dissipation upon the Curie temperature. The phase diagram of the dissipative problem is determined by applying the momentum shell renormalization group and large-N analysis to the partition function of the system [137]. The dissipation depends upon the conduction electron dynamics as mentioned previously: Landau damping for a clean system and electronic diffusion for a dirty system. Silva Neto and Castro Neto show that if the Curie temperature is a function of dissipation, then the Curie temperature decreases faster for Landau damping than for electronic diffusion. The physical interpretation is that the ballistic electrons (from Landau damping) have an infinite mean free path and strongly scatter from the localized magnetic moments in the “cleaner” system. This strong scattering leads to a large amount of thermal and quantum fluctuations in the system. In the other case, the diffusive electrons (from electronic diffusion) have a finite mean free path and do not increase the thermal and quantum fluctuations as much. Interestingly, Silva Neto and Castro Neto predict about a 1% increase for the Curie temperature of a dirty system with a small amount of dissipation compared to the Curie temperature of a dirty system without dissipation (i.e., no disorder). No increase is expected for the

Curie temperature of a clean system with a small amount of dissipation compared to a clean system without any dissipation. The increase of the magnetism due to diffusion appears to be important in the 2D MOSFET problem also [24]. One final note concerning the Curie temperature enhancement involves the importance of the topological term in the competition between the dissipative and topological terms. If a diffusive system has no topological term, then T_C is rapidly suppressed and a slight increase in T_C is not predicted. To summarize the behavior of the Curie temperature between the ballistic/diffusive electrons and the existent/non-existent topological term, a figure taken from Silva Neto and Castro Neto is provided on page 45 [137].

Resistivity measurements should provide insight into whether or not a system is in the ballistic or diffusive case. Silva Neto and Castro Neto state that ballistic electrons have an infinite mean free path while diffusive electrons have a finite mean free path. Thus, $\ell_{\mathrm{b}} > \ell_{\mathrm{d}}$ where $\ell_{(\mathrm{b,d})}$ represent the (ballistic, diffusive) electrons respectively. Since the resistivity, ρ, is inversely proportional to the mean free path [7], then one would expect the resistivity for a diffusive system to be larger than the resistivity for a ballistic system. Thus, not only will magnetic susceptibility measurements be performed on $UCu_2Si_{2-x}Ge_x$ compounds, but also resistivity measurements.

In summary, disorder along with the competition between the RKKY interaction and the Kondo effect may lead to NFL behavior in $UCu_{5-x}Ni_x$ due to magnetic clusters. On the other hand, disorder may lead to electronic diffusion in ferromagnetic $UCu_2Si_{2-x}Ge_x$ and possible Curie temperature enhancement.

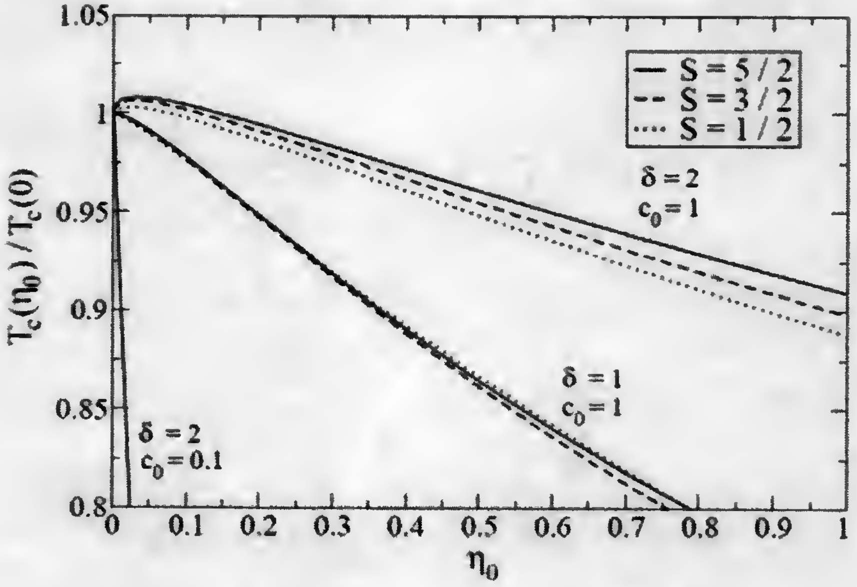

Figure 2–3: Curie temperature predictions by Silva Neto and Castro Neto. The Curie temperature $T_C(\eta_0)/T_C(\eta_0 = 0)$ as a function of dissipation, η_0. S is the total spin. If $\delta = 1$, then the dissipation is in the ballistic (clean) regime while $\delta = 2$ gives the diffusive (dirty) regime. The bare topological constant is represented by c_o and as $c_o \rightarrow 0$, then the topological term disappears.

CHAPTER 3
EXPERIMENTAL TECHNIQUES

All alloys in this dissertation were created by an arc-melting technique. In order to accurately categorize a system or compound, several experimental techniques must be employed. The first experimental technique is x-ray diffraction which confirms whether or not the compound formed into the correct crystal structure. The x-ray pattern is also used to determine the lattice parameter values of the fundamental "building block" of the compound, the unit cell. After confirmation of the correct crystal structure, many techniques are used to determine the correct thermodynamic and transport properties of the particular sample. These techniques (in no particular order) include direct current (dc) magnetic susceptibility, alternating current (ac) magnetic susceptibility, dc resistivity, and heat capacity measurements. All techniques and measurements previously mentioned will be described in further detail below.

3.1 Arc-Melting

The $UCu_{5-x}Ni_x$ and $UCu_2Si_{2-x}Ge_x$ systems had their own unique preparation procedures. The general idea behind the arc-melting process will be discussed first, followed by the preparation of the $UCu_{5-x}Ni_x$ system and $UCu_2Si_{2-x}Ge_x$.

The arc-melting process is based upon a large amount of current (with low voltage) passing through a tungsten electrode and producing an electric arc in Ar gas that runs from the tungsten tip down to a water cooled copper hearth inside a vacuum-tight chamber. Arc-melting is ideal for melting constituent elements with high melting points together. This dc apparatus melts the elements together in a zirconium-gettered argon atmosphere. The arc strikes the zirconium first because zirconium has a high absorption rate for certain residual gas components like oxygen. The argon atmosphere is used because argon is an inert gas and the argon helps raise the pressure inside the vacuum chamber so that the electric arc may be struck. Whenever melting elements together with significantly different melting points, the general principle is to melt the element with the lower melting point first and then draw the higher melting point elements into the molten element. In this respect, the mass loss of the lower melting point element is minimized. This arc-melting process is very similar to tungsten inert gas (TIG) welding.

The arc-melting of the $UCu_{5-x}Ni_x$ involves the melting of three constituent elements. The uranium and nickel have similar melting points and vapor pressures. The copper has the lowest melting point and the highest vapor pressure. Thus, excess copper ($\sim 0.5\%$ of the total Cu mass) was added to each $UCu_{5-x}Ni_x$ sample to account for the copper loss. Each $UCu_{5-x}Ni_x$ sample was arc-melted three to four times. After each melt, the sample bead was flipped over to insure homogeneity.

The effort involved in the arc-melting of the $UCu_2Si_{2-x}Ge_x$ compounds was a bit more intensive. The dilemma in arc-melting the $UCu_2Si_{2-x}Ge_x$ compounds came from the explosive nature of melting two semiconductors together, Si and Ge, along with the electric arc thermally shocking the formed $UCu_2Si_{2-x}Ge_x$ lattice. Two techniques were employed to solve these problems. First, the U, Si, and Ge constituent elements were melted together first and then subsequently melted together a minimum of at least six times. Second, the copper element was then melted into the U, Si, and Ge bead. All elements were melted together a minimum of six times to insure homogeneity. The second technique was employed on all arc-melts after the initial one. Instead of moving the electric arc directly from the zirconium bead to the $UCu_2Si_{2-x}Ge_x$ bead (this tended to blow apart the $UCu_2Si_{2-x}Ge_x$ bead), the electric arc was moved very slowly towards the $UCu_2Si_{2-x}Ge_x$ bead. Thus, the arc's convection and radiant heat would melt the

$UCu_2Si_{2-x}Ge_x$ bead and, before the arc was directly over the $UCu_2Si_{2-x}Ge_x$ bead, the bead would be molten. These techniques were used in the production of all $UCu_2Si_{2-x}Ge_x$ compounds.

Excess mass amounts of Cu, Si, and Ge were added before arc-melting. U has a very high melting point and low vapor pressure, so the mass loss of U was assumed to be negligible. Cu and Ge had almost identical melting points and vapor pressures, so the mass loss of Cu and Ge was assumed to be equal. The melting point of Si is about 50% higher than the melting points of Cu and Ge; thus, it was assumed that the mass loss of Si would be about half the mass loss of Cu or Ge.

The assumptions above were taken into account so that the appropriate extra masses could be added before arc-melting. Since a minimum of 12 arc-melts (as discussed previously) were performed on each $UCu_2Si_{2-x}Ge_x$ sample, all melts would "blow away" approximately 1.5% of the total Ge mass present, 0.50% of the total Cu mass, and about 5% of the total Si mass for compounds on the Ge rich side. Arc-melting compounds on the Si rich side would result in a loss of about 2% of the total Si mass, 5% of the total Ge mass, and 1% of the total Cu mass. Thus, depending on which $UCu_2Si_{2-x}Ge_x$ compound was being synthesized, excess Cu, Ge, and Si was added according to the above conditions.

One final technique that is related to sample preparation and arc-melting is the process of annealing. The purpose of annealing is to eliminate as much disorder as possible. All $UCu_{5-x}Ni_x$ and $UCu_2Si_{2-x}Ge_x$ compounds were annealed. Annealing involves pieces of sample being wrapped in tantalum foil and the wrapped sample is sealed in a quartz tube under vacuum. The samples are placed in ovens for an experimentally determined time such that the mass loss remains acceptably small ($< 0.5\%$ of the total mass) while the order of the crystal lattice is improved. The order in the lattice may be checked by x-ray diffraction.

3.2 X-Ray Diffraction/Lattice Parameter Determination from X-Ray Diffraction

Lattice parameter values can play an important part in determining the site occupation of atoms in a crystal structure along with the lattice values telling the story of whether or not the lattice expands or contracts upon the doping of a certain element. For example, the $UCu_{5-x}Pd_x$ system, which crystallizes in the face-centered cubic (fcc) $AuBe_5$ structure, shows that Pd substitution initially goes onto the larger Be I site until about $x = 0.8$ and for $x > 0.8$, the Pd atoms also start to occupy the smaller Be II sites also. This was seen not only in muon spin rotation (μSR) [92] and extended x-ray-absorption fine-structure (EXAFS) [15] measurements, but also by a change in slope of the lattice parameter values at $x \approx 0.8$ [77].

The present study is similar to those on the $UCu_{5-x}Pd_x$ system. Instead of doping larger (relative to the Cu atom) Pd atoms on the Cu sites, smaller Ni atoms will be doped on the Cu sites. The knowledge of the lattice parameter values at different Ni concentrations is imperative to gain insight on which copper site the Ni atoms are found (i.e., the Be I or Be II site).

Lattice parameters are calculated from x-ray diffraction patterns. X-ray diffraction was run on a Phillips XRD 3720 machine at the Major Analytical Instrumentation Center (MAIC) on the University of Florida campus. The complete x-ray diffraction process is described elsewhere [119].

The particular machine on which the x-rays were generated used two different wavelengths of radiation [copper $K\alpha_1 = 1.54056$ Angstrom (Å) and copper $K\alpha_2 = 1.54439$ Angstrom (Å)]. Also, the intensity of the α_1 beam was twice as great as the α_2 beam. This made resolving two distinct peaks at a particular crystallographic plane sometimes quite difficult since the α_1 peak would conceal the α_2 peak.

The typical x-ray pattern was generated with a 2θ (degrees) domain from 20° to 120° in 0.02° steps where 2θ is the total angle by which the incident X-radiation beam is deflected by a lattice plane. Almost all measurements had a one second step time where the detector on the x-ray machine moved continuously through a 0.02° interval in one second. The reason for such a long total scan time ($\sim$ 90 minutes) was to obtain good resolution around the high angle x-ray peaks ($> 80°$).

The Phillips XRD 3720 machine operation was controlled with a computer interface. Once the x-ray process was complete, the computer would generate a list of peaks from the x-ray pattern. The computer found the peaks at a respective 2θ value by finding the minimum of the 2nd derivative of the peak (i.e., where the change in the slope on the x-ray pattern is least).

Once the peaks along with their particular 2θ values are found via the computer, lattice parameter determination may begin in earnest. The easiest way to explain the lattice parameter calculation [107] is by using an example. The $\mathrm{UCu}_{5-x}\mathrm{Ni}_x$ system will be the example. Since the $\mathrm{UCu}_{5-x}\mathrm{Ni}_x$ system forms in the cubic AuBe_5 crystal structure, this system has very high symmetry and the perpendicular distance between two parallel lattice planes, d, may be written in terms of the Miller indices (hkl) of the plane [119]:

$$\mathrm{d(hkl)} = \frac{a}{\sqrt{\mathrm{h}^2 + \mathrm{k}^2 + \mathrm{l}^2}} \tag{3.1}$$

where lattice parameter value, a, is the side of the cubic crystal one is calculating and the Miller indices are defined as the coordinates of the shortest reciprocal lattice vector normal to a lattice plane, with respect to a specified set of primitive reciprocal lattice vectors (e.g., a plane with Miller indices h,k,l is normal to the reciprocal lattice vector $\mathrm{h}\mathbf{b_1} + \mathrm{k}\mathbf{b_2} + \mathrm{l}\mathbf{b_3}$) [7].

The inter-plane distance, d, is related to half the total angle by which the incident X-radiation beam is deflected, θ, by the well known Bragg condition [7]:

$$\mathrm{n}\lambda = 2\mathrm{d}\sin\theta \tag{3.2}$$

where n is a positive integer and λ is the wavelength of the incident radiation beam. If one combines Eq. 3.1 and Eq. 3.2 and assumes that $\mathrm{n} = 1$, then 'a' may be written in terms of λ, θ, and (hkl):

$$\mathrm{a} = \frac{\lambda\sqrt{\mathrm{h}^2 + \mathrm{k}^2 + \mathrm{l}^2}}{2\sin\theta}. \tag{3.3}$$

The values obtained from Eq. 3.3 will be the ordinate values for the graphical extrapolation method. The reason 'a' cannot be obtained directly from Eq. 3.3 is that Eq. 3.3 would require θ to equal 90° and 2θ would be 180°, which is physically impossible for the XRD machine. If 2θ were 180°, this would mean that the source and detector of the XRD machine were located at the same position. The detector and source at the same position on the XRD machine is not possible. The maximum achievable 2θ angle by the XRD machine is 140°. This justifies why an extrapolation method is needed to obtain 'a'.

The abscissa values used in the graphical extrapolation method take into account some possible sources of error. The function to be used for the x-axis values is advocated by Nelson and Riley [107]: $\frac{1}{2}(\cos^2\theta/\theta + \cos^2\theta/\sin\theta)$. This functional form takes into account possible errors caused by absorption and divergence of the x-ray beam.

Before the 'a' values can be graphed against the functional x-axis form, it has to be determined what (hkl) values correspond with peaks in the x-ray pattern. Thus, a particular θ value may be linked with a set of (hkl) values. Since it is known that $\mathrm{UCu}_{5-x}\mathrm{Ni}_x$ crystallizes in the AuBe_5 structure [153], a theoretical crystal pattern can be calculated with known information [33, 155] such as a lattice parameter constant (in this case, used the known UCu_5 value: 7.043 Å [155]), space group number (216 for UCu_5 structure), and atomic positions in the unit cell. This information was used by the PowderCell computer program to provide a theoretical pattern which included peaks with known (hkl) values. A visual inspection between the theoretical patterns and the experimental patterns of the $UCu_{5-x}Ni_x$ system could link peaks with particular (hkl) values as shown in Fig. A–1 on page 167 for UCu_4Ni annealed 14 days at 750°C. A list was generated with (hkl) values and corresponding 2θ values.

Once the (hkl) values and corresponding 2θ values are obtained, the 'a' values and x-axis values may be obtained from Eq. 3.3 and the Nelson-Riley error function respectively. A graph plotting the 'a' values versus the corresponding error function values for annealed UCu_4Ni is shown in Fig. A–2 on page 168. The values when plotted should show that the extrapolation line has a negative slope. The reason behind this negative slope is because all the sources of error lead to high values of θ and so to low values of the lattice parameters [119]. It should be stressed here that it is very important to have as many (hkl) values with $2\theta°$ values greater than 80° as possible. The importance comes from the fact that θ values close to 90° give Nelson-Riley functional values close to zero, insuring that the extent of extrapolation is not large [119].

The graphical extrapolation method is an excellent technique for determining lattice parameter values on a highly symmetric system such as $UCu_{5-x}Ni_x$. The error in the lattice parameter values as will be seen later for the unannealed and short term annealed $UCu_{5-x}Ni_x$ compounds is on the order of 10^{-3} Å. This error may be improved upon by running a cubic Silicon standard along with the respective experimental compound or by running the Silicon standard alone to determine the offset in the XRD machine. The latter process was done for this dissertation. The determination of lattice parameter values has been facilitated greatly by the advent of computers with software such as Jade.

3.3 Magnetic Susceptibility

Magnetic susceptibility measurements were used to measure the low temperature magnetization of the $UCu_{5-x}Ni_x$ and $UCu_2Si_{2-x}Ge_x$ samples. The susceptibility measurements were taken with two superconducting quantum interference devices (SQUIDs): an MPMS-5S [can measure with a magnetic field from 0 to 5 Tesla(T)] and an MPMS XL (measures up to 7 T) machine, both made by Quantum Design. Both machines could take magnetization measurements in the temperature range from 2 K to 300 K. The MPMS XL machine only had the capability to measure dc magnetic susceptibility while the MPMS-5S machine could measure both ac and dc magnetic susceptibility. Alternating current and dc magnetic susceptibility measurements will be discussed below.

3.3.1 DC Magnetic Susceptibility

Direct current magnetic susceptibilities are usually made in 1 kiloGauss (kG) magnetic fields. If the signal of the sample is comparable to the signal of the addenda (i.e., the plastic straw that holds the sample), then a 1 T magnetic field may be used so that the sample's signal is dominant over all other signals.

Direct current magnetic susceptibility measurements are based upon the principles of Lenz's Law. The sample is magnetized by a 1 kG magnetic field and the magnetic moment as a function of temperature of the sample is measured [94]. The magnetic susceptibility is determined by the following ratio: $\chi = M/H$. The magnetic moment is measured by induction techniques. The inductive measurements are done by moving the sample relative to a set of superconducting pickup coils and the SQUID instruments measure the current induced in superconducting pickup coils. The sample is typically moved 4 cm through the superconducting pickup coils while 48 data points are taken during the sample's movement to produce the magnetization curves. The sample is moved through the coils four times and the average of the four measurements is reported for a particular temperature.

Not only is the dc magnetization measured at various temperatures in a constant magnetic field, but also the dc magnetization is measured in different magnetic fields at a constant temperature. The magnetization versus field curves are typically generated at the lowest possible temperature (2 K). The MPMS XL is a particularly good machine for this type of measurement since it has a secondary impedance line that can maintain low temperatures continuously over an extended period of time (on the order of about 12 hours).

3.3.2 AC Magnetic Susceptibility

Unlike dc magnetic susceptibility measurements where the sample moment is constant during measurement time, ac magnetic susceptibility measurements for the MPMS-5S machine use a small ac drive magnetic field that is superimposed on the dc magnetic field, causing a time-dependent moment in the sample. Alternating current measurements do not require sample motion (as for the dc case) since the field of the time-dependent moment induces a current in the superconducting pickup coils. The measurements are usually made in a narrow frequency band, the fundamental frequency of the ac drive magnetic field. The ac susceptibility measurements in this dissertation were made at three different frequencies: 9.5 Hertz (Hz), 95 Hz, and 950 Hz. These three frequencies stayed within the frequency range of the MPMS-5S machine and avoided any integer multiples of the frequency of a common electrical outlet (60 Hz).

Alternating current magnetic susceptibility measurements yield two quantities: the magnitude of the susceptibility, χ, and the phase shift, ϕ (relative to the ac drive magnetic field). This phase shift comes from the fact that the magnetization of the sample may lag behind the ac drive magnetic field [94]. In terms of complex notation, the ac susceptibility measurements provide an in-phase, or real, component χ' and an out-of-phase, or imaginary, component χ". The ac magnetic susceptibility measurements on certain $UCu_{5-x}Ni_x$ samples were used to determine the antiferromagnetic phase transition temperature, $T_{Néel}$, for each compound. A peak in the real component of the ac magnetic susceptibility indicated the antiferromagnetic phase transition.

3.4 Cryogenics

The remaining two experimental techniques, dc resistivity and heat capacity, are primarily measured in a temperature range from 300 milliKelvin (mK) to about 10 K. In order to achieve such low temperatures, one must make use of liquid nitrogen and liquid helium.

The probe that is used to measure either low temperature resistivity or specific heat is first cooled down to the boiling point of liquid nitrogen (~ 77.4 K [54]). The probe is then quickly lifted out of the liquid nitrogen and placed in a Dewar, a vacuum insulated flask. The Dewar is then filled with liquid helium, which boils at 4.2 K. After a couple of hours, the inside of the probe is cooled down to 4.2 K.

Helium 4 can be cooled to below its boiling temperature by reducing the pressure inside the Dewar to below atmospheric pressure. In fact, using the combination of a large vacuum pump and blower, a pumped bath of liquid helium 4 can cool a probe down to about 1.1 K. If liquid helium 4 is cooled below its transition temperature, or "lambda point" (~ 2.17 K [54]), then the helium 4 starts to become a superfluid helium 4 that behaves as if it had no viscosity, i.e., it can flow through tiny holes. Also, the superfluid helium 4 has no entropy and it flows into a heated area to cool that area and restore the uniform mixture of normal and superfluid helium 4. This last physical property of superfluid helium 4 allows the temperature of the probe to be stable enough such that resistivity or specific heat may be measured. A full dewar of helium 4 in the lab that has a vacuum pump/blower attached to it can maintain a low temperature of 1.1 K for about 12 to 16 hours.

In order to achieve a temperature lower than about 1.1 K, helium 3 needs to be used. Helium 3 boils at 3.2 K [at 1 atmospheric pressure (atm)] [54]. Helium 3 is inserted as a gas into the probe and due to its rarity, helium 3 is trapped inside the probe so that it may be reused. Once the probe is cooled down to 1.1 K with the superfluid helium 4, the helium 3 gas is condensed by coming into contact with the 1.1 K probe and the helium 3 collects in the helium 3 pot. The low temperatures down around 300 mK are achieved by reducing the vapor pressure of the collected liquid helium 3 by using the internal sorption pump (i.e., charcoal on the end of a long rod) [66]. The sorption pump is "turned on" by lowering the charcoal into the vicinity of the helium 3 pot. This cools down the "warmed" charcoal to below 20 K since the charcoal was initially at the top of the probe. The helium 3 liquid is pumped on by the sorption pump while the sample (connected to the helium 3 pot via a weak thermal link) is cooled down to around 300 mK. The probe can stay down at such a low temperature for about three to four hours until all the liquid helium 3 evaporates. The sorption pump is then turned off by raising the charcoal in the probe so that it is above 20 K (i.e., above the ^{4}He level in the dewar) which desorbs the helium 3 gas and allows the helium 3 gas condensation cycle to start over again.

3.5 Probes

In the above discussion concerning cryogenics, the generic term probe has been used. In reality, two kinds of probes were used in the lab. One probe had a helium 4 pot which did not require the entire Dewar to be vacuum pumped upon. The second type of probe had no helium pot and pumping upon the Dewar was imperative to achieve a temperature around 1.1 K.

A probe with a helium 4 pot has its cross section inside the vacuum can shown in Fig. 3–1 on page 58 [71]. The vacuum can is mounted on the flange's probe with a brass taper joint seal that is lightly coated with silicone high vacuum grease, preventing the superfluid helium 4 to penetrate. The sample platform at the bottom is connected to a copper block and a thermally conducting grease is used so that the temperature gradient between the copper block and sample platform is minimal. The other side of the copper block is connected to a helium 3 pot with a brass thermal link and large diameter Cu wires (not shown in Fig. 3–1) run from the copper block to the helium 3 pot for improved thermal conductivity . These connections allow the sample platform to reach low temperatures of 300 mK once the sorption pump is turned on by lowering the charcoal inside the pumping line for the helium 3 pot in Fig. 3–1.

Once the helium 3 cryostat in Fig. 3–1 on page 58 is placed in a Dewar and allowed to reach normal liquid helium temperature ($\sim$ 4.2 K), the helium 4 pot may be pumped upon, which allows the helium 3 gas to condense. As the probe is cooling down inside the Dewar, a line connecting the helium 4 pot and the helium 4 bath inside the Dewar is open so that the helium 4 pot may be filled with liquid helium 4. Once the probe cools down to around 4.2 K, the temperature is lowered further by closing the capillary linking the helium 4 pot and the helium 4 bath with a needle valve and then connecting an external vacuum pump to the pumping line connected to the helium 4 pot. Thus, the liquid helium 4 inside the helium 4 pot is just pumped on instead of the entire helium 4 bath inside the Dewar. The germanium thermometer close to the sample platform in Fig. 3–1 registers a low temperature of about 1.6 K after the helium 4 pot has been pumped on for $\sim$ 20-30 minutes.

The other important aspect to the helium 3 probe concerns the wiring for the electronics to measure DC resistivity and specific heat. The wires come from the

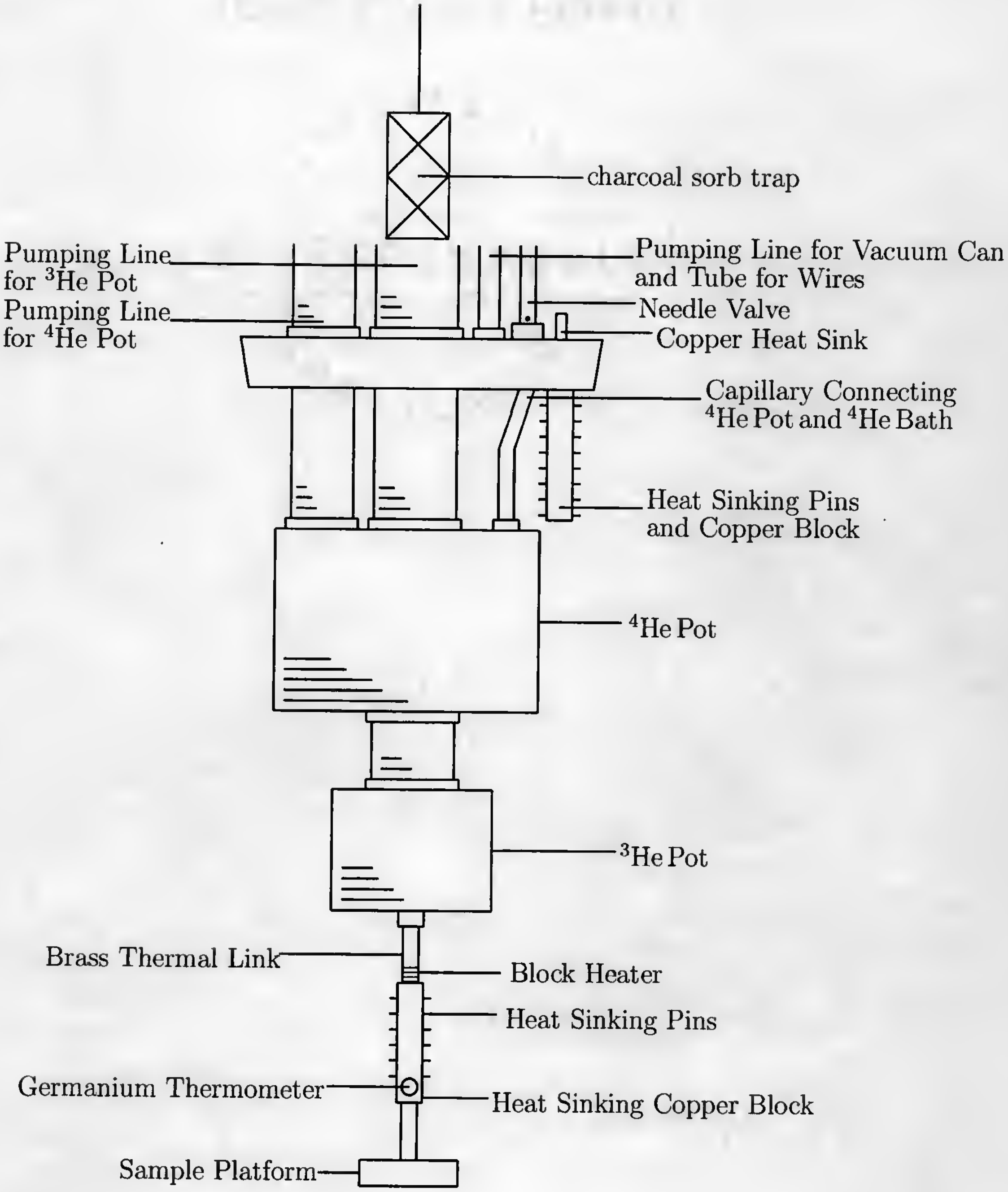
charcoal sorb trap
Pumping Line for ^{3}He Pot
Pumping Line for ^{4}He Pot
Pumping Line for Vacuum Can and Tube for Wires
Needle Valve
Copper Heat Sink
Capillary Connecting ^{4}He Pot and ^{4}He Bath
Heat Sinking Pins and Copper Block
^{4}He Pot
^{3}He Pot
Brass Thermal Link
Block Heater
Heat Sinking Pins
Germanium Thermometer
Heat Sinking Copper Block
Sample Platform

Figure 3–1: Cross-section of a helium 3 probe. This simplified cross-section contains a helium 4 pot. Such a probe is able to achieve a low temperature around 300 mK.

top of the probe and run down the pumping line for the vacuum can in Fig. 3–1. The wires from the top of the probe are soldered to the copper block above the helium 4 pot. The copper block is in temperature equilibrium with the Dewar's helium 4 bath by the copper heat sink in Fig. 3–1. The wires on the top copper block in Fig. 3–1 are then usually connected to the copper block right above the sample platform by more wires wrapped around the helium 3 and helium 4 pots and secured to these pots with General Electric (GE) varnish 7031 (a good thermal conductor). The reason for the wires not running from the top of the probe directly to the copper block above the sample platform concerns the amount of heat that would be transferred from the top of the probe which is at room temperature. The intermediate copper block connections allow the heat flow to be minimized.

The actual wires that are used in the helium 3 probe are either #40 gauge copper or #40 gauge manganin wires. Either type of wire is insulated and requires friction (from sandpaper or an eraser) to remove the insulation. The difference between copper and manganin wires is that manganin wire is about 30 times more electrically resistive than copper wire [71]. The higher electrical resistivity of the manganin wires is associated with less heat being transferred from the top of the probe. Thus, manganin wires should be used for low current loads while copper wires are used for high current loads. The wiring in the probe is composed of pairs of the same type of wiring twisted around each other so that the electrical noise is reduced.

The probe without the helium 4 pot has the exact same configuration as in Fig. 3–1 except for the helium 4 pot and the pumping line for the liquid helium 4. The Dewar itself may be thought of as the helium 4 pot for the case of the probe without the helium 4 pot.

3.6 DC Resistivity

Direct current electrical resistivity is based upon an equation derived from the Drude model for electrical conduction [7]:

$$\rho = \frac{\mathrm{AR}}{\mathrm{L}} \tag{3.4}$$

where ρ is the electrical resistivity that is being solved for, A is the cross sectional area of the resistivity bar being measured, and L is the distance between the voltage wires. The electrical resistivity was measured using a standard four wire technique that is discussed below.

The first part of the four wire technique involves making resistivity bars. The standard way of making resistivity bars involved cutting the particular sample with a diamond saw. The diamond saw could cut resistivity bars with rectangular cross sectional areas that had dimensions on the order of thirty thousandths of an inch. Another way to produce resistivity bars that avoids possible microcracks in the bars is the "sucker" method. The sucker method is done while arc-melting. The idea behind the sucker method is that while the arc has a sample in its molten state, a pressure difference between the arc-melter chamber and an external chamber on the sucker apparatus has enough force to push down the molten sample into a square cross sectional copper area. The copper area is water cooled, so the molten sample should quench as a square resistivity bar ideally. A sucker produced resistivity bar on a UCu_4Ni sample will be discussed later on in this dissertation.

Once the resistivity bars are made, four platinum wires need to be attached to each bar. The platinum wires have a diameter of 0.002 inches and a purity of 99.95%. There are two methods to attach these platinum wires to a resistivity bar. One method is to use EPO-TEK H31LV silver epoxy to "glue" the platinum wires onto the resistivity bar. The only problem with this method is that extra resistance is added to the measurement with the resistance of the silver epoxy and possible oxide barriers on the surface of the sample. The second method of attachment was used in this dissertation. It involved spot welding the four wires onto the resistivity bar. Spot welding minimized the contact resistance. The four wires should be spot welded on the same face of the resistivity bar with two wires on one end of the bar and the other two wires on the opposite end. The two outside platinum wires are the current leads while the two inside platinum wires are the voltage leads. The resistivity bar is then attached to a piece of non-electrically conducting compensated silicon with GE varnish 7031. The varnish is a good thermal conductor and a poor electrical conductor. The four platinum wires are attached to the silicon base with silver epoxy and there is some slack in the platinum wire between the resistivity bar and silver epoxy to account for the contraction at low temperatures. The silicon base is attached to a low temperature probe with a thermally conducting grease such as Apiezon N grease.

The low temperature resistivity measurements gather the resistance of the sample at a particular temperature. The resistance in Eq. 3.4 is then used to calculate the resistivity. One can see from Eq. 3.4 that in order for larger resistance measurements (hence, larger voltage measurements from Ohm's Law), one should maximize the distance between the voltage leads, L, and minimize the cross sectional area of the resistivity bar, A. This helps reduce the scatter in the resistance measurements (another apparatus that would help reduce the scatter is an ac resistance bridge).

The resistance measurements are automated. An HP 9000/300 series computer controls the current sources and voltmeters taking the measurements. The scatter in the resistivity measurements is reduced two ways. One way is to measure the resistivity in one current direction and then reverse the current to measure the resistivity in the opposite direction. The average of these two absolute values should eliminate any (e.g., thermoelectric) offset in the voltmeter taking measurements.

A second procedure should eliminate the effect of any drift in the voltmeter. The computer is programmed with an external and internal loop while taking resistance measurements. The internal loop reverses the polarity of the current as described above while the external loop dictates how may times the internal loop should be performed. The external loop averages the measurements taken by the internal loop. Most resistivity measurements in this dissertation had an external loop value of 10 and an internal loop value of 5.

3.7 Specific Heat

Specific heat is the quantity of heat needed to raise a unit mass of sample by a unit degree of temperature while keeping the property x (in this dissertation, pressure, p) constant during the rise of temperature:

$$\mathrm{C}_x = \lim_{\mathrm{dT}\to 0}\left(\frac{\mathrm{dQ}}{\mathrm{dT}}\right)_x \tag{3.5}$$

Before 1968, the above definition was used in a technique called the adiabatic method [141] to measure specific heat. The adiabatic method added a pulse of power (dQ) to a sample and the temperature rise (dT) in the sample was noted. A couple of drawbacks to the adiabatic method are the large sample size needed to minimize the effects of stray heat leaks and the thermal isolation of the sample from its surroundings [71].

In 1968, Sullivan and Seidel published their ac heat capacity technique [144]. The ac method measures small samples that makes use of a commercially available lock-in amplifier. The strength of this technique is its ability to detect very small changes in heat capacity [141]. However, a drawback to this ac temperature calorimetry is in measuring the absolute value of the specific heat of a sample. This ac method usually provides only a relative measurement of the specific heat [71].

The specific heat technique used in this dissertation is the thermal relaxation method [9]. The thermal relaxation method was constructed from the solution of a one-dimensional heat-flow equation with appropriate boundary conditions [9]:

$$\mathrm{P} = \mathrm{A}\kappa\frac{\partial \mathrm{T}}{\partial \mathrm{z}} + \mathrm{C(T)}\frac{\partial \mathrm{T}}{\partial \mathrm{t}}, \tag{3.6}$$

where P is the power put into the sample, A is the cross sectional area of the wire linking the sample platform to the copper block, κ is the linking wire's thermal conductivity and the heat flows along the z-axis. The solution for C in Eq. 3.6 is $\mathrm{C} = \kappa\tau_1$ where τ_1 is the time constant of

$$\mathrm{T} = \mathrm{T}_0 + \Delta\mathrm{T}e^{-\mathrm{t}/\tau_1} \tag{3.7}$$

with $\Delta\mathrm{T} = \mathrm{T} - \mathrm{T}_0$ and T_0 is the copper block temperature.

The answer above is interpreted by Fig. 3–2 on page 64. In Fig. 3–2, the sample along with all the addenda on the sapphire ($\mathrm{Al_2O_3}$) platform is heated a small $\Delta\mathrm{T}$ above the copper block temperature T_0, by means of power, P, flowing through the platform heater. Once the power is turned off on the heater, the temperature of the sample and platform decay exponentially as in Eq. 3.7 with time constant, τ_1, through the linking wires. The time constant, τ_1, is determined using computer analysis of the temperature decay. By knowing the thermal conductance, κ, of the linking wires, one may determine the total heat capacity of the sample and platform. If the addenda are known as in Fig. 3–2, then one may determine the heat capacity of the sample by subtracting the addenda from the total heat capacity. All components of the addenda will be discussed in detail later on. It should be said that the rise in temperature, $\Delta\mathrm{T}$, should be small enough so that τ_1 does not change appreciably between T_0 and $\mathrm{T}_0 + \Delta\mathrm{T}$ [141]. When performing low temperature specific heat measurements, $\Delta\mathrm{T}$ was usually around 4%. The absolute accuracy of the thermal relaxation method to measure specific heat is estimated to be 5% [71], which is verified by measuring the known specific heat of a high purity standard, e.g., Pt or Au.

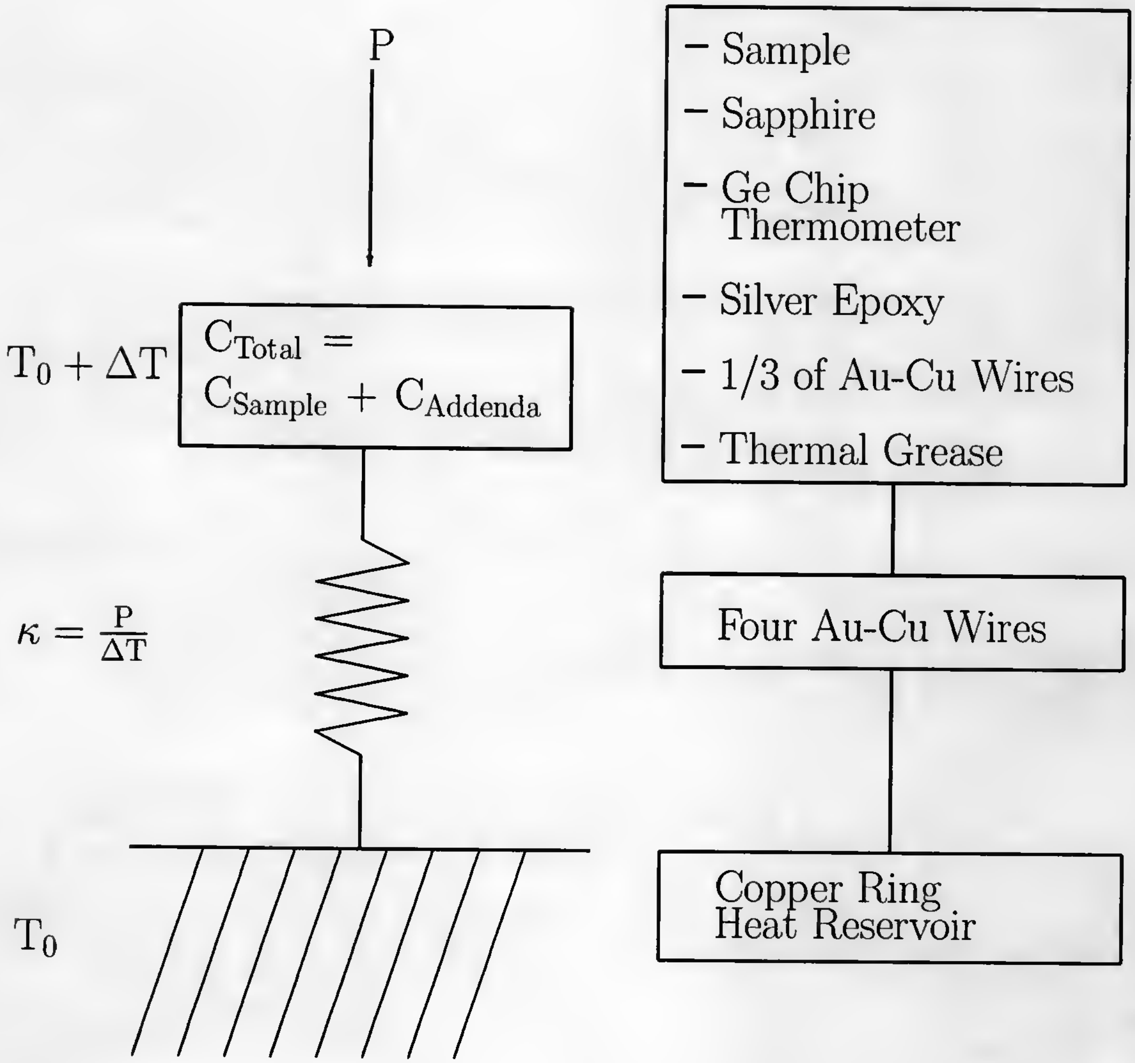

Figure 3–2: Schematic diagram outlining the thermal relaxation method. The thermal relaxation method is used for the specific heat measurements. The addenda is composed of the sapphire, the germanium chip thermometer, EPO-TEK H31LV silver epoxy, 1/3 of the linking wires, and thermal grease. The linking wires are the four Au-Cu wires connecting the sample platform to the copper block.

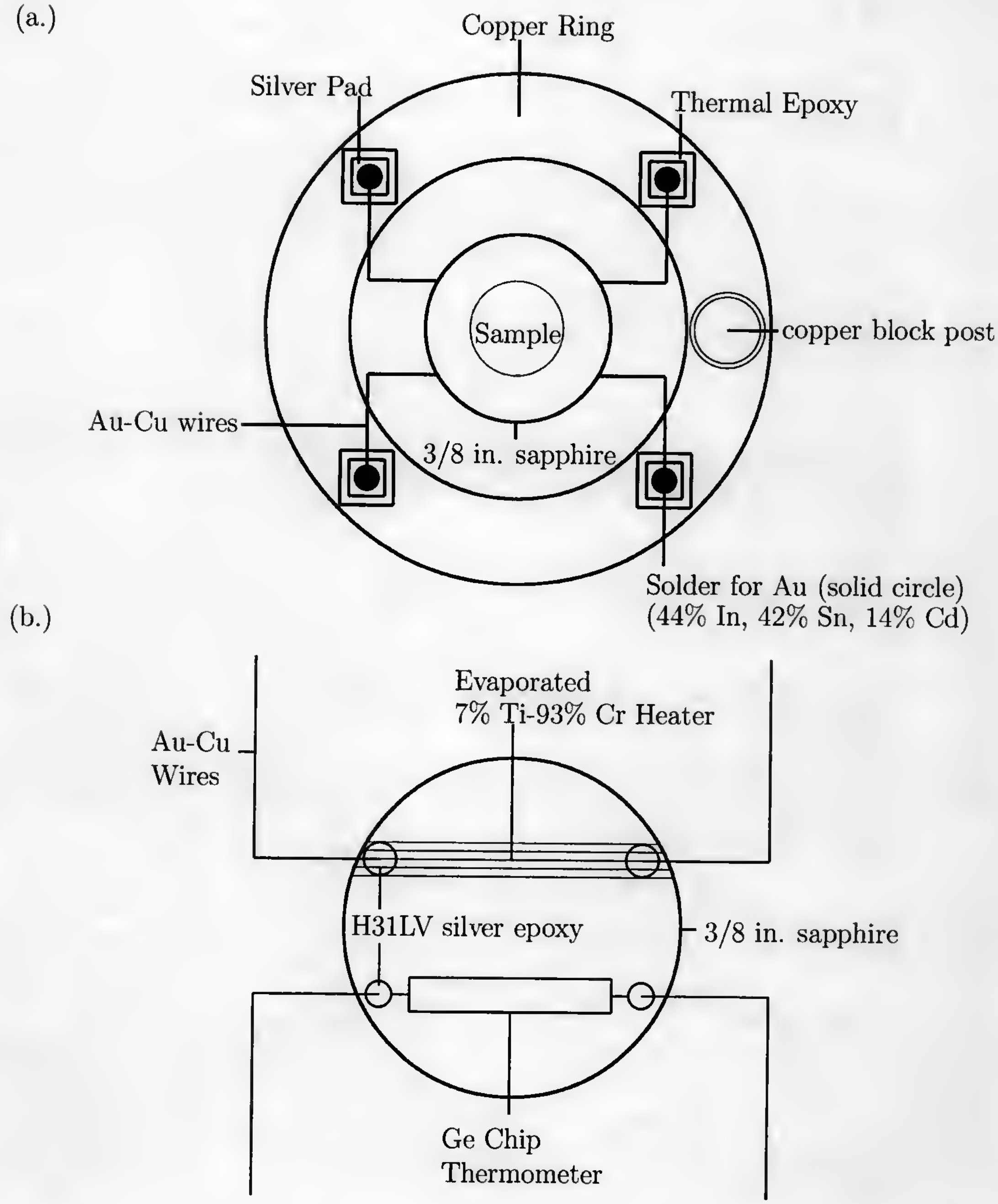

Figure 3–3: An overhead and bottom view of the mounted sample platform. (a.) The thermal epoxy used was a two component Stycast 1266 epoxy. The copper block post connects the copper ring to the copper block as shown in Figure 3–1. The Au-Cu wires connecting the sample platform to the copper ring are Au with 7% Cu to provide the correct magnitude for the thermal link.
(b.) The evaporated 7% Ti and 93% Cr heater is a thin continuous film on the bottom of the sapphire disk. The Ge chip thermometer is linked to the silver epoxy with Au-Cu wires.

In Fig. 3–3, two views of the sample platform are shown. The Au-Cu wires that were used in this dissertation were Au-7% Cu wires. These wires steady the platform on the sapphire and serve as electrical contacts and thermal links to the copper ring (hence the copper block). The thermal conductance of the wires depends on several factors. The first factor has been mentioned indirectly, the composition of elements making up the wires. For example, Au-1% Cu wires have a thermal conductance seven times that of Au-7% Cu, while Cu-2% Be has a thermal conductance five times less than Au-7% Cu. The second factor that varies the thermal conductance in the wires is the diameter of the wire. The specific heat measurements in this dissertation used 0.003 inch (in.) diameter Au-7% Cu wires. The thermal conductance of the 0.003 in. diameter wires is nine times that of the 0.001 in. diameter wires [141]. The reasoning behind choosing the 0.003 in. diameter wires is that 0.001 in. diameter wires are a little too fragile while inserting or removing the sample onto or off of the sample platform.

The Au-7% Cu wires are attached to the copper ring in part (a.) of Fig. 3–3 with special solder (44% In, 42% Sn, 14% Cd) on a silver pad. The silver pad is electrically insulated from the copper ring with a thermal epoxy (in this case, Stycast 1266 epoxy); however, the thermal epoxy is a good thermal conductor. The reason for using the special solder is that regular solder (composed of Pb and Sn) will dissolve the Au-Cu wires.

The sample itself is mounted on the “rough” side of a smaller sapphire disk. The flat part of a sample (for improved thermal conductivity) is attached to the sapphire disk with GE 7031 varnish. Then, the “smooth” side of the sapphire with the sample is mounted on the 3/8 in. sapphire disk in part (a.) of Fig. 3–3 with thermally conductive grease (in this case, Wakefield grease) [9]. Both sapphire disks are pressed firmly together to allow for a continuous and even distribution of thermally conductive grease between the disks. Before each measurement, both sapphire disks have to have the grease cleaned off of them with trichloroethane. The mass of all components (sample, GE 7031, sapphire, and grease) has to be known for accurate specific heat values.

The platform heater in part (b.) of Fig. 3–3 is composed of a thin film of 7% Ti and 93% Cr on the "rough side" of the 3/8 in. sapphire disk. This platform heater is created by evaporating a $Ti_{0.07}Cr_{0.93}$ sample onto the sapphire disk with evaporator instrumentation. The resistance of this platform heater is around 300 Ohms (Ω) [71] and the resistance remains fairly constant with varying temperatures.

The doped germanium chip thermometer (commercially obtained from Cryocal or Lakeshore Cryotronics) in part (b.) of Fig. 3–3 is used for the sample platform thermometer. The reason for using doped germanium was that its resistance is a rapid function of temperature [141]. This sensitivity is vital for the thermal relaxation method since the increase in the platform temperature at each data point is not very large ($\sim$ 4%). The calibration of the germanium chip thermometer's resistance versus temperature will be discussed later on.

The key to an accurate measurement of a sample's specific heat is the proper subtraction of all components (i.e., the addenda) involved in the thermal relaxation method. As mentioned previously, some of the addenda are listed in Fig. 3–2 on page 64. The sapphire disks that serve as the sample platform have high thermal conductivity (about 1 Watt $\mathrm{cm}^{-1}\ \mathrm{K}^{-1}$ at $\mathrm{T} = 4$ K) and low specific heat (2 μJ $\mathrm{gram}^{-1}\ \mathrm{K}^{-1}$ at $\mathrm{T} = 2$ K and $\theta_{\mathrm{D}} \approx 1035\,\mathrm{K}$) [48]. The platform heater in part (b.) of Fig. 3–3 that is composed of $Cr_{0.07}Ti_{0.93}$, which has a mass < 0.01 mg, is assumed to have a negligible contribution to the specific heat of the addenda [71]. The other component on the bottom of the sample platform next to the platform heater is the germanium resistance thermometer that has a specific heat value of 0.018 μJ/K at 2 K with a mass of 3.8 mg [71]. The leads attached by the factory to the germanium resistance thermometer are connected to the Au-7% Cu wires by means of H31LV silver epoxy. The silver epoxy is a source of addenda contribution. For example, a mass of 0.63 mg of silver epoxy has a specific heat value of 0.12 μJ/K at T = 2 K [71]. The GE7031 varnish and Wakefield grease also add to the addenda. At T = 2 K, the Wakefield grease has a heat capacity of 0.16 μJ/K for a mass of 0.12 mg [71]. The final component of the addenda concerns the Au-7% Cu wires. The diameter of the Cu wires not only has to be known (0.003 in.), but also the length of the four wires (each wire was 0.25 in. long) as shown in part (a.) of Fig. 3–3 on page 65. Bachmann *et al.* determined that 1/3 of the Au-7% Cu wire's heat capacity should be included as addendum [9]. At T = 2 K, the amount of addenda for 1.5 mg of Au-7% Cu wires is 0.044 μJ/K. The addenda contribution from the Au-7% Cu wire rises rapidly with temperature due to the low Debye temperature of the wires ($\theta_{\mathrm{D}} \sim 165$ K [141]). The temperature range (0.3 K to 8 K) at which the specific heat was measured for samples in this dissertation avoided too large an addenda contribution from the Au-7% Cu wires. The computer programming language, HPBASIC, used temperature dependent and mass dependent polynomial fits for each addenda contribution mentioned above in order to provide a realtime subtraction for the heat capacity measured at a particular temperature. A standard piece of gold was measured using the thermal relaxation method and it was found that if all the aforementioned addenda was not subtracted off, then the specific heat of gold at 2 K would be about 10% too high from its reported standard value ($\sim 5.001\,\mathrm{mJ\,mole^{-1}\,K^{-1}}$ [13]) [71].

Once the cryostat with all of its components is assembled, the cryostat parts mentioned above need to be interfaced with instrumentation (i.e., voltmeters and current sources) that is controlled by an HP 9000/300 series computer. The block thermometer (i.e., a resistor) is hooked to a voltmeter and current source so that resistance (i.e., temperature) values may be obtained. The block heater (usually made up of a bundle of manganin wire) which controls the temperature of the block thermometer, the copper ring, and the sample platform is connected to a current source so that Joule heating may raise the low temperature of the bottom of the cryostat. The platform heater that provides the small temperature rise to the sample platform is also connected to a current source. The final component concerns the germanium chip platform thermometer whose resistance is very sensitive to small temperature changes. The platform thermometer is half of one arm of an ac Wheatstone bridge. The other half of the arm is connected to a variable resistor (i.e., a resistance box). The other arms of the ac Wheatstone bridge consist of two known resistors (each resistor is 90 kΩ). The platform thermometer has a lock-in amplifier connected across it to provide a source of ac excitation current and to serve as a null detector [9]. The ac excitation current is limited by the self heating of the platform thermometer. The other reason for using the lock-in amplifier is to increase the signal-to-noise ratio [141] by filtering out noise at other than the measurement frequency (~ 2700 Hz) [71]. The lock-in amplifier is connected to the HP 9000/300 series computer through an analog-digital converter. The converter digitizes the signal from the ac Wheatstone bridge for the computer during specific heat measurements.

Before actual specific heat values are measured, proper calibration of the germanium chip thermometer has to be performed. The ac Wheatstone bridge is used to measure the platform thermometer resistance at a known block temperature on the bottom of the cryostat [116]. The reciprocal of the platform temperature, T, is then fitted to a polynomial as a function of the natural logarithm of platform thermometer resistance, R:

$$\frac{1}{\mathrm{T}} = \sum_{i=0}^{n} \mathrm{A}_i (\ln \mathrm{R})^i \qquad (3.8)$$

where n = 4 was used in the calibration. Equation 3.8 is then used (by the HP 9000/300 series computer) to interpolate the platform thermometer temperature value using the resistance value experimentally found.

The final calibration concerns measuring the thermal conductivity, κ, of the four Au-7% Cu wires in Fig. 3–3 on page 65. The thermal conductivity, κ, may be written in terms of the power, P, supplied across the platform heater and the associated temperature rise, ΔT, in the platform thermometer:

$$\mathrm{P} = \kappa \Delta \mathrm{T}. \tag{3.9}$$

If one starts from a base temperature, T_0, on the copper ring and the sample platform in part (a.) of Fig. 3–3, then a small amount of known current is supplied through the platform heater and the corresponding voltage drop across the heater is measured in order to determine the power, P. The platform thermometer resistance is determined before and after the power is supplied to the heater so that T_0 and ΔT are known from the germanium platform thermometer calibration discussed previously. The thermal conductance of the Au-Cu wires is then determined using Eq. 3.9 at a temperature of $\mathrm{T}_0 + \Delta\mathrm{T}/2$. The thermal conductance of the wires divided by temperature, κ/T, may be written as a power series of just temperature or the natural logarithm of temperature

$$\frac{\kappa}{\mathrm{T}} = \sum_{i=0}^{n} \mathrm{A}_i \mathrm{T}^i \quad \text{(or)} \quad \frac{\kappa}{\mathrm{T}} = \sum_{i=0}^{n} \mathrm{B}_i (\ln \mathrm{T})^i \tag{3.10}$$

where n = 4 was usually used by the HP 9000/300 series computer to find an interpolated conductance value at a particular temperature. The advantage of the second form in Eq. 3.10 is that the same conductance equation may be used over a larger temperature range (30 mK to 10 K) while the first form is usually split into a low temperature equation and a high temperature equation where 1.3 K is the approximate dividing temperature.

The calibrated thermal conductivity equation is then checked by either measuring pure palladium, platinum, gold, or copper and comparing to known standard specific heat values of the aforementioned elements [13]. The standard sample used in this dissertation that was measured to check the conductance values was pure platinum (99.9985% purity).

A problem that has to be taken into account when measuring specific heat values by the thermal relaxation method is known as the "τ_2 effect." The τ_2 effect is the thermal lag between the sample and the platform [141]. The τ_2 effect comes from large thermal resistance, poor conductivity of the sample, or of the sample-platform contact and throws the temperature decay off from its exponential shape [71]. A couple of procedures exist to account for this τ_2 effect. First, the temperature decay curve should be composed of the sum of two exponential curves like

$$\mathrm{T(t)} = \mathrm{T_0} + \mathrm{A}\exp\left(\frac{-t}{\tau_1}\right) + \mathrm{B}\exp\left(\frac{-t}{\tau_2}\right) \tag{3.11}$$

where T is the temperature, $\mathrm{T_0}$ is the baseline temperature, t is time, τ_1 is the time constant of the sample and addenda, τ_2 is the second time constant that throws the exponential decay off, and the coefficients A and B are determined by a graphical fit using the HP 9000/300 series computer. The second procedure for improving the τ_2 effect concerns the lock-in amplifier. The signal integration time should be set to less than $\tau_1/40$ for a better τ_2 correction. Not only is the τ_2 effect less smeared, but also a transient, which causes rounding of the exponential decay curve near the beginning, is eliminated.

When the actual specific heat measurements are taken, a program developed by Dr. Bohdan Andraka on the HP 9000/300 series computer controls the measurements. Once all known addenda masses are entered into the computer, the computer first prompts the user for the base temperature, T, at which both the block thermometer and platform thermometer are stabilized. The base temperature, T, is determined by varying the resistance in the ac Wheatstone bridge to match the resistance of the platform thermometer using the lock-in amplifier as the null detector. The experimentally determined resistance is then entered into the computer so that the platform thermometer temperature is interpolated from the calibrated germanium platform thermometer resistance. The computer also "communicates" with the current source and voltmeter to determine the resistance of the block thermometer and hence the temperature of the block thermometer using a calibration curve. The computer then asks for the amount of current to supply to the platform heater such that the temperature rise, ΔT, is about 4% higher than T. Since the time constants that were dealt with in this dissertation were usually under ten seconds, the new platform temperature usually became stable in under one minute. The variable resistor was then changed to determine the new, higher platform temperature. After the higher platform temperature was determined, the resistance box was manually turned to the average of the two determined resistance values with the current to the platform heater still on. The computer then would perform one sweep to determine the temperature decay curve. This sweep entailed the computer turning off the current to the platform heater and then signal averaging 4000 points from the output of the lock-in amplifier for the platform temperature decay curve. The platform temperature decays down to the base temperature. The 4000 points are plotted on a semilogarithmic graph (the distance from the decay curve to the base temperature is plotted on the graph) and a least squares fit is used to determine the time constant value. Multiple sweeps may be performed automatically by the computer and signal averaged to improve the signal-to-noise ratio. Also, the computer allows the user the option of taking into account the τ_2 effect. After the time constant value is determined, the computer outputs the correct specific heat value of the sample after subtracting off the addenda contributions. Then, more current is supplied to the block heater such that the next specific heat value may be determined at a higher temperature. A couple of systematic errors one needs to be aware of that might show up as oscillations in the base temperature concerns changes in block heater current (due to electrical pickup) and fluctuations in the surrounding liquid helium bath [9].

Specific heat measurements were also performed in magnetic fields (2 - 13 T) for this dissertation. The thermal conductance of the Au-7% Cu wires has to be corrected depending upon the amount of magnetic field used. The thermal conductance of the Au-7% Cu wires decreases approximately linearly such that at 12 T, the thermal conductance of the Au-7% Cu wires is 3% less than the 0 T thermal conductance values [120]. Also, calibration curves have to be reconfigured for the block thermometer. A block thermometer calibration curve has to be constructed for every magnetic field using a field correction according to Naughton *et al.* [106]. Some drawbacks to measuring in magnetic fields are that the germanium platform thermometer has a large magnetoresistance $\rho(18\,\mathrm{T})/\rho(0\,\mathrm{T}) \simeq 5.6$ at 4.2 K [141] and a noise problem in magnetic fields [71].

The ease of specific heat measurements has been facilitated by advancements in technology. In fact, Quantum Design sells an automated specific heat measurement system that uses thermal relaxation calorimetry and is named the physical property measurement system (PPMS) [86]. It will be mentioned here that a couple of $\mathrm{UCu_2Si_{2-x}Ge_x}$ samples in this dissertation had their heat capacity values measured on a PPMS at LANL.

CHAPTER 4
$UCu_{5-x}Ni_x$ RESULTS AND DISCUSSION

Nine $UCu_{5-x}Ni_x$ compounds were arc-melted and annealed as described in the "Experimental Techniques" chapter. The nine compositions were x = 0.5, 0.6, 0.75, 0.8, 0.9, 1.0, 1.05, 1.1, and 1.2. The "full spectrum" of measurements was performed upon the $UCu_{5-x}Ni_x$ system. The following sections contain lattice parameter measurements, dc electrical resistivity measurements, ac and dc magnetization measurements, and specific heat measurements (in zero magnetic field and various magnetic fields). The development of the NFL behavior in the $UCu_{5-x}Ni_x$ system will be investigated through the perspective of the Griffiths-phase disorder model. All tables in this chapter are found at the end of the chapter beginning on page 126.

4.1 Lattice Parameter Values for $UCu_{5-x}Ni_x$

The lattice parameter values for the nine cubic $UCu_{5-x}Ni_x$ compounds are found in Table 4–1 on page 126. The unannealed and annealed (for 14 days at 750°C) samples that had their lattice parameter values reported came from the same arc-melted bead. The arc-melted bead was cut in half with a diamond wheel saw and half the bead was used as an unannealed sample while the other half was annealed. All lattice parameters were determined using the graphical extrapolation method described in the preceding "Experimental Techniques" chapter.

The unannealed and annealed lattice parameter values are shown graphically in Fig.s 4–1 and 4–2. The unannealed $UCu_{5-x}Ni_x$ compounds show no signs of a change in the slope of the lattice parameter value versus Ni concentration as occurred in $UCu_{5-x}Pd_x$ [160]. Annealing the $UCu_{5-x}Ni_x$ compounds also shows that there is no existence of preferential occupation by Cu or Ni as occurred with

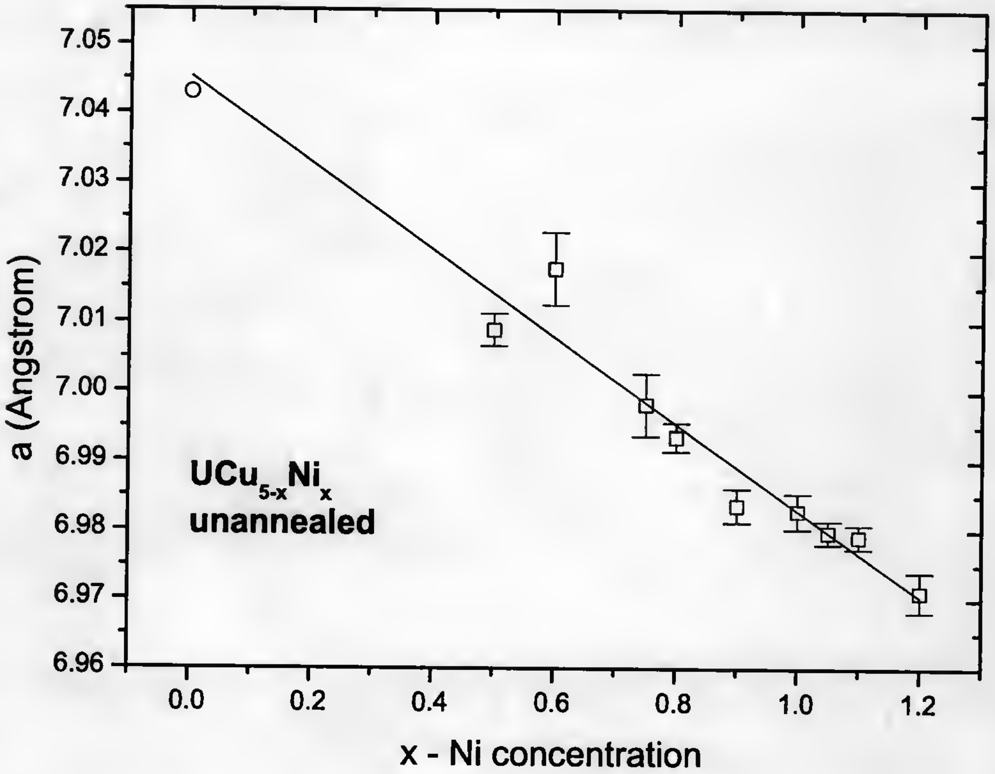

Figure 4–1: Lattice parameter values for unannealed $UCu_{5-x}Ni_x$ compounds. The best fit line is for the nine experimentally determined lattice parameters in this dissertation (represented by hollow squares while the vertical lines are the corresponding error bars). The equation for the best fit line is as follows: a = 7.04521 - 0.06233 x. The UCu_5 value (represented by a hollow circle) is taken from literature [18] and it was an unannealed sample.

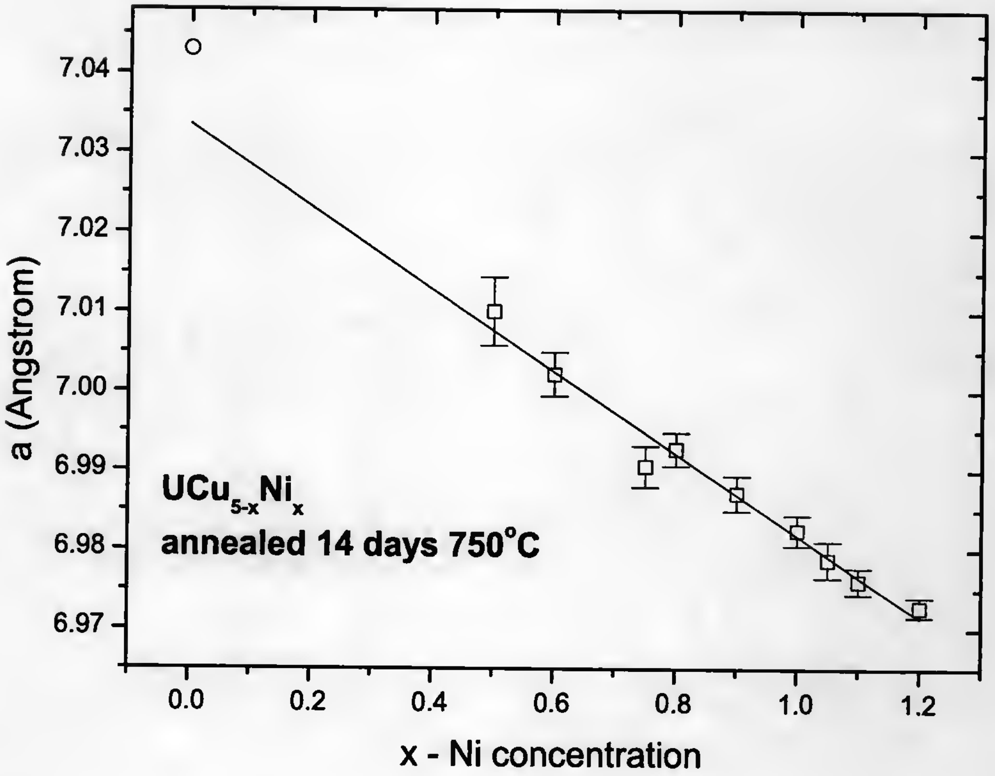

Figure 4–2: Lattice parameter values for annealed $UCu_{5-x}Ni_x$ compounds. The best fit line is for the nine experimentally determined lattice parameters in this dissertation (represented by hollow squares while the vertical lines are the corresponding error bars). The equation for the best fit line is as follows: $a = 7.03348 - 0.05171\ x$. The UCu_5 value (represented by a hollow circle) is taken from literature [18] and it was an unannealed sample.

Pd in $UCu_{5-x}Pd_x$ [143]. In fact, the annealing just sharpens the Vegard's law behavior (i.e., the linear behavior of the lattice parameters as a function of Ni doping since all compounds form in the same crystal structure). The difference in the goodness of fits (i.e., the standard deviations) between the best fit lines for unannealed (larger standard deviation) and annealed $UCu_{5-x}Ni_x$ lattice parameters is greater than a factor of two (the best fit lines are seen in Fig.s 4–1 and 4–2). Virtually all nine of the experimentally determined lattice parameters for annealed $UCu_{5-x}Ni_x$ lie along (within their error bars) a straight line in Fig. 4–2.

Not only do the lattice parameters as a function of annealing show no change in the order of the $UCu_{5-x}Ni_x$ samples, but also high angle x-ray diffraction lines provide insight into the order. The (7 3 1) diffraction line occurs at $\sim 115.9°$ on an x-ray diffraction scan as seen in Fig. A–1 on page 167. The line width for the (7 3 1) peak is the same for the unannealed $UCu_{5-x}Ni_x$ compounds and the $UCu_{5-x}Ni_x$ compounds annealed at 750°C for 14 days. Thus, short term annealing does not increase the order of the $UCu_{5-x}Ni_x$ compounds, contrary to what was observed for $UCu_{5-x}Pd_x$ [160].

The lattice parameters' results also allow one to make a few comments regarding the occupation of atomic positions in the cubic unit cell. In order to get a visual representation of the discussion that follows, one may want to refer back to the conventional $AuBe_5$ crystal structure in Fig. 1–1 on page 3 of the "Introduction" chapter. The lattice parameter results show that the 4a sites in Fig. 1–1 are occupied by the U atoms as occurred in $UCu_{5-x}Pd_x$. The larger minority sites inside the unit cell (i.e., the 4c site) are basically occupied by the larger Cu atoms (relative to the Ni atoms) while the smaller majority sites (the 16e sites) inside the unit cell have approximately 25% of the Ni concentration located at one of the four sites in the unit cell. A small percentage of the Ni concentration does occupy the 4c sites even for the annealed cases. The exact amount would have to be determined by μSR and EXAFS measurements as was done for the $UCu_{5-x}Pd_x$ system [15, 93]. This is in stark contrast to $UCu_{5-x}Pd_x$ where the Pd atoms (larger than the Cu atoms) show preferential sublattice ordering as discussed earlier [143]. To summarize, the 4c sites inside the unit cell for annealed UCu_4Pd have a $> 80\%$ occupation by the Pd atoms while the 16e sites have a less than 5% occupation by Pd [16]. Thus, the partial order present (along with disorder) in the $UCu_{5-x}Pd_x$ system is not a concern in the $UCu_{5-x}Ni_x$ system. The lattice parameters in Fig.s 4–1 and 4–2 reveal this. The $UCu_{5-x}Ni_x$ system has a higher degree of disorder than the $UCu_{5-x}Pd_x$ system with the Ni atoms having a much greater percentage of occupation at the 16e sites as compared to the Pd atoms ($\sim 25\%$ versus $< 5\%$). The lattice parameter results also show that clear distinctions can be made concerning the roles of quantum criticality and disorder in the NFL behavior of $UCu_{5-x}Ni_x$ without the worry of partial order as occurred in $UCu_{5-x}Pd_x$.

The lattice parameter values are used to determine the smallest U-U separation in the lattice. If one goes back to Fig. 1–1 on page 3 in the "Introduction" chapter, one may determine that the smallest U-U distance is ~ 0.707a (the shortest distance is a straight line from a corner 4a site to a nearest face-centered 4a site in Fig. 1–1) where 'a' is the calculated lattice parameter of a particular $UCu_{5-x}Ni_x$ sample. The smallest lattice parameter value is for unannealed $UCu_{3.8}Ni_{1.2}$ where a = 6.97107 Å in Table 4–1. Therefore, the smallest U-U separation is ~ 4.93 Å. This is not close to the Hill limit of 3.5 Å [65] where if the distance of nearest U-U separation, d_{U-U}, is less than 3.5 Å, then the f-electron orbitals of uranium in a lattice will overlap with those of the neighboring U ions and produce itinerant f-electron behavior (i.e., non-magnetic ordering). If $d_{U-U} > 3.5$ Å, then uranium f electrons (barring strong hybridization effects) are localized and magnetic [143]. As one will see in the specific heat section of this chapter, $UCu_{3.8}Ni_{1.2}$ does not display magnetic ordering down to ~ 0.3 K. Thus, there is significant f-electron hybridization with the d-electron orbitals of Cu and Ni in the $UCu_{5-x}Ni_x$ samples since none of the samples in this dissertation have $d_{U-U} < 3.5\,Å$. This is consistent with the conclusions drawn by Chakravarthy *et al.* that said hybridization was responsible for the suppression of the long range magnetic order in $UCu_{5-x}Ni_x$ [22].

4.2 DC Electrical Resistivity Results for $UCu_{5-x}Ni_x$

The low temperature resistivity results for the select $UCu_{5-x}Ni_x$ samples that were measured are shown in Tables 4–2 and 4–3. All but two samples were measured down to ~ 0.3 K (using helium 3 gas as described in the "Experimental Techniques" chapter). The other two samples (UCu_4Ni and $UCu_{3.95}Ni_{1.05}$, both annealed 14 days at 750°C) had their resistivity measured down to 0.060 K using a dilution refrigerator at the NHMFL in Tallahassee, FL. A graph summarizing the resistivity for annealed (14 days 750°C) $UCu_{5-x}Ni_x$ samples in the range $0.9 \leq x \leq 1.2$ along with unannealed $x = 0.75$ is shown in Fig. 4–3.

4.2.1 DC Electrical Resistivity Discussion for $UCu_{5-x}Ni_x$

The $UCu_{5-x}Ni_x$ results in Tables 4–2 and 4–3 show large, varying residual resistivity, ρ_0, values. This was expected since previous literature values for UCu_4Ni were sample dependent with ρ_0 ranging from 400 to 800 $\mu\Omega$ cm [89]. A UCu_4Ni resistivity bar was produced using the "sucker" method discussed in the "Experimental Techniques" chapter to investigate whether or not microcracks in the sample were the cause for the large ρ_0 values. An example of microcracks being the cause of large ρ_0 values is U_2Co_2Sn where an arc-melted U_2Co_2Sn resistivity bar gave $\rho_0 = 800\,\mu\Omega\,cm$ [72] while a "sucker" produced resistivity bar gave $\rho_0 = 60$ $\mu\Omega$ cm [143]. Thus, the sucker method for U_2Co_2Sn avoided microcracks and the ρ_0 values were reduced by a factor of ~ 13. Yet, the quenched UCu_4Ni resistivity bar (i.e., the sucker method) in Table 4–2 (page 127) is only $\sim 30\%$ lower than the arc-melted, unannealed UCu_4Ni resistivity bar. Thus, microcracks

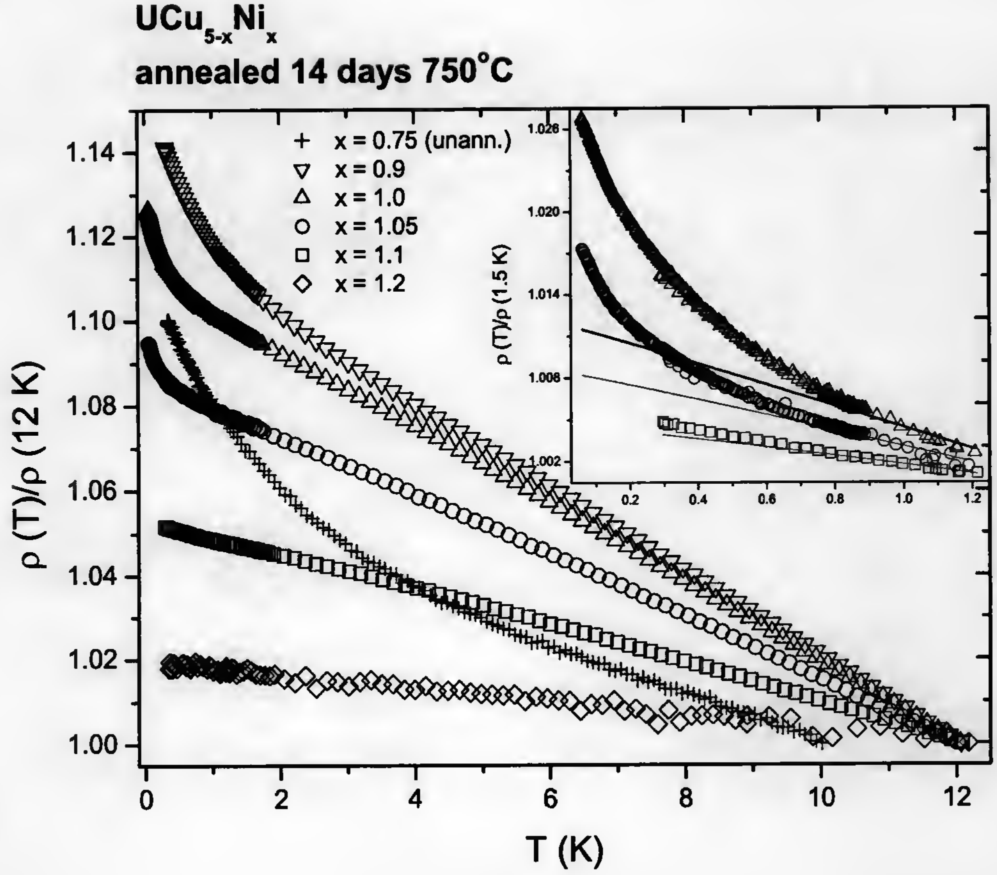

Figure 4–3: Low temperature normalized resistivity for $UCu_{5-x}Ni_x$ samples. The $UCu_{5-x}Ni_x$ samples were annealed 14 days at 750°C and have Ni concentrations between 0.9 and 1.2. Also, the resistivity for unannealed $UCu_{4.25}Ni_{0.75}$ is plotted. The inset shows the extreme low temperature resistivity values for annealed UCu_4Ni, $UCu_{3.95}Ni_{1.05}$, and $UCu_{3.9}Ni_{1.1}$. The graph legend also applies for the inset. The solid lines in the inset are high temperature best fit power law lines (that yield minimum χ^2 values) showing that the UCu_4Ni ρ data begin to deviate from the high temperature fit line around 0.992 K while the $UCu_{3.95}Ni_{1.05}$ and $UCu_{3.9}Ni_{1.1}$ ρ data deviate from the lines beginning at 0.834 K and 0.821 K, respectively. The absolute accuracy of all ρ data is $\sim$ 5%.

do not appear to be the major cause for the large ρ_0 values in the $UCu_{5-x}Ni_x$ samples.

One column in Tables 4–2 and 4–3 that may provide insight into the cause of the behavior of the resistivity for $UCu_{5-x}Ni_x$ samples is the RRR (i.e., the residual resistivity ratio) column. If one compares the RRR values of the $UCu_{5-x}Ni_x$ samples (annealed 14 days 750°C) for $0.9 \leq x \leq 1.2$, one sees a monotonic increase in RRR as the Ni concentration increases. This trend may be irrelevant since the RRR values for all short term annealed (i.e., 14 days at 750°C) $UCu_{5-x}Ni_x$ samples is below 1.0. In Rosch's theoretical work on the interplay of disorder and spin fluctuations near a QCP [126], he defined a parameter x that was a measure of the impurity scattering. 1/x is equivalent to RRR [143] and this means that all $UCu_{5-x}Ni_x$ samples have an x value greater than 1. Rosch stated that $x = 0$ is a perfectly ordered sample while $x \geq 0.1$ is rather disordered [126]. Thus, all $UCu_{5-x}Ni_x$ samples that were annealed for 14 days at 750°C are significantly disordered according to their RRR values.

An investigation of the data in Tables 4–2 and 4–3 (on pages 127 and 128) and the short term annealed data shown graphically in Fig. 4–3 do not indicate any significant changes brought about by annealing as occurred in UCu_4Pd [160]. Annealing UCu_4Pd reduced the residual resistivity by a factor of 2.5 [160] and the A value (with appropriate units) in the power law form ($\rho_0 + AT^{\alpha}$) was reduced by a factor of $\sim$ 10 (-6.3 to -0.6 [143]). Also, a large change in the qualitative behavior of the resistivity curve was brought about by annealing UCu_4Pd. In the temperature region between 2 K and 8 K, the annealed UCu_4Pd resistivity data was fit with a Fermi-liquid expansion $\rho - \rho_r = AT^2 + BT^4$ while the unannealed UCu_4Pd resistivity data showed NFL behavior with $\rho - \rho_r \propto T$ [160]. The $UCu_{5-x}Ni_x$ equivalent to UCu_4Pd, UCu_4Ni, does not show a significant reduction in its ρ_0 value with annealing (only about a 17% decrease). Also, the A values in the temperature regions of 2 K and 10 K, and 2 K and 12 K for unannealed and annealed 14 days 750°C UCu_4Ni do not show a significant difference as occurred in UCu_4Pd (-5.52 for unannealed UCu_4Ni and -5.03 for annealed UCu_4Ni). It is not just the UCu_4Ni sample that shows this lack of significant change. A perusal of all $UCu_{5-x}Ni_x$ samples in Tables 4–2 and 4–3 shows that short term annealing causes no significant changes.

Despite the extreme sample dependence of the $UCu_{5-x}Ni_x$ system which makes any trends in ρ_0 as a function of Ni concentration enigmatic, a few trends in the short term annealed $UCu_{5-x}Ni_x$ samples may be observed in Tables 4–2 and 4–3. First, the absolute values of A for the low temperature fit regions decrease monotonically as the Ni concentration is increased for the short term annealed $UCu_{5-x}Ni_x$ samples with $A = -93.0\ \mu\Omega\,\mathrm{cm}\,\mathrm{K}^{-0.224}$ for x = 0.9 and $A = -3.85\ \mu\Omega\,\mathrm{cm}\,\mathrm{K}^{-0.743}$ for x = 1.1. The “high” temperature fit forms show that the resistivity values for $0.9 \leq x \leq 1.2$ decrease just above a linear rate with $UCu_{3.8}Ni_{1.2}$ decreasing at a rate almost equal to 1 (0.996). Interestingly, Fig. 4–3 on page 80 shows that unannealed $UCu_{4.25}Ni_{0.75}$ (unannealed x = 0.75 and x = 0.80 have very similar low temperature curvatures) has upward curvature over its entire measured temperature range. Yet, this upward curvature present in unannealed x = 0.75 is not apparent until below 2 K for short term annealed x = 0.9. This upward curvature is quite apparent for short term annealed x = 1.0 and x = 1.05 at the lowest measurable temperatures. However, the upward curvature gets less steep with increasing Ni concentration and this is seen in the inset in Fig. 4–3. The “high” temperature fit lines in the inset do not deviate as quickly for x = 1.1 and x = 1.05 as occurred for x = 1.0. In fact, this upward curvature disappears for x = 1.2. The cause of this upward curvature is unknown and remains an open ended question. This upward curvature in the resistivity has also been seen in annealed (14 days at 750°C) UCu_4Pd below 1 K [160] and annealed (7 days at 900°C) UCu_4Ni [88].

Figure 4–3, along with Tables 4–2 and 4–3 raise some interesting points concerning the $UCu_{5-x}Ni_x$ resistivity. First, the resistivity of $UCu_{4.25}Ni_{0.75}$ does not show an antiferromagnetic phase transition at around 1.9 K as was seen in the specific heat (and will be discussed in the specific heat section below). The most interesting point concerns a comparison of the resistivity results of two 8 week 850°C annealed UCu_4Ni samples. The first sample is a UCu_4Ni (production date of 2-27-03 in Table 4–2) resistivity bar that was annealed for 8 weeks at 850°C after the resistivity was measured for the bar when it was unannealed. The ρ_0 value decreases by a factor of ~ 20 and the RRR value is ~ 3.18 (very close to the RRR value of 2.5 for annealed UCu_4Pd [160]). Also, a similar result was obtained for a $UCu_{3.95}Ni_{1.05}$ (7-14-03) resistivity bar that had its resistivity measured when it was an unannealed bar and then was annealed at 850°C for 8 weeks. The only preparation difference between the UCu_4Ni entries (in Tables 4–2 and 4–3) that were annealed for 8 weeks at 850°C was that the (2-27-03) entry (RRR ~ 3.18) had its dimensions sanded really well before annealing so that the spot welded Pt wires were not incorporated into the sample during annealing. The second sample in Table 4–3 is a (10-13-03) entry (RRR ~ 0.313) for UCu_4Ni that had its bar cut from the arc-melted bead after the bead had been annealed for 8 weeks at 850°C with no sanding of the resistivity bar dimensions. These minor differences led to significant changes in the resistivity behavior.

The sanding of the resistivity bar was not the cause of the significant change in the resistivity behavior because the long term annealed UCu_4Ni sample (prod. date: 4-13-04 in Table 4–3) was sanded and cleaned right before the Pt wires were attached while the long term annealed $UCu_{3.95}Ni_{1.05}$ sample (prod. date: 4-14-04) was not sanded before attaching Pt leads. Both samples show similar resistivity behavior and have almost identical RRR values that are below 1. A couple of possible explanations for the strange resistivity behavior have been formulated. One explanation concerns the possibility of a copper oxide layer forming during the 8 week annealing process and that the resistivity of a copper oxide layer was measured for the resistivity bars that were not sanded. A second possible explanation comes from Dr. Bohdan Andraka pertaining to small Cu "islands" possibly existing in the $UCu_{5-x}Ni_x$ samples and that just pure Cu is present in the grain boundaries. Thus, the Pt wires were possibly attached to pure Cu with some impurities mixed in and the resistivity of a sample similar to the classical examples of a Kondo system (i.e., diluted alloys of Fe and Cr in Cu [162]) were measured. Magnetoresistance measurements need to be performed on the same eight week annealed bars (that showed such odd resistivity behavior) in order to test the validity of this theory.

Magnetoresistance measurements were taken on the short term (14 days at 750°C) annealed UCu_4Ni (2-27-03) and $UCu_{3.95}Ni_{1.05}$ (7-14-03) samples. The results are shown in Fig.s B–1 and B–2 of Appendix B. The results in both graphs were taken by Dr. Jungsoo Kim at the NHMFL. The magnetoresistance low temperature results show that for $UCu_{3.95}Ni_{1.05}$, the approximate ρ_0 values in zero field and in a 13 T field only have about a 2.6% difference between them ($\sim$ 929 $\mu\Omega$ cm in 0 T and $\sim$ 905 $\mu\Omega$ cm in 13 T). Similarly, the results for UCu_4Ni show that when a 13 T field is applied, the ρ_0 value is only reduced by about 2.8% ($\sim$ 797 $\mu\Omega$ cm in 0 T and $\sim$ 775 $\mu\Omega$ cm in 13 T). These magnetoresistance measurements suggest that the origin of the large ρ_0 values in the $UCu_{5-x}Ni_x$ samples is not of an electronic nature. One last interesting point that is fairly well seen in both figures of Appendix B is that the upward curvature in the temperature dependence of the graphs in zero field flattens out with the application of magnetic field and the temperature dependence remains fairly constant for fields higher than

4 T. Quantitatively, best fit lines (of the power law form $\rho_0 + AT^{\alpha}$) were fit to each magnetic field data set in Fig.s B–1 and B–2. The α values obtained for UCu_4Ni in 0 T, 4 T, and 13 T fields were 0.432, 0.794, and 0.762 respectively. The α values for $UCu_{3.95}Ni_{1.05}$ in 0 T, 4 T, and 13 T fields were 0.269, 0.722, and 0.711 respectively. The physical reason for these magnetoresistance results is at present unexplained.

A final question that needs to be answered concerning these $UCu_{5-x}Ni_x$ resistivity results is whether or not the short term annealed resistivity provides insight into the inherent properties of $UCu_{5-x}Ni_x$, i.e., does quantum criticality or disorder dominate the behavior in the critical concentration of x = 1.0 (as will also be discussed in the specific heat section)? The answer is no since the short term annealing results for UCu_4Ni do not vary significantly from the unannealed results for UCu_4Ni as seen in Table 4–2. The resistivity results for UCu_4Ni are similar to the resistivity results for unannealed UCu_4Pd [160]. There was a drastic change in the transport properties, e.g., resistivity, of UCu_4Pd after annealing as has been documented earlier. Thus, the unannealed UCu_4Pd gave no insight into the intrinsic disordered NFL behavior. Likewise, the resistivity for short term annealed UCu_4Ni (or any short term annealed $UCu_{5-x}Ni_x$ sample) may not be connected to its intrinsic NFL behavior. The resistivity results for the short term annealed $UCu_{5-x}Ni_x$ samples are most likely stemming from an extrinsic effect that arises from the disorder present in these samples.

4.3 Magnetization Results for $UCu_{5-x}Ni_x$

The magnetization results for the short term annealed $UCu_{5-x}Ni_x$ samples around the critical concentration, x = 1.0, are shown in Table 4–4 on page 129 and Fig. 4–4 on page 87. The numerical information in Table 4–4 is shown graphically in Fig. 4–4. Figure 4–4 shows the excellent agreement between the fit lines and the data while the goodness of fits (the standard deviation and the χ^2 values) in Table 4–4 confirm the excellent agreement. The reason for the low field magnetization being fit to a linear form, M $\sim$ H, and the high field magnetization being fit to a power law form, M $\sim$ H^{λ}, is to investigate whether or not the NFL behavior in the $UCu_{5-x}Ni_x$ system may be fit to the Griffiths phase disorder model [21].

4.3.1 Magnetization Discussion for $UCu_{5-x}Ni_x$

A couple of trends are readily seen in Fig. 4–4 and Table 4–4. First, the field range over which the linear magnetization form fits is widened as the Ni concentration goes from 0.8 to 1.2. The slope of the linear form fit decreases monotonically with increasing Ni concentration. Likewise, the constant in the front of the field term for the power law fit decreases monotonically with increasing Ni concentration. Also, the exponent value, λ, in the power law form increases monotonically for $0.9 \leq x \leq 1.2$. In fact, the high field magnetization power law form (for $UCu_{3.8}Ni_{1.2}$) is very close to a linear form with $\lambda = 0.953$ (for 0.9 T $\leq$ H $\leq$ 7 T). Also, the unphysical constant offsets in the power law form (M = A' + B' H^{λ}) and linear fit form (M = A + B H) for all Ni concentrations listed in Table 4–4 are recognized. These offsets also show a trend as they get less negative with increasing Ni concentration.

The Griffiths phase disorder model of Castro Neto and Jones [21] makes clear predictions concerning such magnetization data shown here. As mentioned earlier, the Griffiths phase disorder model predicts that the magnetization should exhibit low field behavior (M $\sim$ H) that crosses over to high field behavior (M $\sim$ H^{λ}) at some crossover magnetic field, $H_{crossover}$. In other words, the magnetic spin clusters should show some saturation behavior at higher magnetic fields when the Griffiths phase disappears. This is evident in Table 4–4, especially around the critical concentration of 1.0. The short term annealed $UCu_{3.95}Ni_{1.05}$ sample has a little higher λ value (0.860) than the λ values of $Ce_{0.8}Th_{0.2}RhSb$ (0.686 [74]) and $Ce_{0.05}La_{0.95}RhIn_5$ (0.41 [73]), two known samples that fit predictions made by the Griffiths phase disorder model. Also, the magnetization results for samples

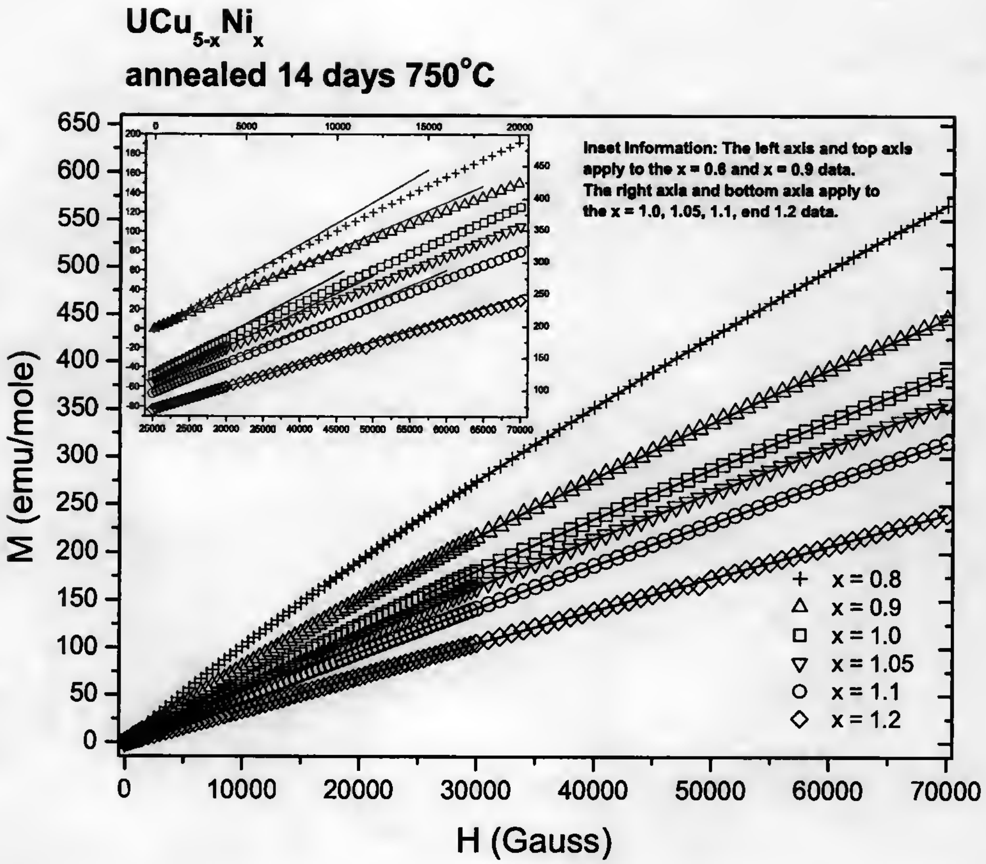

Figure 4–4: Magnetization for $UCu_{5-x}Ni_x$ samples annealed 14 days at 750°C. The magnetization versus field measurements were taken at a constant temperature (2 K). The inset shows where the low field linear form ($M \sim H$) deviates from the data for each sample while the primary graph shows the excellent fit of the high field power law form ($M \sim H^{\lambda}$) to the data.

above the critical concentration (e.g., x = 1.2) do not saturate as quickly as those samples adjacent to x = 1.0 in the phase diagram. This may suggest that the Ni concentration range is limited for which the Griffiths phase model applies. The dc magnetic susceptibility results and the specific heat results are intertwined to the magnetization results in the Griffiths phase model since the λ value from the magnetization power law form should match the low temperature magnetic susceptibility exponent, $\chi \propto T^{-1+\lambda}$, and the exponent in the magnetic field induced peak form in the specific heat, $C/T \sim (H^{2+\lambda/2}/T^{3-\lambda/2})e^{-\mu_{eff}H/k_BT}$, for $H > H_{crossover}$, where $H_{crossover}$ is determined from the magnetization data.

Since saturation is present in the magnetization data, it is recognized that the magnetization and susceptibility of the $UCu_{5-x}Ni_x$ samples may be fit with the Kondo disorder model [143]. However, as will be discussed below in the specific heat section, it is believed that the Kondo disorder model does not apply to $UCu_{5-x}Ni_x$ in light of the fact that the Kondo impurity model, with its four fit parameters, was unable to fit the specific heat data in a magnetic field of isostructural $UCu_{5-x}Pd_x$ [11] and in fact does not reproduce the peak in C(H) observed for $UCu_{5-x}Ni_x$.

Finally, the method (as described in the inset of Fig. 4–4) of determining $H_{crossover}$ from the magnetization data seems rather arbitrary. There was no clear procedure in the literature for describing how $H_{crossover}$ was determined for $Ce_{0.05}La_{0.95}RhIn_5$ ($\approx 0.8\,T$ [73]) and $Ce_{0.8}Th_{0.2}RhSb$ ($\approx 1\,T$ [74]). It was attempted in this $UCu_{5-x}Ni_x$ study that if the Griffiths phase disorder model applied to $UCu_{5-x}Ni_x$, then the rare strongly coupled magnetic clusters (responsible for the NFL behavior) might possibly show hysteresis at each sample's respective $H_{crossover}$. Thus, the zero field cooled (ZFC) magnetization at T = 2 K was measured from 0 to 7 T and immediately afterwards, the field cooled (FC) magnetization was measured from 7 to 0 T. This procedure was performed on three of the short term annealed samples: x = 0.9, 1.05, and 1.2. The results (not shown graphically here) were that the difference in magnetization values between FC and ZFC for all three samples was almost identical at every magnetic field point. In fact, the magnetization difference, $M_{FC} - M_{ZFC}$, for x = 0.9 [with its low $H_{crossover}$ (0.3 T)] began to increase at a slightly higher magnetic field than for x = 1.05 and 1.2. Thus, hysteresis measurements provided no additional insight into $H_{crossover}$. This topic of $H_{crossover}$ will be broached again when dc magnetic susceptibility results at high magnetic fields are presented below.

4.4 AC Magnetic Susceptibility Results for $UCu_{5-x}Ni_x$

The ac magnetic susceptibility for certain $UCu_{5-x}Ni_x$ samples was measured in a SQUID by Quantum Design using the ac susceptibility option. The temperature range of the results was limited by the temperature range of the machine: 2 K - 300 K. Since $UCu_{5-x}Ni_x$ suppresses T_N to zero, only UCu_5, $UCu_{4.4}Ni_{0.6}$, and $UCu_{4.5}Ni_{0.5}$ gave T_N values in the limited temperature range of the ac susceptibility measurements. The results for the unannealed and annealed samples are given in Table 4–5. The T_N values, listed for the three different frequencies (9.5 Hz, 95 Hz, and 950 Hz) at which ac susceptibility measurements were performed, were determined by the location of a peak in the real component, χ'_{AC}, of the ac susceptibility data. Such peaks are shown in Fig. 4–5 for $UCu_{4.5}Ni_{0.5}$ (annealed 14 days at 750°C).

4.4.1 AC Magnetic Susceptibility Discussion for $UCu_{5-x}Ni_x$

The ac susceptibility results in Fig. 4–5 confirm that the transition below 10 K for annealed $UCu_{4.5}Ni_{0.5}$ is antiferromagnetic and not spin glass in nature. If spin glass behavior was apparent, then a temperature shift of the maximum in the ac susceptibility as a function of frequency would occur [77]. A slight temperature shift does occur in Fig. 4–5; however, the results in Table 4–5 show that the temperature shift is practically within the stated error bars. Another indication

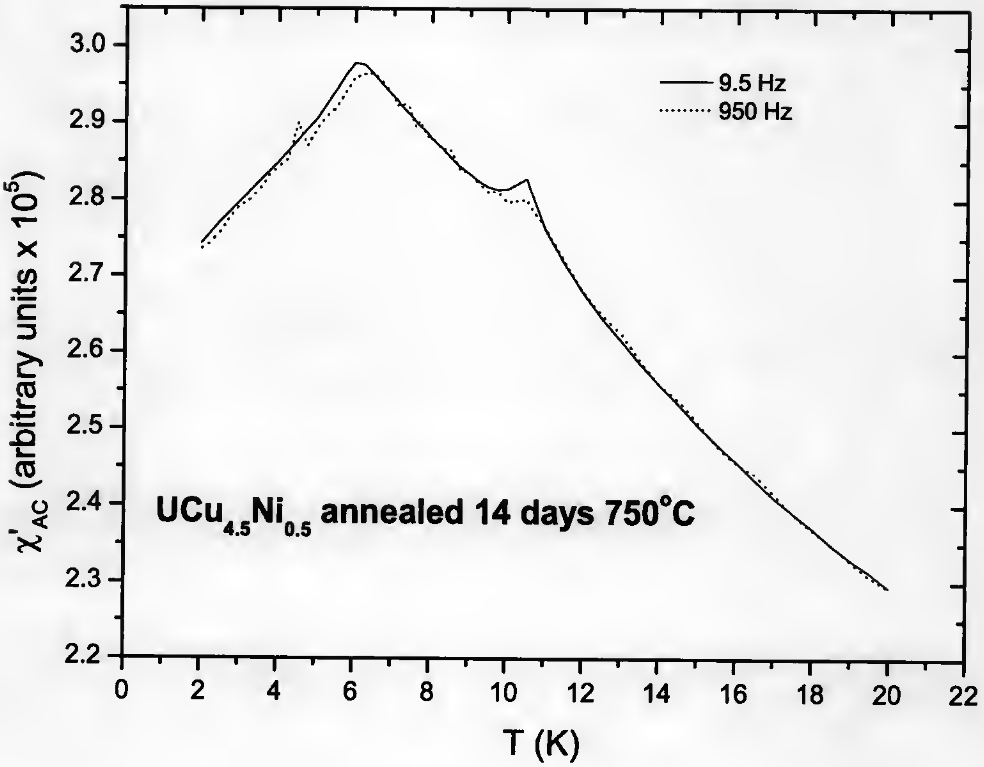

Figure 4–5: AC susceptibility data for annealed $UCu_{4.5}Ni_{0.5}$ samples. The real component of the ac susceptibility data is plotted versus temperature. The ac measurements were performed at two different frequencies (9.5 Hz and 950 Hz) as shown. The peak for the 9.5 Hz data is 6.10 K and the peak for the 950 Hz data is 6.50 K. The shift in the peak between the two different frequencies of measurement is within the error bars in Table 4–5.

that is characteristic of spin glasses is a step in the imaginary component of the ac susceptibility data as was seen in $UCu_{2.7}Pd_{2.3}$ (the data dropped by a factor of ~ 4 at the spin glass temperature [77]). The imaginary component of the ac susceptibility data for annealed $UCu_{4.5}Ni_{0.5}$ (not shown here) does not show such a step, remaining fairly constant. The data in Table 4–5 also indicate that the transition below 10 K for $UCu_{4.4}Ni_{0.6}$ is antiferromagnetic.

The ac susceptibility results disagree with the claims made by López de la Torre *et al.* who claim that the magnetic phase transition for annealed $UCu_{4.5}Ni_{0.5}$ around 6 K is indicative of spin glass or cluster glass behavior [89]. Their claim of this spin glass behavior is based upon the splitting between zero-field cooled (ZFC) and field-cooled (FC) dc magnetic susceptibility results below 6 K. However, Körner *et al.* state that the appropriate method for arguing spin glass behavior is to monitor the temperature shift of the maximum in the ac susceptibility as one varies the frequency [77]. The ac susceptibility results in this dissertation argue against spin glass behavior for $UCu_{4.5}Ni_{0.5}$ and $UCu_{4.4}Ni_{0.6}$, similar to $UCu_{4.4}Pd_{0.6}$ [77].

A phase diagram comparing the $UCu_{5-x}Ni_x$ system to the isoelectronic $UCu_{5-x}Pd_x$ system will be shown later in the chapter; however, it is interesting to compare the T_N values of $UCu_{4.5}Ni_{0.5}$ and $UCu_{4.4}Ni_{0.6}$ to $UCu_{4.5}Pd_{0.5}$ and $UCu_{4.4}Pd_{0.6}$. Chau and Maple report that unannealed $UCu_{4.5}Pd_{0.5}$ has a $T_N \approx 9.9$ K [26] while unannealed $UCu_{4.5}Ni_{0.5}$ has a $T_N \approx 7.5$ K (from 9.5 Hz ac susceptibility measurements). Körner *et al.* state that unannealed $UCu_{4.4}Pd_{0.6}$ has a $T_N \approx 6.3$ K (from 95 Hz ac susceptibility measurements) while unannealed $UCu_{4.4}Ni_{0.6}$ has a $T_N \approx 4.01$ K (from 95 Hz ac susceptibility measurements). This comparison seems to suggest that the dopant Ni atom suppresses the T_N value faster than the dopant Pd atom. One supposition for this faster decrease concerns the possible sublattice ordering with the Pd atoms while such sublattice ordering is not seen with the Ni atoms (from the lattice parameter results); thus, greater hybridization is occurring with the magnetic U atoms for the $UCu_{5-x}Ni_x$ case and is causing the faster suppression rate.

4.5 DC Magnetic Susceptibility Results for $UCu_{5-x}Ni_x$

Figure 4–6 on page 93 shows dc magnetic susceptibility data for annealed (14 days at 750°C) UCu_4Ni in different magnetic fields: 1 kiloGauss (kG), 1 Tesla (T), 2 T, 3 T, and 4 T. The 1 kG data show a high temperature peak around 130 K and that peak is suppressed by the application of a larger magnetic field. At 1 T, a slight amount of curvature remains over the temperature range where the peak occurred in 1 kG. At 2 T, the peak appears completely suppressed. Figure 4–6 is representative of all Ni concentrations around the critical concentration of x = 1.0 (i.e., x = 0.9, 1.05, 1.1, and 1.2). A better perspective of the low temperature susceptibility data for the critical Ni concentration and its adjacent concentrations is shown in Fig. 4–7 on page 94. The reason for the log-log scale and the straight lines will be explained in the discussion section below.

Table 4–6 on page 131 follows the progression of the magnetic susceptibility values at T = 2 K and contains other important values that will be used later in the calculation of the Wilson ratio [142]. Except for a couple of concentrations (x = 0.75 and x = 1.1), Table 4–6 shows that the magnetic susceptibility monotonically decreases with increasing Ni concentration for $0.75 \leq x \leq 1.2$. Also, Table 4–6 provides $\mu_{eff.}$ values [in Bohr magnetons (μ_B)] for each Ni concentration. The $\mu_{eff.}$ values are determined from the inverse magnetic susceptibility values that are in a high temperature range (up to 300 K) above the high temperature peak for each respective $UCu_{5-x}Ni_x$ compound listed in Table 4–6. The inverse susceptibility may be related to the $\mu_{eff.}$ values by rewriting the Curie-Weiss Law [$\chi = N\mu_{eff.}^2\mu_B^2/(3k_B(T - \Theta))$ where $N = 6.022 \times 10^{23}$ atoms/mole, $\mu_B = 9.2741 \times 10^{-21}$ emu G, and $k_B = 1.3807 \times 10^{-16}$ emu G^2 K^{-1}] into the

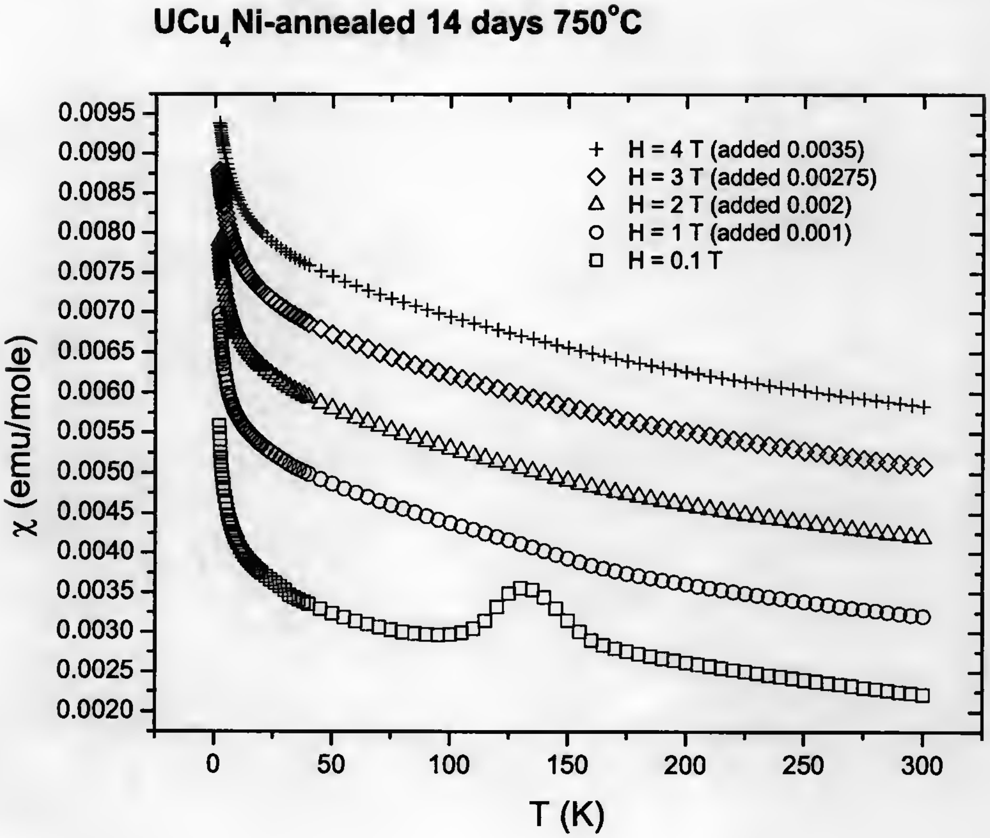

Figure 4–6: DC susceptibility for annealed UCu_4Ni in different magnetic fields. The various magnetic fields were 1 kG, 1 T, 2 T, 3 T, and 4 T. The same piece of sample was used for all 5 magnetic fields. The shifts in the data sets as indicated allow the distinguishing characteristics of each data set to be seen clearly.

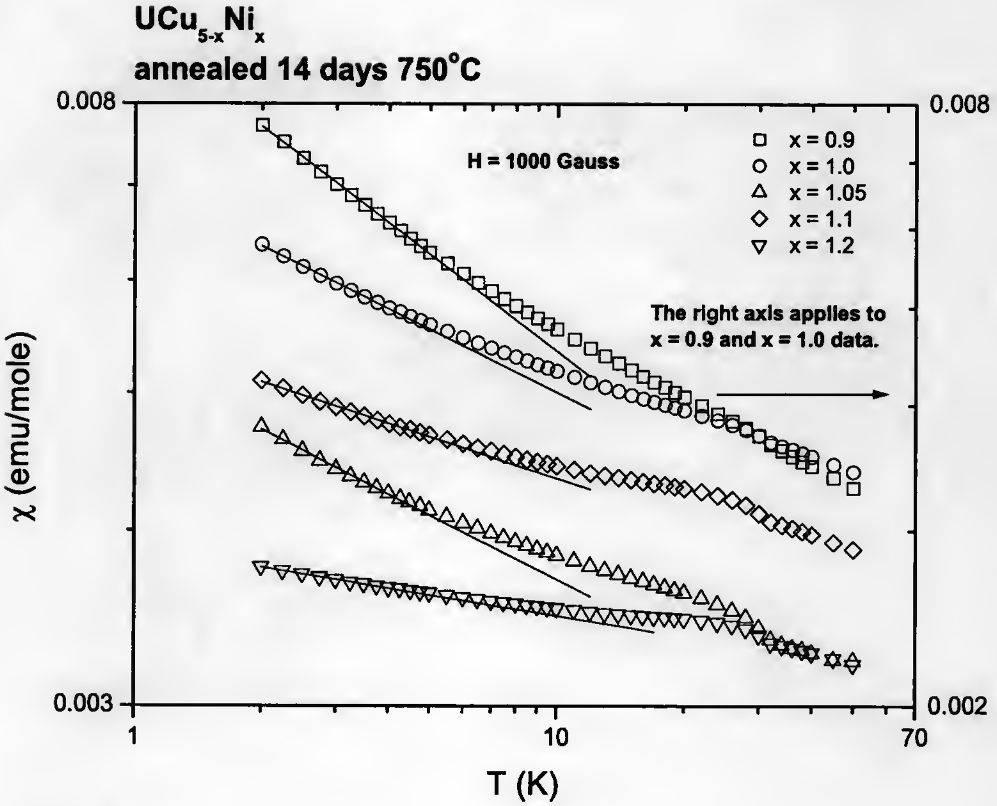

Figure 4–7: Low temperature dc susceptibility for annealed $UCu_{5-x}Ni_x$ samples. All $UCu_{5-x}Ni_x$ samples were annealed 14 days at 750°C. The abscissa and ordinate are on $\log_{10}$ scales. The right ordinate scale applies just to the x = 0.9 and x = 1.0 data. The low temperature fit lines shown are used to determine the λ values for the Griffiths phase disorder model which predicts that magnetic susceptibility has a power law form $\chi(T) \propto T^{-1+\lambda}$. The λ values for the lines shown are listed in Table 4–7.

following form [79]:

$$1/\chi = (7.9972/\mu_{eff.}^2)(\mathrm{T} - \Theta) \tag{4.1}$$

where χ has the units emu/mole, and T and Θ, the paramagnetic Curie temperature, have the units Kelvin (K). There does not appear to be any trend in $\mu_{eff.}$ or the high temperature peak as a function of x. Finally, the $\chi(\mathrm{T} = 0\ \mathrm{K})$ values were extrapolated values by fitting the low temperature magnetic susceptibility data ($2\ \mathrm{K} \leq \mathrm{T} \leq 10\ \mathrm{K}$) to a fifth order polynomial.

4.5.1 DC Magnetic Susceptibility Discussion for $\mathrm{UCu}_{5-x}\mathrm{Ni}_x$

The first part of this discussion will pertain to the high temperature peaks observed in the dc magnetic susceptibility results of the $\mathrm{UCu}_{5-x}\mathrm{Ni}_x$ samples. Interestingly, no previous literature has mentioned the observance of a high temperature peak in the dc magnetic susceptibility for any $\mathrm{UCu}_{5-x}\mathrm{Ni}_x$ sample [89, 90, 153]. The reason why no high temperature peak was observed in two of the articles [89, 90] concerns the field at which the dc magnetization was measured, H = 1 T, while the third article did not show any indications of a high temperature peak in the inverse susceptibility (field unknown) [153]. As has been pointed out previously in Fig. 4-6, 1 T almost suppresses the high temperature peak and the slight curvature that remains at 1 T may have been attributed to experimental uncertainty. A possible interpretation for the high temperature peak may concern spin glass behavior since irreversibility (not shown here) between zero field cooled and field cooled runs at 1 kG begins at the location of the high temperature peak. This possible spin glass behavior will need to be confirmed by ac susceptibility measurements [77] (technical difficulties have not allowed the ac susceptibility measurements to be performed). Another possibility is that the high temperature peak could be antiferromagnetic, stemming from magnetic susceptibility measurements of CuO [166]. This is highly unlikely since the majority of the bulk sample would have to have oxidized. Also, the high temperature peaks in Table 4–6 are not occurring at the T_N value of 230 K for CuO [166].

A comparison of other isostructural compounds may shed light on the high temperature susceptibility peak for $UCu_{5-x}Ni_x$ samples. High temperature susceptibility measurements for $UCu_{5-x}Pd_x$ reveal no high temperature peaks [26]. The isostructural $UCu_{5-x}Pt_x$ compounds do show very broad high temperature peaks for $UCu_{3.25}Pt_{1.75}$, UCu_3Pt_2, and $UCu_{2.75}Pt_{2.25}$ [26]. The high temperature peaks for the $UCu_{5-x}Pt_x$ samples are broader (the peak for $UCu_{3.25}Pt_{1.75}$ covers approximately a 100 K range) and flatter as compared to the sharp, narrow peaks for $UCu_{5-x}Ni_x$ (the peak for UCu_4Ni covers approximately a 75 K range). Unfortunately, the authors for the $UCu_{5-x}Pt_x$ system do not mention the high temperature peaks in their work [26]. The high temperature peaks for the $UCu_{5-x}Ni_x$ samples remain an unexplained subject that will have to be answered by future works.

The next topic concerning the $UCu_{5-x}Ni_x$ dc magnetic susceptibility results is the $\mu_{eff.}$ values listed in Table 4–6. As one can see, the effective moment values lie between $2.79\mu_B$ and $3.59\mu_B$. The interpretation of the effective moment values is that the uranium ions are in a mixed valent state. All the experimentally determined $\mu_{eff.}$ values in Table 4–6 are above the $5f^1$ and $5f^4$ calculated effective moment values ($2.54\mu_B$ and $2.68\mu_B$ respectively [7]). Thus, the determined effective moment values are closer to the calculated effective moment values for the $5f^2$ and $5f^3$ valence states ($3.58\mu_B$ and $3.62\mu_B$ respectively [7]). Since a U atom has a valence shell of $5f^3 6d^1 7s^2$, then $5f^2$ indicates that U^{4+} has four missing valence electrons and is tetravalent while $5f^3$ means that U^{3+} has three missing valence electrons and is trivalent. The determined $\mu_{eff.}$ values are closer to a mixed trivalent and tetravalent state. This is in agreement with the results of van Daal *et al.* [153].

The final part of the discussion focuses on the dc magnetic susceptibility for the critical Ni concentration x = 1.0 and its adjacent concentrations (x = 0.9, 1.05, 1.1, and 1.2). The low temperature dc susceptibility in a 1 kG field is shown in Fig. 4–7. The equations for the low temperature fit lines in Fig. 4–7 are explicitly stated in Table 4–7. Both the figure and table show that the low temperature fit lines do not fit the low temperature magnetic susceptibility data very well. The temperature range for the fit lines does not cover a decade of temperature. Also, Fig. 4–7 shows that the five Ni concentrations have an inflection point occurring around 30 K in their magnetic susceptibility data. The exact source of the inflection point is unknown, but a couple of possible explanations exist. First, the inflection point in the dc susceptibility could be due to an extrinsic effect on the $UCu_{5-x}Ni_x$ samples similar to the supposition made for the resistivity of the short term annealed $UCu_{5-x}Ni_x$ samples. Since the Griffiths phase disorder model is being applied to the $UCu_{5-x}Ni_x$ system, the behavior of strong magnetic clusters (i.e., the Griffiths phase) is what leads to the power law behavior in the magnetic susceptibility: $\chi(T) \propto T^{-1+\lambda}$ [21]. However, the Griffiths phase model predicts that there is a temperature on the order of the average RKKY interaction for a particular system and that above this temperature, the magnetic clusters do not exist as well defined objects since temperature fluctuations can excite isolated spins within the cluster [21]. Thus, the inflection points in Fig. 4–7 could be related to the temperature where the magnetic clusters decompose [20]. Another possible explanation concerning the inflection point is a magnetic origin. If one looks ahead to Fig.s 4–8 and 4–9, one sees that the inflection point disappears at higher magnetic fields. This inflection point will be left for further studies.

The Griffiths phase disorder model also states that the exponent, λ, in the low field magnetic susceptibility power law behavior ($\chi \sim T^{-1+\lambda}$) is equal to the λ in the high field magnetization behavior ($M \sim H^{\lambda}$). If one compares the λ

values for the 1 kG magnetic susceptibility fits in Table 4–7 to the λ values for the magnetization versus field fits in Table 4–4, then one sees that for x = 1.05, the two values are within 2% of each other (0.848 from susceptibility and 0.860 from magnetization) and that the λ values for x = 1.1 and x = 1.2 are almost equal. The susceptibility at 1 kG and the magnetization seem to imply that the antiferromagnetism (i.e., spin fluctuations) suppressed at the quantum critical point concentration of x = 1.0 does not show Griffiths phase behavior with the exponent from the magnetization data (0.841) deviating by more than 2% from the magnetic susceptibility exponent (0.792). Yet, as the Ni concentration is increased slightly (by 5%), the magnetic clusters (and the associated tunneling between energy levels [21]) associated with the Griffiths phase display their behavior in the magnetic susceptibility. The apparent Griffiths phase behavior in the 1 kG magnetic susceptibility continues for x = 1.1 and 1.2 (the highest Ni concentration synthesized for this dissertation).

Since the dc magnetic susceptibility was run in five different magnetic fields for the five concentrations around x = 1.0 to suppress the high temperature peak, an interesting question concerns to what maximum magnetic field does the Griffiths phase model apply for the dc magnetic susceptibility? A semilogarithmic plot and a log-log plot are shown in Fig. 4–8 and Fig. 4–9 respectively for UCu_4Ni annealed 14 days at 750°C. The fit lines in Fig. 4–8 and Fig. 4–9 along with the other four adjacent Ni concentrations are stated explicitly in Tables 4–7, 4–8, and 4–9. The semilog and log-log plots for the other 4 Ni concentrations are shown in Appendix C. The x = 0.9 magnetic susceptibility data will be ignored since there is still an antiferromagnetic transition occurring at $\sim$ 0.4 K (as will be seen in the specific heat data later) despite power law behavior occurring over a large temperature range at 2 T as seen in Table 4–8. The UCu_4Ni data in Table 4–8 show that power law behavior is present over an extended temperature range

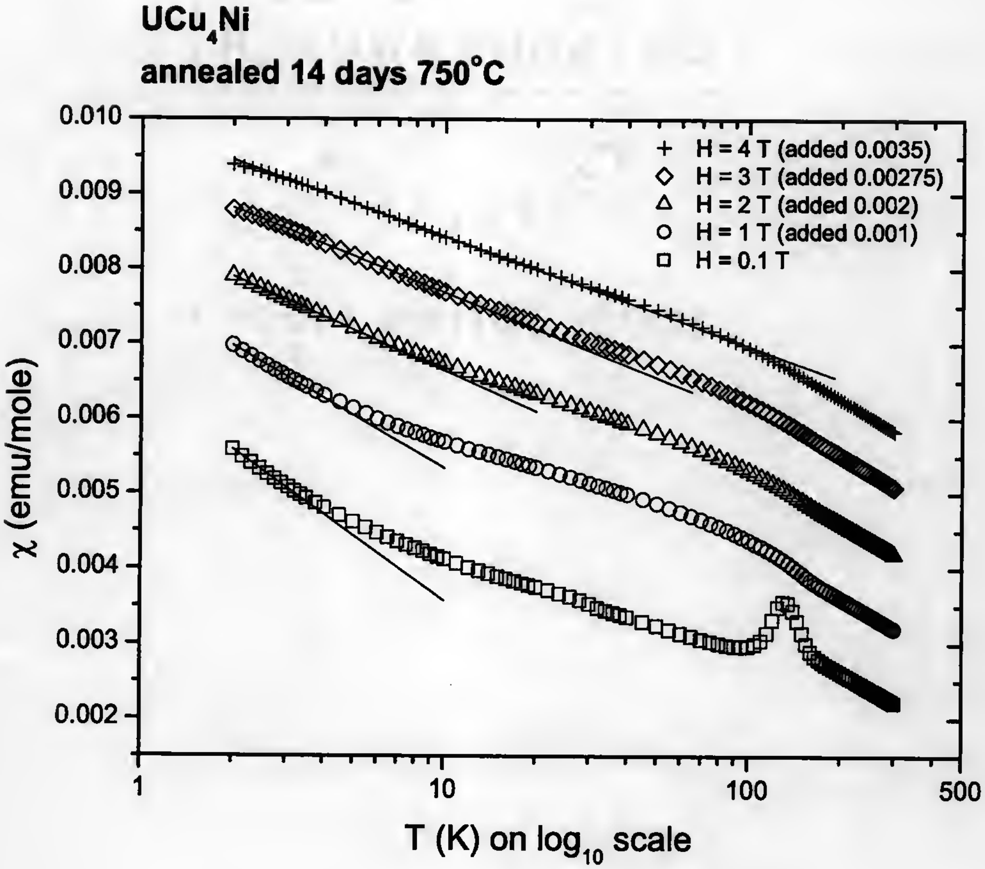

Figure 4–8: Semilog plot of dc magnetic susceptibility for UCu_4Ni. The annealed UCu_4Ni was run at various magnetic fields (1 kG, 1 T, 2 T, 3 T, and 4 T). The temperature axis is on a $\log_{10}$ scale. The equations for the best fit lines are stated in Tables 4–7, 4–8, and 4–9. The shifts in the data and lines are for clarity.

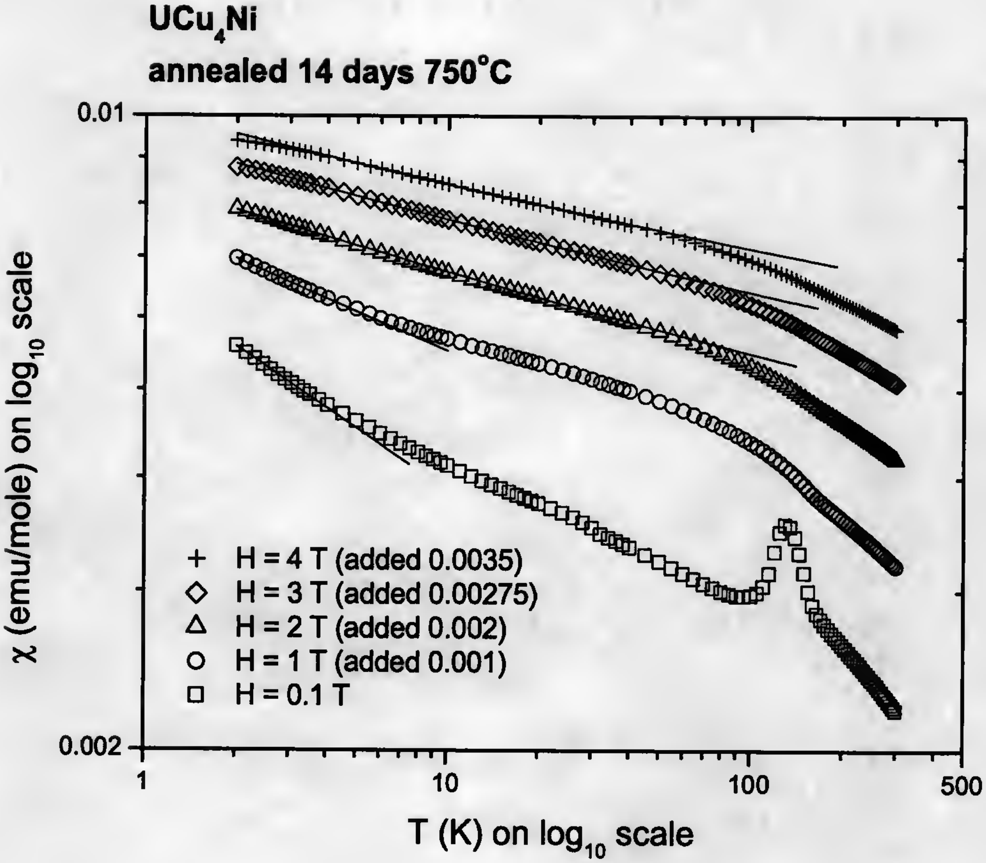

Figure 4–9: Log-log plot of dc magnetic susceptibility for UCu$_4$Ni. The annealed UCu$_4$Ni was run at various magnetic fields (1 kG, 1 T, 2 T, 3 T, and 4 T). The temperature axis and dc susceptibility, χ, axis are on a log$_{10}$ scale. The equations for the best fit lines are stated in Tables 4–7, 4–8, and 4–9. The shifts in the data and lines are for clarity.

(2-40 K) at 2 T. The λ values from the 2 T magnetic susceptibility data and the magnetization data differ by $\sim$ 3%, which is still rather good agreement. However, the magnetization data in Table 4–4 predicts that the Griffiths phase behavior should be suppressed at 2 T with the crossover field being defined as 1.55 T. This crossover field was rather arbitrary in its definition and $Ce_{0.05}La_{0.95}RhIn_5$ had a crossover field of $\sim$ 0.8 T [73] from magnetization data, yet C/T field data did not reveal a peak (predicted to occur when Griffiths phase is suppressed) until 1.5 T. The uncertainty in the crossover field could still allow Griffiths phase behavior to occur at 2 T as is suggested by the magnetic susceptibility of UCu_4Ni. The Griffiths phase behavior for UCu_4Ni starts to disappear as the 3 T magnetic susceptibility starts to fall below the power law fit line at 4 K as shown in Fig. 4–9. The 2 T magnetic susceptibility data for $UCu_{3.95}Ni_{1.05}$ also implies that Griffiths phase behavior (i.e., tunneling between energy levels) is occurring with a power law fit covering over more than a decade of temperature. The λ values from the magnetic susceptibility data and magnetization data are within 5% of each other (0.899 and 0.860 respectively). Interestingly, the 3 T magnetic susceptibility data for $UCu_{3.95}Ni_{1.05}$ shows downward curvature from a power law fit line at lowest measurable temperatures while a semilog line shows excellent behavior (from 2 to 45 K). $UCu_{3.9}Ni_{1.1}$ and $UCu_{3.8}Ni_{1.2}$ at 2 T cease to show power law behavior over a decade of temperature implying that the Griffiths phase is being suppressed with the magnetic field splitting the energy levels far enough apart such that tunneling between the energy levels does not occur. Like the $UCu_{3.95}Ni_{1.05}$ sample, $UCu_{3.9}Ni_{1.1}$ at 3 T shows semilog behavior over a decade of temperature.

The magnetic susceptibility data at various magnetic fields for x = 0.9, 1.0, 1.05, 1.1, and 1.2 seem to suggest that the Griffiths phase disorder model is not sufficient in explaining all the complexities involved in the $UCu_{5-x}Ni_x$ system. For example, as mentioned earlier, the magnetic susceptibility for $UCu_{3.95}Ni_{1.05}$

displays good power law behavior at 2 T despite magnetization versus field data defining $H_{crossover}$ as 1.55 T. An interesting result concerns the semilog behavior at 3 T for the magnetic susceptibility of $UCu_{3.95}Ni_{1.05}$ which suggests that the "two-channel" Kondo model could be a possibility in describing the NFL behavior of $UCu_{3.95}Ni_{1.05}$ [143]. This sort of behavior compares to the comments made by Booth *et al.* [16] who stated that the Kondo disorder model did not match all the experimental data that existed for UCu_4Pd and more complex theories such as the Kondo/quantum spin-glass critical point [56] would need to be involved. In order to form as complete a picture as possible for $UCu_{5-x}Ni_x$, the magnetic susceptibility data will be referred to heavily in the upcoming specific heat sections.

4.6 $UCu_{5-x}Ni_x$ Specific Heat Results

The specific heat was measured for eight of the short term annealed Ni concentrations: x = 0.6, 0.75, 0.8, 0.9, 1.0, 1.05, 1.1, and 1.2. Figure 4–10 on page 103 shows the specific heat for all eight Ni concentrations measured from ~ 0.3 K to the highest measured temperature (~ 8 K). The subtraction made in Fig. 4–10 takes away the lattice contribution. The lattice contribution comes from the specific heat of UNi_5 which was measured by van Daal *et al.* [153]. The data from van Daal *et al.* was replotted by means of a scanner and the low temperature data ($0 < T < 15$ K) fit the specific heat for a normal metal: $C/T = 15.3 + 0.178\ T^2 + 0.00110\ T^4$ (mJ mole^{-1} K^{-2}). Thus, the Debye term (i.e., the T^2 term in the previous equation) and the next higher lattice term may be subtracted from C/T to isolate just the electronic contribution for the $UCu_{5-x}Ni_x$ samples.

Unlike magnetic susceptibility data, the specific heat data in Fig. 4–10 were measured down to ~ 0.3 K. The antiferromagnetic transition in $UCu_{5-x}Ni_x$ is present for x = 0.6, 0.75, and 0.8 as the specific heat has a large upturn with decreasing temperatures and then shows a plateau. The antiferromagnetic transition

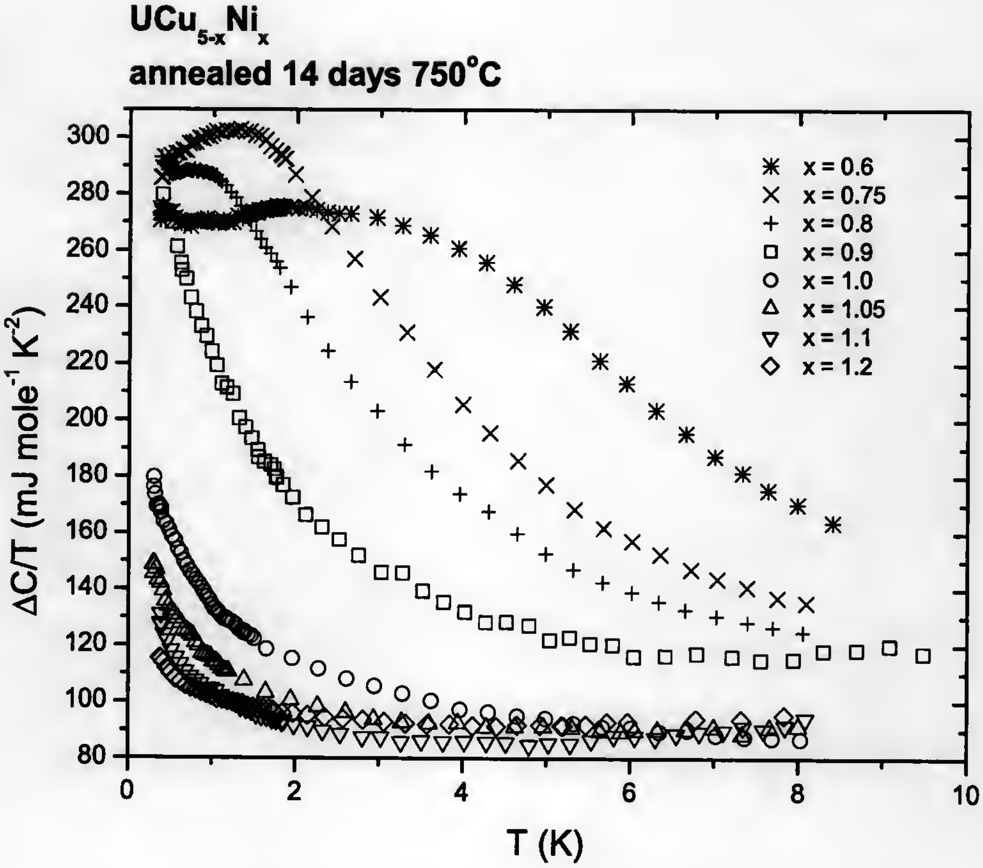

Figure 4–10: Specific heat for eight annealed UCu$_{5-x}$Ni$_x$ samples. The specific heat is plotted from ~ 0.3 K to the highest measured temperature. ΔC/T on the ordinate represents the electronic contribution to the UCu$_{5-x}$Ni$_x$ samples where ΔC/T = C/T - (0.178T^2 + 0.0011T^4) as described in the text.

may be determined from specific heat data. One method of determination is to draw a straight line along the plateau and another straight line along the rapid linear increase of the specific heat data before the data begins to level off to the plateau. The intersection of these two straight lines then gives a $T_{N\acute{e}el}$ value as shown in Fig. D–1 of Appendix D for annealed $UCu_{4.4}Ni_{0.6}$. The semilogarithmic graph in Fig. D–1 was used to better display the plateau below the $T_{N\acute{e}el}$ value. This may be questionable, but the semilog plot was used to consistently determine $T_{N\acute{e}el}$ values (from specific heat data) that are stated in Table 4–10. If one compares the $T_{N\acute{e}el}$ values for annealed $UCu_{4.4}Ni_{0.6}$ in Tables 4–5 and 4–10, then the $T_{N\acute{e}el}$ values are equal to each other within the temperature uncertainty of each measurement.

Figure 4–11 on page 105 shows the specific heat for five $UCu_{5-x}Ni_x$ samples plotted on a semilogarithmic graph: x = 0.8, 0.9, 1.0, 1.05, and 1.1. The fit lines with curvature are Moriya and Takimoto fits that will be explained in the specific heat discussion section. These fit lines along with the y_0 values (listed in Fig. 4–11 and Table 4–10) were determined using a computer program (in Fortran code) developed by Dr.s Tôru Moriya and Tetsuya Takimoto at the Science University of Tokyo [103]. Also, Fig. 4–11 shows that the specific heat measurements for x = 0.9, 1.0, and 1.05 were extended further below 0.3 K. These low temperature measurements were performed by Dr. E.-W. Scheidt at the University of Augsburg using a dilution refrigerator.

The Ni concentrations around the critical concentration of x = 1.0 are also plotted on a log-log plot in Fig. 4–12 on page 106. Figure 4–12 helps in distinguishing whether or not the Griffiths phase ($C/T \sim T^{-1+\lambda}$ [21]) applies to a particular Ni concentration. Many more comments concerning Fig. 4–12 will be made in the specific heat discussion section.

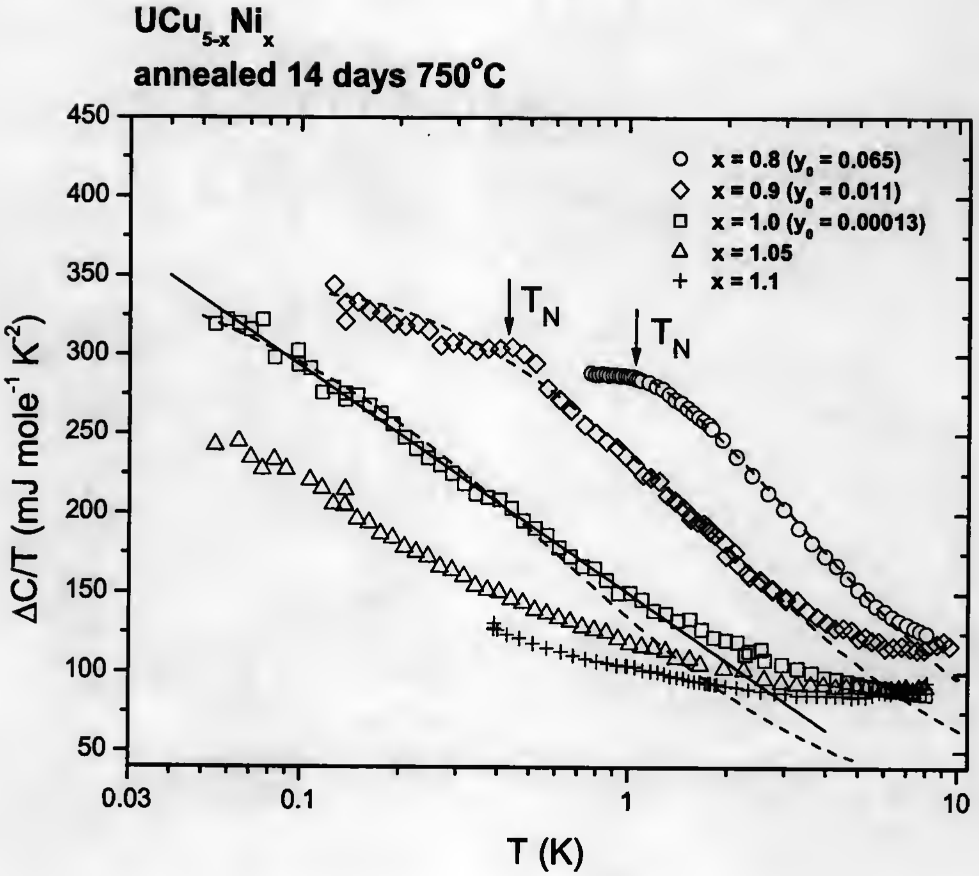

Figure 4–11: $UCu_{5-x}Ni_x$ specific heat results on a semilog plot. ΔC/T on the semilogarithmic graph is defined as follows: $\Delta C/T = C/T - (0.178T^2 + 0.0011T^4)$. The curved lines (dashed for x = 0.8, 0.9, and 1.0) are Moriya and Takimoto fits that predict the specific heat to go like $C/T = \gamma - AT^{1/2}$ at lowest temperatures, followed by $C/T \sim \log T$ at higher temperatures [103]. The y_0 for x = 0.8, 0.9, and 1.0 is the reduced inverse staggered susceptibility that monitors how close a sample is to the quantum critical point. $y_0 = 0$ marks the quantum critical point. The straight line for x = 1.0 is a semilogarithmic fit for $0.0547 \text{ K} < T < 1.30 \text{ K}$: $\Delta C/T = 150 - 143 \log_{10}T$.

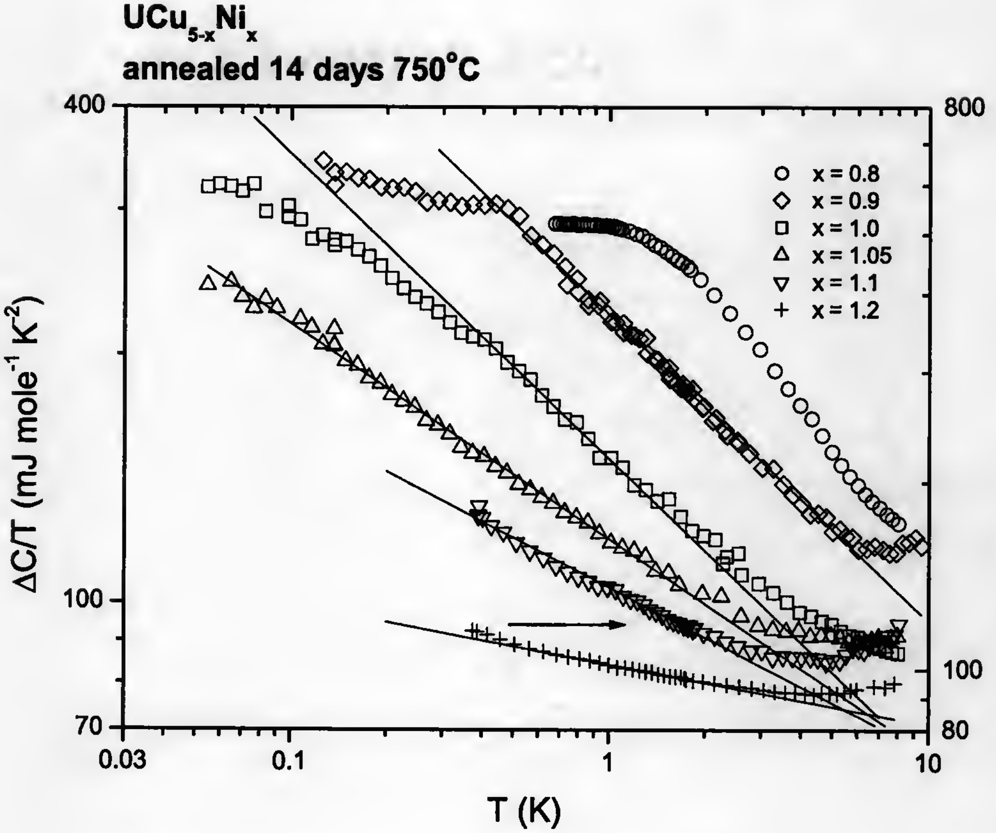

Figure 4–12: $UCu_{5-x}Ni_x$ specific heat results on a log-log plot. The right y-axis applies just to the $UCu_{3.8}Ni_{1.2}$ data. The straight lines are linear fits that cover the widest possible temperature range: x = 0.9 - $\log_{10}(\Delta C/T) = 2.35 - 0.372\log_{10} T$ for $0.440\ K \leq T \leq 6.04\ K$; x = 1.0 - $\log_{10}(\Delta C/T) = 2.17 - 0.370\log_{10} T$ for $0.404 \leq T \leq 2.28$ K; x = 1.05 - $\log_{10}(\Delta C/T) = 2.08 - 0.261\log_{10} T$ for $0.0547 \leq T \leq 1.66$ K; x = 1.1 - $\log_{10}(\Delta C/T) = 2.02 - 0.201\log_{10} T$ for $0.389 \leq T \leq 2.15$ K; and x = 1.2 - $\log_{10}(\Delta C/T) = 2.01 - 0.0970\log_{10} T$ for $0.563 \leq T \leq 1.84$ K.

The specific heat for Ni concentrations including and adjacent to the critical concentration of x = 1.0 was measured in select magnetic fields, typically 3, 6, and 13 T. It was noticed that during the collection of data, a Schottky peak ($C \sim 1/T^2$ [73]) was appearing at the lowest measurable temperatures. The appearance of the Schottky peak is exemplified in Fig. D–2 of Appendix D on page 179. These Schottky peaks were similar to the Schottky-like anomalies observed in $BaCuO_2$ by Fisher *et al.* [46]. Thus, the $UCu_{5-x}Ni_x$ specific heat measured in a magnetic field needed to account for the nuclear hyperfine specific heat coming from the copper nuclei. Fisher *et al.* calculated the nuclear hyperfine specific heat from nuclei $^{63,65}Cu$ and $^{135,137}Ba$ to be $C_{hf}(H) = 0.00329\ (H/T)^2$ mJ mole^{-1} K^{-1} for H in Tesla [46]. It was assumed that the primary contributors to the nuclear hyperfine specific heat were the Cu nuclei. This was confirmed by measuring a pure piece of 99.9999% Cu (etched in nitric acid right before measurement) in Dr. Stewart's laboratory at UF in 6 and 13 T. The coefficient in front of the nuclear splitting term (i.e., the Schottky anomaly term - $C/T \sim 1/T^3$) that was experimentally determined (graph not shown) in the 6 T magnetic field was within 5% of Fisher's value (0.112 versus 0.118 respectively). Similarly, the experimentally determined coefficient in the 13 T magnetic field was within 1% of Fisher's value (0.560 versus 0.556 respectively). Thus, the $\Delta C/T$ values in magnetic fields take into account the nuclear splitting of the Cu: $\Delta C/T = C/T - (5-x)\ 0.00329\ H^2/T^3 - 0.178\ T^2 - 0.0011\ T^4$, where H is in Tesla and x is the Ni concentration. The nuclear splitting term needs to be multiplied by the number of moles of Cu since Fisher's term only accounted for 1 mole of Cu with $BaCuO_2$ [46]. Figures 4–13, 4–14, and 4–15 show the specific heat of $UCu_{4.1}Ni_{0.9}$, $UCu_{3.9}Ni_{1.1}$, and $UCu_{3.8}Ni_{1.2}$ in 0, 3, and 6 T respectively while Fig.s 4–16 and 4–17 show the specific heat of UCu_4Ni and $UCu_{3.95}Ni_{1.05}$ in 0, 2, 3, and 6 T.

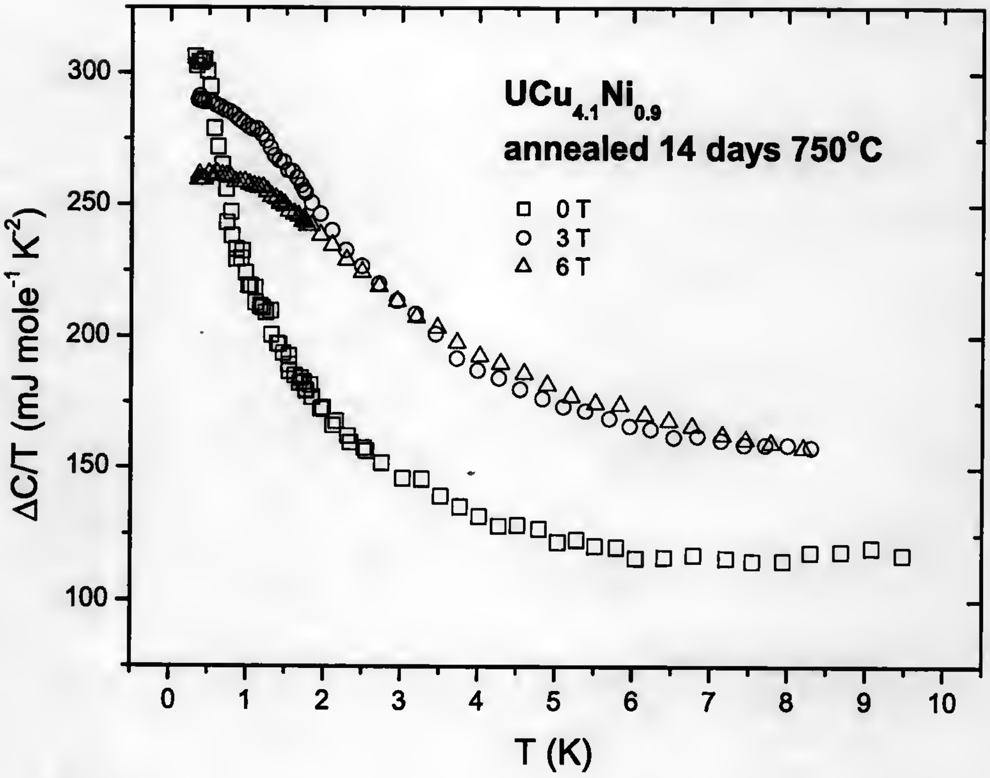

Figure 4–13: Specific heat of $UCu_{4.1}Ni_{0.9}$ in 0, 3, and 6 T. $UCu_{4.1}Ni_{0.9}$ was annealed for 14 days at 750°C. The $\Delta C/T$ values not only have the lattice contribution subtracted off, but also the nuclear hyperfine contribution: $\Delta C/T = C/T - 0.0135H^2/T^3 - 0.178T^2 - 0.0011T^4$ where H is in Tesla. The 0 T data are only shown down to $\sim$ 0.3 K so as not to conceal the 3 T and 6 T data.

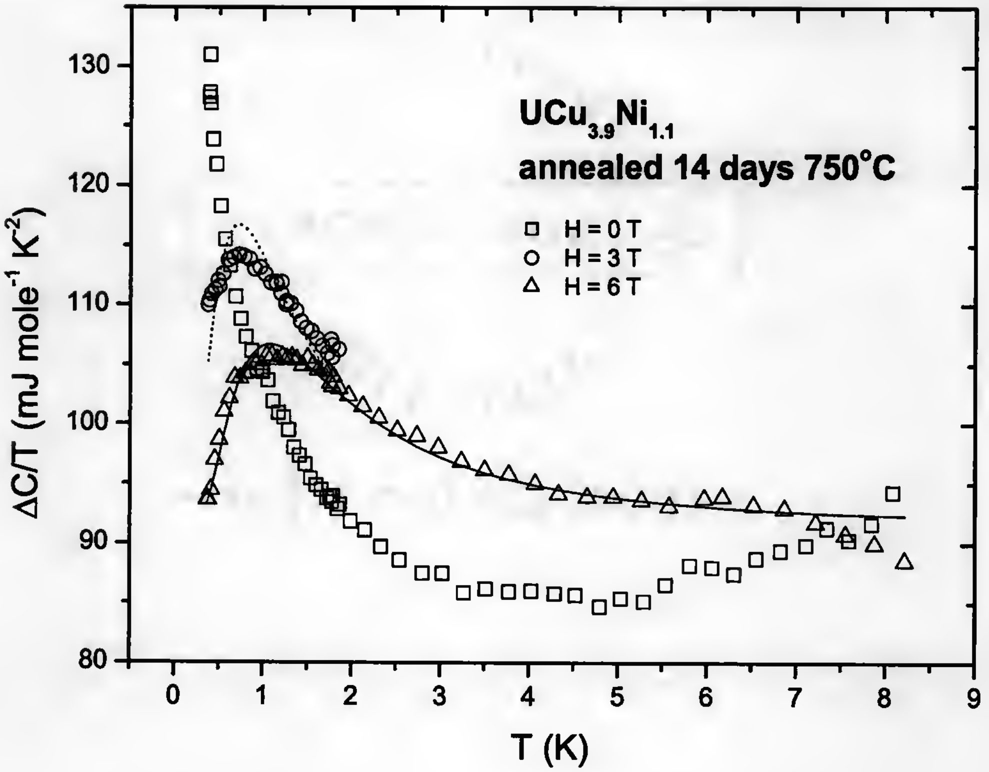

Figure 4–14: Specific heat of $UCu_{3.9}Ni_{1.1}$ in 0, 3, and 6 T. $UCu_{3.9}Ni_{1.1}$ was annealed for 14 days at 750°C. The $\Delta C/T$ values have the lattice and nuclear hyperfine terms subtracted off: $\Delta C/T = C/T - 0.0128H^2/T^3 - 0.178T^2 - 0.0011T^4$. The fits for the 3 T (dotted line) and 6 T (solid line) data are based upon the Castro Neto-Jones model above the crossover magnetic field: $\Delta C/T = A(H^{2+\lambda_\chi/2}/T^{3-\lambda_\chi/2})e^{-H/T} + D$ where A, H, and D are the three variable parameters in the least squares fit while $\lambda_\chi = 0.903$ for $UCu_{3.9}Ni_{1.1}$ (from Tables 4–4 and 4–7). The fits for the 3 T and 6 T data are as follows: 3 T - $A = 29.6$, $H = 1.85$, and $D = 93.1$ for $0.381 \leq T \leq 8.06$ K; and 6 T - $A = 19.7$, $H = 2.74$, and $D = 91.5$ for $0.372 \leq T \leq 8.22$ K. The 3 T data and the 3 T fit beyond 2 K are truncated for clarity.

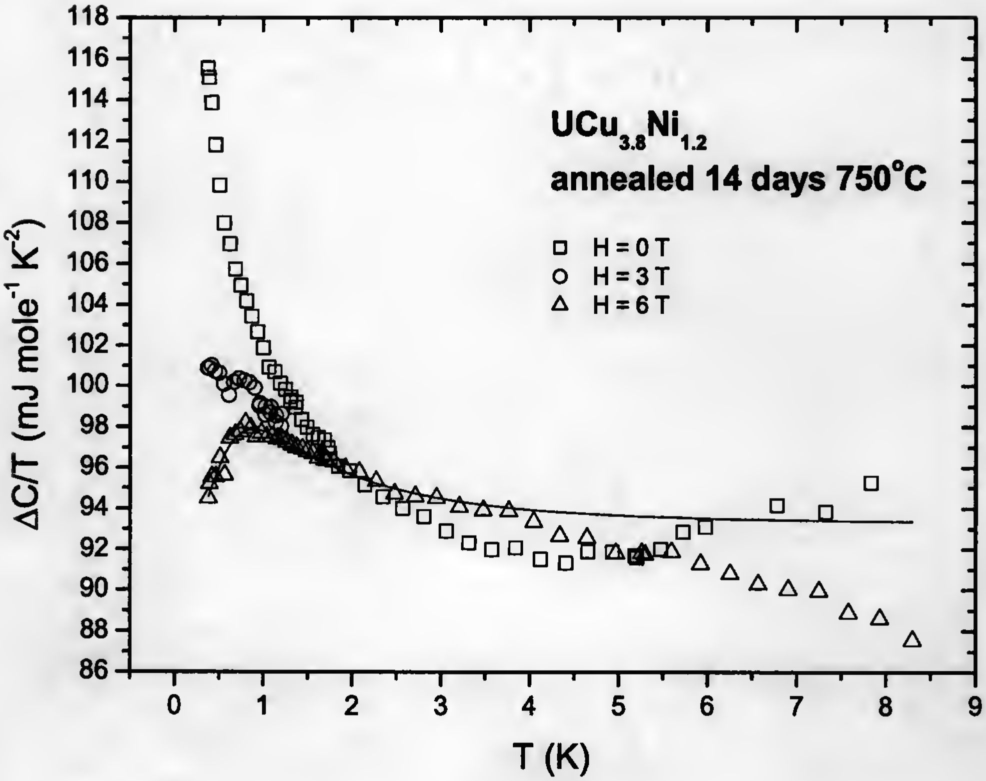

Figure 4–15: Specific heat of $UCu_{3.8}Ni_{1.2}$ in 0, 3, and 6 T. $UCu_{3.8}Ni_{1.2}$ was annealed for 14 days at 750°C. The $\Delta C/T$ values have the lattice and Schottky anomaly terms subtracted off: $\Delta C/T = C/T - 0.125H^2/T^3 - 0.178T^2 - 0.0011T^4$. The fit to the 6 T data is based upon the Castro Neto-Jones model above the crossover magnetic field: $\Delta C/T = A(H^{2+\lambda/2}/T^{3-\lambda/2})e^{-H/T} + D$ where A, H, and D are the three variable parameters in the least squares fit while $\lambda = 0.95$ for $UCu_{3.8}Ni_{1.2}$ (fixed from M vs. H at T = 2 K and χ vs. T at H = 1 kG). The fit covers the low temperature range from 0.381 to 3.77 K with A = 5.87, H = 2.24, and D = 93.2. The 3 T data are truncated at 1.2 K for clarity with the 3 T data above 1.2 K closely following the 0 T data.

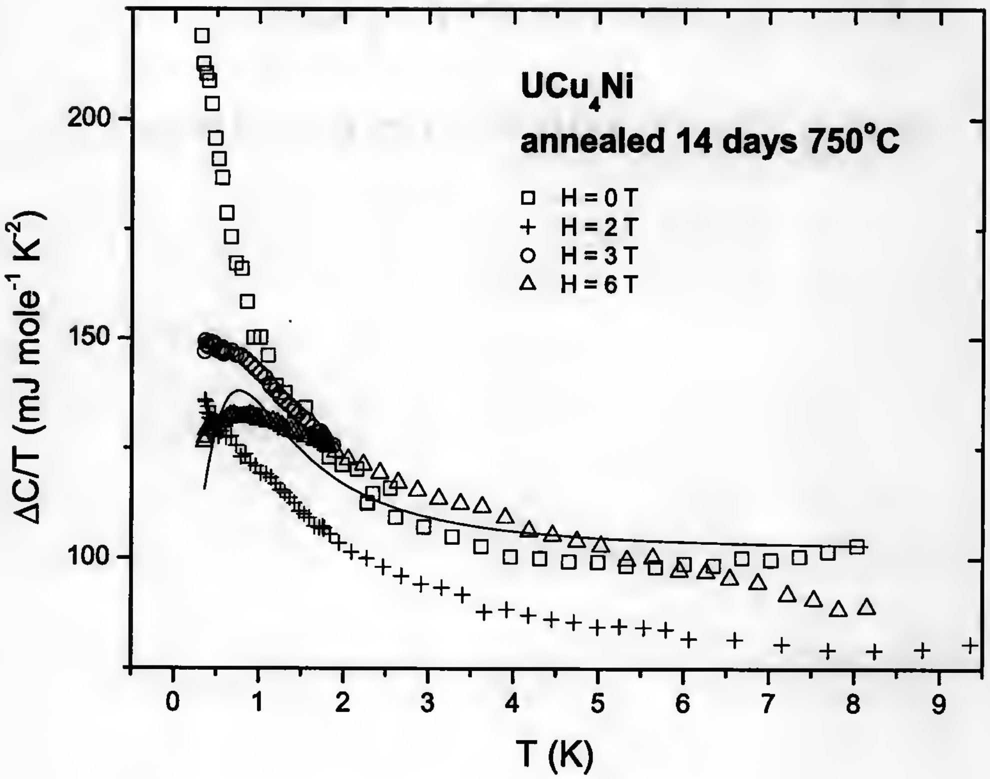

Figure 4–16: Specific heat of UCu_4Ni in 0, 2, 3, and 6 T. UCu_4Ni was annealed for 14 days at 750°C. The $\Delta C/T$ values have the lattice and Schottky anomaly terms subtracted off: $\Delta C/T = C/T - 0.0132H^2/T^3 - 0.178T^2 - 0.0011T^4$. The fit to the 6 T data is from the Castro Neto-Jones model for the specific heat above the crossover magnetic field: $\Delta C/T = A(H^{2+\lambda/2}/T^{3-\lambda/2})e^{-H/T} + D$ where A, H, and D are the three variable parameters in the least squares fit while $\lambda = 0.841$ for UCu_4Ni (fixed from M vs. H at T = 2 K). The 6 T fit has A = 45.7, H = 1.97, and D = 102 for $0.357 \leq T \leq 8.15$ K. The 0 T data goes down to $\sim$ 0.3 K so that the other field data are not concealed and the 3 T data are truncated at $\sim$ 2 K for clarity.

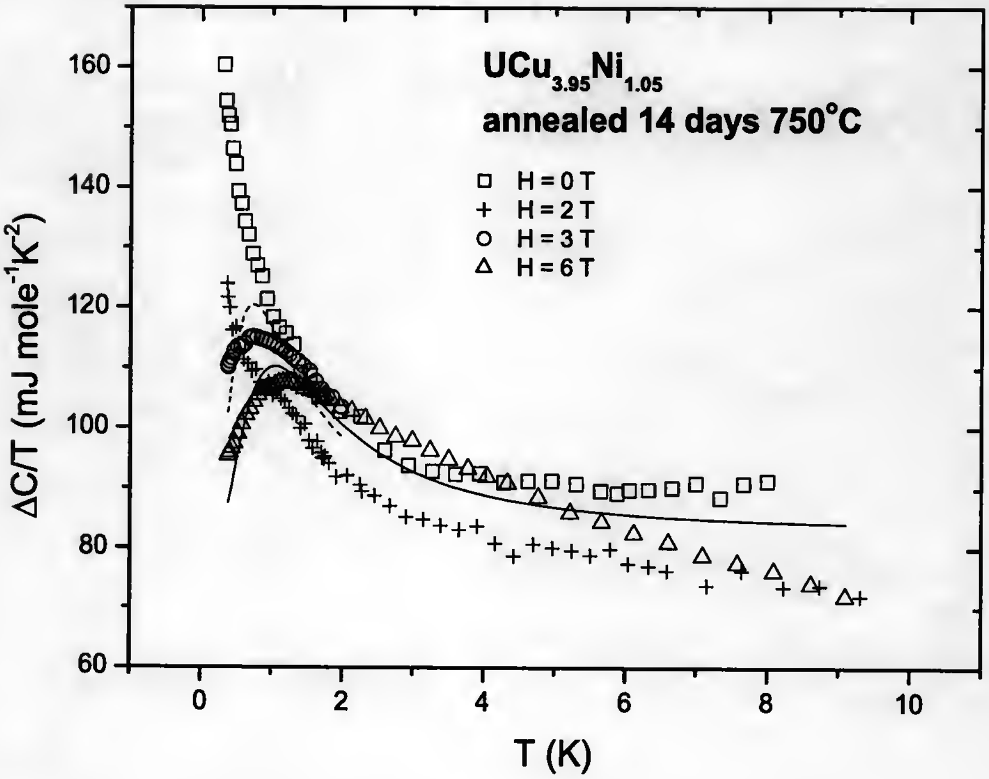

Figure 4–17: Specific heat of $UCu_{3.95}Ni_{1.05}$ in 0, 2, 3, and 6 T. $UCu_{3.95}Ni_{1.05}$ was annealed for 14 days at 750°C. The $\Delta C/T$ values have the lattice and nuclear hyperfine terms subtracted off: $\Delta C/T = C/T - 0.0130H^2/T^3 - 0.178T^2 - 0.0011T^4$. The fits to the 3 T and 6 T data are the Castro Neto-Jones equations for the specific heat above the crossover magnetic field: $\Delta C/T = A(H^{2+\lambda/2}/T^{3-\lambda/2})e^{-H/T} + D$ where A, H, and D are the three variable parameters in the least squares fit while $\lambda = 0.860$ for $UCu_{3.95}Ni_{1.05}$ (fixed from M vs. H at T = 2 K). The 3 T fit (dashed line) has A = 45.8, H = 1.90, and D = 84.2 for $0.385 \leq T \leq 9.01$ K while the 6 T fit (solid line) has A = 35.8, H = 2.68, and D = 83.2 for $0.386 \leq T \leq 9.09$ K. The 0 T data are plotted down to ∼ 0.3 K on this graph for a better view of the field data while the 3 T data and fit are truncated at 2 K for clarity.

Figures 4–14, 4–15, 4–16, and 4–17 have curves that attempt to fit certain magnetic field data. These are Castro Neto-Jones' fits $[\mathrm{C/T} \sim (\mathrm{H}^{2+\lambda/2}/\mathrm{T}^{3-\lambda/2})\mathrm{e}^{-\mu_{eff.}H/k_BT}]$ as was discussed in detail in the "Theory" chapter. These fits are used on the assumption that magnetic spin clusters (disorder induced) are responsible for the NFL behavior in $\mathrm{UCu}_{5-x}\mathrm{Ni}_x$. The fit details are listed in the caption of each figure. The 13 T data were not included in any figure for improved clarity. Also, the Castro Neto-Jones' fits to the 13 T data were rather poor for all Ni concentrations that had their specific heat measured in that magnetic field. An example of how poor the Castro Neto-Jones' model fits 13 T data is provided in Fig. D–3 of Appendix D for $\mathrm{UCu}_4\mathrm{Ni}$ 13 T data.

Finally, it should be noted that the Wilson ratio, R, was calculated for Ni concentrations where $0.75 \leq x \leq 1.2$ in Table 4–10. The Wilson ratio relates the specific heat and dc magnetic susceptibility of a compound [163] and is used in classifying whether or not a heavy-fermion system is magnetic, nonmagnetic, or superconducting [142]. The Wilson ratio is defined as

$$\mathrm{R} = \frac{\pi^2 \mathrm{k}_B^2 \chi(\mathrm{T}=0)}{\mathrm{g}^2 \mu_B^2 \gamma \mathrm{J}(\mathrm{J}+1)} \tag{4.2}$$

where k_B is the Boltzmann constant (1.38 x 10^{-23} J K^{-1}) and $\mathrm{g}^2\mu_B^2\mathrm{J}(\mathrm{J}+1)$ is equal to $\mu_{eff.}^2$ [where $\mu_{eff.}$ is in terms of the Bohr magneton number, μ_B (9.27 x 10^{-24} J T^{-1})]. Equation 4.2 may be simplified down to terms and units that are listed in this dissertation [142]:

$$\mathrm{R} = \frac{218.7\chi(\mathrm{T}=0)}{\gamma \mu_{eff.}^2} \tag{4.3}$$

where $\chi(\mathrm{T}=0)$ has the units of memu mole^{-1} G^{-1}, γ has the units of mJ mole^{-1} K^{-2}, and $\mu_{eff.}$ is a dimensionless number of Bohr magnetons. The $\chi(\mathrm{T}=0)$ and $\mu_{eff.}$ values are listed in Table 4–6 on page 131 as discussed previously. All γ values listed in Table 4–10 were extrapolated using a fifth order polynomial over the entire temperature range measured. This determination of γ may seem arbitrary, but it was consistently done for all Ni concentrations. The extrapolation of χ and $\Delta C/T$ as $T \rightarrow 0$ has been used in Wilson ratio values for samples like $CeCu_2Si_2$ [8] and $YbRh_2Si_2$ [52]. The Wilson ratios in Table 4–10 are by no means definitive, however they will be used for comparisons between samples in the $UCu_{5-x}Ni_x$ system.

4.6.1 $UCu_{5-x}Ni_x$ Specific Heat Discussion

4.6.1.1 Specific Heat in Zero Magnetic Field

Figure 4–11 on page 105 shows that the antiferromagnetism in the annealed (14 days at 750°C) $UCu_{5-x}Ni_x$ samples is not suppressed until x = 1.0 with the plateau at ~ 0.4 K signifying the antiferromagnetic transition temperature (T_N) for $UCu_{4.1}Ni_{0.9}$. Thus, UCu_4Ni is the critical concentration where T_N (or $T_{Néel}$) is suppressed to zero. Although the ac susceptibility results above showed the Ni concentrations with $x < 0.75$ to have a greater effect upon T_N than the Pd concentrations (less than 0.75), $x = 1.0$ is the same concentration where T_N is suppressed to zero for the annealed (14 days at 750°C) $UCu_{5-x}Pd_x$ system [160]. Yet, as discussed before, the UCu_4Ni sample shows no possibility of partial sublattice ordering as seen in UCu_4Pd. Figure 4–18 on page 115 is a phase diagram comparing the T_N values for the $UCu_{5-x}Ni_x$ and $UCu_{5-x}Pd_x$ system.

The $T_{Néel}$ value being suppressed to zero is also confirmed by the Moriya and Takimoto fits in Fig. 4–11. As discussed in the "Theory" chapter, Moriya and Takimoto based their theory upon spin fluctuation mode-mode coupling and as $T \rightarrow 0$, $C/T = \gamma - AT^{1/2}$. The mode-mode coupling increases with increasing temperature and C/T goes like -log T [143]. Figure 4–11 shows that x = 0.9 and x = 1.0 increase logarithmically with decreasing temperature and the $\gamma - AT^{1/2}$ curve fits the lowest temperature data (within the experimental uncertainty). An indicator for how close a sample is to a magnetic instability in the Moriya

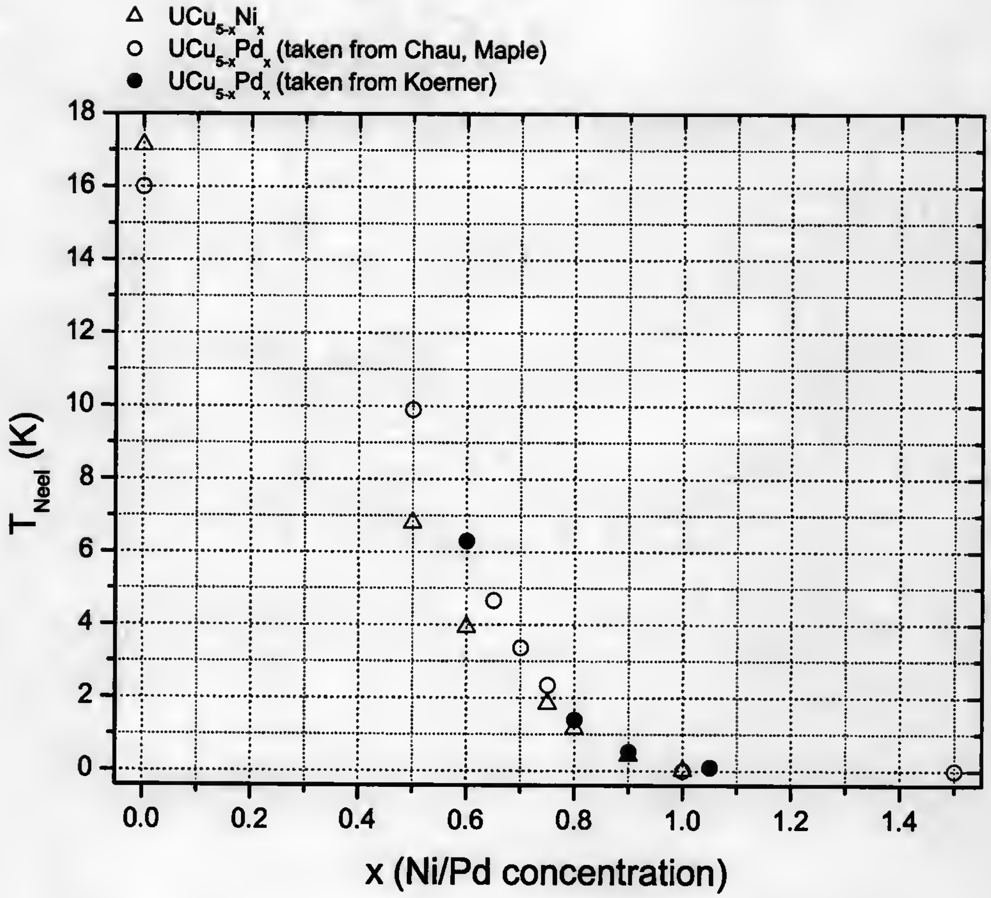

Figure 4–18: Phase diagram for $UCu_{5-x}Ni_x$ and $UCu_{5-x}Pd_x$. The $T_{N\acute{e}el}$ values for x = 0, 0.5, and 0.6 in the $UCu_{5-x}Ni_x$ system (denoted by hollow triangles) are from ac susceptibility measurements in Table 4–5 (the average $T_{N\acute{e}el}$ value for annealed and unannealed samples measured at 9.5 Hz) while the x = 0.75, 0.8, and 0.9 $T_{N\acute{e}el}$ values are those listed in Table 4–10 for annealed (14 days at 750°C) $UCu_{5-x}Ni_x$ samples. The hollow circles are $T_{N\acute{e}el}$ values taken from dc magnetic susceptibility measurements (down to 1.8 K) of Chau and Maple [26] for unannealed $UCu_{5-x}Pd_x$ samples. Similarly, the dark circles are $T_{N\acute{e}el}$ values for unannealed $UCu_{5-x}Pd_x$ reported by Koerner *et al.* [77].

and Takimoto fits is y_0, the reduced inverse staggered susceptibility [103]. The reduced inverse staggered susceptibility equaling zero signifies a quantum critical point and Fig. 4–11 shows that UCu_4Ni yields a y_0 value almost equal to zero. As one approaches x = 1.0 by increasing the Ni concentration (i.e., coming from the ordered side of the phase diagram), the y_0 values get smaller as x approaches 1.0. Thus, UCu_4Ni is at a quantum critical point. Also, the C/T values for x = 1.05 and x = 1.1 below 1 K rise faster than a log T dependence.

The Wilson ratio values in Table 4–10 confirm the conclusions made by the Moriya and Takimoto fits. If one uses the Wilson ratio intervals defined by Stewart (magnetic: $R \sim 0.8$-2.1; nonmagnetic: $R \sim 0.56$-0.75; and superconducting: $R < 0.52$ [142]), then as Ni is increased from 0.9 to 1.0, the Wilson ratio reveals that $UCu_{4.1}Ni_{0.9}$ (0.92) is magnetic while UCu_4Ni (0.50) is nonmagnetic. The Wilson ratios imply that the antiferromagnetism disappears by UCu_4Ni. Also, it should be noted that just because the Wilson ratios for x = 1.0 and x = 1.05 are below 0.52, this does not mean that UCu_4Ni and $UCu_{3.95}Ni_{1.05}$ are superconducting (similar to a nonsuperconducting $CeCu_2Si_2$ crystal that had $R = 0.44$ as reported by Stewart [142]). The Wilson ratio values should be viewed as consistent with the claim that UCu_4Ni is at a quantum critical point.

Table 4–10 and Fig. 4–10 indicate that once the antiferromagnetic fluctuations are suppressed by increasing the Ni concentration, the C/T values decrease monotonically. This is seen numerically by the decrease in the γ values with increasing Ni concentration for $x > 0.9$ in Table 4–10 and visually in Fig. 4–10. Not only are the magnetic fluctuations depressed, but also the associated degrees of freedom, which contribute to the f-electron part of the entropy, $S = \int (C/T)\, dT$, at low temperatures.

Figure 4–12 plots x = 0.9, 1.0, 1.05, 1.1, and 1.2 on a log-log graph to distinguish which Ni concentrations are consistent with the Griffiths phase disorder model. The specific heat in the Griffiths phase model has C/T $\sim$ $T^{-1+\lambda_{C/T}}$ (where $\lambda_{C/T}$ theoretically does not have to equal λ_χ in $\chi \sim T^{-1+\lambda_\chi}$ [73]). The power law form fits the x = 0.9 data above the antiferromagnetic transition over more than a decade of temperature (0.440 - 6.04 K as documented in Fig. 4–12). The power law form fits the x = 1.0 data over a much more limited temperature range (less than a decade of temperature: 0.404 - 2.28 K) and this behavior will be addressed below. As one increases the Ni concentration by 5%, the power law form fits the x = 1.05 data well over a decade of temperature (0.0547 - 1.66 K) and down to the lowest measured temperatures. The Griffiths phase power law form fits the x = 1.1 data fairly well down to the lowest measured temperatures but specific heat values at lower temperatures are desired to confirm if the Griffiths phase is applicable to x = 1.1 data. The power law fit for the x = 1.2 data begins to deviate from the data at $\sim$ 0.5 K as the upward curvature of the x = 1.2 data increases faster than the power law form. Thus, the disorder induced Griffiths phase is adjacent to the critical Ni concentration of x = 1.0 on both sides of the phase diagram. However, the composition range for which Griffiths phase exists is narrow as the spin fluctuations (required for Griffiths phase) are depressed by x = 1.2 (maybe even for x = 1.1). The quantum critical point spin fluctuations at x = 1.0 are surrounded by Griffiths phase behavior for x = 0.9 (above the antiferromagnetic transition) and x = 1.05.

Since UCu_4Ni does not show Griffiths phase behavior in Fig. 4–12, a semilog dependence for UCu_4Ni was discovered by a semilog fit (i.e., the solid straight line) in Fig. 4–11. This C/T $\sim$ -log T dependence covers over a decade of temperature (0.0547 to 1.30 K). The semilog dependence does not match the Griffiths phase disorder model [21], but does match predictions by the Kondo disorder model [11] and predictions for a 2-dimensional quantum critical point [143]. The semilog dependence in the specific heat has been measured in 3-dimensional systems such as $\mathrm{Y}_{1-x}\mathrm{U}_x\mathrm{Pd}_3$ [136], $\mathrm{U}_{1-x}\mathrm{Th}_x\mathrm{Pd}_2\mathrm{Al}_3$ [143], and $\mathrm{Ce}(\mathrm{Ru}_{1-x}\mathrm{Rh}_x)_2\mathrm{Si}_2$ [143]. Also, López de la Torre *et al.* found semilog dependence in the specific heat for annealed (7 days at 900°C) $\mathrm{UCu}_4\mathrm{Ni}$ over a decade of temperature (0.9 - 9 K) as has been discussed previously [90]. López de la Torre also mentioned an upturn in the specific heat at ~ 0.9 K [90] (this upturn causes the specific heat data to increase ~ 29% above the semilog extrapolation at 0.5 K) that is not seen in Fig. 4–12. This upturn may be some sort of magnetic second phase since the antiferromagnetism for x = 0.8 and x = 0.9 in Fig. 4–12 causes a plateau in the specific heat data.

4.6.1.2 Specific Heat in Applied Magnetic Fields

As discussed in the "Theory" chapter, the Griffiths phase disorder model by Castro Neto and Jones makes predictions for the specific heat in applied magnetic fields [21]. A major point in the Griffiths phase model is that above a certain crossover magnetic field (determined from magnetization versus field data), a field is induced in the specific heat and has the form $(\mathrm{H}^{2+\lambda/2}/\mathrm{T}^{3-\lambda/2})\mathrm{e}^{-\mu_{eff}.H/k_BT}$ (where λ is determined from the low temperature magnetic susceptibility and the high field magnetization data). The peak in the specific heat signifies that the tunneling between energy levels (i.e., Griffiths phase) has ceased. Another factor in these specific heat discussions will be how well the Griffiths phase is maintained in the magnetic susceptibility at higher magnetic fields (up to 4 T). Possible correlations in the specific heat and magnetic susceptibility at the same magnetic field will be discussed. The next five paragraphs will discuss the $\mathrm{UCu}_{5-x}\mathrm{Ni}_x$ specific heat in various magnetic fields for x = 0.9, 1.0, 1.05, 1.1, and 1.2 respectively.

The specific heat for annealed (14 days at 750°C) $\mathrm{UCu}_{4.1}\mathrm{Ni}_{0.9}$ in 0, 3, and 6 T magnetic fields is shown in Fig. 4–13 on page 108. The crossover magnetic field, $\mathrm{H}_{crossover}$, for $\mathrm{UCu}_{4.1}\mathrm{Ni}_{0.9}$ was determined to be ~ 0.3 T (from Table 4–4), so a field induced peak should be present by 3 T. However, Fig. 4–13 shows no field induced peak at 3 T and the 6 T data show a very "shallow" peak at lowest temperatures. If one refers back to the dc magnetic susceptibility results in Tables 4–8 and 4–9 and Fig. C–1 in Appendix C, then 2 T dc magnetic susceptibility data fit the Griffiths phase form ($\chi \sim T^{-1+\lambda_\chi}$) very well. As the magnetic field is increased to 3 T and 4 T, the power law form is applicable still over a decade of temperature, but the power law behavior diverges at the lowest temperatures as seen in Fig. C–1. Thus, although the 2, 3, and 4 T dc magnetic susceptibility data suggest possible Griffiths phase behavior, the 3 T specific heat data do not agree with predicted Griffiths phase behavior as shown by the lack of a field induced peak (for $H > H_{crossover}$). The Griffiths phase behavior may exist in a magnetic field slightly less than 6 T since a small peak begins to form in the 6 T specific heat data. Yet, if Griffiths phase were the dominant mechanism in $UCu_{4.1}Ni_{0.9}$, then one would have expected a field induced peak in the 3 T data. Since there is no field induced peak in the 3 T data, possible power law behavior ($C/T \sim T^{-1+\lambda_{C/T}}$) is searched for in the 3 T specific heat data despite the possible inconsistencies with Griffiths phase theory (power law behavior should not exist for $H > H_{crossover}$). Figure D–4 in Appendix D shows the specific heat in 3 T and 6 T fields on a log-log plot. The power law behavior is over a limited temperature range (1.42 - 4.29 K for H = 3 T and 2.10 - 7.46 K for H = 6 T). The data plateau below 1 K for the 3 T and 6 T data and this could be attributed to either an imminent field induced peak at lower temperatures or the antiferromagnetic behavior occurring at ~ 0.4 K.

The specific heat for annealed UCu_4Ni measured in 0, 2, 3, and 6 T magnetic fields is shown in Fig. 4–16. The 2 T data show no signs of a field induced peak despite being above the determined crossover magnetic field (1.55 T from Table 4–4) while the 3 T data are very similar in shape to the 3 T data for $UCu_{4.1}Ni_{0.9}$. Qualitatively, the 6 T data for UCu_4Ni have a "deeper" peak than the 6 T peak for $UCu_{4.1}Ni_{0.9}$. The 2 T data and 3 T data do not suggest possible Griffiths phase behavior occurring (no field induced peak or power law behavior as discussed below) despite the dc magnetic susceptibility results for 2 T and 3 T indicating power law behavior (over almost an entire decade of temperature in Table 4–8 and Fig. 4–9). One must remember the zero field specific heat results that proved quantum critical spin fluctuations were the mechanisms for the NFL behavior in UCu_4Ni, not the magnetic spin clusters for Griffiths phase behavior. The fit from the Griffiths phase model for magnetic fields above the crossover field to the 6 T data in Fig. 4–16 is very poor and suggests that the Griffiths phase model may not be the accurate description of the NFL behavior. Also, the 2 T and 3 T specific heat data for UCu_4Ni are on a log-log graph in Fig. D–5 of Appendix D to investigate possible power law behavior (i.e., Griffiths phase behavior in spite of being above 1.55 T). Figure D–5 shows that the power law behavior is very limited in its temperature range (1.20 - 4.18 K for H = 2 T and 1.73 - 4.49 K for H = 3 T). This suggests that Griffiths phase behavior (tunneling between energy levels) is not existent at 2 and 3 T despite the dc magnetic susceptibility results.

The specific heat of $UCu_{3.95}Ni_{1.05}$ measured in 0, 2, 3, and 6 T magnetic fields is shown in Fig. 4–17. The 2 T data show no field induced peak and suggest possible Griffiths phase behavior along with the dc magnetic susceptibility at 2 T which shows power law behavior ($\chi \sim T^{-1+\lambda_x}$) over a decade of temperature (in Table 4–8 and Fig. C–2). Figure D–6 in Appendix D shows that the 2 T specific heat data of $UCu_{3.95}Ni_{1.05}$ do not signify Griffiths phase behavior. The power law behavior of the 2 T specific heat data is over a very limited temperature range (~ 1 - 3 K). When the magnetic field of $UCu_{3.95}Ni_{1.05}$ is increased from 2 T to 3 T, the specific heat shows a field induced peak at 3 T. Yet, the peak fit from the Griffiths phase disorder model is very poor as shown in Fig. 4–17. The dc magnetic susceptibility at 3 T for $UCu_{3.95}Ni_{1.05}$ also indicates that the Griffiths phase is not the correct description for the data since a semilog dependence fits the $UCu_{3.95}Ni_{1.05}$ dc magnetic susceptibility at 3 T more accurately (i.e., over a wider temperature range in Table 4–8). The 3 T specific heat and dc magnetic susceptibility data for $UCu_{3.95}Ni_{1.05}$ are suggestive of a more complex model (than the Griffiths phase disorder model) that might include elements of the Griffiths phase disorder model. The 6 T specific heat data for $UCu_{3.95}Ni_{1.05}$ also display a field induced peak which has greater depth than the 6 T field induced peak for UCu_4Ni (12.2 mJ $mole^{-1}$ K^{-2} for $UCu_{3.95}Ni_{1.05}$ versus 5.98 mJ $mole^{-1}$ K^{-2} for UCu_4Ni where depth is defined as the difference between the maximum $\Delta C/T$ value on the peak and the $\Delta C/T$ value at the lowest measured temperature). However, Fig. 4–17 shows that the field induced equation from the Griffiths model does not fit the 6 T $UCu_{3.95}Ni_{1.05}$ specific data very well. Although the specific heat data of $UCu_{3.95}Ni_{1.05}$ in magnetic fields qualitatively match the predictions of the Griffiths model by having the field induced peak move up to higher temperatures and broaden with increasing magnetic field as occurred in $Ce_{1-x}La_xRhIn_5$ [73] and $Ce_{1-x}Th_xRhSb$ [74], the quantitative description of the Griffiths phase model for field induced peaks ($C/T \sim (H^{2+\lambda/2}/T^{3-\lambda/2})e^{-\mu_{eff}.H/k_BT}$ [21]) does not describe the specific heat data of $UCu_{3.95}Ni_{1.05}$ in magnetic fields well.

The specific heat data of $UCu_{3.9}Ni_{1.1}$ in 0, 3, and 6 T magnetic fields are shown in Fig. 4–14. The 3 T specific heat data of $UCu_{3.9}Ni_{1.1}$ show a field induced peak at 3 T (as expected by the determined crossover field of 1.9 T in Table 4–4). Yet, just as occurred for the 3 T $UCu_{3.95}Ni_{1.05}$ heat capacity data, the Griffiths phase model does not match the 3 T specific heat data for $UCu_{3.9}Ni_{1.1}$. A possible hint of the Griffiths model not being correct is provided by the dc magnetic susceptibility results at 3 T in Table 4–8. A semilog equation fits the $UCu_{3.9}Ni_{1.1}$ dc magnetic susceptibility more accurately than a power law equation. This suggests that tunneling between energy levels in a Griffiths phase is not the accurate description at 3 T for $UCu_{3.9}Ni_{1.1}$. Interestingly, the 6 T data for $UCu_{3.9}Ni_{1.1}$ are fit very well by a Griffiths phase field induced peak over almost the entire temperature range (0.372 to 8.22 K) in Fig. 4–14. A possible explanation for the good fit at 6 T may be taken from Fig. 2–2 of the "Theory" chapter where the 3 T data may be too close to the crossover behavior line, T $\sim$ H, and the scaling becomes muddled. However, once H is increased, the scaling of the specific heat becomes $g_\lambda(H/T) \sim (H/T)^{2+\lambda/2}e^{-H/T}$ as shown in Fig. 2–2.

The final specific heat data measured in magnetic fields concern $UCu_{3.8}Ni_{1.2}$ in Fig. 4–15. Unfortunately, the dc magnetic susceptibility for $UCu_{3.8}Ni_{1.2}$ gave no hints about possible Griffiths phase behavior since power law behavior (or semilog behavior) was not observed over one decade of temperature for any of the magnetic fields. A peak is not seen in the 3 T $UCu_{3.8}Ni_{1.2}$ specific heat data which is consistent with the crossover magnetic field of 3.3 T stated in Table 4–4. The 3 T specific heat data of $UCu_{3.8}Ni_{1.2}$ is explored further in Fig. D–7 of Appendix D. The power law behavior (i.e., Griffiths phase behavior, $C/T \sim T^{-1+\lambda_{C/T}}$) is over a very limited temperature range ($\sim$ 1 - 3.5 K) and this may be due to the proximity of the crossover field to 3 T and the scaling function in Fig. 2–2 may become "blurred" (a similar argument was suggested for the 3 T specific heat $UCu_{3.9}Ni_{1.1}$ data). As the magnetic field is increased from 3 T to 6 T, the field induced peak form of the Castro Neto-Jones model fits the 6 T $UCu_{3.8}Ni_{1.2}$ specific heat data over almost a decade of temperature (0.381 to 3.77 K) in Fig. 4–15. This is very similar to the $UCu_{3.9}Ni_{1.1}$ results except that the Griffiths theory in the high magnetic field limit fits the 6 T $UCu_{3.9}Ni_{1.1}$ specific heat data over a little larger temperature range. The smaller temperature range for 6 T $UCu_{3.8}Ni_{1.2}$ data may suggest the start of deviation from Griffiths phase behavior.

The discussion of the specific heat data in magnetic fields has raised an interesting point and that concerns the evolution of the 6 T specific heat data for

$UCu_{5-x}Ni_x$ samples that are above the critical concentration of x = 1.0. Figure 4–19 shows the 6 T specific heat data for x = 1.0, 1.05, 1.1, and 1.2. The depths of the peaks (as defined earlier) in Fig. 4–19 are 5.98, 12.2, 12.1, and 3.68 for x = 1.0, 1.05, 1.1, and 1.2 respectively. The conclusions drawn from the zero magnetic field specific heat data were that quantum critical fluctuations were the dominant mechanism for x = 1.0 while x = 1.05 (and possibly x = 1.1) had Griffiths phase disorder fluctuations and x = 1.2 did not show Griffiths phase behavior very well. A possible correlation may exist between the depths of these peaks at 6 T and the fluctuations responsible for the NFL behavior with the "deeper" peaks (in x = 1.05 and x = 1.1) corresponding to Griffiths phase fluctuations. Also, Fig. 4–19 shows that for temperatures above the field induced peak, the specific heat values for x = 1.0 and x = 1.05 decrease monotonically (almost linearly) while the x = 1.1 and x = 1.2 (better seen in Fig. 4–15) data show curvature above the field induced peaks. The curvature (which helps the Castro Neto-Jones model fit the data so well) for x = 1.1 continues up to ∼ 6 K while the curvature for x = 1.2 continues up to ∼ 4 K. Beyond the two temperatures just mentioned, the x = 1.1 and 1.2 data fall monotonically like the x = 1.0 and x = 1.05 data. The curvature evolving into a monotonic decrease might suggest that $UCu_{3.9}Ni_{1.1}$ and $UCu_{3.8}Ni_{1.2}$ have a secondary magnetic phase transition.

The specific heat data when combined with the dc magnetic susceptibility data portray a pretty unclear story concerning the Griffiths phase theory for the $UCu_{5-x}Ni_x$ system. UCu_4Ni is the concentration on the phase diagram where the quantum critical point occurs and the zero field UCu_4Ni specific heat data suggest quantum critical spin fluctuations to be the primary mechanisms for the NFL behavior. The Griffiths phase theory does not fit the UCu_4Ni specific heat data in magnetic fields, but the dc magnetic susceptibility data at higher magnetic fields (i.e., above the crossover magnetic field) indicate power law

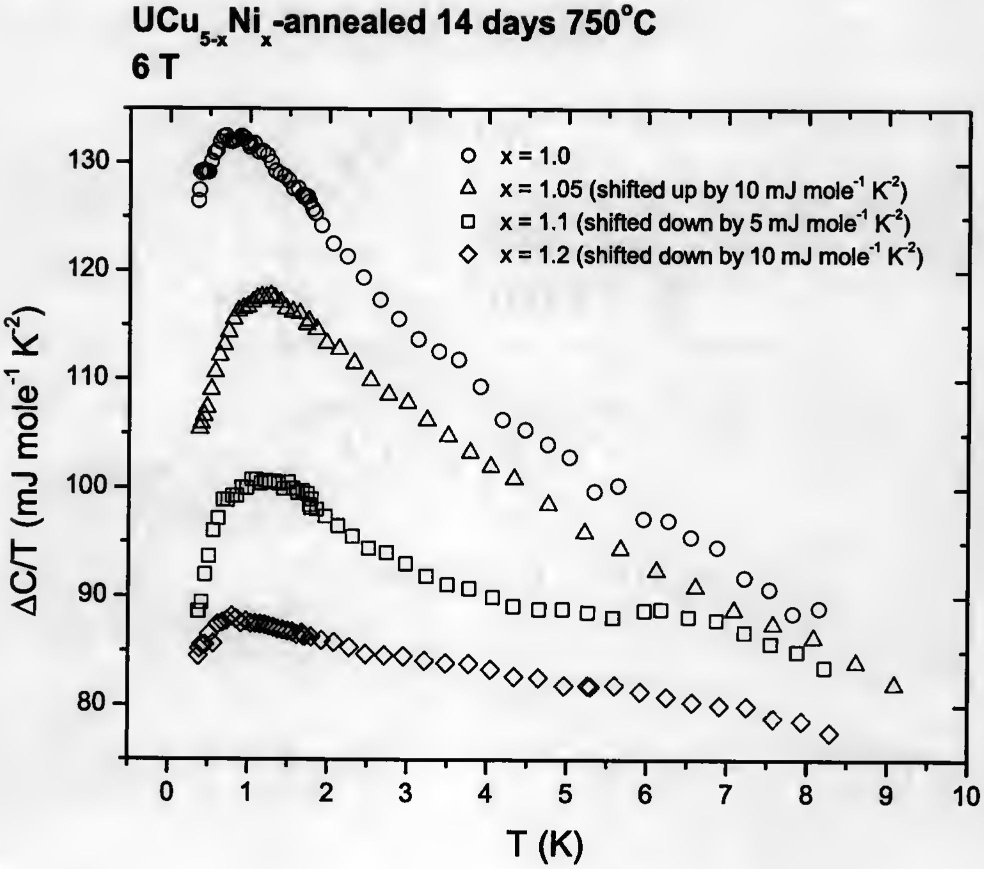

Figure 4–19: Specific heat data at 6 T for $UCu_{5-x}Ni_x$ samples. Annealed (14 days at 750°C) samples are UCu_4Ni, $UCu_{3.95}Ni_{1.05}$, $UCu_{3.9}Ni_{1.1}$, and $UCu_{3.8}Ni_{1.2}$. The specific heat values had their lattice and Schottky anomaly contributions subtracted off: $\Delta C/T = C/T - (0.178T^2 + 0.0011T^4) - (5\text{-}x)0.118/T^3$ where x is the number of moles of Ni for each sample. The indicated shifts in the data are for improved clarity.

behavior ($\chi \sim T^{-1+\lambda_\chi}$), predicted by the Griffiths phase theory at fields lower than the crossover magnetic field. If the Ni concentration is increased by 5%, then the zero magnetic field specific heat data indicate Griffiths phase behavior. However, the $UCu_{3.95}Ni_{1.05}$ specific heat data in magnetic fields do not match the predictions made by the Griffiths phase theory. The dc magnetic susceptibility goes from power law behavior at 2 T to semilog behavior (predicted in a two-channel Kondo model [143]) at 3 T. The Griffiths phase theory matches the $UCu_{3.9}Ni_{1.1}$ specific heat data at 6 T well while semilog behavior covers a wider temperature range in the 3 T dc magnetic susceptibility data than power law behavior. The Castro Neto-Jones model matches the $UCu_{3.8}Ni_{1.2}$ specific heat data at 6 T over a more limited temperature range (compared to $UCu_{3.9}Ni_{1.1}$) while the dc magnetic susceptibility (between 1 kG and 4 T) gives no hint about a possible theoretical model since semilog and log-log relationships are over limited temperature ranges.

Clearly, the data show that no known theoretical model to date can predict all the intricate behaviors presented in the specific heat and dc magnetic susceptibility data. Magnetic spin clusters that allow tunneling to occur between energy levels (the premise upon which the Griffiths phase theory is based) may be part of the correct theory since there are elements of the Castro Neto-Jones model that explain some of the data correctly.

Table 4–1: Lattice parameter values for the nine $UCu_{5-x}Ni_x$ compounds. a_{un} and $\sigma_{a_{un}}$ represent the lattice parameter values for the unannealed $UCu_{5-x}Ni_x$ compounds and the corresponding errors associated with the unannealed compounds. Likewise, a_{an} and $\sigma_{a_{an}}$ represent the lattice parameter values for $UCu_{5-x}Ni_x$ compounds annealed for 14 days at 750°C and their associated error bars.

x (Ni conc.):	a_{un} (Å):	$\sigma_{a_{un}}$ (Å):	a_{an} (Å):	$\sigma_{a_{an}}$ (Å):
0.5	7.00891	0.00232	7.01007	0.00432
0.6	7.01762	0.00520	7.00217	0.00277
0.75	6.99817	0.00450	6.99054	0.00260
0.8	6.99353	0.00205	6.99272	0.00211
0.9	6.98361	0.00247	6.98714	0.00223
1.0	6.98279	0.00258	6.98246	0.00194
1.05	6.97971	0.00166	6.97879	0.00226
1.1	6.97907	0.00171	6.97612	0.00165
1.2	6.97107	0.00291	6.97282	0.00123

Table 4–2: The low temperature resistivity results for $UCu_{5-x}Ni_x$ samples. The resistivity data were fit to a power law form, $\rho_0 + AT^\alpha$. The $UCu_{5-x}Ni_x$ samples with $0.9 \leq x \leq 1.1$ had a low temperature power law fit (below 2 K) and a high temperature power law fit (above 2 K) and the low temperature fit results are separated from the high temperature fit results by a slash, /. Samples that were annealed with the same production date as the unannealed samples were cut and annealed from the unannealed samples. RRR is the residual resistivity ratio and χ^2 is the measure of the difference between the power law form and the experimental data. The absolute uncertainty of all resistivity measurements is 5%.

x-(Ni conc.) (prod. date):	unannealed/ annealed/ quenched:	ρ_0 ($\mu\Omega$ cm):	RRR:	A ($\mu\Omega$ cm $K^{-\alpha}$):	α:	T depend. range (K):	χ^2 (goodness of fit):
0.75 (4-3-03)	unannealed	781		-56.7	0.285	0.337 - 10.0	0.459
0.80 (2-27-03)	unannealed	1015		-70.2	0.292	0.344 - 10.0	0.807
0.9 (4-3-03)	unannealed	1150/1030	0.279	-123/-8.52	0.161/1.03	0.319 - 2.06/ 1.91 - 10.0	0.0681/0.0678
0.9 (4-3-03)	ann. 14 d. 750°C	1130/1040	0.297	-93.0/-8.95	0.224/1.01	0.306 - 2.06/ 1.91 - 12.1	0.102/0.0700
1.0 (2-27-03)	unannealed	981/944		-41.1/-5.52	0.252/1.12	0.435 - 2.06/ 1.99 - 10.0	0.490/0.260
1.0 (2-27-03)	ann. 14 d. 750°C	816/778	0.320	-42.5/-5.03	0.196/1.09	0.0611 - 2.04/ 1.89 - 12.1	0.0345/0.00487
1.0 (2-27-03)	ann. 8 wks. 850°C (ρ measured unann.)	48.4/43.8	3.18	-4.76/-0.215	0.0380/0.468	0.345 - 2.41/ 1.63 - 8.40	0.00116/0.00108
1.0 (8-15-03)	quenched	673/644	0.374	-30.5/-3.26	0.243/1.09	0.383 - 2.05/ 1.97 - 12.1	0.0816/0.0147

Table 4–3: The low temperature resistivity results for $UCu_{5-x}Ni_x$ samples. This table is a continuation of Table 4–2.

x-(Ni conc.) (prod. date):	unannealed/ annealed/ quenched:	ρ_0 ($\mu\Omega$ cm):	RRR:	A ($\mu\Omega$ cm $K^{-\alpha}$):	α:	T depend. range (K):	χ^2 (goodness of fit):
1.0 (10-13-03)	ann. 8 wks. 850°C	1030/988	0.313	-47.6/-6.96	0.237/1.06	0.339 - 2.12/ 1.93 - 10.2	0.0158/ 0.0191
1.0 (4-13-04)	ann. 4 months 850°C	650/633	0.370	-19.6/-3.73	0.309/1.05	0.348 - 2.10/ 1.78 - 12.1	0.0111/0.00569
1.05 (7-14-03)	unannealed	677/667	0.437	-12.2/-3.10	0.411/1.11	0.297 - 2.06/ 1.90 - 12.1	0.00534/0.00157
1.05 (7-14-03)	ann. 14 d. 750°C	908/884	0.341	-27.6/-4.25	0.216/1.12	0.0611 - 2.07/ 1.91 - 12.0	0.0339/0.00817
1.05 (7-14-03)	ann. 8 wks. 850°C (ρ measured unann.)	64.9/64.0	2.88	-0.908/-0.0689	0.166/0.954	0.349 - 2.11/ 1.95 - 8.52	0.00335/0.00455
1.05 (10-13-03)	ann. 8 wks. 850°C	1200/1180	0.344	-15.6/-4.46	0.496/1.19	0.339 - 2.11/ 1.88 - 12.4	0.0087/0.216
1.05 (4-14-04)	ann. 4 months 850°C	929/919	0.378	-14.5/-4.46	0.443/1.07	0.352 - 2.12/ 1.80 - 12.2	0.0180/0.0164
1.1 (5-8-03)	unannealed	706/702	0.408	-6.47/-2.38	0.546/1.15	0.324 - 2.06/ 1.90 - 12.1	0.0278/0.00192
1.1 (5-8-03)	ann. 14 d. 750°C	782/780	0.527	-3.85/-2.24	0.743/1.14	0.297 - 2.05/ 1.90 - 12.1	0.00293/0.0031
1.2 (3-26-03)	ann. 14 d. 750°C	453	0.724	-0.703	0.996	0.350 - 12.2	0.147

Table 4–4: Magnetization data for $UCu_{5-x}Ni_x$ annealed 14 days at 750°C. The magnetization data was taken at $T = 2$ K for Ni concentrations around the critical concentration of $x = 1.0$. The linear fit form was $M = A+BH$ while the power law fit form was $M = A'+B'H^{\lambda}$. The linear fit regions and power law fit regions were selected by finding the minimum standard deviation/χ^2 values over the largest possible field range. The linear fit standard deviation and the power law fit χ^2 values were calculated using MicroCal Origin 5.0. The crossover field was arbitrarily defined as the point on the standard deviation versus field range curve where a minimum value was found (for $x = 0.9$, 1.05, and 1.2) or where an inflection point (the change in the standard deviation slope was a minimum) occurred (for $x = 1.0$ and 1.1). The H values for the linear fits and the power law fits are in units of Tesla. The linear fits and power law fits are shown graphically in Fig. 4–4 on page 87.

x Ni conc.:	Linear Fit Region(T):	Linear Fit ($M =$):	Linear Fit std. dev.:	Crossover Field(T):	Power Law Fit Region(T):	Power Law Fit ($M =$):	Power Law Fit χ^2:	Griffiths phase λ ($M \sim H^{\lambda}$):
0.8	0 - 0.125	-1.09+110H	0.00468		1.7 - 7	$-27.1+126H^{0.798}$	0.0126	0.798
0.9	0 - 0.3	-0.344+81.7H	0.0297	0.3	1.9 - 7	$-27.9+103H^{0.783}$	0.00793	0.783
1.0	0 - 1.55	0.0196+62.3H	0.271	1.55	1.55 - 7	$-18.1+78.8H^{0.841}$	0.00137	0.841
1.05	0 - 1.65	-0.889+56.1H	0.0840	1.65	1.6 - 7	$-15.9+70.0H^{0.860}$	0.00173	0.860
1.1	0 - 1.9	-0.545+48.0H	0.125	1.9	1.8 - 7	$-10.2+56.5H^{0.903}$	0.00332	0.903
1.2	0 - 3.3	-1.04+35.4H	0.161	3.3	0.9 - 7	$-4.44+38.3H^{0.953}$	0.253	0.953

Table 4–5: AC susceptibility results for select $UCu_{5-x}Ni_x$ samples. AC susceptibility was run for UCu_5 (unannealed), $UCu_{4.5}Ni_{0.5}$ (unannealed and annealed), and $UCu_{4.4}Ni_{0.6}$ (unannealed and annealed). The ac susceptibility measurements were performed on a SQUID with a temperature range of 2 K to 300 K. The T_N value was determined by finding the temperature value where a peak in the real component, χ', of the ac susceptibility data was located. AC susceptibility measurements were performed at three different frequencies: 9.5 Hz, 95 Hz, and 950 Hz.

x- Ni conc.:	unann./ ann. (14 d. 750°C):	$T_N(\chi'_{AC})$[K] 9.5 Hz:	$T_N(\chi'_{AC})$[K] 95 Hz:	$T_N(\chi'_{AC})$[K] 950 Hz:
0	unann.	17 ± 0.25	16.5 ± 0.25	16.75 ± 0.25
0.5	unann.	7.50 ± 0.25	6.75 ± 0.25	8.00 ± 0.50
0.5	ann.	6.10 ± 0.10	6.00 ± 0.10	6.50 ± 0.25
0.6	unann.	3.76 ± 0.25	4.01 ± 0.25	3.76 ± 0.25
0.6	ann.	4.01 ± 0.10	4.31 ± 0.10	

Table 4–6: DC magnetic susceptibility results for annealed $UCu_{5-x}Ni_x$. The $UCu_{5-x}Ni_x$ samples were annealed for 14 days at 750°C. The χ values at 2 K are reported with their standard deviation value (not the standard deviation of the mean). The $UCu_{4.5}Ni_{0.5}$ and $UCu_{4.4}Ni_{0.6}$ samples had their low temperature χ values reported at 6.0 K and 3.5 K respectively, i.e., the temperature values where the low temperature susceptibility was a maximum. The $\mu_{eff.}$ values were determined with a Curie-Weiss fit for susceptibility values above the reported high temperature peaks. The $\chi(T = 0\ K)$ values were extrapolated from low temperature susceptibility data (≤ 10 K) using a fifth order polynomial fit. All χ data in this table were measured in a 1000 Gauss field.

x- Ni conc.:	$\chi(T = 2\,K) \pm \sigma_\chi$ (memu mole^{-1} G^{-1}):	$\mu_{eff.}(\mu_B)$:	Hi-T peak (K):	$\chi(T = 0\,K)$ (memu mole^{-1} G^{-1}):
0.5	8.7 ± 0.1	3.35	140 K	
0.6	8.2 ± 0.4	3.09	115 K	
0.75	10.1 ± 0.5	3.23	125 K	16.3
0.8	10.3 ± 0.1	3.34	125 K	16.0
0.9	7.6 ± 0.3	2.79	130 K	11.8
1.0	5.8 ± 0.2	3.37	130 K	8.2
1.05	4.7 ± 0.2	3.59	155 K	6.2
1.1	5.1 ± 0.5	3.56	135 K	6.1
1.2	3.8 ± 0.4	3.32	150 K	4.1

Table 4–7: Fit results for $UCu_{5-x}Ni_x$ dc susceptibility data at 1 kG and 1 T. The lines were plotted on semilog graphs and log-log graphs. The temperature ranges were selected such that the maximum temperature range yielded minimum standard deviation values. The λ values were obtained from the Griffiths phase power law form ($\chi \sim T^{-1+\lambda}$) and the respective magnetic field's log-log behavior.

	x = 0.9	x = 1.0	x = 1.05	x = 1.1	x = 1.2
1 kG Semilog Behavior ($\chi =$):	$0.00903 - 0.00492\log_{10}T$	$0.00653 - 0.00258\log_{10}T$	$0.00521 - 0.00163\log_{10}T$	$0.00545 - 0.00117\log_{10}T$	$0.00389 - 0.000423\log_{10}T$
1 kG Semilog T Range (K):	2 - 4.5	2 - 4	2 - 3.75	2 - 3.76	2 - 3.76
1 kG Log-Log Behavior ($\log_{10}\chi =$):	$-2.02 - 0.320\log_{10}T$	$-2.18 - 0.208\log_{10}T$	$-2.28 - 0.152\log_{10}T$	$-2.26 - 0.0971\log_{10}T$	$-2.41 - 0.0496\log_{10}T$
1 kG Log-Log T Range (K):	2 - 4.5	2 - 4	2 - 4.26	2 - 4.75	2 - 4.01
$\lambda_{1 kG}$:	0.680	0.792	0.848	0.903	0.950
1 T Semilog Behavior ($\chi =$):	$0.00887 - 0.00427\log_{10}T$	$0.00668 - 0.00234\log_{10}T$	$0.00598 - 0.00166\log_{10}T$	$0.00521 - 0.00101\log_{10}T$	$0.00397 - 0.000314\log_{10}T$
1 T Semilog T Range (K):	2 - 3.50	2 - 3.05	2 - 3.05	2 - 3.20	2 - 3.50
1 T Log-Log Behavior ($\log_{10}\chi =$):	$-2.04 - 0.263\log_{10}T$	$-2.17 - 0.173\log_{10}T$	$-2.22 - 0.132\log_{10}T$	$-2.28 - 0.0890\log_{10}T$	$-2.40 - 0.0334\log_{10}T$
1 T Log-Log T Range (K):	2 - 4	2 - 4	2 - 3.75	2 - 4	2 - 5.50
$\lambda_{1 T}$:	0.737	0.827	0.868	0.911	0.967

Table 4–8: Fit results for $UCu_{5-x}Ni_x$ dc susceptibility data at 2 T and 3 T. The lines were plotted on semilog graphs and log-log graphs. The temperature ranges were selected such that the maximum temperature range yielded minimum standard deviation values. The λ values were obtained from the Griffiths phase power law form ($\chi \sim T^{-1+\lambda}$) and the respective magnetic field's log-log behavior.

	x = 0.9	x = 1.0	x = 1.05	x = 1.1	x = 1.2
2 T Semilog Behavior ($\chi =$):	0.00823 - 0.00315$\log_{10}$T	0.00644 - 0.00180$\log_{10}$T	0.00588 - 0.00128$\log_{10}$T	0.00513 - 0.000789$\log_{10}$T	0.00400 - 0.000214$\log_{10}$T
2 T Semilog T Range (K):	2 - 6	2 - 4	2 - 5	2 - 3.75	2 - 8
2 T Log-Log Behavior ($\log_{10}\chi =$):	-2.07 - 0.215$\log_{10}$T	-2.19 - 0.134$\log_{10}$T	-2.23 - 0.101$\log_{10}$T	-2.29 - 0.0695$\log_{10}$T	-2.40 - 0.0246$\log_{10}$T
2 T Log-Log T Range (K):	2 - 55	2 - 40	2 - 28	2 - 17	2 - 9.5
λ_{2T}:	0.785	0.866	0.899	0.930	0.975
3 T Semilog Behavior ($\chi =$):	0.00800 - 0.00287$\log_{10}$T	0.00655 - 0.00162$\log_{10}$T	0.00578 - 0.00111$\log_{10}$T	0.00523 - 0.000744$\log_{10}$T	0.00408 - 0.000229$\log_{10}$T
3 T Semilog T Range (K):	2.9 - 8.5	2.3 - 8.5	2 - 45	2 - 20	2 - 5
3 T Log-Log Behavior ($\log_{10}\chi =$):	-2.07 - 0.215$\log_{10}$T	-2.17 - 0.131$\log_{10}$T	-2.23 - 0.102$\log_{10}$T	-2.28 - 0.0688$\log_{10}$T	-2.39 - 0.0261$\log_{10}$T
3 T Log-Log T Range (K):	4 - 45	4 - 38	2.75 - 30	2 - 14	2 - 6
λ_{3T}:	0.785	0.869	0.898	0.931	0.974

Table 4–9: Fit results for $UCu_{5-x}Ni_x$ dc susceptibility data at 4 T. The lines were plotted on semilog graphs and log-log graphs. The temperature ranges were selected such that the maximum temperature range yielded minimum standard deviation values. The λ values were obtained from the Griffiths phase power law form ($\chi \sim T^{-1+\lambda}$) and the 4 T's log-log behavior.

	x = 0.9	x = 1.0	x = 1.05	x = 1.1	x = 1.2
4 T Semilog Behavior ($\chi =$):	0.00773 - 0.00261$\log_{10}$T	0.00639 - 0.00146$\log_{10}$T	0.00569 - 0.00105$\log_{10}$T	0.00516 - 0.000723$\log_{10}$T	0.00406 - 0.000218$\log_{10}$T
4 T Semilog T Range (K):	3.75 - 10	2.9 - 20	2 - 32	3.5 - 18	2 - 4
4 T Log-Log Behavior ($\log_{10}\chi =$):	-2.08 - 0.210$\log_{10}$T	-2.18 - 0.129$\log_{10}$T	-2.23 - 0.0995$\log_{10}$T	-2.29 - 0.0666$\log_{10}$T	-2.39 - 0.0263$\log_{10}$T
4 T Log-Log T Range (K):	4 - 40	4 - 36	3.2 - 28	2.75 - 13	2 - 6
λ_{4T}:	0.790	0.871	0.901	0.933	0.974

Table 4–10: Specific heat results for annealed $UCu_{5-x}Ni_x$ samples. The $UCu_{5-x}Ni_x$ samples were annealed 14 days at 750°C. The $T_{N\acute{e}el}$ values were obtained from specific heat measurements in H = 0 T as exemplified in Fig. D–1. The y_0 values were calculated from Moriya and Takimoto fits shown in Fig. 4–11. The $\lambda_{C/T}$ values were garnered from the fits displayed in Fig. 4–12. The γ values were extrapolated from fifth order polynomial fits of the specific heat over the entire measured temperature range. The Wilson ratios were calculated using $218.7\ \chi(T=0)/\gamma\mu^2_{eff.}$ where $\chi(T=0)$ and $\mu_{eff.}$ are listed in Table 4–6.

x (Ni conc.):	$T_{N\acute{e}el} \pm \sigma_{T_N}$ (K):	y_0:	$\lambda_{C/T}$ in C/T $\sim T^{-1+\lambda_{C/T}}$:	γ (mJ $mole^{-1}$ K^{-2}):	R (Wilson Ratio):
0.6	4.06 ± 0.33				
0.75	1.82 ± 0.03			254	1.4
0.8	1.27 ± 0.06	0.065		273	1.2
0.9	0.426 ± 0.035	0.011	0.628	359	0.92
1.0		0.00013	0.630	318	0.50
1.05			0.739	234	0.45
1.1			0.799	148	0.71
1.2			0.903	96.2	0.85

CHAPTER 5

$UCu_2Si_{2-x}Ge_x$ RESULTS AND DISCUSSION

The $UCu_2Si_{2-x}Ge_x$ samples (x = 0, 0.2, 0.4, 0.6, 1, 1.4, 1.6, 1.8, and 2) were broken in half after arc-melting. One half had its dc magnetic susceptibility measured; several unannealed compounds had their dc electrical resistivity measured. The other half of each sample was annealed for 14 days at 875°C. The length of time and temperature at which annealing occurred gave small mass losses ($< 0.5\,\%$ of the total mass of the sample to be annealed) and the sharpest magnetic transitions (these transitions are discussed below). The sample of UCu_2Ge_2 (made in year 2002, listed in Table 5–4) was only annealed for 10 days at 875°C due to the larger mass loss (1.21% of the total mass of the sample was lost during annealing) observed in the pure Ge compound. Two other samples of UCu_2Ge_2 (made in years 2003 and 2004 that are characterized in Table 5–4) were arc-melted with excess Cu and Ge mass (as discussed in the "Experimental Techniques" chapter) to compensate for the mass loss during annealing and were then annealed for 14 days at 875°C. X-ray diffraction peaks of UCu_2Si_2 and UCu_2SiGe showed single phase samples in the tetragonal $ThCr_2Si_2$ structure. Lattice parameters were not necessary since the interest is in the magnetic properties of the $UCu_2Si_{2-x}Ge_x$ compounds.

The $UCu_2Si_{2-x}Ge_x$ compounds had their dc magnetic susceptibility measured in a 1000 Gauss (G) magnetic field. The dc magnetic susceptibility was measured in a SQUID from 2 K to 300 K with a particular emphasis (enhanced temperature resolution) from 95 K to 115 K, the range over which T_C occurs in $UCu_2Si_{2-x}Ge_x$. In order to eliminate as much as possible effects due to preferred crystalline orientation, each sample was aligned such that the bottom of the sample that touched the copper hearth on the arc-melter after the final arc-melt was parallel to the SQUID's magnetic field. The orientation of all samples was consistent.

The dc magnetic susceptibility versus temperature data were used to determine the T_C value for each compound. T_C was taken to be the inflection point on the $\chi(T)$ curve, i.e., the temperature where $d^2\chi/dT^2 = 0$. Although this method seems arbitrary, previous works have used the same method to determine T_C for UCu_2Si_2 [128, 127]. The computer program MicroCal Origin 5.0 was used to calculate the numerical derivatives. In order to calculate the first derivative, the average of the slopes of two adjacent points for each data point, (T_i, χ_i), is taken using the following generic equation:

$$\frac{d\chi}{dT} = \frac{1}{2}\left(\frac{\chi_{i+1}-\chi_i}{T_{i+1}-T_i} + \frac{\chi_i-\chi_{i-1}}{T_i-T_{i-1}}\right). \tag{5.1}$$

Then, the second derivative is taken by following the same procedure above using first derivative data points. The temperature where $d^2\chi/dT^2 = 0$ is then the T_C value. A graph demonstrating the T_C determination for annealed UCu_2Ge_2 is shown on page 138. The uncertainty in the T_C values is then the temperature interval around T_C for which susceptibility values were taken. In most cases the interval was 0.5 K while some measurements were taken in 0.25 K intervals.

The dc electrical resistivity for each compound was measured for at least one decade of temperature: $1 K \leq T \leq 10 K$. The low-temperature resistivity data were then fit to a three variable power law form: $\rho = \rho_0 + AT^\alpha$. The absolute accuracy of the resistivity is $\sim$ 4% with almost all of the uncertainty stemming from the geometrical factors of the resistivity bars (the uncertainty for the dimensions of the resistivity bar is 0.001 in. while each dimension is on the order of 0.030 in.). However, the temperature precision is good enough (especially for the annealed samples) to determine the resistivity as a function of temperature (i.e., the exponent α mentioned above) quite accurately. An example of the

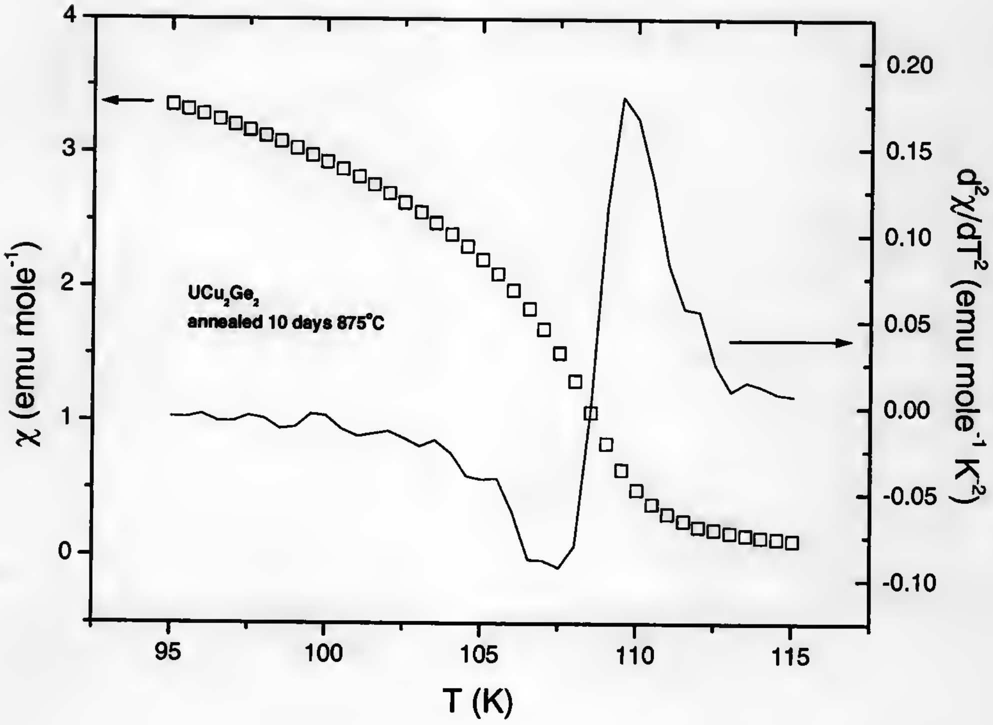

Figure 5–1: T_C determination for annealed UCu_2Ge_2. The hollow squares are the magnetic susceptibility values versus temperature around the ferromagnetic transition of annealed UCu_2Ge_2. The solid line is the numerical second derivative showing that T_C occurs at 108.4 K.

precision is shown for the annealed sample of UCu_2SiGe in Fig. 5–2 on page 140. Finally, resistivity values at room temperature (i.e., ∼ 300 K) were taken for each sample in order to determine the RRR values, $\rho(300\,K)/\rho(0)$.

5.1 $UCu_2Si_{2-x}Ge_x$ Results

The $UCu_2Si_{2-x}Ge_x$ results are shown extensively in four tables at the end of this chapter. The first two tables on pages 153 and 154 concern data for unannealed $UCu_2Si_{2-x}Ge_x$ compounds while the last two tables on pages 155 and 156 show data for $UCu_2Si_{2-x}Ge_x$ compounds annealed 14 days at 875°C (except for one UCu_2Ge_2 sample as indicated).

A few general comments may be made concerning the tables of data. First, if one compares the T_C interval (the temperature range where the numerical second derivative goes from its minimum value to its maximum value as seen in Fig. 5–2) for unannealed samples and then the exact same samples that were annealed for 14 days at 875°C, one sees that generally the T_C interval is narrower for the annealed samples. Therefore, these better ordered samples were used to check the theory of Silva Neto and Castro Neto [137]. The narrower T_C interval justifies the previous statement that annealing does "sharpen" the ferromagnetic transition. Also, particular attention was paid to the actual stoichiometry of the $UCu_2Si_{2-x}Ge_x$ compounds as seen in the tables (using the assumptions for mass losses mentioned in the "Experimental Techniques" chapter). These actual stoichiometries show that minor changes in the stoichiometry for the annealed UCu_2Ge_2 samples (in Table 5–4) have a negligible effect upon the T_C values (taking into consideration the error bars for T_C). The original annealed UCu_2Ge_2 sample (i.e., the one made in year 2002) and the annealed "check" samples (the ones made in years 2003 and 2004) have nearly identical T_C values: 108.4 K (year 2002), 108.9 K (year 2003), and 108.7 K (year 2004). The average of these three annealed UCu_2Ge_2 samples is ∼ 108.7 K. This average is within the experimental

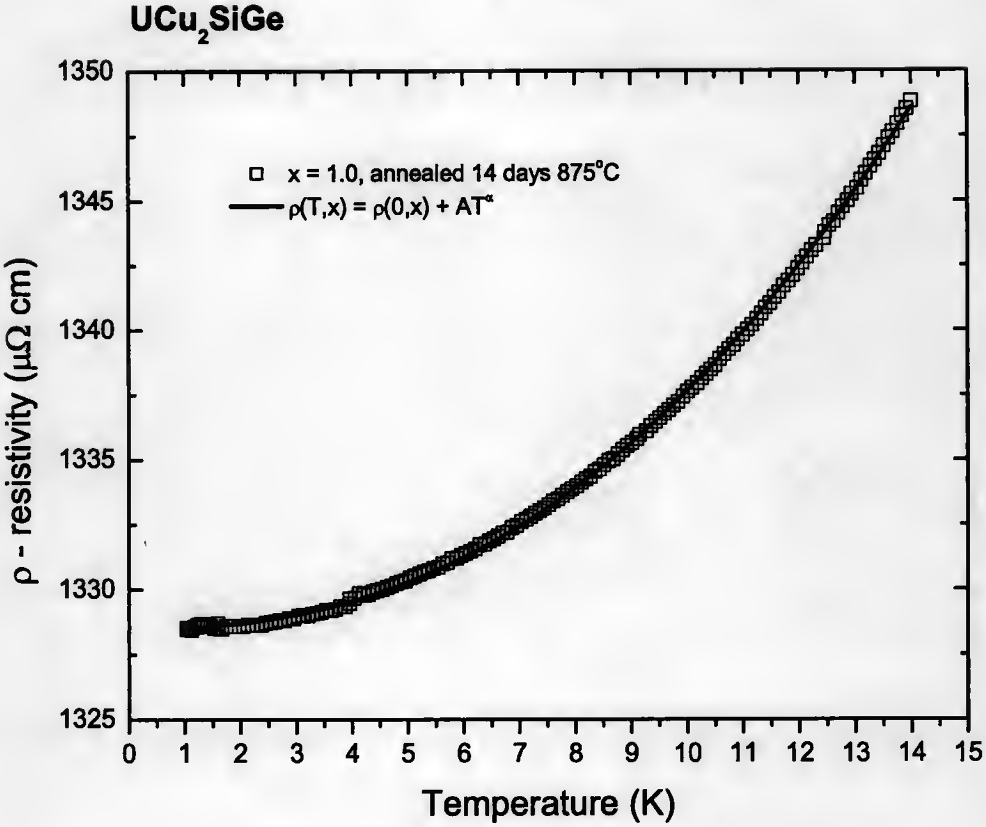

Figure 5–2: Resistivity versus temperature for UCu_2SiGe. UCu_2SiGe was annealed for 14 days at 875°C. The graph shows the good precision at which the resistivity values were obtained. The power law fit in the graph yields $\rho(0, x = 1.0) = 1328\ \mu\Omega$ cm, A $= 0.0426\ \mu\Omega\ \mathrm{K}^{-2.33}$ and $\alpha = 2.33$. Graph is taken from the work of Silva Neto *et al.* [138].

uncertainty of all three annealed UCu_2Ge_2 T_C values. On the opposite side of the $UCu_2Si_{2-x}Ge_x$ phase diagram, the annealed UCu_2Si_2 samples do show some deviations in T_C. The original annealed UCu_2Si_2 sample (year 2002) and the annealed check sample (year 2004) deviate by about 2%: 102.9 K (year 2002) versus 100.7 K (year 2004). In addition, the average of these two annealed UCu_2Si_2 samples (101.8 K) is outside the uncertainty of the two annealed UCu_2Si_2 T_C values. However, the data show that the nonmonotonic behavior in T_C is on the Ge rich side; thus, effects on T_C caused by deviations in stoichiometry are experimentally shown to be moot for this study. In fact, the nonmonotonic behavior area of the annealed $UCu_2Si_{2-x}Ge_x$ phase diagram was completely redone with annealed UCu_2Ge_2, $UCu_2Si_{0.4}Ge_{1.6}$, and $UCu_2Si_{0.6}Ge_{1.4}$ samples made again in the year 2004 as shown in Table 5–4 on page 156. The new UCu_2Ge_2, $UCu_2Si_{0.4}Ge_{1.6}$, and $UCu_2Si_{0.6}Ge_{1.4}$ samples (made in year 2004) are more accurate in their actual concentrations (to the nominal stoichiometry) compared to the original UCu_2Ge_2, $UCu_2Si_{0.4}Ge_{1.6}$, and $UCu_2Si_{0.6}Ge_{1.4}$ samples (made in year 2002). The nominal concentrations UCu_2Ge_2, $UCu_2Si_{0.4}Ge_{1.6}$, and $UCu_2Si_{0.6}Ge_{1.4}$ made in the year 2002 had actual concentrations of $UCu_{1.93}Ge_{1.95}$, $UCu_{1.97}Si_{0.39}Ge_{1.59}$, and $UCu_{1.97}Si_{0.58}Ge_{1.38}$ (using the mass loss assumptions for Cu, Si, and Ge as discussed in the "Experimental Techniques" chapter) compared to the year 2004 actual concentrations of $UCu_{1.96}Ge_{1.96}$, $UCu_{1.98}Si_{0.41}Ge_{1.58}$, and $UCu_{1.99}Si_{0.59}Ge_{1.38}$. The T_C values and their respective error bars in Table 5–4 for the aforementioned year 2002 samples almost exactly match (within their error bars) the T_C values for the more accurate year 2004 samples. Thus, the nonmonotonic behavior in T_C is confirmed.

One point that should be noted concerns the effect annealing has upon the UCu_2Ge_2 samples. The original sample and the check samples undergo almost exactly the same losses of Cu and Ge atoms (based on elemental vapor pressure tables) during annealing: about a 2% decrease in the Cu and Ge concentrations. However, the change with annealing in the ferromagnetic transition temperature is consistently the same for all three UCu_2Ge_2 samples: a 2.5 K rise for the 2002 and 2003 samples (2002 - from 105.9 K for unannealed in Table 5–2 to 108.4 K for annealed in Table 5–4; 2003 - from 106.4 K for unannealed in Table 5–2 to 108.9 K for annealed in Table 5–4) and a 2.6 K rise for the 2004 sample (from 106.1 K for unannealed in Table 5–2 to 108.7 K for annealed in Table 5–4; one sample was made unannealed while the other sample was made for annealing purposes).

A brief scan of the resistivity data in both tables shows that all low temperature resistivity data (except for unannealed $UCu_2Si_{0.4}Ge_{1.6}$) fit a power law form very close to $\rho_0 + AT^2$. Thus, the resistivity data fit a Fermi-liquid form and the T^2 variation was predicted by Kaiser and Doniach [70] for conduction electrons (in this case, Cu electrons) scattering from localized spin fluctuations (i.e., the localized U spins). Also, large residual resistivity (ρ_0) values were obtained for annealed samples where Si/Ge doping was greatest and some of the ρ_0 values are on the order of the Ioffe-Regel values ($\sim$ 200-1000 $\mu\Omega\,$cm), the theoretical limit for metallic conduction [89].

5.2 $UCu_2Si_{2-x}Ge_x$ Discussion

5.2.1 T_C Enhancement

The original annealed $UCu_2Si_{2-x}Ge_x$ samples (made in year 2002) show that T_C as a function of Ge doping, x, is not monotonic. In fact, the x = 1.6 sample has a maximum T_C value of 109.8 K, an increase of 1.29% from the T_C value of the annealed UCu_2Ge_2 sample (108.4 K). This is in agreement with the prediction made by the theory of Silva Neto and Castro Neto that for small enough dissipation, a 1% increase of T_C with respect to the case of no dissipation would result [137]. Now, the phrase "small enough dissipation" may be quantified for the case of $UCu_2Si_{2-x}Ge_x$, a value of x = 1.6 or 20% Si doping on the Ge site.

The phase diagram for the original annealed $UCu_2Si_{2-x}Ge_x$ samples is shown in Fig. 5–3 on page 144. The theoretical line drawn in Fig. 5–3 is from Silva Neto *et al.* that takes into account both spin fluctuations and dissipation introduced by the electronic bath [138]. The continuous line is from the following equation [138, 137]:

$$\frac{1}{\mathrm{g}_0} = \int \frac{\mathrm{d}^3\mathbf{k}}{(2\pi)^3} \int_{-\Omega^0_\mathrm{k}}^{\Omega^0_\mathrm{k}} \frac{\mathrm{d}\omega}{\pi} \frac{\mathrm{k}\gamma_0(\mathrm{k}\ell)\omega \mathrm{n_B}(\omega/\mathrm{T}_C)}{[\mathrm{k}(\mathrm{k}^2 - \mathrm{c}_0\omega)]^2 + [\gamma_0(\mathrm{k}\ell)\,\omega]^2}, \tag{5.2}$$

where $\mathrm{n_B}(\omega/\mathrm{T}_C) = (\mathrm{e}^{\omega/\mathrm{T}_C} - 1)^{-1}$ is the Bose-Einstein distribution function, $\Omega^0_\mathrm{k} = (2\mathrm{k_F})^2\mathrm{k}/\gamma_0(\mathrm{k}\ell)$ is an energy cutoff, $\mathrm{g}_0 = \mathrm{Na}/2\mathcal{J}_\mathrm{H}\mathrm{J}^2$ is the coupling constant, $\mathrm{c}_0 = 1/\mathcal{J}_\mathrm{H}\mathrm{Ja}^2$ is the topological constant, and $\mathcal{J}_\mathrm{H} = \mathcal{J}^2(\mathrm{k_F a})^3/4\pi^2\mathrm{E_F}[1 - \mathrm{a}^3\mathrm{N}(0)\mathrm{U_C}]$. $\mathcal{J}_\mathrm{H}$ plays the role of the effective exchange between the U *f* states and conduction electrons. In the calculation (units were used where $\hbar = \mathrm{k_B} = 1$), further definitions include $\mathrm{N}(0) = \mathrm{m}^*\mathrm{k_F}/\pi^2$, the density of states at the Fermi energy $\mathrm{E_F} = \mathrm{k_F^2}/2\mathrm{m}^*$; $\mathrm{k_F} = (3\pi^2 n)^{1/3}$, the Fermi wave vector; $\mathrm{n} = \mathrm{N_e}/\mathrm{a}^3$, the electronic density per unit cell with lattice spacing a ($\mathrm{a} = \mathrm{a_{Si}}(2 - \mathrm{x})/2 + \mathrm{a_{Ge}}\mathrm{x}/2$ where $\mathrm{a_{Si}} = 5.4$ Å and $\mathrm{a_{Ge}} = 5.527$ Å were chosen so that the volume of the tetragonal unit cell was reproduced [138]); ℓ is the electronic mean free path; $\mathrm{v_F} = \mathrm{k_F}/\mathrm{m}^*$, the Fermi velocity; and the dissipation coefficient, $\gamma_0(\mathrm{k}\ell)$, is from Fulde and Luther [50]:

$$\gamma_0(\mathrm{k}\ell) = \frac{8\mathrm{k_F^2}}{\mathrm{v_F}[1 - \mathrm{a}^3\mathrm{N}(0)\mathrm{U_C}]} \frac{\arctan(\mathrm{k}\ell)}{1 - (\mathrm{k}\ell)^{-1}\arctan \mathrm{k}\ell}. \tag{5.3}$$

The mathematical details of using Eq. 5.2 to create the continuous line in Fig. 5–3 is beyond the scope of this dissertation. However, Fig. 5–3 shows excellent agreement between the theoretical line and the experimental data.

5.2.2 Resistivity displaying electrons in the ballistic or diffusive regime

The data in Fig. 5–3 raises an interesting question. A small amount of Si doping on the Ge site induces nonmonotonic behavior in T_C. Thus, one might ask why a small amount of Ge doping on the Si site does not induce a similar

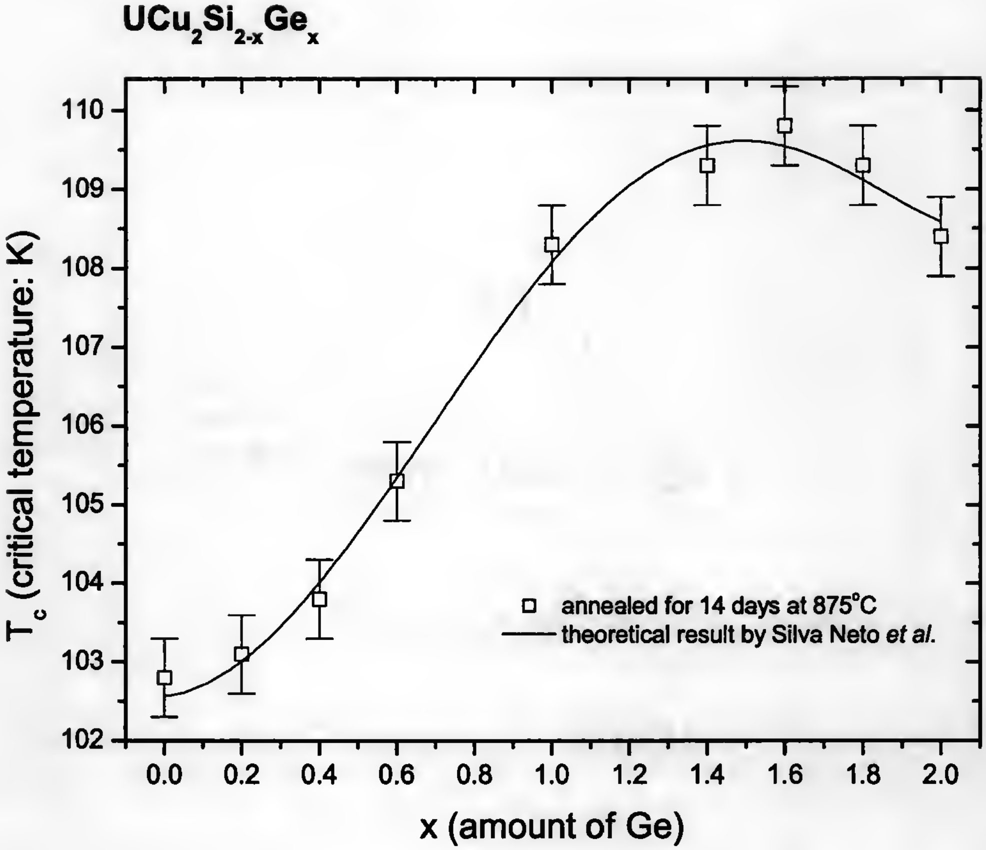

Figure 5–3: T_C phase diagram for $UCu_2Si_{2-x}Ge_x$. The phase diagram plots Curie temperature values (T_C) as a function of Ge doping. The experimental values are the hollow squares while the solid line is from the theoretical efforts of Silva Neto *et al.* as described in the text. This figure was taken from the work of Silva Neto *et al.* [138]. The vertical error bar for each data point is 0.5 K as described in Tables 5–3 and 5–4.

nonmonotonic behavior in T_C? A partial answer is provided with an investigation of the annealed $UCu_2Si_{2-x}Ge_x$ resistivity.

The annealed $UCu_2Si_{2-x}Ge_x$ low temperature resistivity results show a Fermi-liquid form (the temperature dependence for all samples is very close to T^2), implying that the Cu conduction electrons are being scattered by magnetic excitations [70]. If the residual resistivity values for the $UCu_2Si_{2-x}Ge_x$ samples, $\rho(0, x)$, are assumed to take a functional form of a random binary alloy [138], then $\rho(0, x) = \rho_{Si}(2 - x)/2 + \rho_{Ge}x/2 + \overline{\rho}x(2 - x)$ where ρ_{Si} is the ρ_0 value for annealed UCu_2Si_2 (8.44 $\mu\Omega$ cm), ρ_{Ge} is the ρ_0 value for annealed UCu_2Ge_2 (159 $\mu\Omega$ cm), and $\overline{\rho}$ is the contribution from Nordheim's rule [167]. The above functional form for a random binary alloy is expected to be parabolic; however, a brief look at the ρ_0 values for annealed $UCu_2Si_{2-x}Ge_x$ samples in Tables 5–3 and 5–4 reveals a non-parabolic nature. One would expect the largest ρ_0 value to occur where the most disorder was created, i.e., at UCu_2SiGe. Yet the data reveals a local maximum ρ_0 value occurring for $UCu_2Si_{0.4}Ge_{1.6}$, the same compound that also has the maximum T_C value in Fig. 5–3. The reason that the $UCu_2Si_{2-x}Ge_x$ compounds do not obey the random binary alloy form may be attributed to microcracks in the $UCu_2Si_{2-x}Ge_x$ samples due to internal stresses arising from doping [138]. The microcrack effects were cancelled out by dividing the residual resistivity of each sample, $\rho(0, x)$, by the room temperature resistivity of each sample, $\rho(300\,K, x)$. Hence, one obtains the reciprocal of the RRR values listed in Tables 5–3 and 5–4. A plot of RRR^{-1} for annealed $UCu_2Si_{2-x}Ge_x$ compounds and the theoretical function for a random binary alloy are shown in Fig. 5–4. The functional form for a random binary alloy, $\rho_{Si}(2 - x)/2 + \rho_{Ge}x/2 + \overline{\rho}x(2 - x)$, also has to be normalized. $\rho(0\,K)/\rho(300\,K)$ for annealed UCu_2Si_2 is $\sim$ 0.0159 and replaces ρ_{Si} in the previous equation. $\rho(0\,K)/\rho(300\,K)$ for annealed UCu_2Ge_2 is $\sim$ 0.164 and replaces ρ_{Ge} in the above equation. The normalized $\overline{\rho}$ from Nordheim's rule (based upon theory

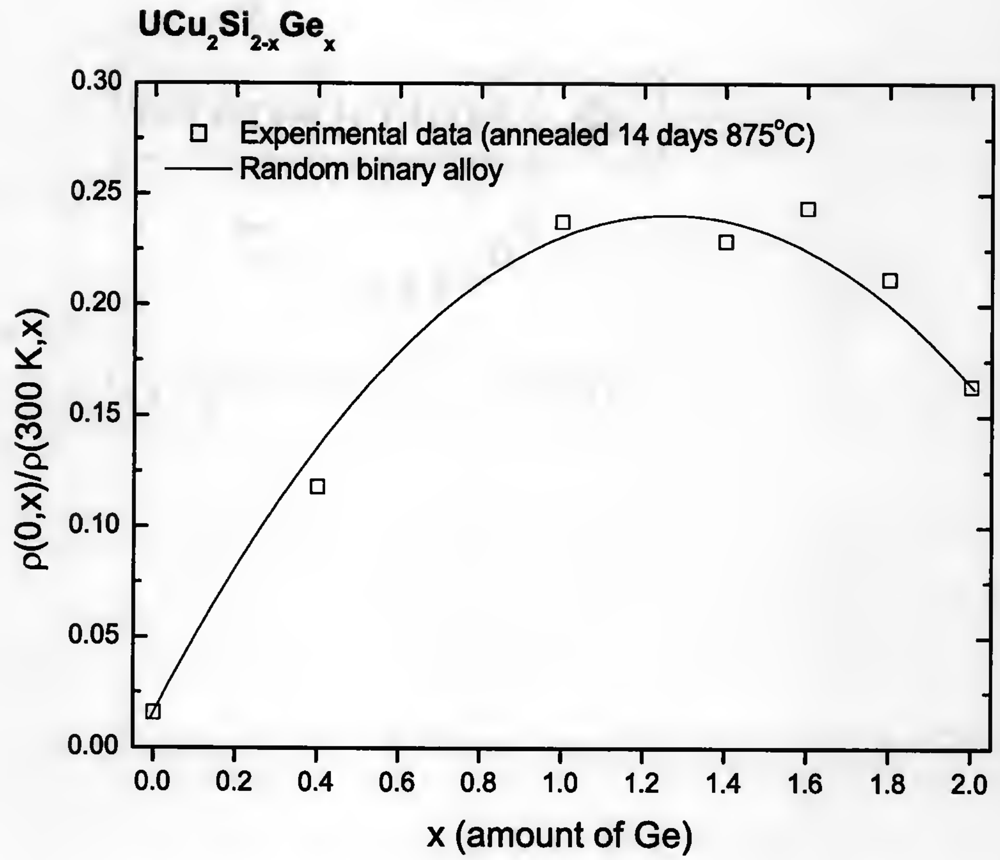

Figure 5–4: The reciprocal RRR values for annealed $UCu_2Si_{2-x}Ge_x$. Hollow squares represent the $UCu_2Si_{2-x}Ge_x$ compounds (made in year 2002). The solid line is a theoretical function for a random binary alloy by Silva Neto *et al.* [138] as described in the text. The absolute accuracy of each normalized residual resistivity value is less than 0.5%.

of transport phenomena in solids [138]) that was used in Fig. 5–4 was ~ 0.141. Figure 5–4 shows the good agreement between the random alloy expression and the experimental data.

Figure 5–4 may also be used to deduce information about the electronic mean free path and the electronic dynamics. The Drude relation is used to relate the resistivity to the mean free path, ℓ: $\rho = m^* \mathrm{v}_F / n e^2 \ell$. Qualitatively looking at the normalized ρ values in Fig. 5–4, one sees that the endpoints of the phase diagram, e.g., UCu_2Si_2, have lower resistivity values, implying that the endpoint compounds have larger mean free paths than the compounds with disorder (i.e., those in the middle of the phase diagram).

One may calculate the mean free path values for the $UCu_2Si_{2-x}Ge_x$ compounds. First, to match the volume of the tetragonal unit cell and to account for the change in the size of the unit cell with Ge doping in $UCu_2Si_{2-x}Ge_x$, one may write a Vegard's law type equation:

$$\mathrm{a} = \mathrm{a}_{Si}(2 - \mathrm{x})/2 + \mathrm{a}_{Ge}\mathrm{x}/2 \tag{5.4}$$

where $\mathrm{a}_{Si} = 5.4\,\text{Å}$ and $\mathrm{a}_{Ge} = 5.527\,\text{Å}$ [138]. The electronic density per unit cell, $\mathrm{N}_e/\mathrm{a}^3$, may now be calculated with the conduction electrons coming from the Cu atoms and $\mathrm{N}_e = 8$ with each Cu^{2+} contributing one electron to the conduction band and there are 8 Cu atoms per unit cell as seen in Fig. 1–2 on page 18. The electronic density, n ~ $5.08 \times 10^{-2}\ \text{Å}^{-3}$, is independent of the Si/Ge concentration in the $UCu_2Si_{2-x}Ge_x$ compounds. Now, the Fermi wave vector, k_F, is ~ $1.15\ \text{Å}^{-1}$ and it is independent of Si/Ge concentration too. k_F is on the same order of magnitude as that for a normal metal. If one takes the residual resistivity value for UCu_2Si_2 ($8.44 \times 10^{-8}\ \Omega$ m from Table 5–3) and uses the previous values in the Drude formula relating the resistivity to the mean free path [$\ell = \hbar \mathrm{k}_F / \rho \mathrm{n} e^2$ (MKS units)], then the mean free path value for annealed UCu_2Si_2 is $\ell \sim 110$ Å and the product, $k_F\ell$, is $\sim$ 127. This is an interesting result because the mean free path for annealed UCu_2Si_2 is on the same order of magnitude as the mean free path of Cu wire at room temperature ($\ell \sim 390$ Å [2]) despite annealed UCu_2Si_2 having a $\rho_0 \sim 1000$ times bigger than for normal metals. However, the mean free path should be scaled down by about a factor of 10. The reason concerns a factor of 10 difference between the (smaller) measured values and the (larger) predicted values (from Drude's formula) for the "drift velocity" in a Cu wire at room temperature [138, 2]. Since the drift velocity is directly proportional to the mean free path, the mean free path is divided by 10 so that the correct current density (= -nev where v is the drift velocity) at room temperature is obtained [2]. Since Cu wire and annealed UCu_2Si_2 have similar transport properties, the mean free path is also scaled down (by a factor of 10) to $\sim$ 10 Å and the product $k_F\ell$ is $\sim$ 10. If one moves across the $UCu_2Si_{2-x}Ge_x$ phase diagram to $UCu_2Si_{0.4}Ge_{1.6}$, then the lattice spacing, a, expands to $\sim$ 5.5016 Å using Eq. 5.4. Hence the electronic density and Fermi wave vector become 4.80×10^{-2} Å^{-3} and 1.12 Å^{-1}, respectively. The residual resistivity for $UCu_2Si_{0.4}Ge_{1.6}$ ($6.90 \times 10^{-6}\,\Omega$ m from Table 5–4) is then used in Drude's formula and the calculated mean free path is $\sim$ 1.39 Å. Instead of scaling down by a factor of 10, $UCu_2Si_{0.4}Ge_{1.6}$ is only scaled down by a factor of 2 since the Si concentration has been reduced by a factor of 5. The corrected mean free path is $\sim$ 0.70 Å and the product, $k_F\ell$, for annealed $UCu_2Si_{0.4}Ge_{1.6}$ is $\sim$ 0.80 [138]. Thus, the mean free path for UCu_2Si_2 is more than an order of magnitude larger than the mean free path for $UCu_2Si_{0.4}Ge_{1.6}$. Figure 5–4 shows that the smallest mean free path (or the largest resistivity by the Drude relation) theoretically occurs at around x = 1.3, very close to x = 1.6, the compound which has the highest T_C value. This implies that the conduction electron dynamics for $UCu_2Si_{0.4}Ge_{1.6}$ are in the diffusive regime (also, the product, $k_F\ell$, being of order one for $UCu_2Si_{0.4}Ge_{1.6}$ signifies that the electrons are in the diffusive regime).

Referring back to Fig. 2–3 on page 45 in the "Theory" chapter, one may assume that the Ge rich end of the $UCu_2Si_{2-x}Ge_x$ phase diagram is in the diffusive regime and $\delta = 2$ (along with $c_0 = 1$) for Fig. 2–3. Thus, Fig. 2–3 in the "Theory" chapter predicts the nonmonotonic behavior in T_C for the Ge rich end of $UCu_2Si_{2-x}Ge_x$ due to the electron dynamics being in the diffusive regime. The normalized Ge rich end resistivity values in Fig. 5–4 justify the placement of the electrons in the diffusive regime since it is known that electrons in the ballistic regime (i.e., on the Si rich side since $k_F\ell \sim 10$ for UCu_2Si_2) have a mean free path (resistivity) larger (smaller) than electrons in the diffusive regime [137].

Figure 2–3 also sheds light on two other important results from the $UCu_2Si_{2-x}Ge_x$ phase diagram on page 144. A small amount of dissipation, indicated by η_0 in Fig. 2–3, is predicted to increase T_C by about 1% [137]. The dissipation is controlled by the disorder (for the Ge rich end of $UCu_2Si_{2-x}Ge_x$, disorder is introduced by Si doping). Thus, 20% Si doping on the Ge site in UCu_2Ge_2 is a small enough amount of dissipation to induce approximately a 1% increase in T_C and create nonmonotonic behavior in T_C for $UCu_2Si_{2-x}Ge_x$ compounds. Also, having taken into consideration Fig. 2–3 from the "Theory" chapter, one may now explain why no nonmonotonic behavior is found on the Si rich side of the $UCu_2Si_{2-x}Ge_x$ phase diagram. In the previous paragraph, it was determined that the UCu_2Si_2's electrons were in the ballistic regime. In fact, from Fig. 5–4 on page 146, one sees that the mean free paths for Si rich end compounds are much larger than the mean free paths for Ge rich end compounds, implying that the Si rich $UCu_2Si_{2-x}Ge_x$ compounds have electrons that are in the ballistic regime. Electrons that are in the ballistic regime are notated with $\delta = 1$ in Fig. 2–3 of the "Theory" chapter and one sees that the theoretical curve gives monotonic behavior for electrons in the ballistic regime, even when a small amount of disorder (i.e., dissipation) is introduced. Correspondingly, the T_C values on the Si rich side of Fig. 5–3 on page 144 increase monotonically as more Ge is doped on the Si sites. This is expected from Fig. 2–3 in the "Theory" chapter since the electrons are in the ballistic regime. Thus, the nonmonotonicity in T_C as a function of Ge doping for $UCu_2Si_{2-x}Ge_x$ is attributed to the conduction electrons' scattering being modified by disorder. In particular, the conduction electron behavior moves from the ballistic regime to the diffusive regime as more Ge replaces Si in $UCu_2Si_{2-x}Ge_x$ compounds.

Since the $UCu_2Si_{2-x}Ge_x$ system proves the theory of Silva Neto and Castro Neto concerning the interplay of disorder and spin fluctuations in a ferromagnetic alloy, are there other ferromagnetic alloys that could give credence to this theory or is $UCu_2Si_{2-x}Ge_x$ just a sport? One work that provides a summary of some ferromagnetic materials is by DeLong *et al.* [37]. Two ferromagnetic samples from that work, UIrAl ($T_C \sim 64$ K) and UPtAl ($T_C \sim 52$ K), were made as endpoints of a phase diagram and disorder was created on the Ir/Pt sites. Preliminary results show that the T_C values are nonmonotonic for unannealed $UIr_{1-x}Pt_xAl$ in Fig. 5–5 on page 152. However, the $UIr_{1-x}Pt_xAl$ system may not be applicable to the theory of Silva Neto and Castro Neto. One reason concerns the structure of UPtAl and UIrAl. Both compounds belong to the hexagonal ZrNiAl-type crystal structure [6]. The hexagonal crystal structure is composed of alternating two types of basal-plane atomic layers along the c-axis. One plane is composed of all U atoms and 1/3 of the Pt/Ir atoms while the other plane contains the rest of the Pt/Ir atoms with all of the Al atoms [6]. The concern is disorder affecting the magnetic sublattice since there is hybridization of 5f states (from the U atoms) with valence electron states of ligands (from the Pt/Ir atoms). Thus, disorder affecting the conduction electrons may not be the only mechanism having a role upon the magnetism in the $UIr_{1-x}Pt_xAl$ system. Obviously, further measurements need to be performed, namely, low temperature resistivity measurements to investigate whether or not electronic dynamics in the $UIr_{1-x}Pt_xAl$ compounds are in the ballistic or diffusive regime. Finally, if the dissipation theory of Silva Neto and Castro Neto does not accurately describe the nonmonotonic behavior in the $UIr_{1-x}Pt_xAl$ system, then other compounds mentioned by De Long *et al.* may be good candidates since the magnetic sublattice would not be directly affected as it might be in $UIr_{1-x}Pt_xAl$. Other possible compounds would include $UCoGa_{1-x}Sn_x$ (the endpoints have a T_C range from 51 K to 88 K), $UPtAl_{1-x}Ga_x$ (52 K - 79 K), $UPtGa_{1-x}Sn_x$ (79 K - 30 K), $UIrGa_{1-x}Sn_x$ (63 K - 33 K), and $URhAl_{1-x}Ga_x$ (28 K - 44 K) [37]. All of these compounds form in the hexagonal ZrNiAl structure; however, the disorder in the aforementioned compounds should occur only on the basal planes without the U magnetic moments [6] just as the disorder did not affect the magnetic sublattice in the $UCu_2Si_{2-x}Ge_x$ compounds.

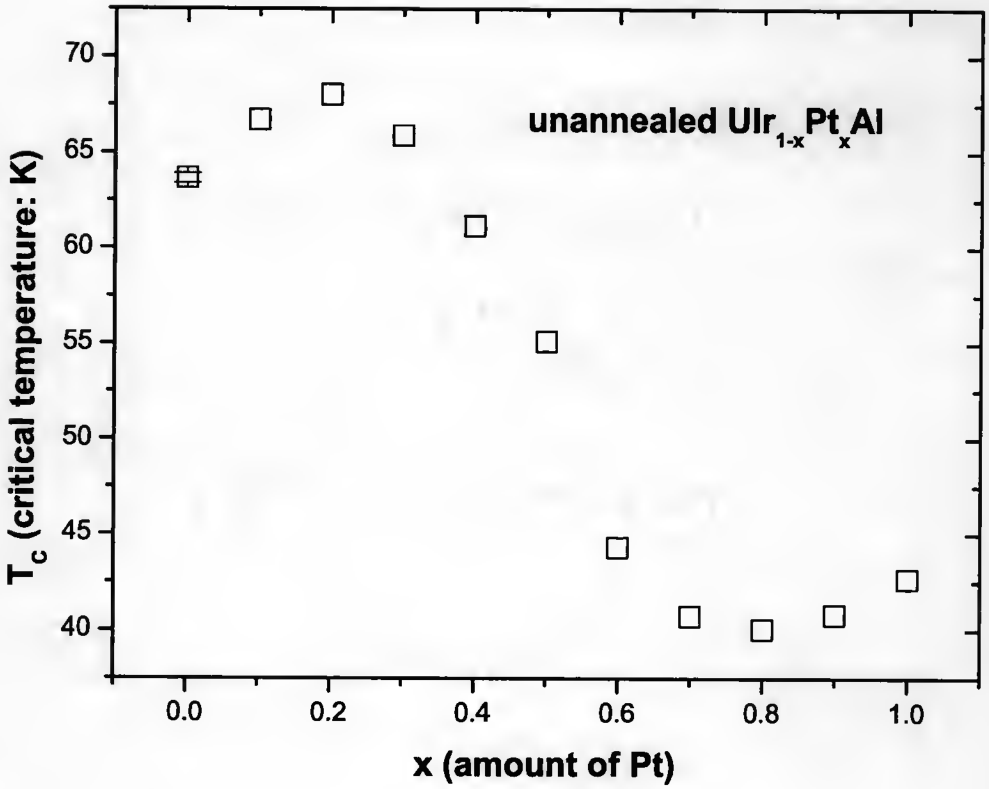

Figure 5–5: Phase diagram for unannealed $\mathrm{UIr}_{1-x}\mathrm{Pt}_x\mathrm{Al}$ system. The hollow squares represent the T_C values versus Pt doping for unannealed $\mathrm{UIr}_{1-x}\mathrm{Pt}_x\mathrm{Al}$ compounds. The unannealed samples show nonmonotonic behavior in T_C at the Ir rich end and the Pt rich end of the phase diagram. The vertical error bars for each sample are 0.25 K as shown on the UIrAl T_C data point.

Table 5–1: Magnetic susceptibility and resistivity results for unannealed $UCu_2Si_{2-x}Ge_x$ samples (I). The T_C values were obtained from magnetic susceptibility results. The T_C interval was arbitrarily defined as the temperature range where the numerical second derivative went from its minimum value to its maximum while passing through zero (i.e., the T_C value). The resistivity data were fit to a power law form, $\rho_0 + AT^{\alpha}$, that minimized chi squared.

Nominal Stoichiometry (prod. date):	Actual Stoichiometry:	$T_C(K) \pm \sigma_{T_C}(K)$:	T_C Interval (K):	RRR:	ρ_0 $(\mu\Omega\,cm)$:	A $(\mu\Omega\,cm\,K^{-\alpha})$:	α:	T Range (K):
UCu_2Si_2 (10-23-02)	$UCu_{1.97}Si_{1.99}$	102.3 ± 0.5	4.00	21	17.4	0.00438	2.31	1.12-12.1
UCu_2Si_2 (10-10-02)	$UCu_{1.99}Si_{1.98}$	102.4 ± 0.25	3.49					
UCu_2Si_2 (10-8-04)	$UCu_{2.00}Si_{1.99}$	100.9 ± 0.25	1.99					
$UCu_2Si_{1.8}Ge_{0.2}$ (10-17-02)	$UCu_{1.98}Si_{1.76}Ge_{0.17}$	102.9 ± 0.5	3.97					
$UCu_2Si_{1.6}Ge_{0.4}$ (11-18-02)	$UCu_{1.98}Si_{1.60}Ge_{0.38}$	103.9 ± 0.5	3.00	4.91	249	0.0118	2.43	1.05-12.0
$UCu_2Si_{1.4}Ge_{0.6}$ (11-21-02)	$UCu_{1.98}Si_{1.37}Ge_{0.58}$	105.3 ± 0.5	2.50					
UCu_2SiGe (11-25-02)	$UCu_{1.99}Si_{1.00}Ge_{1.00}$	107.9 ± 0.5	2.49	4.54	136	0.0218	1.76	1.05-13.0
$UCu_2Si_{0.6}Ge_{1.4}$ (12-3-02)	$UCu_{1.99}Si_{0.58}Ge_{1.41}$	108.3 ± 0.5	2.01					

Table 5–2: Magnetic susceptibility and resistivity results for unannealed $UCu_2Si_{2-x}Ge_x$ samples (II). The T_C values were obtained from magnetic susceptibility results. The T_C interval was arbitrarily defined as the temperature range where the numerical second derivative went from its minimum value to its maximum while passing through zero (i.e., the T_C value). The resistivity data were fit to a power law form, $\rho_0 + AT^{\alpha}$, that minimized chi squared.

Nominal Stoichiometry (prod. date):	Actual Stoichiometry:	$T_C(K) \pm \sigma_{T_C}(K)$:	T_C Interval (K):	RRR:	ρ_0 ($\mu\Omega\,cm$):	A ($\mu\Omega\,cm\,K^{-\alpha}$):	α:	T Range (K):
$UCu_2Si_{0.6}Ge_{1.4}$ (9-21-04)	$UCu_{2.00}Si_{0.59}Ge_{1.39}$	108.1 ± 0.25	1.00					
$UCu_2Si_{0.4}Ge_{1.6}$ (12-5-02)	$UCu_{1.99}Si_{0.39}Ge_{1.61}$	107.9 ± 0.5	2.50	3.65	107	0.389	0.835	1.21-10.3
$UCu_2Si_{0.4}Ge_{1.6}$ (9-22-04)	$UCu_{2.00}Si_{0.39}Ge_{1.60}$	108.2 ± 0.25	1.74					
$UCu_2Si_{0.2}Ge_{1.8}$ (11-1-02)	$UCu_{1.99}Si_{0.18}Ge_{1.81}$	107.3 ± 0.5	2.50					
UCu_2Ge_2 (11-8-02)	$UCu_{1.98}Ge_{1.99}$	105.9 ± 0.5	4.49	4.13	75.8	0.00861	1.76	1.10-10.0
UCu_2Ge_2 (1-9-03)	$UCu_{1.99}Ge_{2.00}$	106.4 ± 0.5	4.01					
UCu_2Ge_2 (9-3-04)	$UCu_{1.99}Ge_{2.00}$	106.1 ± 0.25	2.24					

Table 5–3: Magnetic susceptibility and resistivity results for annealed $UCu_2Si_{2-x}Ge_x$ samples (I). All $UCu_2Si_{2-x}Ge_x$ samples were annealed for 14 days at 875°C. The T_C interval was arbitrarily defined as the temperature range where the numerical derivative went from its minimum value to its maximum value while passing through T_C. The resistivity data were fit to a form of $\rho_0 + AT^{\alpha}$.

Nominal Stoichiometry (prod. date):	Actual Stoichiometry:	$T_C(K) \pm \sigma_{T_C}(K)$:	T_C Interval (K):	RRR:	ρ_0 ($\mu\Omega\, cm$):	A ($\mu\Omega\, cm\, K^{-\alpha}$):	α:	T Range (K):
UCu_2Si_2 (10-23-02)	$UCu_{1.95}Si_{1.99}$	102.9 ± 0.5	3.49	63	8.44	0.00189	2.57	1.06-12.0
UCu_2Si_2 (10-7-04)	$UCu_{1.99}Si_{1.99}$	100.7 ± 0.25	1.01					
$UCu_2Si_{1.8}Ge_{0.2}$ (10-17-02)	$UCu_{1.97}Si_{1.76}Ge_{0.16}$	103.1 ± 0.5	3.48					
$UCu_2Si_{1.6}Ge_{0.4}$ (11-18-02)	$UCu_{1.97}Si_{1.60}Ge_{0.37}$	103.8 ± 0.5	3.50	8.47	132	0.00984	2.38	1.09-12.1
$UCu_2Si_{1.4}Ge_{0.6}$ (11-21-02)	$UCu_{1.97}Si_{1.37}Ge_{0.57}$	105.3 ± 0.5	2.52					
UCu_2SiGe (11-25-02)	$UCu_{1.98}Si_{1.00}Ge_{0.99}$	108.3 ± 0.5	2.00	4.21	1330	0.0426	2.33	1.03-14.0
$UCu_2Si_{0.6}Ge_{1.4}$ (12-3-02)	$UCu_{1.97}Si_{0.58}Ge_{1.38}$	109.3 ± 0.5	2.01	4.37	352	0.0341	2.12	1.04-13.0

Table 5–4: Magnetic susceptibility and resistivity results for annealed $UCu_2Si_{2-x}Ge_x$ samples (II). All $UCu_2Si_{2-x}Ge_x$ samples were annealed for 14 days at 875°C except for one UCu_2Ge_2 sample (annealed only for 10 days due to a large mass loss during annealing-1.21% of the total mass) as indicated by a *. The T_C interval was arbitrarily defined as the temperature range where the numerical derivative went from its minimum value to its maximum value while passing through T_C. The resistivity data were fit to a form of $\rho_0 + AT^{\alpha}$.

Nominal Stoichiometry (prod. date):	Actual Stoichiometry:	$T_C(K) \pm \sigma_{T_C}(K)$:	T_C Interval (K):	RRR:	ρ_0 ($\mu\Omega\, cm$):	A ($\mu\Omega\, cm\, K^{-\alpha}$):	α:	T Range (K):
$UCu_2Si_{0.6}Ge_{1.4}$ (11-9-04)	$UCu_{1.99}Si_{0.59}Ge_{1.38}$	109.4 ± 0.25	0.75					
$UCu_2Si_{0.4}Ge_{1.6}$ (12-5-02)	$UCu_{1.97}Si_{0.39}Ge_{1.59}$	109.8 ± 0.5	2.00	4.10	690	0.0120	2.63	1.26-11.0
$UCu_2Si_{0.4}Ge_{1.6}$ (11-10-04)	$UCu_{1.98}Si_{0.41}Ge_{1.58}$	109.7 ± 0.25	0.74					
$UCu_2Si_{0.2}Ge_{1.8}$ (11-1-02)	$UCu_{1.98}Si_{0.18}Ge_{1.80}$	109.3 ± 0.5	1.90	4.72	391	0.0125	2.44	1.13-13.0
*UCu_2Ge_2 (11-8-02)	$UCu_{1.93}Ge_{1.95}$	108.4 ± 0.5	2.01	6.11	159	0.0216	2.16	1.22-10.0
UCu_2Ge_2 (1-9-03)	$UCu_{1.95}Ge_{1.96}$	108.9 ± 0.25	1.24					
UCu_2Ge_2 (10-6-04)	$UCu_{1.96}Ge_{1.96}$	108.7 ± 0.25	1.00					

CHAPTER 6
CONCLUSIONS AND FUTURE WORK

6.1 $UCu_{5-x}Ni_x$ Conclusions

The disorder created in the $UCu_{5-x}Ni_x$ system by the substitution of Ni atoms for ligand Cu atoms suppresses the antiferromagnetism in UCu_5 and creates NFL behavior. The lattice parameters for unannealed and annealed (14 days at 750°C) $UCu_{5-x}Ni_x$ show no possibility of partial sublattice ordering as has been debated in the $UCu_{5-x}Pd_x$ system. The smaller Ni atoms (compared to the Cu atoms) are distributed equally ($\sim$ 25%) on the 4 smaller Be sites in the $AuBe_5$ crystal structure as compared to less than 5% of the Pd atoms occupying each smaller Be site in $AuBe_5$. This lack of sublattice ordering meant that distinctions between quantum criticality and disorder could be made.

The specific heat for $UCu_{5-x}Ni_x$ showed that annealed (14 days at 750°C) UCu_4Ni exhibited NFL behavior down to the lowest temperature of measurement and the NFL behavior was due to quantum critical point spin fluctuations. The quantum critical point, $T_N \rightarrow 0$, was demonstrated by the UCu_4Ni specific heat data showing no antiferromagnetic transition down to its lowest measured temperature ($\sim$ 0.060 K) as occurred in annealed $UCu_{4.1}Ni_{0.9}$ ($T_N \sim 0.4$ K). Also, fitting of the C/T $UCu_{5-x}Ni_x$ data to the spin fluctuation theory of Moriya and Takimoto predicts a quantum critical point, $y_0 \rightarrow 0$, in agreement with the UCu_4Ni data. A third justification of quantum criticality occurring at UCu_4Ni concerns the Wilson ratio that was qualitatively consistent with UCu_4Ni crossing over from magnetic to nonmagnetic. Small variations in the Ni concentration around UCu_4Ni were performed in order to investigate the roles of quantum criticality and disorder in $UCu_{5-x}Ni_x$.

The Griffiths phase disorder model was used to examine the NFL behavior in $UCu_{5-x}Ni_x$. The Griffiths phase disorder model is a combination of the quantum critical point phenomena with disorder. The Griffiths phase is brought about by rare strongly coupled magnetic spin clusters close to a quantum critical point. The closeness for $UCu_{5-x}Ni_x$ is a 5% increase of the Ni concentration from the quantum critical concentration of UCu_4Ni. The Griffiths phase for $UCu_{3.95}Ni_{1.05}$ was characterized by power law behavior for dc magnetic susceptibility and specific heat (i.e., $\chi \sim T^{-1+\lambda_\chi}$; $C/T \sim T^{-1+\lambda_{C/T}}$). According to the specific heat the Griffiths phase existed for $UCu_{3.95}Ni_{1.05}$ (down to ~ 0.060 K) and $UCu_{3.9}Ni_{1.1}$ (down to ~ 0.3 K); $UCu_{3.8}Ni_{1.2}$ began to deviate from the Griffiths phase behavior at ~ 0.5 K, signifying that $UCu_{3.8}Ni_{1.2}$ was too far from the spin fluctuations of the quantum critical point.

The specific heat of $UCu_{5-x}Ni_x$ samples around the quantum critical concentration of UCu_4Ni was measured in various magnetic fields. The Griffiths phase disorder model predicts that the Griffiths phase disappears above a certain crossover magnetic field (determined from magnetization versus field data where the magnetization crosses over from linear behavior to power law behavior). The Griffiths phase disorder model predicts a magnetic field induced peak above the crossover field for the specific heat. $UCu_{4.1}Ni_{0.9}$ does not show a field induced peak above its determined crossover field and this lack of a peak (at 3 T) might have a correlation with the antiferromagnetism still present in $UCu_{4.1}Ni_{0.9}$. UCu_4Ni also does not show a field induced peak above its crossover magnetic field and this may be related to the quantum critical spin fluctuations present in UCu_4Ni. $UCu_{3.95}Ni_{1.05}$ does show Griffiths phase (in zero field specific heat data) and a field induced peak above its crossover magnetic field at 3 T. However, the quantitative fit of the Griffiths phase disorder model does not match the $UCu_{3.95}Ni_{1.05}$ data at 3 T or 6 T. $UCu_{3.9}Ni_{1.1}$ is the only concentration where the Griffiths phase disorder model matches the specific heat data above the determined crossover magnetic field (i.e., at 6 T) and over the entire measured temperature range. The Griffiths phase disorder model matches the $UCu_{3.8}Ni_{1.2}$ 6 T specific heat data above the determined crossover magnetic field, yet the temperature range is limited compared to the $UCu_{3.9}Ni_{1.1}$ fit.

Finally, the dc magnetic susceptibility was measured in higher magnetic fields to provide further insight into the behavior of the Griffiths phase. The dc magnetic susceptibility at higher magnetic fields for $UCu_{5-x}Ni_x$ just added to the inconsistencies of the Griffiths phase disorder model, especially when compared to specific heat data measured at the same magnetic field. For example, the magnetic susceptibility at 2 T for UCu_4Ni showed power law behavior over more than a decade of temperature, implying possible Griffiths phase behavior. However, specific heat data at 2 T do not show power law behavior (predicted by the Griffiths phase disorder model) and it has been already established by the zero field specific heat data that quantum critical fluctuations, not magnetic spin cluster fluctuations, were the phenomena occurring in UCu_4Ni. This type of inconsistency was found at some magnetic field for every Ni concentration around the quantum critical concentration of x = 1.0. Thus, a theoretical model more complex than the Griffiths phase disorder model may be needed to explain all characteristics of the $UCu_{5-x}Ni_x$ data.

6.2 Future Work Derived from $UCu_{5-x}Ni_x$ Results

The future work on $UCu_{5-x}Ni_x$ will be divided into two parts. The first part involves measurements directly upon the $UCu_{5-x}Ni_x$ system while the second part involves other projects related to the $UCu_{5-x}Ni_x$ system.

The most obvious future work on the $UCu_{5-x}Ni_x$ system would involve measuring the specific heat and magnetic susceptibility for the concentrations around x = 1.0 down to dilution refrigerator temperatures in zero field (or a low field for susceptibility) and 0.5 T field intervals up to ~ 6 T. One might be able to say then where the NFL behavior in $UCu_{3.9}Ni_{1.1}$ is attributable to Griffiths phase and where the theory explaining the NFL behavior in $UCu_{3.9}Ni_{1.1}$ should be developed more by possibly combining different components of the Kondo disorder model, self-consistent renormalization model, and quantum Griffiths phase together. Also, one could determine a little more accurately which Ni concentrations had their NFL behavior described sufficiently by Griffiths phase behavior. Those Ni concentrations described by Griffiths phase would have a little smaller range for where the crossover magnetic field occurs due to the onset of a field induced peak, signifying that the splitting between energy levels is too large such that tunneling ceases. Additional insight could be gained about Griffiths phase behavior ending with $UCu_{3.8}Ni_{1.2}$ being too far from the quantum critical point and its spin fluctuations.

Further measurements upon the $UCu_{5-x}Ni_x$ samples would be performed to investigate the amount of disorder in the $UCu_{5-x}Ni_x$ system. For example, EXAFS measurements should be carried out on UCu_4Ni to determine how much Ni is on the larger Be site and the smaller Be sites in the $AuBe_5$ structure just as was done on unannealed and annealed UCu_4Pd [15, 16]. It would also be interesting to perform μSR and NMR studies upon UCu_4Ni so that further insight might be gained into the disorder in the $UCu_{5-x}Ni_x$ system.

A further extension of this dissertation would concern more doping of the ligand Cu atoms with Ni to search for the onset of spin-glass behavior. Work by Chau and Maple along with work by Koerner *et al.* determined that spin glass behavior began above $UCu_{3.5}Pd_{1.5}$ [26, 77]. One might expect spin glass behavior to begin above $UCu_{3.5}Ni_{1.5}$ in light of the fact that antiferromagnetism is suppressed for annealed UCu_4Pd [160] and annealed UCu_4Ni.

The second part of this future work's section concerns new projects that are offshoots of the $UCu_{5-x}Ni_x$ system just as $UCu_{5-x}Ni_x$ was an offshoot of $UCu_{5-x}Pd_x$. Other transition metals have been tried as dopants for UCu_5. Chau and Maple suppressed antiferromagnetism in $UCu_{5-x}Pt_x$ and found NFL behavior while the doping of Cu using Ag or Au did not result in the suppression of magnetic ordering or NFL behavior [26]. For this dissertation, two other elements on the same row of the periodic table as Ni were attempted: Fe and Co. UCu_4Fe had its magnetic susceptibility measured and the susceptibility values were on the order of hundreds of memu/mole (as compared to $UCu_{5-x}Ni_x$ being on the order of just memu/mole) and did not show NFL behavior. The $UCu_{5-x}Co_x$ system had magnetic susceptibility values that were on the order of memu/mole as shown in Fig. 6–1 on page 162. Figure 6–1 also shows that the variation in Co concentrations ($0.75 \leq x \leq 1.5$) does not suppress the antiferromagnetic transition temperature, T_N, or show NFL behavior at low temperatures. A couple of explanations may exist for the lack of suppression in $UCu_{5-x}Co_x$. First, when the Cu is doped with Co, the hybridization may move the $4s^1$ valence electron from the Cu atom [7] and combine it with the $3d^7 4s^2$ valence electrons from the Co atom [7] and create a filled $3d^{10}$ valence shell. Chau and Maple have suggested that a completely filled d-electron shell may be the reason why $UCu_{5-x}Ag_x$ or $UCu_{5-x}Au_x$ does not show NFL behavior. Second, the ligand atoms used in $UCu_{5-x}Ni_x$, $UCu_{5-x}Pd_x$, and $UCu_{5-x}Pt_x$ are involved in hybridization effects with the U $5f$ electrons [117] that lead to the good possibility of an intermediate electronic configuration of the uranium ions (U^{3+} and U^{4+} as discussed previously). Schneider *et al.* have done photoemission work and concluded that there was no evidence for two different final-state $5f$ multiplets in the valence-band spectrum of UCu_5 [133]. Thus, hybridization between the U, Cu, and Co/Fe atoms could result in an integral valency

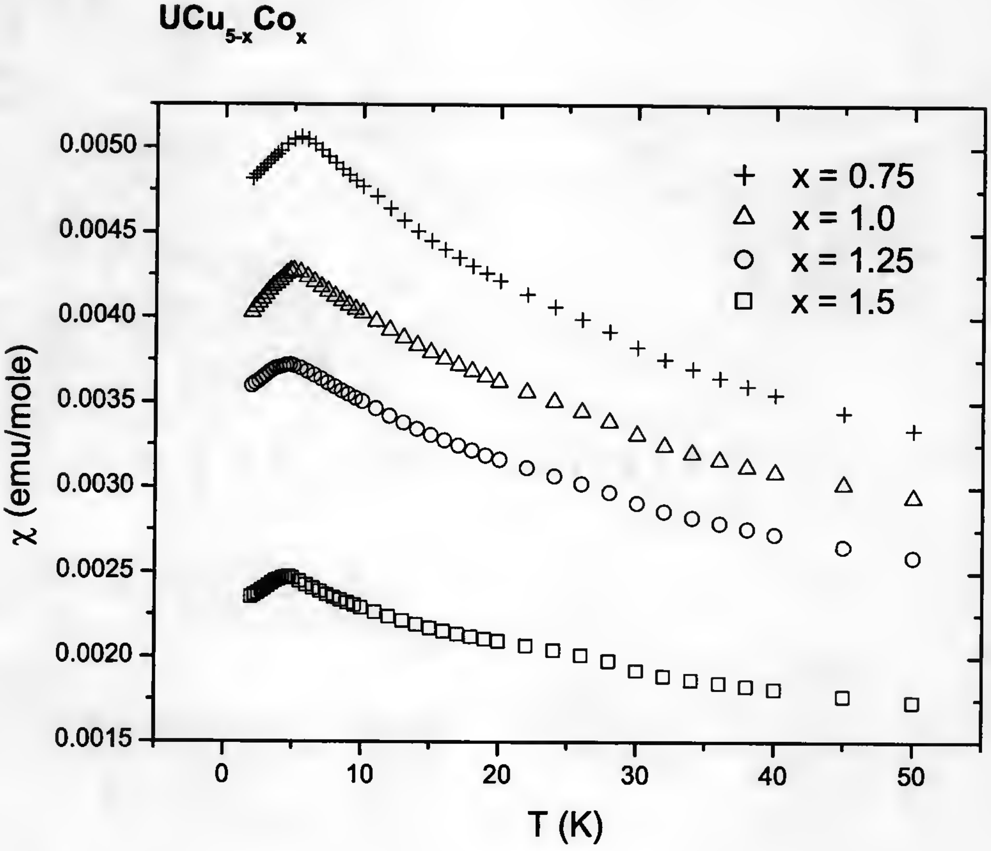

Figure 6–1: DC magnetic susceptibility results for $UCu_{5-x}Co_x$. The low temperature dc magnetic susceptibility for $UCu_{5-x}Co_x$ samples was measured in a 1 kG magnetic field. The antiferromagnetic transition temperature, T_N, is not suppressed with the change in Co concentration. The T_N values are the maximum χ values in the graph: T_N = 5.50 K for $UCu_{4.25}Co_{0.75}$; T_N = 5.00 K for UCu_4Co; T_N = 4.75 K for $UCu_{3.75}Co_{1.25}$; and T_N = 4.75 K for $UCu_{3.5}Co_{1.5}$.

of the uranium ions. This integral valency could be the reason for the persistent ordering temperature in samples like $UCu_{5-x}Co_x$ and UCu_4Fe.

A couple of systems involving exploratory synthesis to investigate possible NFL behavior are $UCu_{5-x}Rh_x$, $UCu_{5-x}Mn_x$ and $UCu_{5-x}Cr_x$. One possible negative to $UCu_{5-x}Rh_x$ and $UCu_{5-x}Ir_x$ is that hybridization could create a completely filled *d* shell using the $4s^1$ valence electron of Cu and the valence electrons of Rh and Ir. The possible full *d*-electron shell could hinder NFL behavior according to Chau and Maple [26]. A similar type of argument might be made for $UCu_{5-x}Cr_x$ since the $4s^1$ valence electrons of Cr and Cu could combine to create a stable configuration with the $3d^5$ and $3d^{10}$ valence electrons of Cr and Cu respectively. If the Cu in UCu_5 were doped with Mn, a partially filled *d* shell would probably occur as happened in $UCu_{5-x}Ni_x$, $UCu_{5-x}Pd_x$, and $UCu_{5-x}Pt_x$. The only concern (although this should not inhibit one from synthesizing a few samples) about doping Cu with Mn is that hybridization between the U, Cu, and Mn atoms could lead to an integral valency in uranium as was discussed at the end of the previous paragraph. Thus, the possibility of $UCu_{5-x}Mn_x$ not showing NFL behavior could occur as happened with $UCu_{5-x}Co_x$ and UCu_4Fe.

6.3 $UCu_2Si_{2-x}Ge_x$ Conclusions

The disorder created in the $UCu_2Si_{2-x}Ge_x$ system by doping the Si atoms with Ge atoms does create nonmonotonic behavior in T_C on the Ge rich side of the phase diagram with a maximum T_C value occurring for $UCu_2Si_{0.4}Ge_{1.6}$ as seen in Fig. 5–3. The T_C behavior of the $UCu_2Si_{2-x}Ge_x$ system is directly attributable to the Si/Ge disorder since the magnetic sublattice of the $UCu_2Si_{2-x}Ge_x$ system is not affected by the Si/Ge substitution and minor stoichiometric differences in the Cu, Si, and Ge do not vary the T_C values. The Si/Ge disorder brings about dissipation as electrons scatter from localized moments. The dissipation combined with the thermal and quantum fluctuations is responsible for the nonmonotonic behavior in T_C.

The reason for nonmonotonic behavior occurring on the Ge rich side of $UCu_2Si_{2-x}Ge_x$ and not the Si rich side is due to the source of dissipation. The dissipation on the Ge rich side is due to diffusive electrons which are predicted by Silva Neto and Castro Neto [137] to increase T_C by $\sim 1\%$ compared to the ferromagnetic case without dissipation (i.e., UCu_2Ge_2). The dissipation on the Si rich side is brought about by ballistic electrons. The dissipation by ballistic electrons when combined with quantum and thermal fluctuations is not predicted to enact nonmonotonic behavior on T_C as confirmed by the Si rich side of $UCu_2Si_{2-x}Ge_x$.

The distinction between diffusive and ballistic electrons is made by the normalized residual resistivity values. The ballistic electrons have a much larger mean free path than the diffusive electrons which experimentally means that the resistivity values in the ballistic regime should be much smaller than the resistivity values in the diffusive regime. The normalized residual resistivity values are about a factor of 10 larger for $UCu_2Si_{0.6}Ge_{1.4}$ and $UCu_2Si_{0.4}Ge_{1.6}$ (i.e., the diffusive regime) compared to UCu_2Si_2 (i.e., the ballistic regime). The occurrence of the diffusive regime in $UCu_2Si_{0.6}Ge_{1.4}$ and $UCu_2Si_{0.4}Ge_{1.6}$ is also the place in the $UCu_2Si_{2-x}Ge_x$ phase diagram where nonmonotonic behavior in T_C occurs (i.e., $\sim 1\%$ increase in the T_C value of $UCu_2Si_{0.4}Ge_{1.6}$ as compared to the T_C value of UCu_2Ge_2).

6.4 $UCu_2Si_{2-x}Ge_x$ Future Work

Some of the future work pertaining to $UCu_2Si_{2-x}Ge_x$ has already been addressed in the "$UCu_2Si_{2-x}Ge_x$ Results and Discussion" chapter. The primary focus of any future work would be to try and find possible ternary (and maybe binary) systems that display nonmonotonic behavior with T_C increasing compared to a non-disordered ferromagnet. Creating disorder in a ferromagnetic system is not difficult to achieve; however, creating structural disorder so that it is the only different physical mechanism is difficult since structural disorder usually affects the magnetic sublattice in a system such as $U(Ni_{1-x}Cu_x)_2Si_2$ [81]. The $UIr_{1-x}Pt_xAl$ system in Fig. 5–5 of the "$UCu_2Si_{2-x}Ge_x$ Results and Discussion" chapter shows nonmonotonic behavior in T_C as a function of Pt concentration. The future work for $UIr_{1-x}Pt_xAl$ concerns measuring the resistivity to see if the electronic behavior may be separated into a diffusive and ballistic regime as occurred for $UCu_2Si_{2-x}Ge_x$.

Other ferromagnetic systems that could be candidates for nonmonotonic behavior in T_C are listed in the work of De Long *et al.* [37]. Possible systems that could be synthesized to measure their T_C values for nonmonotonic behavior are $URhGa_{1-x}Sn_x$, $URhGa_{1-x}Al_x$, $UIrAl_{1-x}Sn_x$, $UIrGa_{1-x}Sn_x$, $UCoGa_{1-x}Sn_x$, and $UPtGa_{1-x}Sn_x$. The endpoint compounds for all the systems listed previously crystallize in the hexagonal ZrNiAl structure. The structural disorder would be created on the basal plane (of the ZrNiAl structure) not containing the U atoms; thus, the structural disorder should not affect the magnetic sublattice.

APPENDIX A
LATTICE PARAMETER GRAPHS

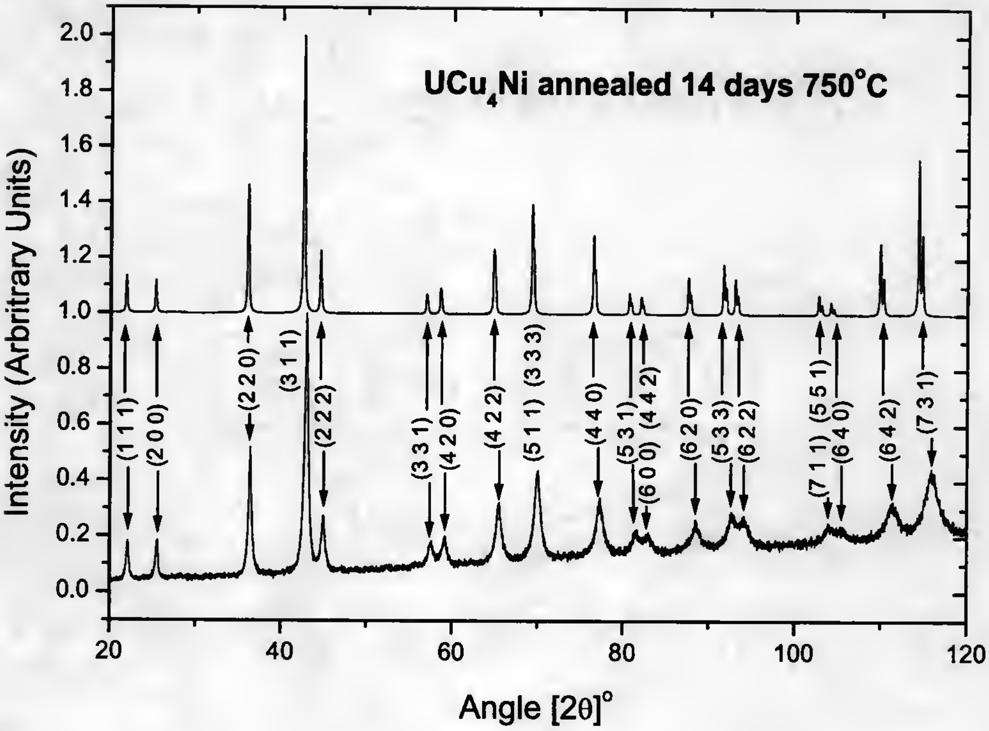

Figure A–1: Theoretical and experimental x-ray diffraction patterns for annealed UCu_4Ni. The top x-ray diffraction pattern is the theoretical pattern for UCu_5 that was generated from literature values [33, 155]. The bottom x-ray diffraction pattern is the experimental diffraction pattern for UCu_4Ni that was annealed 14 days at 750°C. The (hkl) values are pointed out for the theoretical and experimental x-ray diffraction patterns.

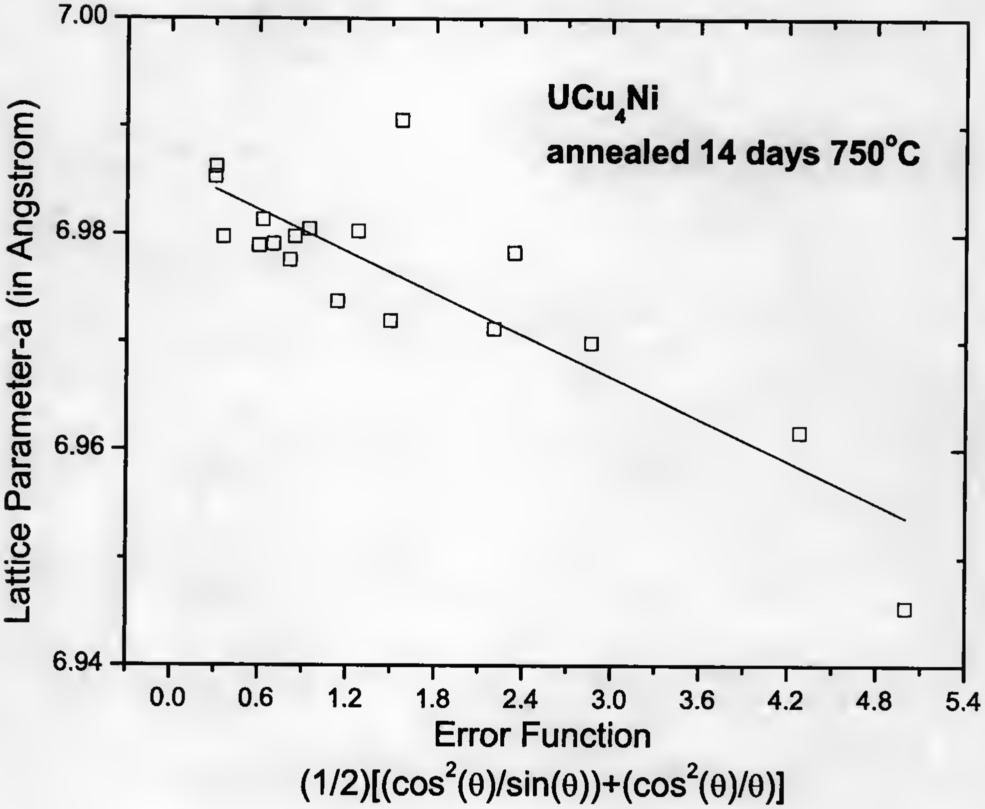

Figure A–2: Lattice parameter values versus corresponding error function values for annealed UCu_4Ni. The lattice parameter values are represented by the hollow squares. The best fit line equation for the lattice parameter values (a) versus the error function values (f) is a = 6.98616 - 0.00649 f. Thus, the intercept provides the lattice parameter value for annealed UCu_4Ni. The intercept has 0.00370 Å subtracted from it due to the x-ray machine's offset determined by running a standard piece of Si as discussed in the dissertation. After the subtraction, the 6.98246 Å value matches the value reported in Table 4–1 for annealed UCu_4Ni.

APPENDIX B
MAGNETORESISTANCE GRAPHS

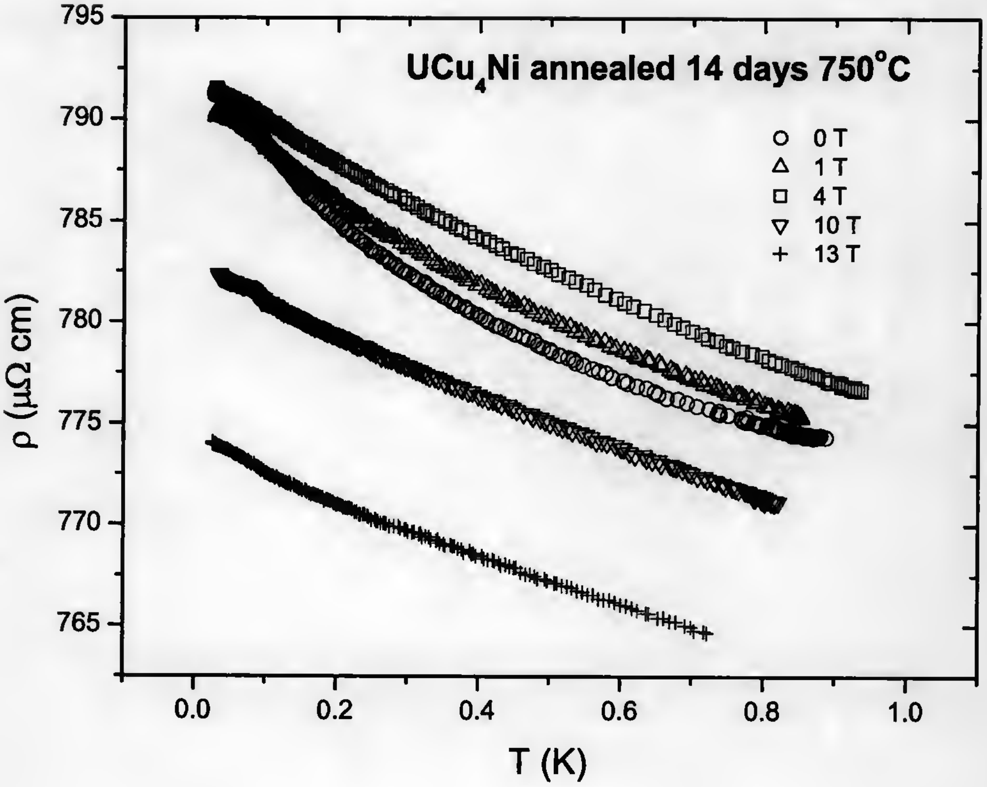

Figure B–1: Low temperature magnetoresistance measurements of annealed UCu_4Ni. The resistivity measurements were taken in fields of 0, 1, 4, 10, and 13 T. Best fit lines (not shown in the graph) were determined for each set of data: $\rho = 797 - 24.8\ T^{0.432}$ for H = 0 T, $\rho = 792 - 18.9\ T^{0.721}$ for H = 1 T, $\rho = 793 - 17.0\ T^{0.794}$ for H = 4 T, $\rho = 783 - 14.3\ T^{0.780}$ for H = 10 T, and $\rho = 775 - 13.0\ T^{0.762}$ for H = 13 T.

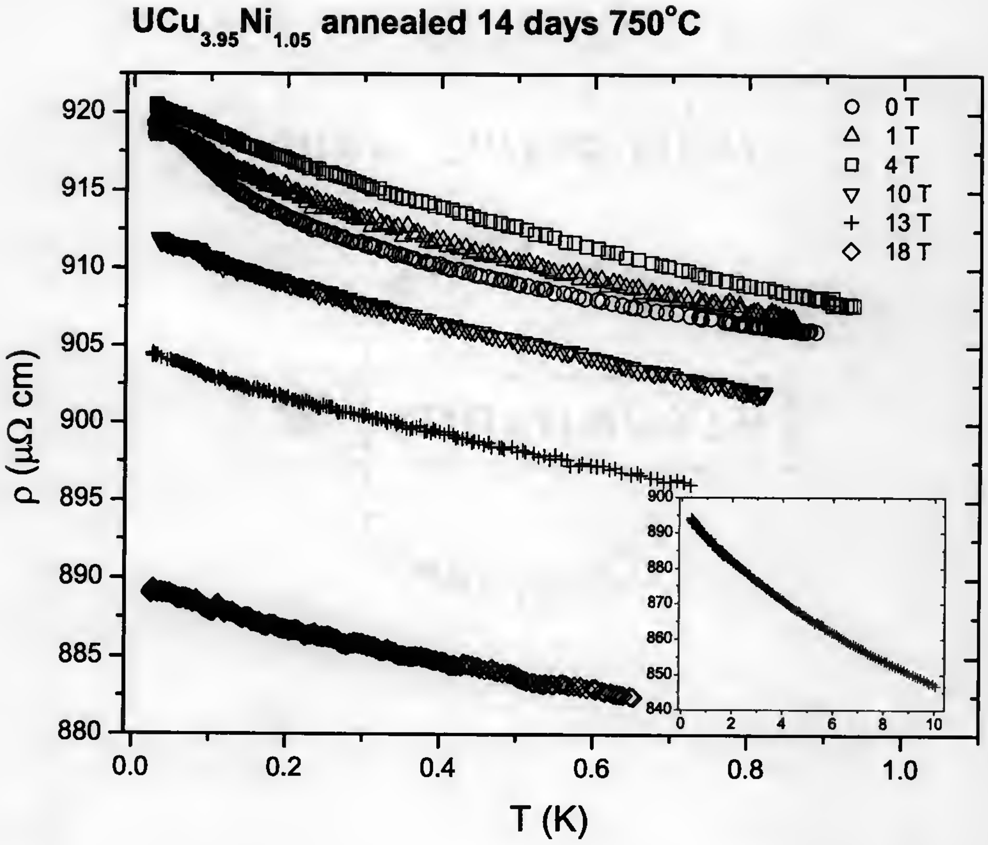

Figure B–2: Low temperature magnetoresistance measurements of annealed $UCu_{3.95}Ni_{1.05}$. The resistivity measurements were taken in fields of 0, 1, 4, 10, 13, and 18 T. The inset shows a larger temperature range for 13 T. The 13 T data in the inset and the primary graph are within 0.7% of each other at ~ 0.38 K despite having their resistivity taken with different probes. Best fit lines (not shown in the graph) were determined for each set of data: $\rho = 929 - 23.8\ T^{0.269}$ for H = 0 T, $\rho = 921 - 15.7\ T^{0.593}$ for H = 1 T, $\rho = 922 - 14.7\ T^{0.722}$ for H = 4 T, $\rho = 913 - 12.7\ T^{0.745}$ for H = 10 T, $\rho = 905 - 11.6\ T^{0.711}$ for H = 13 T, and $\rho = 890 - 10.4\ T^{0.750}$ for H = 18 T. $\rho = 900 - 11.7\ T^{0.662}$ is the best fit line for the 13 T data in the inset.

APPENDIX C
$UCu_{5-x}Ni_x$ MAGNETIC SUSCEPTIBILITY GRAPHS

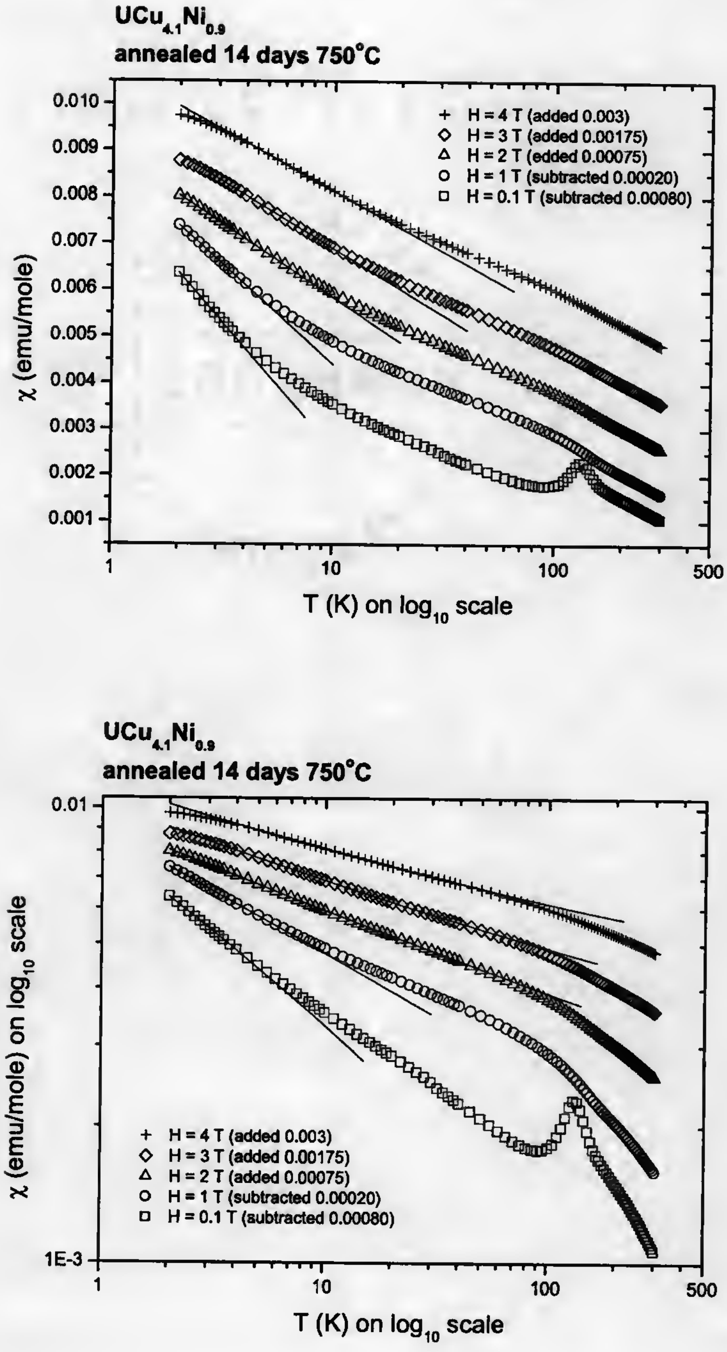

Figure C–1: Semilog and log-log plots of $UCu_{4.1}Ni_{0.9}$ dc susceptibility. The top graph is a semilog plot of annealed (14 days at 750°C) $UCu_{4.1}Ni_{0.9}$ dc magnetic susceptibility at various magnetic fields. The bottom graph is a log-log plot of the same dc magnetic susceptibility data. All best fit lines are stated explicitly in Tables 4–7, 4–8, and 4–9.

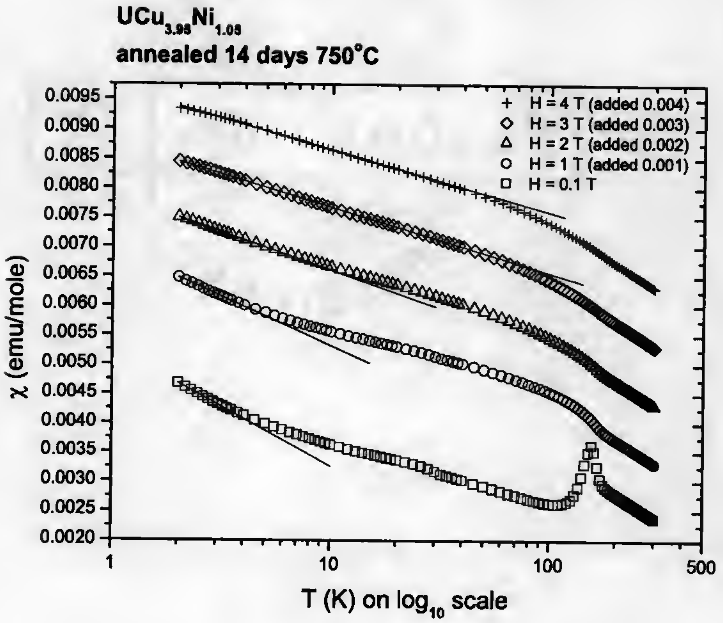

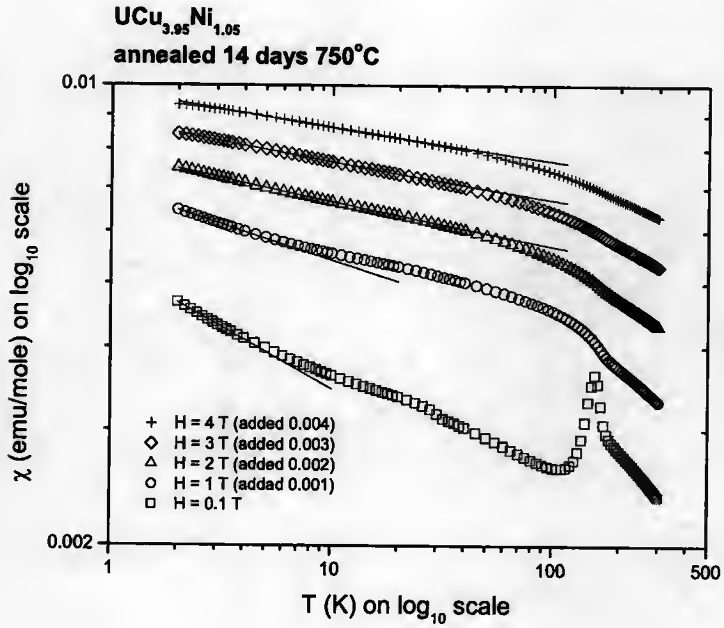

Figure C–2: Semilog and log-log plots of $UCu_{3.95}Ni_{1.05}$ dc susceptibility. The top graph is a semilog plot of annealed (14 days at 750°C) $UCu_{3.95}Ni_{1.05}$ dc magnetic susceptibility at various magnetic fields. The bottom graph is a log-log plot of the same dc magnetic susceptibility data. All best fit lines are stated explicitly in Tables 4–7, 4–8, and 4–9.

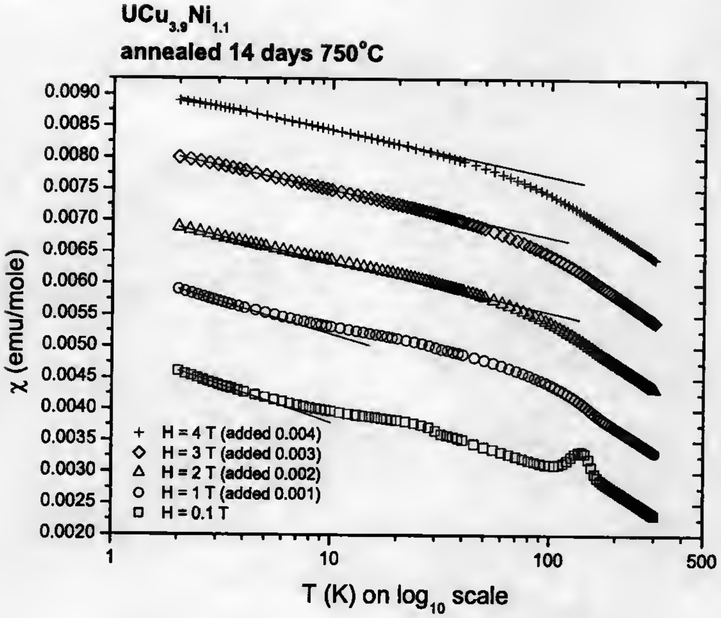

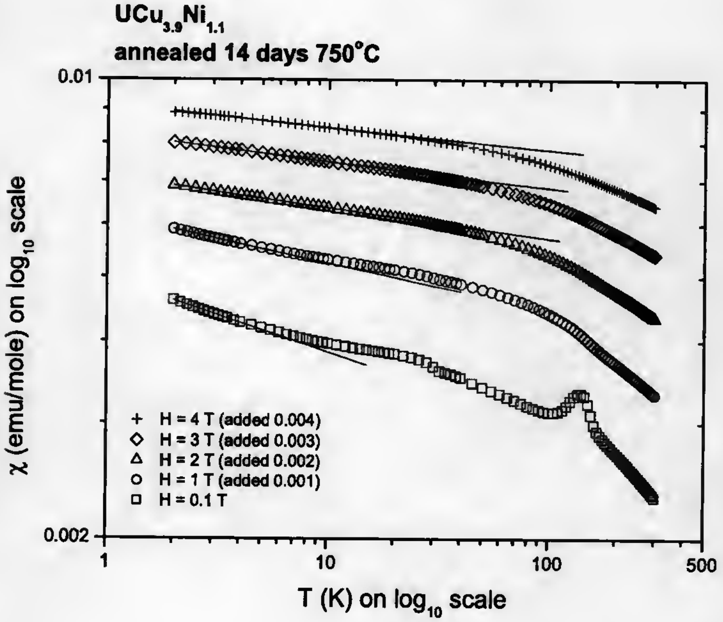

Figure C–3: Semilog and log-log plots of $UCu_{3.9}Ni_{1.1}$ dc susceptibility. The top graph is a semilog plot of annealed (14 days at 750°C) $UCu_{3.9}Ni_{1.1}$ dc magnetic susceptibility at various magnetic fields. The bottom graph is a log-log plot of the same dc magnetic susceptibility data. All best fit lines are stated explicitly in Tables 4–7, 4–8, and 4–9.

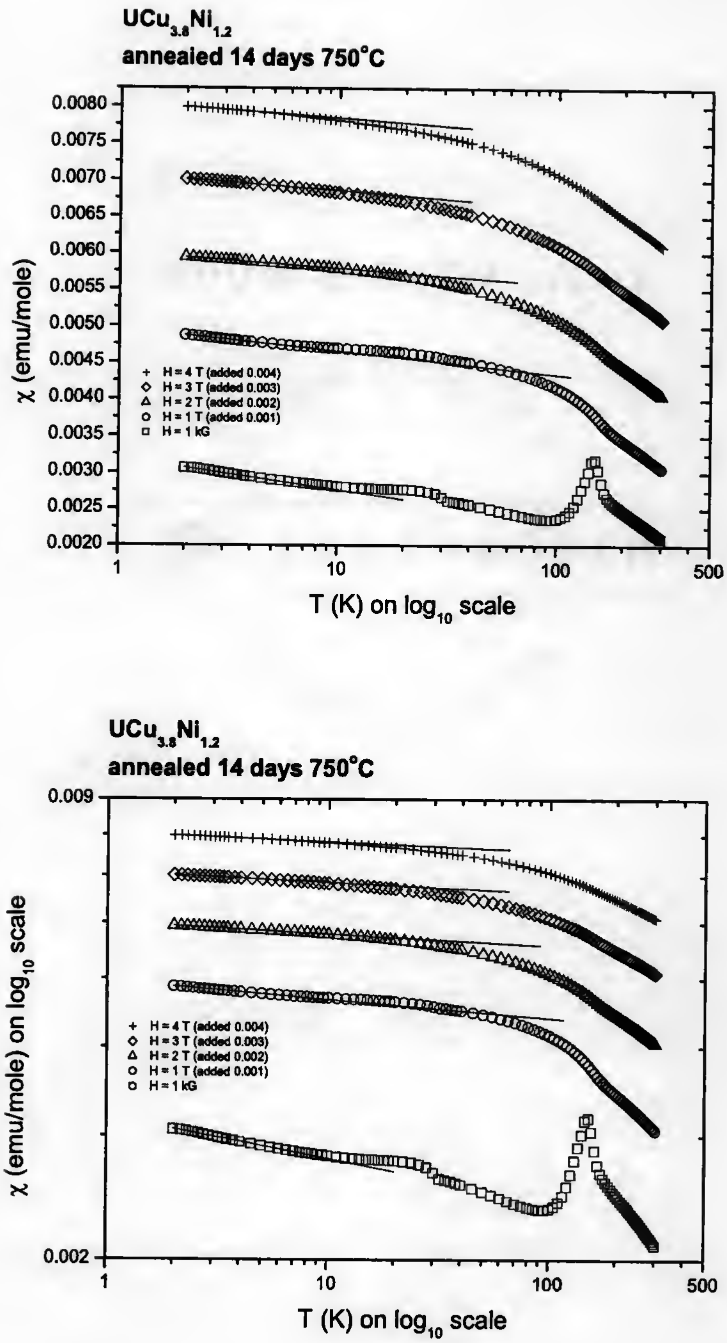

Figure C–4: Semilog and log-log plots of $UCu_{3.8}Ni_{1.2}$ dc susceptibility. The top graph is a semilog plot of annealed (14 days at 750°C) $UCu_{3.8}Ni_{1.2}$ dc magnetic susceptibility at various magnetic fields. The bottom graph is a log-log plot of the same dc magnetic susceptibility data. All best fit lines are stated explicitly in Tables 4–7, 4–8, and 4–9.

APPENDIX D
$UCu_{5-x}Ni_x$ SPECIFIC HEAT GRAPHS

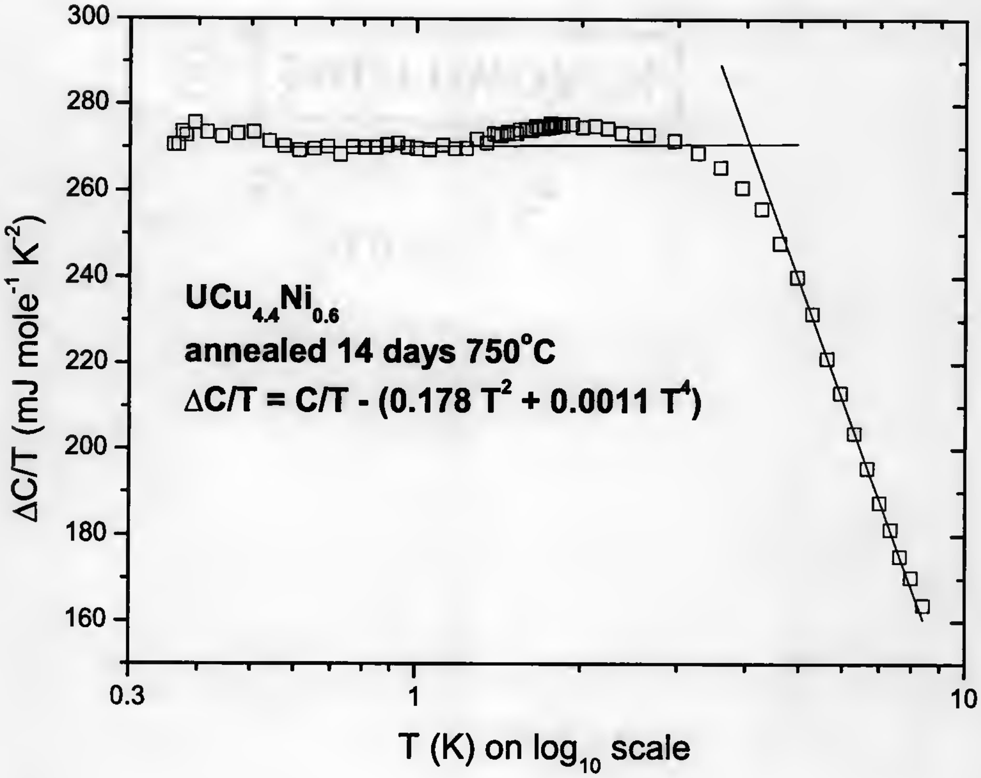

Figure D–1: The determination of $T_{Néel}$ for annealed $UCu_{4.4}Ni_{0.6}$. The determination was performed using annealed (14 days at 750°C) $UCu_{4.4}Ni_{0.6}$ specific heat results. The semilog plot was used to better illuminate the plateau below the $T_{Néel}$ value. The intersection of the two straight lines occurs at ~ 4.06 K with an uncertainty of 0.33 K, the temperature interval data points were taken around 4 K.

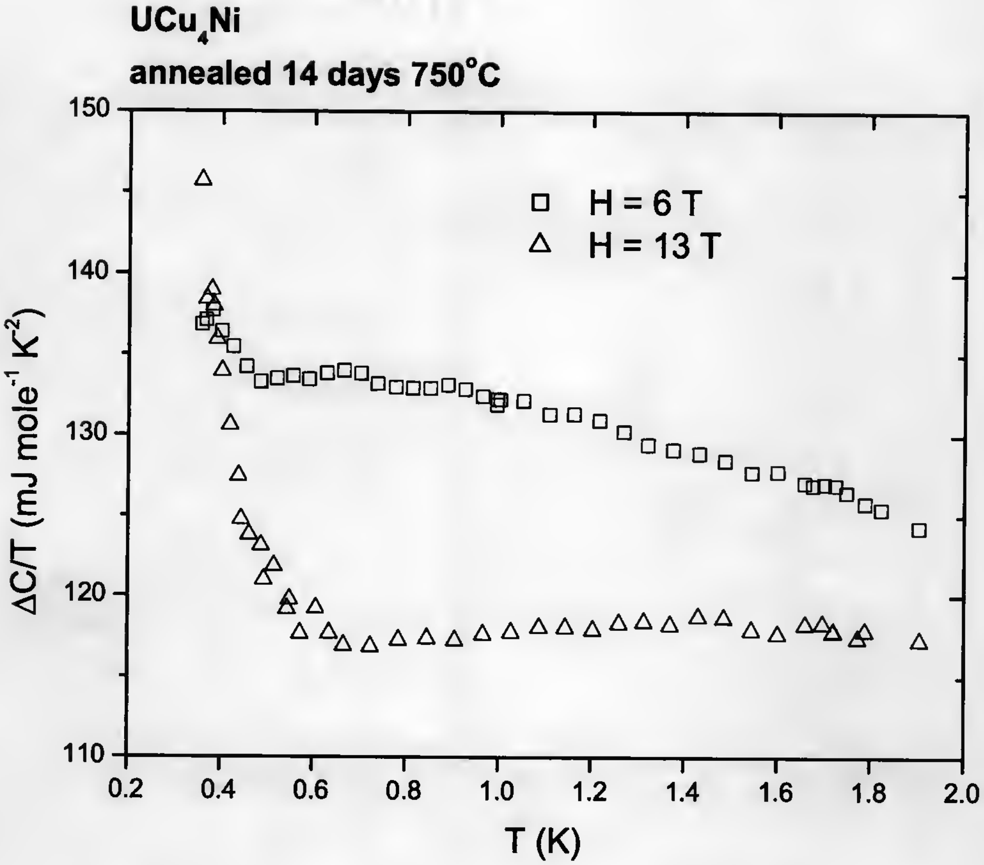

Figure D–2: Specific heat of annealed UCu_4Ni in 6 and 13 T. The specific heat data below 2 K is shown. The specific heat for both sets of data had the lattice contribution subtracted off: $\Delta C/T = C/T - 0.178T^2 - 0.0011T^4$. The upturns at the lowest measured temperatures are believed to be Schottky like anomalies due to the Cu atoms.

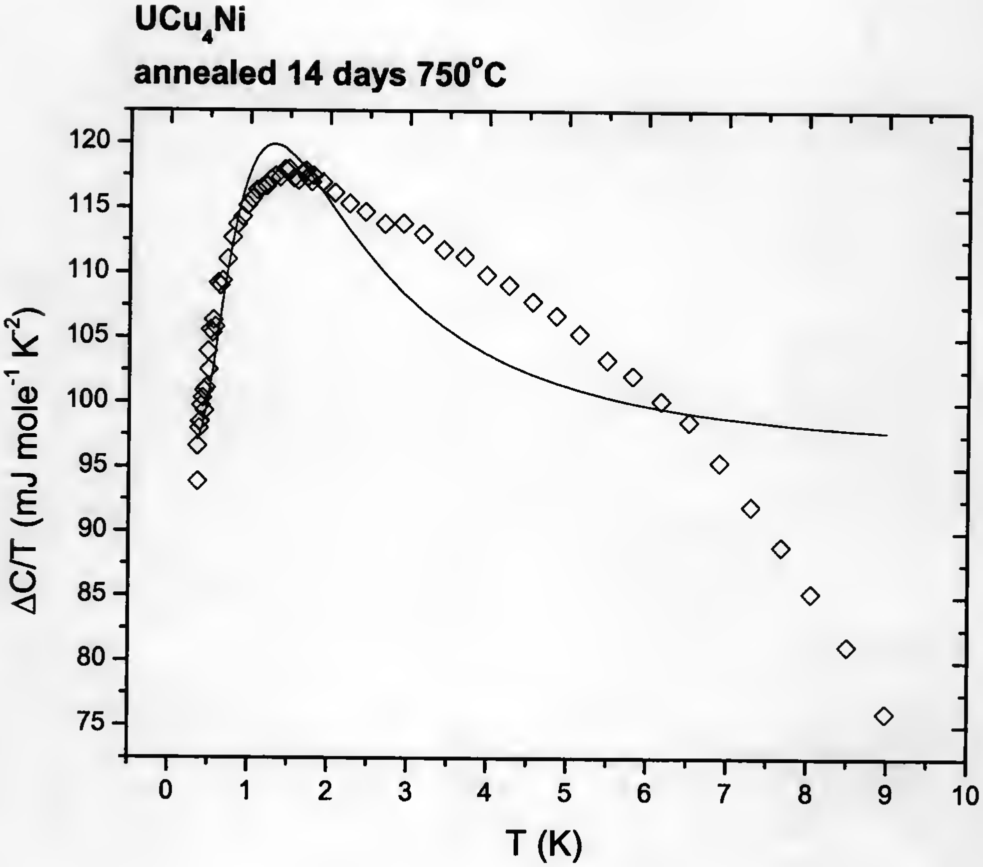

Figure D–3: Specific heat of UCu_4Ni in 13 T with Castro Neto-Jones fit. UCu_4Ni was annealed for 14 days at 750°C. The specific heat had its lattice and Schottky anomaly contributions subtracted off: $\Delta C/T = C/T - 0.178T^2 - 0.0011T^4 - 2.22/T^3$. The solid line is a Castro Neto-Jones fit to the 13 T data from 0.357 K to 8.98 K: $\Delta C/T = AH^{2+\lambda/2}e^{-H/T}/T^{3-\lambda/2} + D$ where $A = 32.7$, $H = 3.35$, $\lambda = 0.841$ (fixed from magnetization versus field data in Table 4–4), and $D = 96.3$.

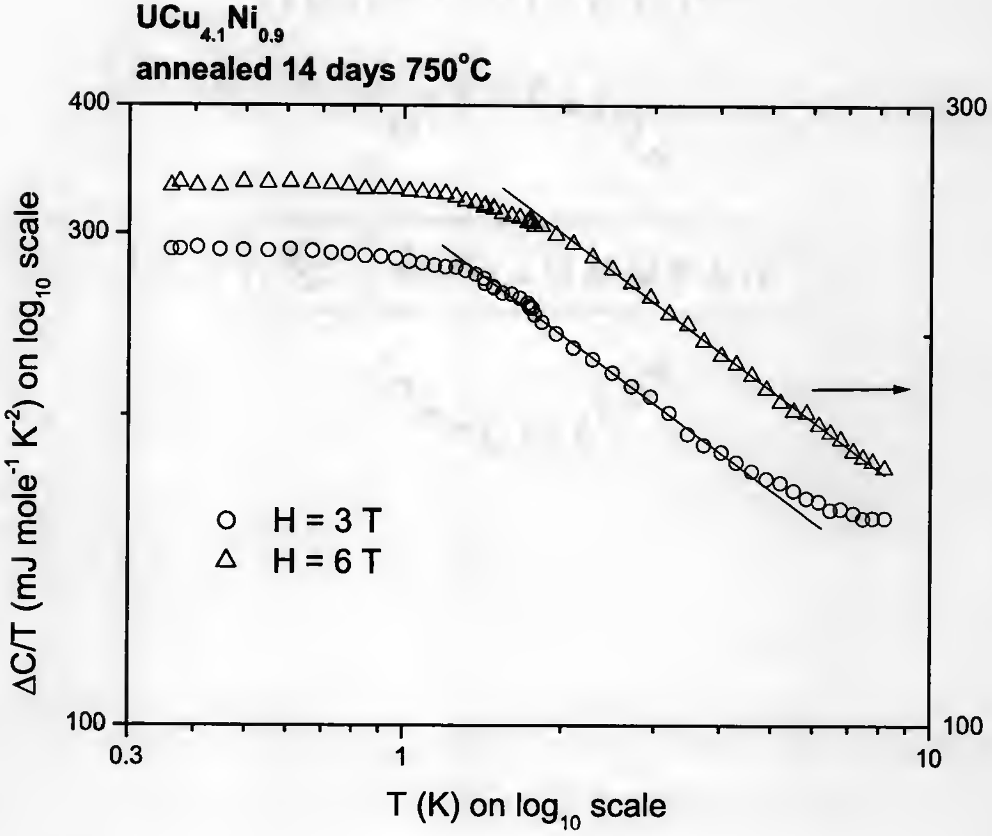

Figure D–4: $UCu_{4.1}Ni_{0.9}$ specific heat data in 3 T and 6 T on a log-log plot. The right hand axis applies to the 6 T data. The linear fits were determined with the maximum temperature range yielding the minimum standard deviation: H = 3 T - $\log_{10}(\Delta C/T) = 2.49 - 0.380\log_{10}T$ for $1.42 \leq T \leq 4.29$ K; and H = 6 T - $\log_{10}(\Delta C/T) = 2.47 - 0.303\log_{10}T$ for $2.10 \leq T \leq 7.46$ K. The specific heat data had the lattice contribution and Schottky anomaly contribution subtracted off: $\Delta C/T = C/T - (0.178T^2 + 0.0011T^4) - 0.0135H^2/T^3$.

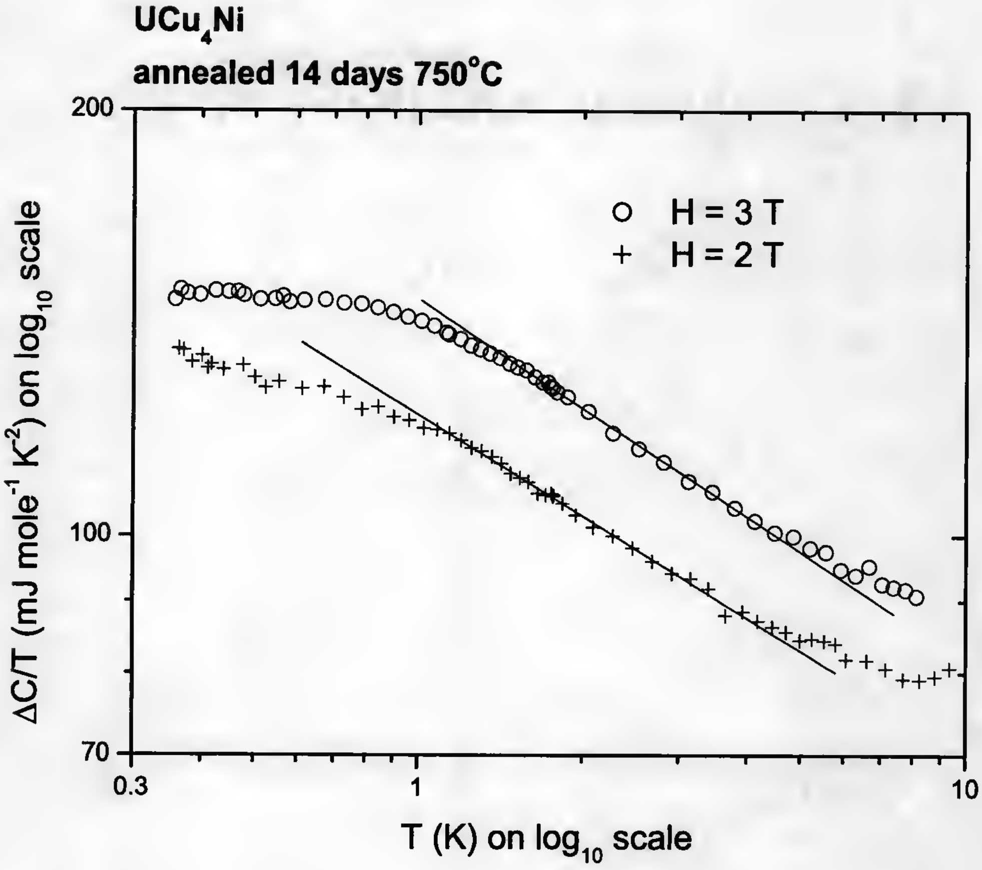

Figure D–5: UCu_4Ni specific heat data in 2 T and 3 T on a log-log plot. UCu_4Ni was annealed 14 days at 750°C. The linear fits were determined with the maximum temperature range yielding the minimum standard deviation: H = 2 T - $\log_{10}(\Delta C/T) = 2.09 - 0.239\log_{10}T$ for $1.20 \leq T \leq 4.18$ K; and H = 3 T - $\log_{10}(\Delta C/T) = 2.17 - 0.256\log_{10}T$ for $1.73 \leq T \leq 4.49$ K. The specific heat data have the lattice contribution and Schottky anomaly contribution subtracted off: $\Delta C/T = C/T - (0.178T^2 + 0.0011T^4) - 0.0132H^2/T^3$.

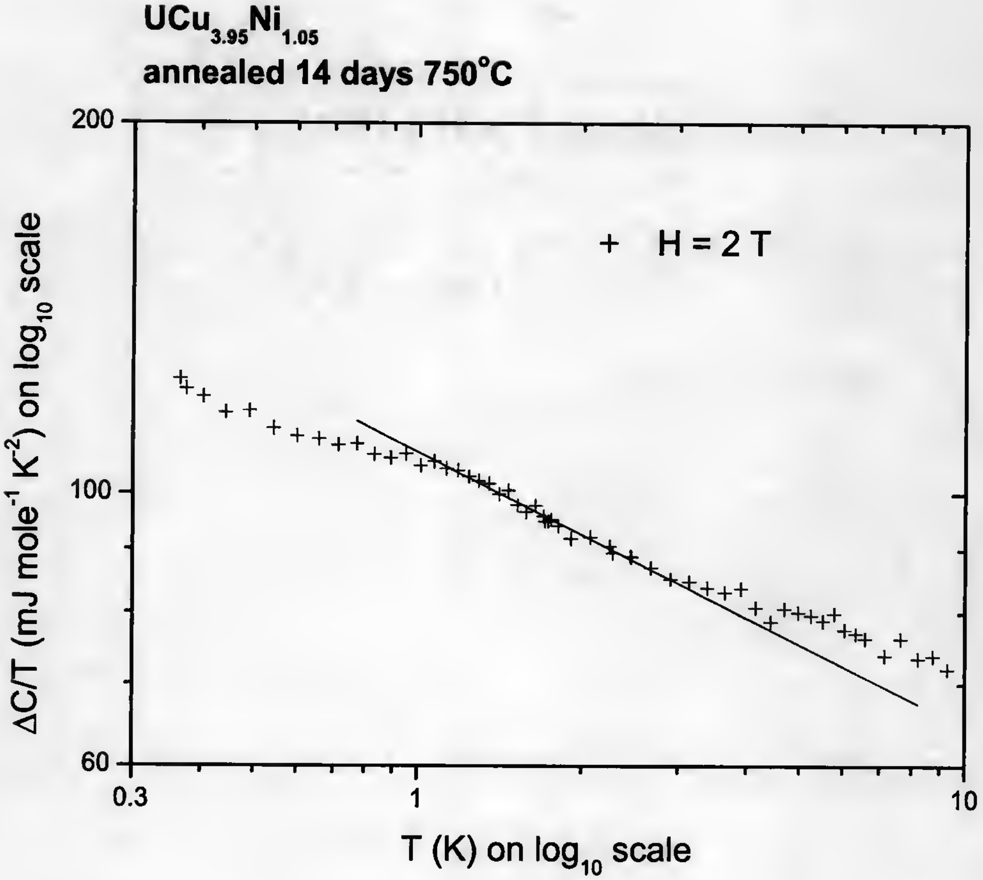

Figure D–6: $UCu_{3.95}Ni_{1.05}$ specific heat data in 2 T on a log-log plot. $UCu_{3.95}Ni_{1.05}$ was annealed for 14 days at 750°C. The linear fit was determined with the maximum temperature range yielding the minimum standard deviation: H = 2 T - $\log_{10}(\Delta C/T) = 2.03 - 0.223 \log_{10}T$ for $1.07 \leq T \leq 2.90$ K. The specific heat data have the lattice contribution and nuclear hyperfine contribution subtracted off: $\Delta C/T = C/T - (0.178T^2 + 0.0011T^4) - 0.0130H^2/T^3$.

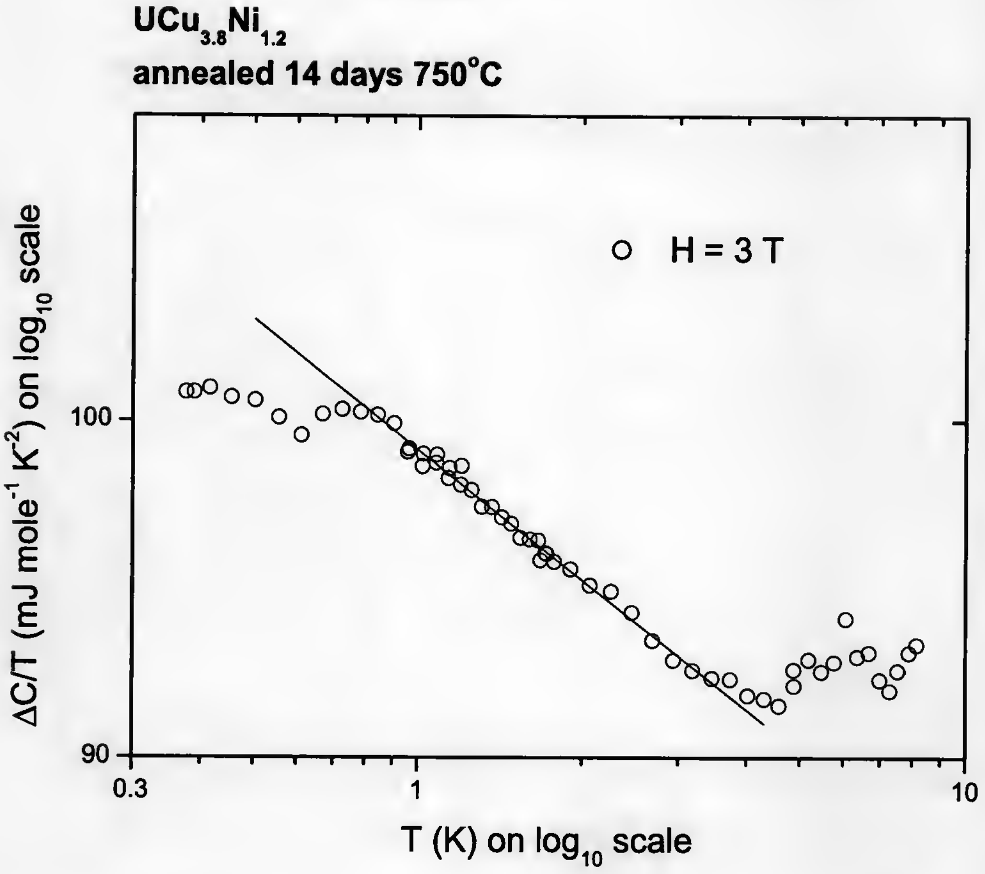

Figure D–7: $UCu_{3.8}Ni_{1.2}$ specific heat data in 3 T on a log-log plot. $UCu_{3.8}Ni_{1.2}$ was annealed for 14 days at 750°C. The linear fit was determined with the maximum temperature range yielding the minimum standard deviation: $\log_{10}(\Delta C/T) = 2.00 - 0.0587 \log_{10}T$ for $0.902 \leq T \leq 3.46$ K. The specific heat data have the lattice contribution and Schottky anomaly contribution subtracted off: $\Delta C/T = C/T - (0.178T^2 + 0.0011T^4) - 0.0125H^2/T^3$.

REFERENCES

[1] I. Affleck, A.W.W. Ludwig, H.-B. Pang, and D.L. Cox. *Phys. Rev. B*, 45:7918, 1992.

[2] M. Alonso and E. J. Finn. *Physics.* Addison-Wesley (Reading, MA), 1970.

[3] A. Amato, R. Feyerherm, F.N. Gygax, A. Schenck, H. von Löhneysen, and H.G. Schlager. *Phys. Rev. B*, 52:54, 1995.

[4] B. Andraka and G.R. Stewart. *Phys. Rev. B*, 47:3208, 1993.

[5] B. Andraka and A.M. Tsvelik. *Phys. Rev. Lett.*, 67:2886, 1991.

[6] A.V. Andreev, M. Diviš, P. Javorský, K. Prokeš, V. Sechovský, J. Kuneš, and Y. Shickawa. *Phys. Rev. B*, 64:144408.

[7] N.W. Ashcroft and N.D. Mermin. *Solid State Physics.* Holt, Rinehart, and Winston (New York), 1976.

[8] W. Assmus, M. Herrmann, U. Rauchschwalbe, S. Riegel, W. Lieke, H. Spille, S. Horn, G. Weber, F. Steglich, and G. Cordier. *Phys. Rev. Lett.*, 52:469, 1984.

[9] R. Bachmann, F.J. Disalvo Jr., T.H. Geballe, R.L. Greene, R.E. Howard, C.N. King, H.C. Kirsch, K.N. Lee, R.E. Schwall, H.-U. Thomas, and R.B. Zeebeck. *Rev. Sci. Instrum.*, 43:205, 1972.

[10] S.E. Barrett, R. Tycko, L.N. Pfeiffer, and K.W. West. *Phys. Rev. Lett.*, 72:1368, 1994.

[11] O.O. Bernal, D.E. MacLaughlin, H.G. Lukefahr, and B. Andraka. *Phys. Rev. Lett.*, 75:2023, 1995.

[12] R.N. Bhatt and D.S. Fisher. *Phys. Rev. Lett.*, 68:3072, 1992.

[13] B.M. Boerstoel, J.J. Zwart, and J. Hansen. *Physica*, 54:442, 1971.

[14] B. Bogenberger and H.v. Löhneysen. *Phys. Rev. Lett.*, 74:1016, 1995.

[15] C.H. Booth, D.E. MacLaughlin, R.H. Heffner, R. Chau, M.B. Maple, and G.H. Kwei. *Phys. Rev. Lett.*, 81:3960, 1998.

[16] C.H. Booth, E.-W. Scheidt, U. Killer, A. Weber, and S. Kehrein. *Phys. Rev. B*, 66:140402, 2002.

[17] E. Brezin. *Journal of Physics*, 43:15, 1982.

[18] K.H.J. Buschow, M. Brouha, H.J. van Daal, and A.R. Miedema. *Proceedings of an International Conference, Rochester, New York, 1976*, Valence Instabilities and Related Narrow-Band Phenomena:125–135, 1977.

[19] K.H.J. Buschow, A.S. van der Goot, and J. Birkhan. *Journal of the Less-Common Metals*, 19:433, 1969.

[20] A.H. Castro Neto, G. Castilla, and B.A. Jones. *Phys. Rev. Lett.*, 81:3531, 1998.

[21] A.H. Castro Neto and B.A. Jones. *Phys. Rev. B*, 62:14975, 2000.

[22] R. Chakravarthy, S.K. Paranjpe, and L. Madhav Rao. *Physica B*, 174:30, 1991.

[23] T.V. Chandrasekhar Rao, P. Raj, Sk. Mohammad Yusuf, L. Madhav Rao, A. Sathyamoorthy, and V.C. Sahni. *Philosophical Magazine B*, 74:275, 1996.

[24] C. Charmon and E.R. Mucciolo. *Phys. Rev. Lett.*, 85:5607, 2000.

[25] R. Chau. *Heavy Fermion and Non-Fermi Liquid Behavior in* $UCu_{5-x}M_x$ *(M = Pd,Pt)*. PhD thesis, University of California, San Diego, 1997.

[26] R. Chau and M.B. Maple. *J. Phys. Condens. Matter*, 8:9939, 1996.

[27] R. Chau, M.B. Maple, and R.A. Robinson. *Phys. Rev. B*, 58:139, 1998.

[28] L. Chełmicki, J. Leciejewicz, and A. Zygmunt. *J. Phys. Chem. Solids*, 46:529, 1985.

[29] X. Chen, M. Na, M. Cheon, S. Wang, H. Luo, B.D. McCombe, X. Liu, Y. Sasaki, T. Wojtowicz, J.K. Furdyna, S.J. Potashnik, and P. Schiffer. *Appl. Phys. Lett.*, 81:511, 2002.

[30] B. Coqblin and J.R. Schrieffer. *Physical Review*, 185:847, 1969.

[31] T.A. Costi and G. Zarand. *Phys. Rev. B*, 59:12398, 1999.

[32] D.L. Cox and A. Zawadowski. *Advances in Physics*, 47:599, 1998.

[33] J.L.C. Daams, P. Villars, and J.H.N. van Vucht. *Atlas of crystal structure types for intermetallic phases.* ASM International (Materials Park, OH), 1991.

[34] Y. Dalichaouch and M.B. Maple. *Physica B*, 199-200:176, 1994.

[35] Y. Dalichaouch, M.B. Maple, M.S. Torikachvili, and A.L. Giorgi. *Phys. Rev. B*, 39:2423, 1989.

[36] S. Das Sarma, E.H. Hwang, and A. Kaminski. *Solid State Communications*, 127:99, 2003.

[37] L.E. De Long, J.G. Huber, and K.S. Bedell. *J. Magn. Magn. Mat.*, 99:171, 1991.

[38] R.P. Dickey, A. Amann, E.J. Freeman, M.C. de Andrade, and M.B. Maple. *Phys. Rev. B*, 62:3979, 2000.

[39] V. Dobrosavljević, T.R. Kirkpatrick, and G. Kotliar. *Phys. Rev. Lett.*, 69:1113, 1992.

[40] S. Doniach. *Physica B*, 91:231, 1977.

[41] M. Dubman, H. Ettedgui, and M. Kuznietz. *J. Magn. Magn. Mat.*, 269:311, 2004.

[42] A.E. Dwight. *Trans. Am. Soc. Metals*, 53:479, 1961.

[43] A.E. Dwight. *The Rare Earths in Modern Science and Technology: [proceedings]*, volume 13. Plenum (New York), 1978.

[44] I.E. Dzyaloshinskii and P.S. Kondratenko. *Sov. Phys.-JETP*, 70:1987, 1976.

[45] T. Endstra, A.J. Dirkmaat, S.A.M. Mentink, A.A. Menovsky, G.J. Nieuwenhuys, and J.A. Mydosh. *Physica B*, 163:309, 1990.

[46] R.A. Fisher, D.A. Wright, J.P. Emerson, B.F. Woodfield, N.E. Phillips, Z.-R. Wang, and D.C. Johnston. *Phys. Rev. B*, 61:538, 2000.

[47] Z. Fisk, N.O. Moreno, and J.D. Thompson. *J. Phys. Condens. Matter*, 15:S1917, 2003.

[48] R.Q. Fugate and C.A. Swenson. *J. Appl. Phys.*, 40:3034, 1969.

[49] P. Fulde and A. Luther. *Physical Review*, 175:337, 1968.

[50] P. Fulde and A. Luther. *Phys. Rev.*, 170:570, 1968.

[51] J. Gal, M. Kroupp, Z. Hadari, and I. Nowik. *Phys. Rev.*, B16:3913, 1977.

[52] P. Gegenwart, J. Custers, C. Geibel, K. Neumaier, T. Tayarna, K. Tenya, O. Trovarelli, and F. Steglich. *Phys. Rev. Lett.*, 89:056402, 2002.

[53] P. Gegenwart, C. Langhammer, C. Geibel, R. Helfrich, M. Lang, G. Sparn, F. Steglich, R. Horn, L. Donnevert, A. Link, and W. Assmus. *Phys. Rev. Lett.*, 81:1501, 1998.

[54] Cryogenics Goddard Space Flight Center and Fluids Branch. Introduction to Liquid Helium.

http://cryowwwebber.gsfc.nasa.gov/introduction/liquid_helium.html, 02/22/2005.

[55] T. Graf, J.D. Thompson, M.F. Hundley, R. Movshovich, Z. Fisk, D. Mandrus, and R.A. Fisher. *Phys. Rev. Lett.*, 78:3769, 1997.

[56] D.R. Grempel and M.J. Rozenberg. *Phys. Rev. B*, 60:4702, 1999.

[57] R.B. Griffiths. *Phys. Rev. Lett.*, 23:17, 1969.

[58] F.M. Grosche, S.R. Julian, N.D. Mathur, and G.G. Lonzarich. *Physica B*, 223-224:50, 1996.

[59] F.D.M. Haldane. *Phys. Rev. Lett.*, 61:1029, 1988.

[60] J.A. Hertz. *Phys. Rev. B*, 14:1165, 1976.

[61] K. Heuser, J.S. Kim, E.-W. Scheidt, T. Schreiner, and G.R. Stewart. *Physica B*, 259-261:392, 1999.

[62] K. Hiebl. *Journal of the Physical Society of Japan*, 67:2048, 1998.

[63] K. Hiebl and P. Rogl. *Journal of Nuclear Materials*, 144:193, 1987.

[64] K. Hiebl, P. Rogl, C. Horvath, K. Remschnig, and H. Noël. *J. Appl. Phys.*, 67:943, 1990.

[65] H.H. Hill. *Plutonium 1970 and Other Actinides.* Met. Soc. AIME (New York), 1970.

[66] CRYO Industries. 3he Cryostats. http://www.cryoindustries.com/3he.pdf, 02/22/2005.

[67] S. Jin, T.H. Tiefel, M. McCormack, R.A. Fastnacht, R. Ramesh, and L.H. Chen. *Science*, 264:413, 1994.

[68] S.R. Julian, C. Pfleiderer, F.M. Grosche, N.D. Mathur, G.J. McMullan, A.J. Diver, I.R. Walker, and G.G. Lonzarich. *J. Phys. Condens. Matter*, 8:9675, 1996.

[69] M.H. Jung, K. Umeo, T. Fujita, and T. Takabatake. *Phys. Rev. B*, 62:11609, 2000.

[70] A.B. Kaiser and S. Doniach. *Intern. J. Magnetism*, 1:11, 1970.

[71] J. S. Kim. *Doping Experiments in Heavy Fermion Superconductors.* PhD thesis, University of Florida, 1992.

[72] J.S. Kim, J. Alwood, S.A. Getty, F. Sharifi, and G.R. Stewart. *Phys. Rev. B*, 62:6986, 2000.

[73] J.S. Kim, J. Alwood, D. Mixson, P. Watts, and G.R. Stewart. *Phys. Rev. B*, 66:134418, 2002.

[74] J.S. Kim, E.W. Scheidt, D. Mixson, B. Andraka, and G.R. Stewart. *Phys. Rev. B*, 67:184401, 2003.

[75] Tae-Suk Kim and D.L. Cox. *Phys. Rev. Lett.*, 75:1622, 1995.

[76] J. Kondo. *Progress of Theoretical Physics*, 32:37, 1964.

[77] S. Körner, A. Weber, J. Hemberger, E.-W. Scheidt, and G.R. Stewart. *Journal of Low Temperature Physics*, 121:105, 2000.

[78] M. Kuznietz. *J. Phys. Condens. Matter*, 15:8957, 2003.

[79] M. Kuznietz, H. Pinto, H. Ettedgui, and M. Melamud. *Phys. Rev. B*, 48:3183, 1993.

[80] M. Kuznietz, H. Pinto, and M. Melamud. *J. Magn. Magn. Mat.*, 83:321, 1990.

[81] M. Kuznietz, H. Pinto, and M. Melamud. *Phys. Rev. B*, 51:16410, 1995.

[82] M. Kuznietz, H. Pinto, and M. Melamud. *Physica B*, 223 & 224:234, 1996.

[83] L.D. Landau. *Sov. Phys.-JETP*, 3:920, 1957.

[84] L.D. Landau. *Sov. Phys.-JETP*, 5:101, 1957.

[85] L.D. Landau. *Sov. Phys.-JETP*, 8:70, 1958.

[86] J.C. Lashley, M.F. Hundley, A. Migliori, J.L. Sarrao, P.G. Pagliuso, T.W. Darling, M. Jaime, J.C. Cooley, W.L. Hults, L. Morales, D.J. Thoma, J.L. Smith, J. Boerio-Goates, B.F. Woodfield, G.R. Stewart, R.A. Fishers, and N.E. Phillips. *Cryogenics*, 43:369, 2003.

[87] M. Lenkewitz, S. Corsépius, G.-F. v. Blanckenhagen, and G.R. Stewart. *Phys. Rev. B*, 55:6409, 1997.

[88] M.A. López de la Torre, M.A. Arranz, M. Ellerby, and K.A. McEwen. *J. Phys. Condens. Matter*, 15:2599, 2003.

[89] M.A. López de la Torre, M. Ellerby, M. Watmough, and K.A. McEwen. *J. Magn. Magn. Mat.*, 177-181:445, 1998.

[90] M.A. López de la Torre, J.A. González, A. Izquierdo, S. Vieira, M. Ellerby, and K.A. McEwen. *J. Appl. Phys.*, 87:5126, 2000.

[91] A.W.W. Ludwig and I. Affleck. *Phys. Rev. Lett.*, 67:3160, 1991.

[92] D.E. MacLaughlin, R.H. Heffner, G.J. Nieuwenhuys, G.M. Luke, Y. Fudamoto, Y.J. Uemura, R. Chau, M.B. Maple, and B. Andraka. *Phys. Rev. B*, 58:11849, 1998.

[93] D.E. MacLaughlin, M.S. Rose, Ben-Li Young, O.O. Bernal, R.H. Heffner, G.D. Morris, K. Ishida, G.J. Nieuwenhuys, and J.E. Sonier. *Physica B*, 326:381, 2003.

[94] Dinesh Martien. Introduction to AC Susceptibility. http://www.qdusa.com/resources/pdf/1078-201.pdf, 02/22/2005.

[95] N.D. Mathur, F.M. Grosche, S.R. Julian, I.R. Walker, D.M. Freye, R.K.W. Haselwimmer, and G.G. Lonzarich. *Nature(London)*, 394:39, 1998.

[96] M.W. McElfresh, L. Rebelsky, M.S. Torikachvili, H. Borges, K. Reilly, S. Horn, and M.B. Maple. *J. Appl. Phys.*, 67:5218, 1990.

[97] A.J. Millis. *Phys. Rev. B*, 48:7183, 1993.

[98] E. Miranda, V. Dobrosavljević, and G. Kotliar. *J. Phys. Condens. Matter*, 8:9871, 1996.

[99] E. Miranda, V. Dobrosavljević, and G. Kotliar. *Physica B*, 230-232:569, Feb 1997.

[100] E. Miranda, V. Dobrosavljević, and G. Kotliar. *Phys. Rev. Lett.*, 78:290, 1997.

[101] A. Misiuk, J. Mulak, and A. Czopnik. *Bull. Acad. Pol. Sci.*, 21:487, 1973.

[102] Sk. Mohammad Yusuf, L. Madhav Rao, and P. Raj. *Phys. Rev. B*, 53:28, 1996.

[103] T. Moriya and T. Takimoto. *Journal of the Physical Society of Japan*, 64:960, 1995.

[104] A. Murasik, S. Ligenza, and A. Zygmunt. *Phys. Status Solidi (a)*, page K163, 1974.

[105] J.A. Mydosh. *Spin glasses: an experimental introduction.* Taylor and Francis (London; Washington, DC), 1993.

[106] M.J. Naughton, S. Dickinson, R.C. Samaratunga, J.S. Brooks, and K.P. Martin. *Rev. Sci. Instrum.*, 54:1529, 1983.

[107] J.B. Nelson and D.P. Riley. *Proc. Phys. Soc.*, 57:160, 1945.

[108] D.R. Noakes, A.M. Umarji, and G.K. Shancy. *J. Magn. Magn. Mat.*, 39:309, 1983.

[109] C.H. de Novion, J. Gal, and J.L. Buevoz. *J. Magn. Magn. Mat.*, 21:85, 1980.

[110] H. Ohno. *Science*, 281:951, 1998.

[111] H. Ohno. *Science*, 281:951, 1998.

[112] H. Ohno. *J. Magn. Magn. Mater.*, 200:110, 1999.

[113] H. Ohno, H. Munekata, T. Penney, S. von Molnár, and L. Chang. *Phys. Rev. Lett.*, 68:2664, 1992.

[114] H. Ohno, A. Shen, F. Matsukura, A. Oiwa, A. Endo, S. Katsumoto, and Y. Iye. *Appl. Phys. Lett.*, 69:363, 1996.

[115] Y. Onuki, T. Yamazeki, I. Ukon, T. Komatsubara, H. Sato, Y. Sugiyama, I. Sakamoto, and K. Yonemitsu. *J. Phys. (Paris) Suppl.*, 12:49,C8–481, 1988.

[116] D.W. Osborne, H.E. Flotow, and F. Schreiner. *Rev. Sci. Instrum.*, 38:159, 1967.

[117] H.R. Ott, H. Rudigier, E. Felder, Z. Fisk, and B. Batlogg. *Phys. Rev. Lett.*, 55:1595, 1985.

[118] Y.D. Park, A.T. Hanbicki, S.C. Irwin, C.S. Hellberg, J.M. Sullivan, J.E. Mattson, T.F. Ambrose, A. Wilson, G. Spanos, and B.T. Jonker. *Science*, 295:651, 2002.

[119] H.S. Peiser, H.P. Roaksby, and A.J.C. Wilson, editors. *X-Ray Diffraction by Polycrystalline Materials.* Reinhold Publishing Corporation (London), 1960.

[120] W.P. Pratt, S.S. Rosenblum, W.A. Steyert, and J.A. Barclay. *Cryogenics*, 17:689, 1977.

[121] V. Privman and M.E. Fisher. *Journal of Statistical Physics*, 33:385, 1983.

[122] H. Ptasiewicz-Bak, J. Leciejewicz, and A. Zygmunt. *J. Phys. F: Metal Phys.*, 11:1225, 1981.

[123] N. Read and S. Sachdev. *Nuclear Physics B*, 316:609, 1989.

[124] N. Read and S. Sachdev. *Phys. Rev. Lett.*, 75:3509, 1995.

[125] M.L. Reed, N.A. El-Masry, H.H. Stadelmaier, M.K. Ritums, M.J. Reed, C.A. Parker, J.C. Roberts, and S.M. Bedair. *Appl. Phys. Lett.*, 79:3473, 2001.

[126] A. Rosch. *Phys. Rev. Lett.*, 82:4280, 1999.

[127] S.B. Roy, A.K. Pradhan, and P. Chaddah. *Physica B*, 223&224:198, 1996.

[128] S.B. Roy, A.K. Pradhan, P. Chaddah, and B.R. Coles. *Solid State Communications*, 99:563, 1996.

[129] P.D. Sacramento and P. Schlottmann. *J. Phys. Condens. Matter*, 3:9687, 1991.

[130] E.-W. Scheidt, T. Schreiner, K. Heuser, S. Koerner, and G.R. Stewart. *Phys. Rev. B*, 58(16), 1998.

[131] A.I. Schindler and M.J. Rice. *Phys. Rev.*, 164:759, 1967.

[132] P. Schlottmann and P.D. Sacramento. *Advances in Physics*, 42:641, 1993.

[133] W.D. Schneider, B. Reihle, N. Mårtenson, and A.J. Arko. *Phys. Rev. B*, 26:423, 1982.

[134] A.J. Schofield. *Contemporary Physics*, 40:95, 1999.

[135] K.D. Schotte and U. Schotte. *Phys. Lett.*, 55A:38, 1975.

[136] C.L. Seaman, M.B. Maple, B.W. Lee, S. Ghamaty, M.S. Torikachvili, J.-S. Kang, L.Z. Liu, J.W. Allen, and D.L. Cox. *Phys. Rev. Lett.*, 67:2882, 1991.

[137] M.B. Silva Neto and A.H. Castro Neto. *Europhysics Letters*, 62:890, 2003.

[138] M.B. Silva Neto, A.H. Castro Neto, D. Mixson, J.S. Kim, and G.R. Stewart. *Phys. Rev. Lett.*, 91:257206, 2003.

[139] S.L. Sondhi, S.M. Girvin, J.P. Carini, and D. Shahar. *Rev. Mod. Phys.*, 69:315, 1997.

[140] F. Steglich, B. Buschinger, P. Gegenwart, M. Lohmann, R. Helfrich, C. Langhammer, P. Hellmann, L. Donnevert, S. Thomas, A. Link, C. Geibel, M. Lang, G. Sparn, and W. Assmus. *J. Phys. Condens. Matter*, 8:9909, 1996.

[141] G.R. Stewart. *Rev. Sci. Instrum.*, 54:1, 1983.

[142] G.R. Stewart. *Rev. Mod. Phys.*, 56:755, 1984.

[143] G.R. Stewart. *Rev. Mod. Phys.*, 73:797, 2001.

[144] P.F. Sullivan and G. Seidel. *Phys. Rev. B*, 173:679, 1968.

[145] T. Takeshita, S.K. Malik, and W.E. Wallace. *J. Solid State Chem.*, 23:225, 1977.

[146] N. Theodoropoulou, A.F. Hebard, M.E. Overberg, C.R. Abernathy, S.J. Pearton, S.N.G. Chu, and R.G. Wilson. *Phys. Rev. Lett.*, 89:107203, 2002.

[147] M.J. Thill and D.A. Huse. *Physica A*, 214:321, 1995.

[148] C. Tien, C.S. Wur, I.J. Jang, K.J. Lin, J.S. Hwang, H.M. Duh, and J.I. Yuh. *Phys. Rev. B*, 51:1297, 1995.

[149] B.B. Triplett and N.E. Phillips. *Proceedings of the 12th International Conference on Low Temperature Physics, Kyoto, September 1970.* Academic Press of Japan, Keigaku Publ. Co. (Tokyo, Japan), 1971.

[150] R. Troc', V.H. Tran, and Z. Zolnierek. *J. Magn. Magn. Mater.*, 90-91:405, 1990.

[151] O. Trovarelli, C. Geibel, S. Mederle, C. Langhammer, F.M. Grosche, P. Gegenwart, M. Lang, G. Sparn, and F. Steglich. *Phys. Rev. Lett.*, 85:626, 2000.

[152] A. Tsvelik and M. Reizer. *Phys. Rev. B*, 48:9887, 1993.

[153] H.J. van Daal, K.H.J. Buschow, P.B. van Aken, and M.H. van Maaren. *Phys. Rev. Lett.*, 34:1457, 1975.

[154] C.M. Varma, P.B. Littlewood, S. Schmitt-Rink, E. Abrahams, and A.E. Ruckestein. *Phys. Rev. Lett.*, 63:1996, 1989.

[155] P. Villars and L.D. Calvert. *Pearson's handbook of crystallographic data for intermetallic phases.* ASM International (Materials Park, OH), second edition, 1991.

[156] R. Vollmer, S. Mock, T. Pietrus, H.v. Löhneysen, R. Chau, and M.B. Maple. *Physica B*, 230-232:603, 1997.

[157] H. von Löhneysen. *J. Phys. Condens. Matter*, 8:9689, 1996.

[158] H. von Löhneysen, T. Pietrus, G. Portisch, H.G. Schlager, A. Schröder, M. Sieck, and T. Trappmann. *Phys. Rev. Lett.*, 72:3262, 1994.

[159] U. Waltzer, M. Loewenhaupt, E. Holland-Moritz, and W. Schlabitz. *Phys. Rev. B*, 36:1981, 1987.

[160] A. Weber, S. Körner, E.-W. Scheidt, S. Kehrein, and G.R. Stewart. *Phys. Rev. B*, 63:205116, 2001.

[161] R. Welter, K. Halich, and B. Malaman. *Journal of Alloys and Compounds*, 353:48, 2003.

[162] R.M. White and T.H. Geballe. *Long Range Order in Solids.* Academic Press (New York), 1979.

[163] K.G. Wilson. *Rev. Mod. Phys.*, 47:773, 1975.

[164] Y. Yamamoto, Y. Miyako, S. Kawarazaki, T. Takeuchi, M. Ocio, P. Pari, J. Hammann, I. Watanabe, K. Nishiyama, K. Simomura, and K. Nagamine. *Physica B*, 259-261:66, 1999.

[165] Y. Yamamoto, Y. Miyako, T. Takeuchi, M. Ocio, P. Pari, J. Hammann, I. Watanabe, K. Nishiyama, K. Shimomura, and K. Nagamine. *RIKEN Rev., Inst. Phys. Chem. Res. (RIKEN)*, 20:44, 1999.

[166] X.G. Zheng, T. Mori, K. Nishiyama, W. Higemoto, and C.N. Xu. *Solid State Communications*, 132:493, 2004.

[167] J.M. Ziman. *The Theory of Transport Phenomena in Solids.* Oxford University Press (London), 1962.

BIOGRAPHICAL SKETCH

Daniel Mixson was born in Orlando, FL, on May 17, 1977. Daniel lived in Gainesville, FL, from 1978 to 1990. Daniel moved with his family to Melbourne, FL, and lived there from 1990 to 1995. During the Summer of 1994, he participated in the Summer Science Training Program (SSTP) at the University of Florida (UF). In 1995, Daniel graduated from Eau Gallie High School.

Daniel lived in Starkville, MS, from 1995 to 1999 where he attended Mississippi State University (MSU). Daniel graduated from MSU in 1999 with a Bachelor of Science in physics.

Daniel lived in Gainesville, FL, from 1999 to 2005 to attend UF for graduate studies. One of the highlights of his graduate career was being able to work at Los Alamos National Laboratory (LANL) in New Mexico for the Summer of 2004.

I certify that I have read this study and that in my opinion it conforms to acceptable standards of scholarly presentation and is fully adequate, in scope and quality, as a dissertation for the degree of Doctor of Philosophy.

G R Stewart

Gregory R. Stewart, Chair
Professor of Physics

I certify that I have read this study and that in my opinion it conforms to acceptable standards of scholarly presentation and is fully adequate, in scope and quality, as a dissertation for the degree of Doctor of Philosophy.

Bohdan Andraka
Associate Scientist of Physics

I certify that I have read this study and that in my opinion it conforms to acceptable standards of scholarly presentation and is fully adequate, in scope and quality, as a dissertation for the degree of Doctor of Philosophy.

Pradeep Kumar

Pradeep Kumar
Professor of Physics

I certify that I have read this study and that in my opinion it conforms to acceptable standards of scholarly presentation and is fully adequate, in scope and quality, as a dissertation for the degree of Doctor of Philosophy.

Dinesh O. Shah

Dinesh Shah
Professor of Chemical Engineering

I certify that I have read this study and that in my opinion it conforms to acceptable standards of scholarly presentation and is fully adequate, in scope and quality, as a dissertation for the degree of Doctor of Philosophy.

David Tanner
Distinguished Professor of Physics

This dissertation was submitted to the Graduate Faculty of the Department of Physics in the College of Liberal Arts and Sciences and to the Graduate School and was accepted as partial fulfillment of the requirements for the degree of Doctor of Philosophy.

May 2005

Dean, Graduate School

DIFFERING ROLES OF DISORDER: NON-FERMI-LIQUID BEHAVIOR IN $UCu_{5-x}Ni_x$ AND CURIE TEMPERATURE ENHANCEMENT IN $UCu_2Si_{2-x}Ge_x$

Daniel J. Mixson II
(352) 392–0477
Department of Physics
Chair: Gregory R. Stewart
Degree: Doctor of Philosophy
Graduation Date: May 2005

Disorder is created when an element on the periodic chart of elements replaces atoms of another element in a metallic compound. Cu atoms in UCu_5 are replaced by Ni atoms while Si atoms are replaced by Ge atoms in UCu_2Si_2.

The low temperature (< 20 K) magnetic behavior of UCu_5 is suppressed towards zero as the Ni atoms replace the Cu atoms. The magnetism is suppressed to zero for UCu_4Ni and the low temperature physical properties for UCu_4Ni (and adjacent Ni concentrations) display atypical metallic properties. The $UCu_{5-x}Ni_x$ results test theorists' predictions that try to describe such abnormal, low temperature properties.

The replacement of semiconducting Si atoms by semiconducting Ge atoms enhances the magnetic transition temperature nonlinearly in UCu_2Si_2. Measurements upon $UCu_2Si_{2-x}Ge_x$ reveal information about the interactions occurring on the microscopic level. These interactions that lead to transition temperature enhancement could have important implications for semiconductor technology.

LD
1780
20 05
.M685

UNIVERSITY OF FLORIDA
3 1262 08554 2602